

# **Tribochemical Investigation of ZDDP Tribofilm**

by

Mao Ueda

Thesis submitted to Imperial College London for the Degree of Doctor of  
Philosophy and Diploma of Imperial College (D.I.C.)

Department of Mechanical Engineering  
Imperial College London

September 2021

## **DECLARATION of AUTHORSHIP**

I, Mao Ueda, declare that this thesis titled, “Tribochemical investigation of ZDDP tribofilm” and the work presented in it is my own.

I confirm that:

- This dissertation is the result of my own work done during my PhD studentship at Imperial College London.
- Where I have consulted the published work of others, this is always clearly attributed.
- Where I have quoted from the work of others, the source is always given.
- I have acknowledged all main sources of help.
- Where the thesis is based on work done by myself jointly with others, I have made clear exactly what was done by others and what I have contributed myself.

The copyright of this thesis rests with the author and is made available under a Creative Commons Attribution Non-Commercial No Derivatives licence. Researchers are free to copy, distribute or transmit the thesis on the condition that they attribute it, that they do not use it for commercial purposes and that they do not alter, transform or build upon it. For any reuse or redistribution, researchers must make clear to others the licence terms of this work.

Mao Ueda,

Date: 29.09.2021

## ABSTRACT

The current trend for using lower-viscosity lubricants with the aim of improving fuel efficiency of mechanical systems means that machine components are required to operate for longer periods in thin oil film, mixed and boundary lubrication conditions, where the risk of surface damage is increased. For this reason, the role of tribofilms generated from the antiwear additive zinc dialkyldithiophosphate (ZDDP) in providing surface protection has become increasingly important. However, the properties, performance and the mechanisms of tribofilm formation are not fully understood. Therefore, this thesis aims to further understand the tribochemical behaviour of ZDDPs. Several inter-connected areas of research are described in this thesis. These all investigate the formation of tribofilms by ZDDP and the impact of tribofilm formation on wear. Taken together they contribute to our understanding of the mechanisms of tribological behaviour of ZDDPs and should assist in the design of lubricants and rubbing components.

Firstly, the evolution of ZDDP tribofilm properties, in particular, tribofilm durability and the origins of this durability, are examined. It is found that ZDDP tribofilms undergo a structural transformation during rubbing from a predominantly amorphous structure to one that is nanocrystalline, resulting in the tribofilm becoming much stronger and more durable.

Secondly, the reaction mechanisms of tribofilm formation on various non-ferrous metal and non-metallic materials are studied, both by ion-implanting various alloying elements into steel surfaces, and by using non-metallic rubbing materials. It is found that a potentially important factor in the formation of ZDDP tribofilms is the presence and concentration of ferrous and/or non-ferrous metal atoms at the surface. Non-ferrous metals may act as adsorption sites for ZDDP in a similar manner to Fe in steel, enabling formation of ZDDP tribofilms.

Thirdly, to further understand the antiwear performance of ZDDP, its impact on the wear of a-C:H DLC in the presence of molybdenum dialkyldithiocarbamate (MoDTC), which is known to be problematic, is investigated. It is well known that MoDTC can produce very high wear of DLC and that this can be mitigated by the presence of ZDDP in the lubricant. From this research it is shown that ZDDPs reduce DLC wear in the presence of MoDTC mainly by forming thick antiwear tribofilms and reducing the ratio of  $\text{MoO}_3/\text{MoS}_2$  in the tribofilm.

Fourthly, although ZDDP is very effective for reducing most types of wear, it is known that ZDDP can promote one particular form of wear, micropitting wear. In this research a new method of studying micropitting that enables both micropitting and tribofilm formation to be studied in parallel is developed which is key to assessing the impact of lubricant chemistry on micropitting. This is used to show that the influence of ZDDP on micropitting originates from its tendency to prevent running-in of the contacting surfaces. The mechanism by which a widely-used black oxide coating limits micropitting is explored and it is shown that this relatively soft coating provides adequate running-in even in the presence of ZDDP-containing oils. Finally, the impact of friction on micropitting is studied by isolating its effects from those of running-in, by controlling separately the formation of ZDDP and MoDTC tribofilms. Results show that friction has a very significant impact on micropitting.



## **ACKNOWLEDGEMENT**

First of all, I would like to express my deepest gratitude towards my supervisors, Professor Hugh Spikes and Dr. Amir Kadiric for their persistent and enormous support throughout my work. I really appreciate that they always welcome me to discuss my research. Discussions with them were always fruitful and made me motivated, thus I could make great accomplishments and acquire a great variety of knowledge and experience.

I am also very thankful to the academic and visiting staff in Tribology Group, Professor Daniele Dini, Dr. Marc Masen, Dr. Thomas Reddyhoff, Dr. Janet Wong, Professor Philippa Cann and Dr. Ian Taylor for valuable technical advice and constructive discussions. I would also acknowledge the support staff, Mrs. Chrissy Stevens and Mr. Pawel Orzlowski. Without their support, I could not have completed my research.

I would also like to appreciate my company, Showa Shell Sekiyu K.K. (now Shell Lubricants Japan K.K.) for giving me such a great opportunity and sponsoring my PhD study. Also, I am very thankful to Shell Lubricants Japan K.K. for supporting my PhD study and supplying samples, especially to Dr. Eiji Nagatomi. Without his help, I could not even get this opportunity of PhD study.

My sincere thanks to my colleagues in Tribology Group as well. They were always kind, friendly and helpful. They made my life in the UK valuable and unforgettable. I enjoyed every moment with them; having meals and chatting together, drinking in pubs, nights out, barbecues, playing sports and travelling. In addition, they were very knowledgeable and professional in their work. Technical discussions with them were very useful and productive.

Finally, my greatest gratitude to my parents, Junko Ueda, and my wife, Akari Ueda for selfless and heartfelt support.

## **PUBLICATIONS**

The following peer-reviewed journal papers resulted from my PhD research. All papers are published as open access and relevant chapters of this thesis (as indicated in brackets below) rely on the content of the corresponding paper.

M. Ueda, A. Kadiric, H.A. Spikes, On the crystallinity and of ZDDP tribofilm, *Tribol. Lett.* 67 (2019) 1–13. (Chapter 5)

M. Ueda, A. Kadiric, H.A. Spikes, Influence of steel surface composition on ZDDP tribofilm growth using ion implantation, *Tribol. Lett.* 69.2 (2021) 1-14. (Chapter 6)

M. Ueda, A. Kadiric, H.A. Spikes, ZDDP tribofilm formation on non-metallic surfaces, *Tribology Online* 15.5 (2020): 318-331. (Chapter 7)

M. Ueda, A. Kadiric, H.A. Spikes, Wear of hydrogenated DLC in MoDTC-containing oils, *Wear of hydrogenated DLC in MoDTC-containing oils. Wear* (2021): 203869. (Chapter 8)

M. Ueda, H. Spikes, A. Kadiric, In-situ observations of the effect of the ZDDP tribofilm growth on micropitting, *Tribol. Int.* 138 (2019) 342–352. (Chapter 9)

M. Ueda, H. Spikes, A. Kadiric, Influence of black oxide coating on micropitting and ZDDP tribofilm formation, *Tribol. Trans.* (2021) 1-21. (Chapter 10)

M. Ueda, B. Wainright, H. Spikes, A. Kadiric, The effect of friction on micropitting, *Wear*, 488 (2022): 204130 (Chapter 11)

## Table of Contents

1	Thesis Outline and Research Question.....	1
2	Background.....	4
2.1	Solid-solid Friction .....	4
2.2	Wear .....	5
2.2.1	Adhesive Wear.....	5
2.2.2	Abrasive Wear .....	5
2.2.3	Corrosive Wear .....	5
2.2.4	Fatigue Wear.....	6
2.3	Lubrication.....	8
2.3.1	Hydrodynamic Lubrication (HL) Regime .....	9
2.3.2	Elasto-Hydrodynamic Lubrication (EHL) Regime .....	9
2.3.3	Boundary Lubrication Regime .....	9
2.3.4	Mixed Lubrication Regime.....	10
2.4	Regulation and Trend of Automobiles .....	10
2.4.1	Improvement of Fuel Efficiency.....	11
2.4.2	Introduction of Eco-friendly Vehicles .....	13
2.4.3	Reduction of Mechanical Loss .....	14
2.4.4	Reduction of Pollutants .....	17
2.5	Specification and Trend of Engine oils.....	17
2.5.1	Fuel Efficiency Requirement.....	18
2.5.2	Technology to Improve Engine Oil Fuel Efficiency.....	19
2.5.3	Exhaust Aftertreatment System Compatibility .....	23
2.6	Components in Engine Oil.....	24
2.6.1	Antiwear Additives .....	25
2.6.2	Extreme Pressure Additives.....	26
2.6.3	Friction Modifiers.....	27
2.6.4	Antioxidants .....	28
2.6.5	Detergents .....	29

2.6.6	Dispersants .....	29
2.6.7	Viscosity Modifiers.....	30
2.6.8	Pour Point Depressants .....	31
2.6.9	Corrosion Inhibitors.....	31
2.6.10	Rust Inhibitors .....	31
2.6.11	Foam Inhibitors .....	32
2.6.12	Base Oils.....	32
2.7	Summary.....	35
3	General Introduction and Literature Review of ZDDP .....	36
3.1	Properties of ZDDP Tribofilm .....	36
3.1.1	Chemical Characterization .....	36
3.1.2	Physical Characterization .....	42
3.1.3	ZDDP Tribofilm Durability .....	46
3.1.4	ZDDP Tribofilm Structure .....	47
3.1.5	Properties of ZDDP Thermal Film .....	48
3.2	Reaction Mechanism of Tribofilm Formation .....	49
3.2.1	Thermal Decomposition .....	49
3.2.2	Hydrolytic Decomposition .....	50
3.2.3	Thermo-oxidative Decomposition.....	50
3.2.4	ZDDP Tribofilm Formation.....	51
3.2.4.1	Surface Adsorption.....	51
3.2.4.2	Formation of FeS/FeS <sub>2</sub> .....	52
3.2.4.3	Polymerisation.....	53
3.2.4.4	Ion Exchange and Depolymerisation .....	53
3.2.5	Influence of Steel Surface Composition on ZDDP Tribofilm Growth using Ion Implantation .....	54
3.2.6	Effect of Non-metallic Material on Tribofilm Formation .....	55
3.2.7	Driving Force of ZDDP Tribofilm Formation .....	56
3.2.7.1	Temperature.....	56

3.2.7.2	Pressure .....	56
3.2.7.3	Triboemission.....	57
3.2.7.4	Surface Catalysis .....	57
3.2.7.5	Shear Stress .....	57
3.2.8	Comparison of the Reaction Mechanism of ZDP Tribofilm Formation...	59
3.2.9	ZDDP Thermal Film Formation .....	60
3.3	Studies of ZDDP Tribofilm Performance .....	60
3.3.1	Antiwear Performance .....	60
3.3.1.1	Alkyl Groups .....	61
3.3.1.2	Phosphorus Concentration.....	61
3.3.1.3	Contaminants.....	61
3.3.1.4	Coexisting additives .....	62
3.3.1.5	Rubbing Conditions .....	63
3.3.1.6	Tribofilm Properties .....	63
3.3.2	Effect of ZDDP on Friction .....	64
3.3.3	Studies of Effect of MoDTC on ZDDP Properties .....	66
3.3.3.1	Tribofilm Formation and Properties of Tribofilms.....	66
3.3.3.2	Friction Behaviour.....	67
3.3.3.3	Antiwear Performance on Steel Tribopairs .....	69
3.3.3.4	Wear of Hydrogenated DLC in MoDTC-containing Oils .....	70
3.4	Influence of ZDDP on Micropitting.....	70
3.4.1	Effect of ZDDP Tribofilm Growth on Micropitting .....	70
3.4.2	Influence of Black Oxide Coating on Micropitting and ZDDP Tribofilm	73
3.4.3	Effect of Friction on Micropitting in ZDDP-Containing Oils.....	74
3.5	Summary and Research Questions .....	75
4	Test Methods.....	78
4.1	Test Materials.....	78
4.1.1	Base Oils.....	78
4.1.2	ZDDPs .....	79

4.1.3	MoDTC.....	79
4.1.4	MTM and ETM Test Specimen .....	79
4.2	Tribometers .....	80
4.2.1	Mini Traction Machine - Spacer Layer Interferometry (MTM-SLIM) .....	80
4.2.2	Extreme Pressure Traction Machine (ETM) .....	81
4.3	Chemical Characterization of Tribofilm and Material.....	81
4.3.1	X-ray Photoelectron Spectroscopy (XPS) .....	81
4.3.2	Raman Spectroscopy .....	82
4.3.3	Focused Ion Beam (FIB) .....	82
4.3.4	Transmission Electron Microscopy (TEM) and Scanning Transmission Electron Microscopy and Energy-Dispersive X-ray Spectroscopy (STEM-EDX) .	83
4.3.5	Scanning Electron Microscope and Energy-Dispersive X-ray Spectroscopy (SEM-EDX).....	83
4.4	Mechanical Characterization of Tribofilm and Material .....	83
4.4.1	Atomic Force Microscope (AFM).....	83
4.4.2	Optical Microscopy .....	84
4.4.3	Stylus Profilometer.....	85
4.4.4	White Light Interferometry .....	85
4.4.5	Nanoindentation .....	85
4.5	Adsorption: Quartz Crystal Microbalance with Dissipation Monitoring (QCM-D) .....	85
5	Crystallinity and Durability of ZDDP Tribofilm .....	88
5.1	Introduction.....	88
5.2	Test Method .....	89
5.2.1	Test Lubricants and Materials.....	89
5.2.2	Test Procedure and Condition.....	89
5.3	Tribofilm Analysis .....	91
5.4	Results.....	91
5.4.1	Evolution of ZDDP Tribofilm Durability .....	91
5.4.2	ZDDP Tribofilm Crystallinity.....	93

5.4.2.1	Tribofilm Crystallinity after Rubbing in ZDDP Solution .....	93
5.4.2.2	Tribofilm Crystallinity after Rubbing in PAO.....	95
5.4.3	Tribofilm Chemical Structure.....	96
5.4.4	Influence of Temperature and ZDDP Alkyl Structure on Tribofilm Properties .....	97
5.4.4.1	Tribofilm Durability .....	97
5.4.4.2	Tribofilm Crystallinity .....	98
5.4.4.3	Tribofilm Polyphosphate Structure .....	99
5.5	Discussion.....	100
5.6	Conclusions.....	105
6	Influence of Steel Surface Composition on ZDDP Tribofilm Growth using Ion Implantation.....	107
6.1	Introduction.....	107
6.2	Test Materials.....	109
6.2.1	Test Lubricants .....	109
6.2.2	MTM Test Specimens.....	109
6.2.3	Mechanical Properties of Disc and Ball Specimens.....	109
6.2.4	Chemical Composition of Disc and Ball Specimens.....	111
6.3	Test Methods.....	116
6.3.1	MTM Test Rig .....	116
6.3.2	Test Conditions and Procedures .....	116
6.3.3	Tribofilm Analysis.....	117
6.4	Results.....	117
6.4.1	Effect of Ion Implantation on Tribofilm Formation .....	117
6.4.2	Effect of ZDDP Concentration on Tribofilm Formation .....	121
6.4.3	Chemical Analysis of Tribofilms.....	124
6.4.4	Elemental Distribution in Tribofilms (STEM-EDX).....	124
6.4.5	Chemical Bonds in Tribofilms (XPS).....	125
6.4.6	Crystallinity of Tribofilms (TEM).....	126
6.5	Discussion.....	127

6.5.1	Surface Adsorption .....	128
6.5.2	Polymerization and Depolymerization .....	129
6.6	Conclusions.....	130
7	ZDDP Tribofilm Formation on Non-metallic Surfaces .....	132
7.1	Introduction.....	132
7.2	Test Method .....	133
7.2.1	Test lubricants and Materials .....	133
7.2.2	Test Procedure and Conditions .....	135
7.2.3	Tribofilm Analysis .....	138
7.2.3.1	Tribofilm Thickness and Topography .....	138
7.2.3.2	Tribofilm Characterization .....	138
7.2.4	ZDDP Adsorption Study using QCM-D.....	138
7.3	Results.....	139
7.3.1	Tribofilm Formation in Boundary Lubrication Conditions .....	139
7.3.2	Tribofilm Formation in Full Film EHL Conditions.....	142
7.3.3	Effect of ZDDP Concentration on Tribofilm Formation in Full Film EHL Conditions.....	144
7.3.4	QCM-D Results on ZDDP Adsorption .....	145
7.3.5	Chemical Analysis of ZDDP Tribofilms Formed under Boundary Lubrication Conditions.....	146
7.3.5.1	STEM-EDX Results on the Elemental Distribution of Tribofilms .	146
7.3.5.2	XPS Results.....	147
7.3.5.3	TEM Results on the Crystallinity of Tribofilms .....	149
7.4	Discussion.....	150
7.4.1	Surface Adsorption .....	150
7.4.2	Polymerisation .....	153
7.4.3	Depolymerisation .....	153
7.5	Conclusions.....	154
8	Wear of Hydrogenated DLC in MoDTC-containing Oils .....	156
8.1	Introduction.....	156



8.2	Test Method .....	157
8.2.1	Test Lubricants and Materials.....	157
8.2.2	Test Procedure and Condition.....	159
8.2.3	Tribofilm Analysis .....	160
8.3	Results.....	160
8.3.1	DLC Disc Wear.....	160
8.3.2	Tribofilm Formation on Steel Balls .....	163
8.3.3	Friction Behaviour .....	166
8.3.4	Elemental Distribution of Tribofilm on Steel .....	167
8.3.5	Raman Spectra of Steel Wear Tracks.....	168
8.3.6	XPS Analysis of Steel Wear Tracks.....	170
8.4	Discussion .....	172
8.4.1	Formation of Thick Antiwear Tribofilm .....	173
8.4.2	Increase of MoS <sub>2</sub> :MoO <sub>3</sub> Ratio .....	175
8.4.3	Reduction of MoDTC Tribofilm Formation.....	176
8.5	Conclusions.....	177
9	In-situ Observations of the Effect of ZDDP Tribofilm Growth on Micropitting ..	179
9.1	Introduction.....	179
9.2	Test Procedure.....	180
9.2.1	Test Materials and Lubricants.....	180
9.2.2	Test Procedures and Conditions .....	181
9.3	Results.....	182
9.3.1	Effect of Lambda on Micropitting and ZDDP Tribofilm Formation .....	182
9.3.1.1	Evolution of Surface Damage on Balls .....	182
9.3.1.2	Evolution of Surface Roughness of Counterface Discs .....	185
9.3.1.3	ZDDP Tribofilm Evolution.....	186
9.3.2	Effect of ZDDP Concentration on Micropitting and Tribofilm .....	187
9.3.2.1	Evolution of Surface Damage on Balls .....	187
9.3.2.2	Evolution of Surface Roughness of Counterface Discs .....	191
9.3.2.3	Friction Behaviour.....	192

9.3.2.4	Evolution of the ZDDP Tribofilm on the Ball.....	193
9.3.3	Effect of ZDDP Alkyl Structure on Micropitting and ZDDP Tribofilm .	194
9.3.3.1	Evolution of surface damage on balls .....	194
9.3.3.2	Evolution of Surface Roughness of Counterface Discs .....	196
9.3.3.3	Friction Behaviour.....	197
9.3.3.4	Evolution of the ZDDP Tribofilm on The Ball.....	197
9.4	Discussion.....	199
9.4.1	Pros and Cons of the MTM-SLIM to Study Micropitting.....	199
9.4.2	Mechanism by which ZDDP Influences Micropitting.....	200
9.4.3	Effect of Lambda on Micropitting and Tribofilm Formation .....	201
9.4.4	Effect of ZDDP Concentration and Alkyl Structure on Micropitting.....	202
9.5	Conclusions.....	203
10	Influence of Black Oxide Coating on Micropitting and ZDDP Tribofilm Formation	205
10.1	Introduction.....	205
10.2	Test Methodology .....	206
10.2.1	Test Conditions .....	206
10.2.2	Micropitting Tests with Rough Disc Counterface .....	206
10.2.3	Tribofilm Formation Tests with Smooth Disc Counterface.....	207
10.2.4	Test Lubricants .....	208
10.2.5	BO Coating Properties.....	208
10.2.6	Test Procedures.....	210
10.2.7	ZDDP Adsorption using QCM-D .....	211
10.2.8	Calculation of Distribution of Contact Pressure.....	211
10.3	Results.....	211
10.3.1	Effect of BO Coating on Micropitting.....	211
10.3.1.1	Evolution of Surface Damage on Balls .....	211
10.3.1.2	Evolution of Surface Roughness of Counterface Discs .....	214
10.3.1.3	Friction Behaviour.....	216
10.3.1.4	Evolution of ZDDP Tribofilm in Micropitting Tests.....	217

10.3.2	Influence of BO Coating on Tribofilm Formation using Smooth Discs	220
10.3.2.1	Wear of Balls and Discs	221
10.3.2.2	Friction Behaviour	221
10.3.3	Observation of ZDDP Tribofilm Formation	222
10.3.4	ZDDP Adsorption on Black Oxide Coating	224
10.4	Discussion	225
10.4.1	Chemical Effects of Black Oxide on Micropitting	226
10.4.2	Mechanical Effects of Black Oxide on Micropitting	227
10.4.3	Mechanisms of Influence of BO Coating on Micropitting	233
10.5	Conclusions	236
11	Effect of Friction on Micropitting	238
11.1	Introduction	238
11.2	Test Methodology	239
11.2.1	Experimental Equipment	239
11.2.2	Test Conditions	239
11.2.3	Test Lubricants	240
11.2.4	Test Procedures	240
11.2.5	Calculation of Contact Pressure and Stress	241
11.2.6	Tribofilm Elastic Modulus	241
11.3	Results	242
11.3.1	Effect of MoDTC Addition at the Beginning of the Test (Method 1)	242
11.3.1.1	Friction Behaviour	242
11.3.1.2	Evolution of Surface Damage on Balls	243
11.3.1.3	Evolution of Surface Roughness of Counterface Discs	245
11.3.1.4	Evolution of Tribofilm	245
11.3.2	Effect of MoDTC Addition after Running-in (Method 2)	247
11.3.2.1	Friction Behaviour	247
11.3.2.2	Evolution of Surface Damage on Balls	248
11.3.2.3	Evolution of Surface Roughness of Counterface Discs	251

11.3.2.4	Evolution of the Tribofilm on the Ball .....	252
11.4	Discussion .....	253
11.4.1	Other Factors that may Influence Micropitting .....	253
11.4.2	Mechanism by which Friction Influences Micropitting .....	256
11.4.2.1	Influence of Friction on Near-surface Stresses .....	258
11.4.2.2	Effect of Friction on Observed Crack Morphology .....	261
11.5	Conclusions.....	263
12	Conclusions and Future Work .....	265
12.1	Main Conclusions .....	265
12.1.1	ZDDP Tribofilm Properties .....	265
12.1.2	Reaction Mechanism of ZDDP Tribofilm on Non-ferrous Surfaces .....	265
12.1.3	ZDDP Tribofilm Performance .....	266
12.2	Suggestions for Future Work .....	267
References	.....	270

## List of Tables

Table 2-1 The standards of gasoline and diesel engine oil in the EU, the US and Japan [42–44] .....	18
Table 2-2 Fuel efficiency requirement of ACEA [42,45] .....	18
Table 2-3 Fuel efficiency requirement of ILSAC and API [43] .....	19
Table 2-4 Chemical limit of passenger car engine oil [42–44].....	23
Table 2-5 Lubricant Additives .....	24
Table 2-6 The effect of ZDDP structure on its thermal stability and antiwear performance .....	26
Table 2-7 API categories of base oils [100].....	32
Table 3-1 Tribofilm composition in wt.% measured using EDX on wear scar after 6 h tests. 002A: ZDDP, 003A: MoDTC, 004A: ZDDP + MoDTC solutions [238] .....	67
Table 4-1 Base oils used in this study.....	78
Table 4-2 ZDDPs used in this study .....	79
Table 4-3 Focused ion beam conditions for ZDDP tribofilm cross section preparation	82
Table 5-1 General MTM test conditions.....	90
Table 5-2 Specific test conditions.....	90
Table 6-1 Measured properties of MTM discs and balls. ....	110
Table 6-2 Measured chemical composition of MTM discs and balls (atomic %).....	112
Table 6-3 Chemical composition of MTM discs using XPS (atomic %) .....	116
Table 6-4 MTM test conditions .....	116
Table 7-1 Measured properties of MTM (a) discs and (b) balls.....	134
Table 7-2 Measured chemical composition of MTM (a) discs and (b) balls (atomic %) .....	135
Table 7-3 MTM test conditions (boundary lubrication conditions) .....	136
Table 7-4 ETM test conditions (full film EHL conditions) .....	137
Table 8-1 Test oil formulations (Mo denotes MoDTC).....	158
Table 8-2 MTM test conditions (boundary lubrication conditions) .....	159
Table 9-1 Test oil formulations and lambda value.....	181
Table 9-2 MTM specimen materials and test conditions.....	182
Table 10-1 Measured properties of MTM specimens and micropitting test conditions	206
Table 10-2 Measured properties of MTM specimens and film forming test conditions .....	207
Table 11-1 Test oil formulations .....	240

## List of Figures

Figure 2-1 Examples of surface-originated pit. Circle mark in (a) shows the crack initiation site [3, 4] .....	6
Figure 2-2 Micropitting on (a) a bearing and (b) a gear [8] .....	7
Figure 2-3 Schematic illustration of surface crack initiation and propagation of micropitting [9].....	7
Figure 2-4 Stribeck curve and corresponding engine sliding parts [11].....	8
Figure 2-5 Global CO <sub>2</sub> emissions by sector in 2017 [13] .....	11
Figure 2-6 CO <sub>2</sub> emissions and fuel consumption of (a) passenger vehicles (2014) [14] and (b) light duty vehicles (2017) [15] normalized to NEDC.....	12
Figure 2-7 Light vehicle sales forecast (in millions of units) [17] .....	13
Figure 2-8 Distribution of (a) total energy in diesel combustion engine and (b) total mechanical friction losses [20] .....	14
Figure 2-9 The evolution of average engine displacement of passenger vehicle (2016) [23] .....	15
Figure 2-10 Ternary phase diagram of amorphous carbons. The three corners correspond to diamond, graphite, and hydrocarbons, respectively [29] .....	16
Figure 2-11 The effect of DLC and ceramic coated piston rings on friction coefficient [33] .....	16
Figure 2-12 The trend of engine oil viscosity of gasoline passenger vehicle in the US (2020) [47].....	20
Figure 2-13 The effect of HTHS viscosity on fuel consumption measured in an diesel engine [49].....	21
Figure 2-14 Stribeck curves for five friction modifier ZDDP blends after 2 h rubbing [52] .....	22
Figure 2-15 The effect of DLC coatings on friction using a SRV tribometer [55].....	23
Figure 2-16 Representative antiwear additive; zinc dialkyldithiophosphate (ZDDP) ...	25
Figure 2-17 Representative EP additives.....	26
Figure 2-18 Reaction mechanism of sulphur-type EP additives [70].....	27
Figure 2-19 Representative friction modifiers [71] .....	28
Figure 2-20 Representative antioxidants [76] .....	28
Figure 2-21 Representative detergents [80,81].....	29
Figure 2-22 Representative dispersant; succinimide [86,87] .....	30
Figure 2-23 Representative viscosity modifier [91,92] .....	30
Figure 2-24 Representative corrosion inhibitor [95] .....	31

Figure 2-25 Representative form inhibitor; polydimethylsiloxane [98,99].....	32
Figure 2-26 Representative mineral base oils [101].....	33
Figure 2-27 Representative poly alphaolefin [101].....	34
Figure 2-28 Representative esters [101].....	34
Figure 3-1 (a) IR peaks of ZDDP tribofilms and thermal films and .....	37
Figure 3-2 Raman spectra of (a) pure crystalline orthophosphate ( $\alpha$ - $\text{Zn}_3(\text{PO}_4)_2$ ), tribofilms formed after a sliding test of a steel/steel contact (b) at room temperature and (c) at 120 °C [111].....	37
Figure 3-3 O 1s XPS spectra on (a) non-contact areas and (b) regions with 5 N tribostress at different temperatures, (NBO at 531.8 and BO at 533.4 eV) .....	38
Figure 3-4 Phosphorus K-edge XANES spectra collected in TEY mode for ZDDP tribofilms and reference samples [119] .....	39
Figure 3-5 Element distribution in cross-sectional of ZDDP tribofilm on a mixed $\text{Fe}_3\text{O}_4$ and FeO substrate using STEM-EDX [143].....	40
Figure 3-6 P and Fe distribution in cross-sectional of ZDDP tribofilm using STEM-EDX [144] .....	40
Figure 3-7 (a) 3 D APT of needle shape specimen showing the Cr capping layer, ZDDP tribofilm and steel substrate and (b) spatial distribution of Fe, Zn, S/O, FeO, PO and Cr atoms [145].....	41
Figure 3-8 Proposed ZDDP tribofilm structures (a) [123] , (b) [146], (c) [116] and (d) [127] .....	42
Figure 3-9 The evolution of pad-like structures of ZDDP tribofilms using AFM with rubbing time (A) 10 min, (B) 40 min, (C) 60min and (D) 120 min. [150].....	43
Figure 3-10 TEM observation of a FIB cross section preparation of the ZDDP tribofilm [152] .....	44
Figure 3-11 ZDDP tribofilm thickness measured by various techniques [171] .....	45
Figure 3-12 The evolution of hardness of ZDDP tribofilm measured in CSM [178] ....	46
Figure 3-13 The Schematic diagram of ZDDP film structures [67] .....	46
Figure 3-14 The effect of PAO rubbing on tribofilm removal after (a) 25 and (b) 180 minutes rubbing [119].....	47
Figure 3-15 The crystalline phase of ZDDP tribofilm [161] .....	48
Figure 3-16 The effect of oil temperature on ZDDP thermal film developments after immersion for 12 h in a solution of 1.2 wt% ZDDP in group 2 base oil [167] .....	49
Figure 3-17 Mechanism of the thermal decomposition of ZDDPs [181].....	50
Figure 3-18 Hydrolytic reaction of ZDDPs [188] .....	50
Figure 3-19 Schematic diagram of antioxidant reaction of ZDDPs [106] .....	51

Figure 3-20 Suggested reaction sequence of tribofilm formation [127] .....	51
Figure 3-21 Conversion of dialkylthiophosphates to dothionylphosphates [67,201].....	52
Figure 3-22 Polymerisation to polyphosphates [67,183].....	53
Figure 3-23 Depolymerisation to Zn/Fe phosphates [67].....	53
Figure 3-24 Phosphates formed from ZDDPs [67] .....	54
Figure 3-25 Tribofilm volumetric growth rate dependence on (a) contact pressure and (b) temperature [232] .....	58
Figure 3-26 Chemical structure of (a) ZDDP and (b) ZDP [220] .....	59
Figure 3-27 Tribofilm thickness growth of ZDP-secC6 and ZDDP-sec C6 at 100 °C [220] .....	59
Figure 3-28 Proposed reaction mechanism of ZDP tribofilm formation [221] .....	60
Figure 3-30 The effect of ZDDP concentration on wear [225] .....	61
Figure 3-31 The effect of relative humidity on wear [226] .....	62
Figure 3-32 Antiwear characteristics of oxidatively degraded ZDDPs [232] .....	63
Figure 3-32 Friction -speed curves using a ZDDP solution and (b) collapse of friction curves when plotted against lambda ratio [149].....	65
Figure 3-33 The effect of ZDDP alkyl groups on boundary lubrication friction [73]....	66
Figure 3-34 Effect of MoDTC concentration in a ZDDP oil on friction coefficient [237] .....	68
Figure 3-35 Friction behaviour of MoDTC containing oil. 001A: PAO6, 002A: PAO6 + ZDDP, 003A: PAO6 + MoDTC, 004A: PAO6 + ZDDP + MoDTC. [238,239] .....	68
Figure 3-36 Chemical process of the MoS <sub>2</sub> formation from MoDTC in the presence of ZDDP [244] .....	69
Figure 3-37 Wear factors tested in 6 hours using a reciprocating pin-on-plate tests, 001A: PAO6, 002A: PAO6 + ZDDP, 003A: PAO6 + MoDTC, 004A: PAO6 + ZDDP + MoDTC [239] .....	69
Figure 3-38 The expected trends in micropitting behaviour with specific film lambda for cases with and without the presence of mild wear [248].....	71
Figure 3-39 Evolution of micropitting as a function of contact cycles during the test with different lubricants [251] .....	72
Figure 4-1 Schematic image of the MTM–SLIM set-up .....	80
Figure 4-2 Procedure to measure ZDDP tribofilm thickness and morphology using AFM .....	84
Figure 5-1 ZDDP2 tribofilm evolution and its durability after different Stage 1 rubbing times at 100 °C (Tests 2, 5, 7 and 8).....	92



Figure 5-2 ZDDP2 tribofilm evolution and its durability after 60 minutes in Stage 1 and different Stage 2 rubbing times at 100 °C (Tests 3, 4 and 5).....	92
Figure 5-3 TEM images and FFTs of the upper and lower side of tribofilms after 30, 60 and 180 minutes rubbing in ZDDP2 solution (Tests 1, 3 and 6). Steel substrate is the dark gray region at the bottom of these images while the upper black regions are gold layer. ....	94
Figure 5-4 Magnified view of crystalline region of ZDDP tribofilm in upper side (Test 6) .....	94
Figure 5-5 TEM images and FFTs of ZDDP tribofilm formed after 60 minutes rubbing in ZDDP2 solution (Test 3) and after additional 5 minutes rubbing in PAO (Test 4) .....	95
Figure 5-6 O 1s XPS spectra of ZDDP tribofilm in different rubbing time with the BO/NBO ratio (Tests 1, 3, 4 and 6) .....	96
Figure 5-7 ZDDP tribofilm evolution and its durability at 100 °C (Tests 7 and 8) and 60 °C (Tests 10 and 11).....	97
Figure 5-8 The effect of ZDDP alkyl structure on tribofilm durability after different Stage 1 rubbing times (ZDDP1: Tests 13, 15 and 16, ZDDP2: Tests 7 and 8).....	98
Figure 5-9 TEM images and electron FFTs of ZDDP tribofilm at 60 °C and from primary ZDDP1.....	99
Figure 5-10 O 1s XPS spectra of ZDDP tribofilm at 60 °C from primary ZDDP1 .....	100
Figure 5-11 EDX line profiles in (a) Tests 5 and (b) 7 and (c) Fe/P atomic ratio of the tribofilm.....	104
Figure 6-1 Depth profile of nano-indentation hardness of ion-implanted steels (a) up to 2 µm and (b) up to 0.2 µm.....	111
Figure 6-2 STEM-EDX analysis of a cross section of (a) an unrubbed Ni-implanted disc and (b) rubbed Mo-implanted disc in ZDDP solution. Approximate position of each surface is marked with a dashed line. ....	113
Figure 6-3 Example XPS spectra of (a) Ni-, (b) Mo-, (c) Cr-, (d) V-, (e) W-implanted disc .....	115
Figure 6-4 The evolution of ZDDP tribofilm thickness on the original unimplanted and ion-implanted steel balls during rubbing. ....	118
Figure 6-5 Optical micrographs of ZDDP tribofilm on the MTM balls and discs after 4 hours rubbing. The scale bar shown in upper left image is applicable to all images. ...	119
Figure 6-6 Evolution of MTM friction coefficient versus entrainment speed curves during 4 hours rubbing on (a) original 52100 steel, (b) Ni-implanted steel and (c) Cr-implanted steel.....	120

Figure 6-7 Surface profiles after rubbing of (a) steel disc, (b) Ni implanted disc, (c) Mo-implanted disc, (d) Cr implanted disc and (e) V implanted disc .....	121
Figure 6-8 The effect of ZDDP concentration on tribofilm thickness on (a) original 52100 steel, (b) Ni-implanted steel (c) Mo-implanted steel and (d) Cr-implanted steel (Note that values quoted in the legend are ppm of P).....	124
Figure 6-9 STEM images and EDX line profiles of the tribofilms on Ni- and Mo-implanted steels .....	125
Figure 6-10 O 1s XPS spectra of ZDDP tribofilms on Ni-, Mo- and Cr-implanted steels .....	126
Figure 6-11 TEM images and FFTs of ZDDP tribofilms on Ni-and Mo-implanted steels .....	127
Figure 7-1 Optical micrographs and AFM profiles of ZDDP tribofilm on the disc of each material after 3 hours rubbing in thin film conditions.....	139
Figure 7-2 The evolution of ZDDP tribofilm thickness on each material during rubbing in thin film conditions .....	140
Figure 7-3 The evolution of ZDDP tribofilm area coverage on wear track of each material during rubbing in thin film conditions.....	141
Figure 7-4 The effect of 30 min rubbing in pure PAO on ZDDP tribofilm removal for each material in thin film conditions (ZDDP solution was replaced with pure PAO after 180 minutes rubbing).....	141
Figure 7-5 Optical micrographs and AFM profiles of ZDDP tribofilm on the discs of each material after 3 hours in full film EHL conditions .....	143
Figure 7-6 The evolution of ZDDP tribofilm thickness with rubbing time on each material in full film EHL conditions.....	144
Figure 7-7 The evolution of ZDDP tribofilm thickness with different ZDDP concentrations on steel and Si <sub>3</sub> N <sub>4</sub> in full film EHL conditions .....	145
Figure 7-8 QCM-D results showing ZDDP mass adsorbed on sensors made of, or coated with, each of the 5 studied materials .....	146
Figure 7-9 STEM images and EDX line profiles of sections of tribofilms formed on steel, WC and Si <sub>3</sub> N <sub>4</sub> surfaces after 3 hours of rubbing in boundary lubrication conditions..	147
Figure 7-10 (a) C 1s and (b) O 1s XPS spectra of ZDDP tribofilms on steel, Si <sub>3</sub> N <sub>4</sub> and WC after 3 hours of rubbing in thin film conditions .....	148
Figure 7-11 TEM images and FFTs of ZDDP tribofilms on steel, Si <sub>3</sub> N <sub>4</sub> and WC after 3 hours of rubbing in boundary lubrication conditions .....	150
Figure 7-12 The adsorption of ZDDP molecule on ferrous surface and the formation of Fe dithiophosphate.....	151

Figure 8-1 Optical micrographs, WLI 3D profiles and depth profiles of wear tracks on DLC discs (Note that the colour scale is not applicable to the image with delamination obtained from PAO rubbing since its depth scale is much larger than others.).....	162
Figure 8-2 Wear volume of DLC wear tracks measured using WLI (area: 400 $\mu\text{m} \times 600 \mu\text{m}$ in Figure 8-1).....	163
Figure 8-3 Optical micrographs of the wear tracks on the steel balls after three hours rubbing tests.....	164
Figure 8-4. The evolution of tribofilm thickness on the steel balls during the tests measured by using SLIM and, for PAO+Mo+OFM, using a stylus profilometer. ....	165
Figure 8-5 The evolution of friction coefficient during the tests.....	167
Figure 8-6 TEM image, STEM-EDX image and element distribution of tribofilm on the steel ball rubbed in PAO+Mo after a 3 hour test .....	168
Figure 8-7 Raman spectra from the wear tracks on the steel balls after 3 hour tests and from the fresh DLC disc surface .....	169
Figure 8-8 C 1s XPS spectra of tribofilms on the wear tracks on the steel balls .....	171
Figure 8-9 Mo 3d XPS spectra of tribofilms on the wear tracks on the steel balls (a) PAO, (b) PAO+Mo+ZDDP(25), (c) PAO+Mo+ZDDP(50), (d) PAO+Mo+ZDDP(800), (e) PAO+Mo+EP, (f) PAO+Mo+Ca(OB), (g) PAO+Mo+Ca(Neu), (h) PAO+Mo+Disp, (i) PAO+Mo+Disp(B), (j) PAO+Mo+OFM, (k) PAO+Mo+PAMA.....	172
Figure 8-10 Chemical composition of tribofilms formed in PAO+Mo and PAO+Mo+OFM using SEM-EDX .....	174
Figure 8-11 The relationship between Mo <sup>4+</sup> /Mo <sup>6+</sup> and wear volume of DLC disc ...	177
Figure 9-1 Optical micrographs of rubbing tracks on balls at different lambda values (Note: the scale bar included in the top right corner of the figure applies to all images shown) .....	184
Figure 9-2 Measured depth of ball wear track at different lambda values .....	185
Figure 9-3 Optical micrograph of the cross section of the ball rubbing track in the rolling direction at the end of the test with the lambda = 0.3 showing typical surface-initiated cracks and resulting micropits. ....	185
Figure 9-4 Disc roughness evolution at different lambda values .....	186
Figure 9-5 ZDDP tribofilm thickness development at different lambda values.....	187
Figure 9-6 Optical micrographs of ball rubbing tracks from tests conducted with oils with different ZDDPM concentrations .....	190
Figure 9-7 Depth of the wear track on balls in tests.....	191
Figure 9-8 Evolution of counterface disc roughness .....	191

Figure 9-9 Friction behaviour in tests conducted with oils with different ZDDPM concentrations.....	192
Figure 9-10 SLIM images of ball running track recorded in tests conducted with oils with different ZDDPM concentrations .....	193
Figure 9-11 Tribofilm thickness development measured in tests conducted with oils with different ZDDPM concentrations .....	194
Figure 9-12 Optical micrographs of ball rubbing tracks from tests conducted with oils containing different ZDDP alkyl structures, mixed (ZDDPM) and primary (ZDDP1) 195	
Figure 9-13 Depth of the wear track on balls in tests conducted with oils containing different ZDDP alkyl structures.....	196
Figure 9-14 Evolution of counterface disc roughness in tests conducted with oils containing different ZDDP alkyl structures.....	196
Figure 9-15 Friction behaviour in tests conducted with oils containing different ZDDP alkyl structures.....	197
Figure 9-16 SLIM images recorded in tests conducted with oils containing different ZDDP alkyl structures .....	198
Figure 9-17 Tribofilm thickness evolution measured in tests conducted with oils with different ZDDP alkyl structures.....	198
Figure 9-18 Example optical micrographs of ball rubbing track showing surface cracks generated with and without ball shaft skew on the MTM rig.....	200
Figure 10-1 SEM image of BO-coated steel disc (Ra 8 nm) and EDX analyses .....	209
Figure 10-2 Depth profile of (a) hardness and (b) elastic modulus of steel disc and BO-coated steel disc measured using nano-indentation in CSM mode. Note that values are taken from the range between 0.05 $\mu\text{m}$ and 0.1 $\mu\text{m}$ from the surfaces. ....	210
Figure 10-3 Optical micrographs of wear tracks on balls of the tribopairs with BO coating. (steel/BO denotes steel ball on BO-coated disc and vice versa). It is important to note that the scale bar included in the top right corner of the figure applies to all image.....	213
Figure 10-4 Measured depth of ball wear track of the tribopairs with BO coating (steel/BO denotes steel ball on BO-coated disc and vice versa).....	214
Figure 10-5 Disc roughness evolution of the tribopairs with BO coating (steel/BO denotes steel ball on BO-coated disc and vice versa).....	215
Figure 10-6 Disc surface profiles recorded before the test and at 1000 cycles for (a) steel disc tested against a steel ball and (b) BO-coated disc tested against a steel ball .....	216
Figure 10-7 Friction behaviour in tests of the tribopairs with BO coating (steel/BO denotes steel ball on BO-coated disc and vice versa).....	217

Figure 10-8 SLIM images of ball running track recorded in tests conducted in the tribopairs with BO coating (steel/BO means steel ball on BO-coated disc and vice versa). .....	218
Figure 10-9 Tribofilm evolution on the ball wear tracks for steel/steel and steel/BO tribopairs.....	219
Figure 10-10 Surface profiles before and after EDTA treatment of (a) the ball and (b) the disc of steel/steel contact and (c) the ball and (d) the disc of steel/BO contact after 0.1 million cycles.....	220
Figure 10-11 Wear evolution of the balls and the discs of steel/steel and BO/BO tribopairs (Note that BO coating thickness is approximately 1 $\mu\text{m}$ ). ....	221
Figure 10-12 Friction coefficient of steel/steel and BO/BO tribopairs. ....	222
Figure 10-13 Optical micrographs of the ball and the disc wear tracks of steel/steel and BO/BO tribopairs.....	223
Figure 10-14 SLIM images obtained from the ball wear tracks of steel/steel and BO/BO tribopairs.....	224
Figure 10-15 ZDDP adsorption on $\text{Fe}_2\text{O}_3$ and $\text{Fe}_3\text{O}_4$ using QCM-D.....	225
Figure 10-16 Predicted surface pressure distribution and deformation for (a) steel/steel contact with original (fresh) roughness, (b) steel/steel tribopair with roughness measured after 1000 cycles under conditions in Table 1 (c) steel/BO tribopair with fresh roughness and (d) steel/BO tribopair with roughness after 1000 cycles. All roughnesses measured using a stylus profilometer. (Note: purely elastic solution are shown in all cases to clearly illustrate the effects of running-in; this may result in some asperity pressures with fresh roughnesses appearing unrealistically high).....	230
Figure 10-17 SEM images cross sections of steel disc from steel/steel test and BO-coated disc from steel/BO test at different number of. The scale bar shown in the top right image is applicable to all images.....	231
Figure 10-18 Schematic illustration of the primary mechanism by which BO coating mitigates micropitting.....	235
Figure 11-1 Micropitting test procedures .....	241
Figure 11-2 Friction behaviour in tests conducted with oils having different concentrations of MoDTC from the outset.....	243
Figure 11-3 Typical examples of optical micrographs of wear tracks on balls from tests conducted with different MoDTC concentrations from the outset as well as measured percentage of micropitted area on ball wear track after 8 million cycles (Note: the scale bar included in the top right corner of the figure applies to all images shown) .....	244

Figure 11-4 Disc roughness evolution with oils containing different MoDTC concentrations when MoDTC is present from the start of the test .....	245
Figure 11-5 Tribofilm evolution in tests with oils containing different MoDTC concentrations present from the start of the test .....	246
Figure 11-6 Friction behaviour in tests conducted where oils with different MoDTC concentrations were added after 0.1 million cycles. (a) 0 - 8 million cycles and (b) the same data by zoomed in to highlight the 0 - 0.5 million cycles range. ....	248
Figure 11-7 Typical optical micrographs of wear tracks on balls in tests conducted where oils with different MoDTC concentrations were added after 0.1 million cycles of running-in with ZDDP solution.....	249
Figure 11-8 Typical SEM images of polished cross-sections of the ball rubbing track along the rolling-direction in tests conducted where oils with different MoDTC concentrations were added after 0.1 million cycles. These show the appearance of typical micropits formed by crack propagation (Note: the cross-section obtained in ZDDP with low magnification shown in the upper-most image was captured using an optical microscope.) .....	250
Figure 11-9 Measured percentage of micropitted area on ball wear track in tests in which different MoDTC concentrations were added after 0.1 million cycles of running in with ZDDP solution.....	251
Figure 11-10 Disc roughness evolution in tests conducted where oils with different MoDTC concentrations are added after 0.1 million cycles .....	252
Figure 11-11 Evolution of tribofilm thickness in tests conducted where oils with different MoDTC concentrations were added after 0.1 million cycles of running-in with ZDDP solution .....	253
Figure 11-12 Elastic modulus of ZDDP tribofilm formed on AISI 52100 steel substrate after 0.3 million cycles of rubbing in ZDDP only solution as measured by nano indentation in CSM mode. The measured ZDDP tribofilm thickness was 175 nm.....	255
Figure 11-13 Predicted contact pressure distributions for a steel-on-steel contact and an equivalent steel on 175 nm thick ZDDP tribofilm on steel substrate contact. Analysis uses measured roughness profile from a fresh MTM disc with $R_a \sim 0.43 \mu\text{m}$ and measured elastic modulus of ZDDP film ( $E = 37.7 \text{ GPa}$ ). Note that the results shown are from a pure elastic analysis to illustrate the extreme case. ....	258
Figure 11-14 Surface pressure distribution, contours of positive (tensile) $\sigma_{xx}$ stress (compressive $\sigma_{xx}$ stresses set to zero for clarity) and contours of maximum shear stress in the central plane ( $y = 0$ ) in the rolling direction in the contact of an MTM ball and disc under normal load of 75 N and friction as stated: (a) smooth MTM ball on the rough disc	

(disc roughness as used in present tests and measured using a stylus profilometer); (b) smooth ball on smooth disc under same loading conditions. All stresses have been normalised by the maximum Hertz pressure. Note that the top of the figures of stress distribution ( $z = 0$ ) are the contact surfaces.....	261
Figure 11-15 Relationship between crack subsurface length and crack angle relative to the surface as measured for all cracks observed in the prepared cross sections of the balls in the rolling direction at 8 million cycles for the lubricant blends containing different amounts of MoDTC as stated. Parts of the relevant cross sections are shown in Figure 11-8.....	263

## List of Abbreviations

ZDDP	zinc dialkyldithiophosphate
RCF	rolling contact fatigue
NEDC	New European driving cycle
HEV	hybrid electric vehicle
PHEV	plug-in hybrid electric vehicle
EV	electric vehicle
FCV	fuel cell vehicle
DLC	diamond like carbon
a-C:H	hydrogenated amorphous carbon
TiN	titanium nitride
TiC	titanium carbide
CrN	chromium nitride
NO <sub>x</sub>	nitrogen oxides
SO <sub>x</sub>	sulfur oxides
PM	particle matter
HC	hydrocarbons
SCR	selective catalytic reduction
DPF	diesel particulate filter
TWC	three-way catalytic converters
EGR	exhaust gas recirculation
ACEA	European automobile manufacturers' association
ILSAC	international lubricant standardization and approval committee
API	American petroleum institute
JASO	Japanese automotive standards organization
FEI	fuel efficiency improvement
SAPS	sulfated ash, phosphorus and sulfur
HTHS	high temperature and high shear
SFC	specific fuel consumption
GMP	glycerol mono oleate
EP	extreme pressure
FM	friction modifier
MoDTC	molybdenum dialkyldithiocarbamate



VI	viscosity index
VM	viscosity modifier
PMA	polymethacrylate
OCP	olefin copolymer
SCP	styrene-diene copolymer
PPD	pour point depressant
GTL	gas to liquids
PAO	poly alpha olefin
IR	infrared spectroscopy
Raman	Raman spectroscopy
XPS	X-ray photoelectron spectroscopy
XANES	X-ray adsorption near edge spectroscopy
TEM	transmission electron microscopy
STEM	scanning transmission electron microscopy
EDX	energy dispersive X-ray spectroscopy
BO	bridging oxygen, black oxide
NBO	non-bridging oxygen
FIB	focused ion beam
APT	atom probe tomography
AFM	atomic force microscopy
WLI	white light interferometer
SWLI	Scanning White Light Interferometry
ECR	electrical contact resistance
SLIM	spacer layer interferometry
EDTA	ethylenediaminetetraacetic
FFT	fast Fourier transform
MTM	mini traction machine
CSM	continuous stiffness measurement
XRD	X-ray diffraction
NMR	nuclear magnetic resonance
UV	Ultraviolet
MEVVA	metal vapor vacuum arc
ZDP	zinc dialkylphosphates
CB	carbon black
SRR	slide-roll-ratio
MPR	micropitting rig

# 1 Thesis Outline and Research Question

The current trend of lower-viscosity lubricants with the aim of improving fuel efficiency of mechanical systems means that machine components are required to operate for longer periods in thin oil film, mixed and boundary lubrication conditions, where the risk of surface damage is increased. For this reason, the ability of tribofilms generated from zinc dialkyldithiophosphate (ZDDP) antiwear lubricant additive to provide adequate surface protection has become increasingly important. However, the properties and performance of these tribofilms and the reaction mechanisms of tribofilm formation are not fully understood. Therefore, this thesis describes research aimed at further understanding the tribochemical behaviour of ZDDP. After this initial chapter, the structure of the thesis is as follows.

**Chapter 2:** An introduction to the fundamentals of tribology, wear mechanisms and lubrication is presented. Also, the regulations and trends of automobiles and engine oils are described.

**Chapter 3:** Previous tribochemical investigations of ZDDP tribofilms are reviewed. This review identifies a number of important areas where understanding is currently limited and these areas provide the key research questions to be addressed in this study. Also, the aims of this research are listed.

**Chapter 4:** Details of the experimental methods used in this research are provided. These include lubricants, solid materials, tribometers, surface analysis, test procedures and test conditions.

**Chapter 5:** In previous research the chemical and mechanical properties of ZDDP tribofilms have been investigated and it has been found that tribofilms have a layered structure composed of mainly zinc and iron phosphates with a patchy morphology. However, the properties of these films are not yet fully understood, especially in the context of crystallinity and durability. This chapter describes new research into the evolution of ZDDP tribofilm crystallinity during its formation and the effect of this on the tribofilm durability. Reaction mechanisms of tribofilm crystallinity formation are also suggested.

**Chapter 6:** Most tribometer tests to measure the friction and wear properties of lubricants are based on AISI 52100 1% Cr bearing steel. However, many important machine components such as gears and cams employ quite different alloy steels, and it has recently been shown that tribofilm formation on such alloys is not the same as that on conventional bearing steel. This difference might originate from differences in mechanical properties, such as hardness or topography, and/or differences in surface chemical composition. To explore this further, this study examines the influence on ZDDP tribofilm formation of ion-implanting various alloying elements, Ni, Mo, Cr, V and W, into bearing steel surfaces.

**Chapter 7:** Most research on ZDDP to date has studied its behavior on steel and research on tribofilm formation on other materials is quite limited. This chapter describes investigations to understand the extent to which ZDDP tribofilms form on non-metallic surfaces in rubbing contacts and, if they do form, the chemical properties of these tribofilms. Of particular interest is the impact of different materials on the mechanism of tribofilm formation compared to its formation mechanism on steel substrates.

**Chapter 8:** Severe wear of hydrogenated DLC rubbed against steel in an MoDTC solution has been widely reported. Although the mechanisms of this type of wear have been investigated, the possible ways to reduce such wear and the mechanisms of how this wear can be reduced have not been well examined. In this chapter, the effect on MoDTC-promoted a-C:H DLC wear of adding various surface-active additives used in engine lubricants, including ZDDP, an ashless EP additive, Ca detergents, dispersants, an OFM and a PAMA, to an MoDTC is studied. Relevant mechanisms by which these additives reduce the impact of MoDTC on DLC wear are suggested.

**Chapter 9:** ZDDP tribofilms may prevent direct asperity contact, resulting in excellent antiwear performance. However, it has been found in the past that ZDDPs promote fatigue wear, especially micropitting wear. It has been suggested that this increase of micropitting may result from inadequate running-in due to the rapid formation of protective antiwear tribofilms, but direct investigation of the effect of ZDDP tribofilms on micropitting has not yet been made. This research correlates ZDDP tribofilm growth rates and the evolution of micropitting by developing a new technique to observe the evolution of ZDDP tribofilm in-situ and any accompanying micropitting during the same test.

**Chapter 10:** In order to alleviate micropitting, one potential solution is to apply black oxide coating,  $\text{Fe}_3\text{O}_4$ , on steel surfaces. It has been reported that black oxide has considerably lower hardness than steel, resulting in fast running-in, thereby reducing asperity stresses on rubbing surfaces. Consequently, micropitting on such surfaces is reduced. However, the relevant mechanisms by which black oxide coating mitigates micropitting have not been fully understood, especially the effect of black oxide coating on antiwear tribofilm formation and its subsequent effect on micropitting. This study provides a new understanding of the impact of black oxide coating on ZDDP tribofilm formation and micropitting.

**Chapter 11:** It has been found that the addition of MoDTC to a ZDDP oil can mitigate micropitting. This may result from MoDTC producing low friction and/or MoDTC promoting adequate running-in with ZDDP-containing oils by reducing ZDDP tribofilm formation. However, the relative contribution of these two factors on micropitting have not been isolated so that the impact of friction reduction on micropitting is still unclear. This research aims to understand the effect of friction on micropitting and the relative mechanisms by which friction influences micropitting by isolating the friction from other influential factors.

**Chapter 12:** Conclusions and achievements of this research are listed and suggestions for future work are presented.

## 2 Background

Tribology is defined as the science of interacting surfaces in relative motion and related subjects. Most machines contain components whose solid surfaces are loaded and rub together. Unless they are effectively lubricated, the interaction of such surfaces provides high friction and surface damage.

### 2.1 Solid-solid Friction

Friction is the resistance to motion encountered when one body tangentially moves over another. It exists between all pairs of moving surfaces; lubricated or dry, smooth or rough. Amontons [1] studied sliding friction in unlubricated contact and found;

- Friction is proportional to applied load;  
 $F = \mu W$   
( $F$ : friction,  $\mu$ : friction coefficient and  $W$ : load)
- Friction is not dependent on geometrical contact area
- Friction is only very slightly dependent upon sliding speed

Much later, Bowden and Tabor [2] developed a more mechanistic model based on solid/solid adhesion with the concept that a macro-scale contact is made of lots of contacting asperities. Based on this they showed that;

- $\mu = F / W = \tau_f / H$   
( $\tau_f$ : effective shear strength,  $H$ : effective surface hardness)

There are other solid-solid friction models proposed and they all show that the ratio of interfacial shear strength to hardness is a crucial parameter in determining adhesive friction. To obtain low adhesive friction between rubbing surfaces in contact, a low shear strength surface film and high subsurface hardness are needed. A great deal of research has been reported on controlling friction in many practical applications such as engines, bearings, clutch and brake systems, by modifying operation conditions, materials and lubricants.

## 2.2 Wear

Wear is progressive damage occurring on a rubbing surface. The most widely accepted wear rate equation is called Archard's wear equation and is as follows [1].

- $R_L = k_A W / H$   
( $R_L$ : wear rate per unit sliding distance,  $k_A$ : Archard wear coefficient,  $W$ : load and  $H$ : hardness of material)

This equation is useful for some systems, in particular for dry wear, but it is not universal or highly accurate. There are four main wear types as described below.

### 2.2.1 Adhesive Wear

When pairs of metal surfaces rub together without protective lubricant films or low shear strength chemical layers, they experience strong metallic bonding forces between them. These forces promote junction growth, resulting in the adhesion of metal asperities. In consequence, when the subsurface is weaker than the welded junction, material is torn from one surface. Torn material often remains on the counterface, and it can be knocked off because of repeated asperity contacts, resulting in adhesive wear.

### 2.2.2 Abrasive Wear

Abrasion is ploughing-out of material from rubbing surfaces by interlocking and relative motion. There are two types of abrasive wear. One is two-body abrasion; when one of the rubbing surfaces is harder than the other and its asperities indent and plough material from the softer surface. The other is three-body abrasion; when hard particles are present and are dragged between the two rubbing surfaces; these particles abrade one or both rubbing surfaces.

### 2.2.3 Corrosive Wear

Metal surfaces are chemically attacked by corrosive compounds such as oxygen, water, acids and some lubricant additives. Corroded metal surfaces are generally more brittle than metals themselves, resulting in more wear.

#### 2.2.4 Fatigue Wear

Fatigue wear is defined as the continuous removal of material induced by applied cyclic stresses in rubbing materials. It occurs when these stresses exceed the elastic limit of material. The main fatigue mechanism is rolling contact fatigue (RCF). RCF affects the life of rolling elements; bearings and gears subjected to high contact stresses. Two modes of RCF are commonly recognized; pitting and micropitting.

Pitting is characterized by the formation of deep crates or pits on the macro-contact level, typically a millimeter or so deep. Pitting is initiated from the subsurface and surface due to cyclic Hertzian stresses from repeated over-rolling. Cracks propagate rapidly under continued running, resulting in the removal of quite large fragments of material. Figure 2-1 shows examples of pitting failure on bearing raceways initiated from a surface-originated crack which has propagated into the depth of the material to undermine a piece of material that is then dislodged [3,4].

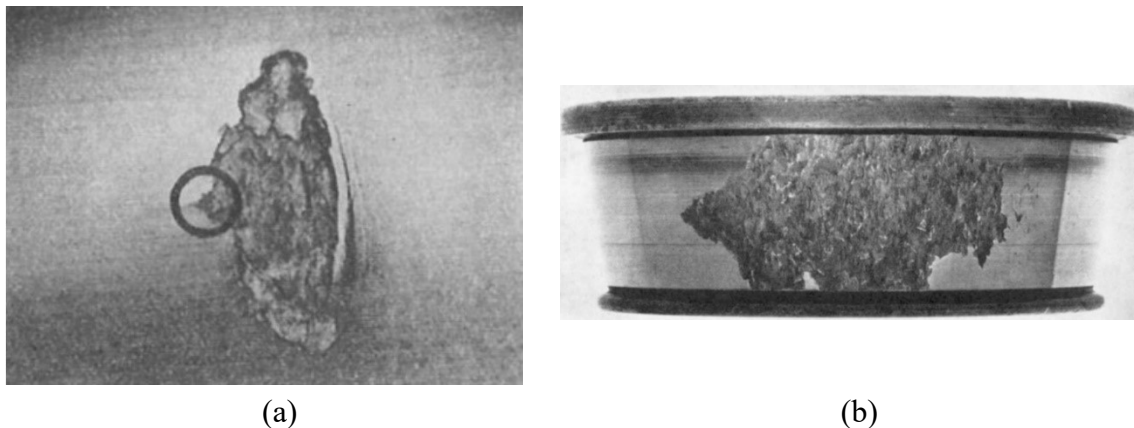


Figure 2-1 Examples of surface-originated pit. Circle mark in (a) shows the crack initiation site [3, 4]

Recently, an increase of energy density of machines and reduction of lubricant viscosity has promoted higher contact stresses and also a general decrease of lubricant film thickness, with resulting increased solid-solid interactions. As a consequence, many rolling bearings and gears operate mainly in thin oil film with asperity contact (in the boundary to mixed lubrication regimes described in Section 2.4) [5–7]. This causes more surface-initiated damage such as micropitting.

Micropitting is a type of surface fatigue damage caused by stress fluctuations due to roughness asperity interactions in rolling-sliding contacts such as in rolling bearings and gears, as shown in Figure 2-2 [8]. These asperity stress cycles result in fatigue damage accumulation in the near-surface regions, leading to eventual initiation of numerous surface fatigue cracks. These cracks always penetrate the surface aligned in the opposite direction to the frictional force on the asperities. These cracks then propagate under cyclical application of asperity stresses until a tiny fragment of material detaches from the surface as shown in Figure 2-3 [9]. This damage manifests itself as numerous small pits, tens of microns in size, that give the surface a frosted appearance. When it progresses, substantial loss of material occurs, and this is a common failure mode in gears and rolling bearings. Micropitting is surface-initiated damage that occurs in thin oil film condition, and it is significantly affected by lubricant additives.

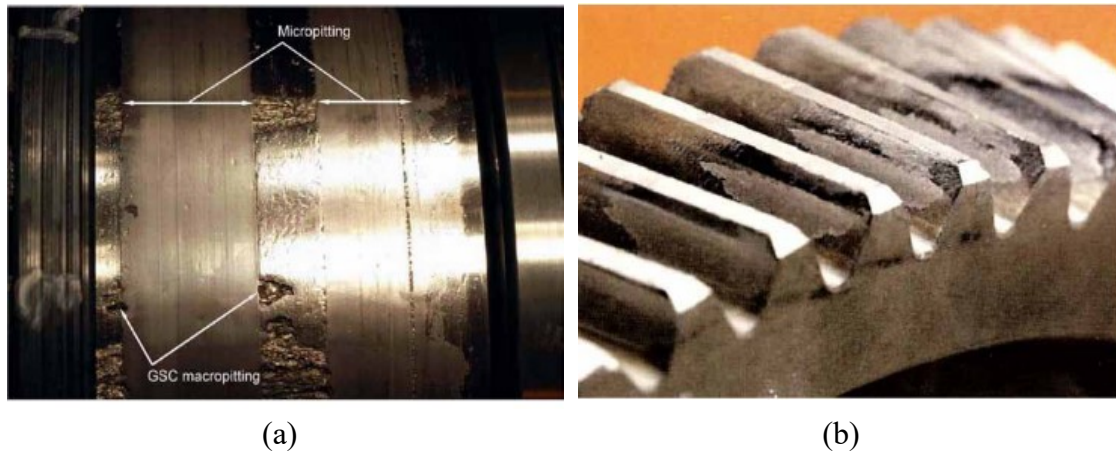


Figure 2-2 Micropitting on (a) a bearing and (b) a gear [8]

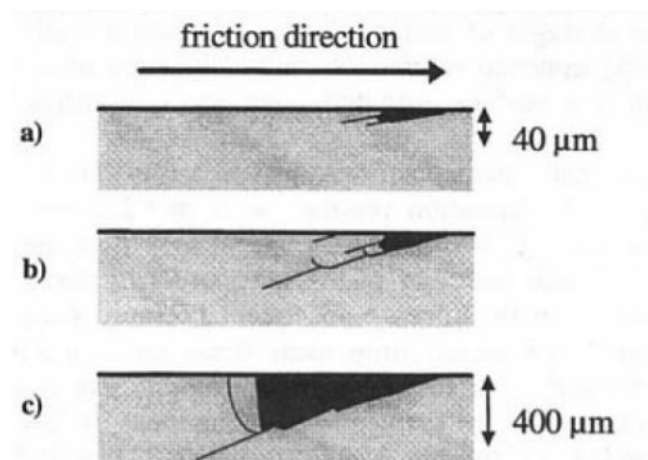


Figure 2-3 Schematic illustration of surface crack initiation and propagation of micropitting [9]



### 2.3 Lubrication

Lubrication is the effective interposition of a layer of solid, liquid or gas between two solid bodies [1,10]. In general, this layer has low shear strength, and thus reduces friction. It also limits direct contact of the asperities on opposing surfaces and the consequent stresses, which reduce surfaces damage.

There are four types of lubrication regime which can be defined using a Stribeck curve as shown in Figure 2-4 [11]; Hydrodynamic, Mixed, Boundary and Elasto-Hydrodynamic. This curve shows the relationship between log (friction coefficient) and log (oil film thickness). The latter depends on the parameters of viscosity, speed and load arranged as shown in the figure. As film thickness increases with the increase of viscosity and speed and the decrease of load, rubbing surfaces are progressively separated by a hydrodynamic (or elasto-hydrodynamic) film, that results in varying friction. Figure 2-4 also shows the lubrication regimes where engine components operate.

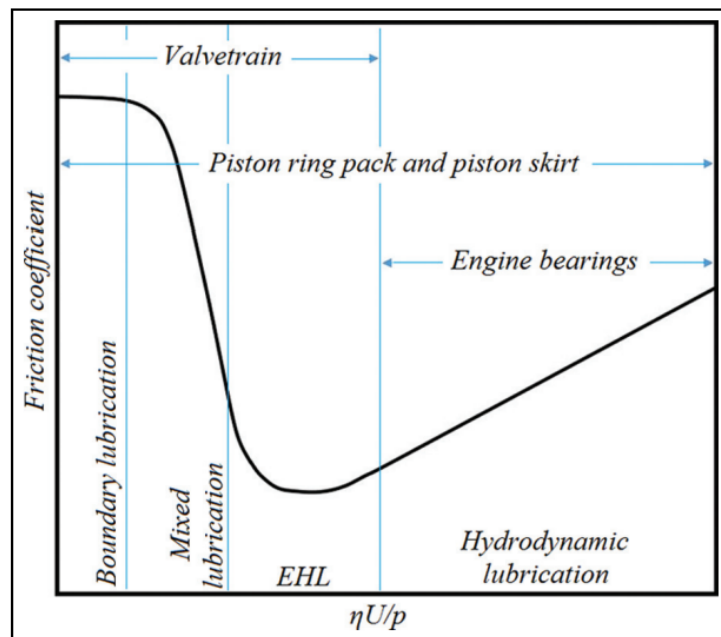


Figure 2-4 Stribeck curve and corresponding engine sliding parts [11]

### **2.3.1 Hydrodynamic Lubrication (HL) Regime**

In the HL regime, two surfaces in sliding contact are completely separated by a thick oil film [1,10]. This film is drawn between the surfaces (entrained) by the moving surface, where it becomes pressurized and can thus hold the surfaces apart under load. The lubricant film thickness is generally between 1-100  $\mu\text{m}$ , and it can support pressures up to about 200 MPa. Pressures encountered in the HL regime are not enough to significantly deform the rubbing surfaces or to greatly increase the lubricant viscosity. In general, the friction of a hydrodynamic lubricated contact is low since it results only from shearing in the oil film and thus depends on the oil film viscosity. Typical components that operate in the Hydrodynamic regime are plain journal bearings, piston skirts and thrust pad bearings.

### **2.3.2 Elasto-Hydrodynamic Lubrication (EHL) Regime**

EHL occurs between nominally point or line contacts where all the loading is concentrated over a small contact area [1,10]. This concentrated or non-conformal contact results in high peak pressures of typically 2 GPa between surfaces and such high pressures cause elastic flattening of the contacting surfaces, forming a localized conforming contact. Also, high pressure increases the viscosity of the lubricant in the contact inlet. As a result, the motion of the surfaces can entrain an oil film that is able to support very high (GPa) pressures. EHL films can be up to 5  $\mu\text{m}$  thick but are often much thinner and comparable to the surface roughness of normal components. Typical components that operate in the EHL regimes are ones where both surfaces move relative to the contact (mixed rolling-sliding) such as rolling element bearings, most gears, and cams and tappets.

### **2.3.3 Boundary Lubrication Regime**

Boundary lubrication occurs when there is insufficient hydrodynamic or elastohydrodynamic film to separate the rubbing surfaces. This occurs particularly in conditions of slowly moving contacts, high temperature and with very low viscosity lubricants [1,10]. Film thickness is very small and less than the mean surface roughness, so the applied load is supported predominantly by asperity contact. This contact provides high friction and surface damage. Valve train systems are lubricated in the boundary lubrication regime for part of their cycle.

### 2.3.4 Mixed Lubrication Regime

In the mixed lubrication regime, film thickness is of the same order as the mean surface roughness of the rubbing surfaces. This means that there are areas in the contact interface that are fully separated by a pressurized lubricant film (hydrodynamic or elasto-hydrodynamic film) and areas in which asperity-asperity contact takes place [1,10]. The film thickness is usually in the range of 0.02 - 1  $\mu\text{m}$ . Many practical machine components such as cams and piston rings/liners operate in mixed lubrication regime for parts of their operating cycles.

One commonly-used way to describe the extent of hydrodynamic lubrication is by the lambda ratio. This is the ratio of the predicted minimum HL or EHL film thickness to the composite root mean square surface roughness; *i.e.*

$$\lambda = \frac{h_{min}}{\sqrt{R_{q1} + R_{q2}}}$$

where  $R_{q1}$  and  $R_{q2}$  are the root mean square roughnesses of each surface. If the lambda ratio is greater than about 2, the asperities are almost completely separated and the contact operates in the full hydrodynamic or EHL regime [10]. If the lambda ratio is less than about 0.05 the contact is in full boundary lubrication. Between these the contact is in the mixed lubrication regime [10].

The way to control friction and reduce surface damage is dependent on the lubrication regime, as described in Section 2.6. Before this, regulations and trends of automobiles and engine oils are outlined.

## 2.4 Regulation and Trend of Automobiles

Protecting the environment from global warming and pollution are currently two of the most important global issues for society. Greenhouse gases and pollutants are emitted by several industrial sectors, including the transport sector. Within this sector, the automobile industry accounts for the largest proportion of the emission of these gases. Since these exhaust gases from automobiles have become strictly regulated, automobile and parts manufacturers, including lubricant suppliers, have been developing more environmentally-friendly products to meet these strict regulations. The key environmental issues of automobiles are described as follows.

### 2.4.1 Improvement of Fuel Efficiency

One of the biggest environmental issues for the automobile industry is global warming caused by greenhouse gases. The emission of greenhouse gases has been regulated in the Kyoto Protocol (1997) and the Paris Agreement (2015). For example, the Paris Agreement aims to limit the rise of global temperature to less than 2 °C above pre-industrial levels, with an aspirational 1.5 °C limit [12]. In order to achieve these limits, the EU, for example, has proposed 40% reduction of greenhouse gas emission by 2030 compared to 1990. Greenhouse gas includes carbon dioxide (CO<sub>2</sub>), methane (CH<sub>4</sub>), dinitrogen oxide (N<sub>2</sub>O) and fluorocarbons. Among these, very large amounts of CO<sub>2</sub> are emitted from automobiles through the combustion of petroleum fuel. Figure 2-5 shows the ratio of CO<sub>2</sub> emission from fuel combustion by each sector in 2017 [13]. This indicates that large amounts of CO<sub>2</sub> were emitted by the transport sector (*ca.* 20%); thus, an important mission of the automobile industry is to reduce the emission of CO<sub>2</sub> by increasing engine fuel efficiency.

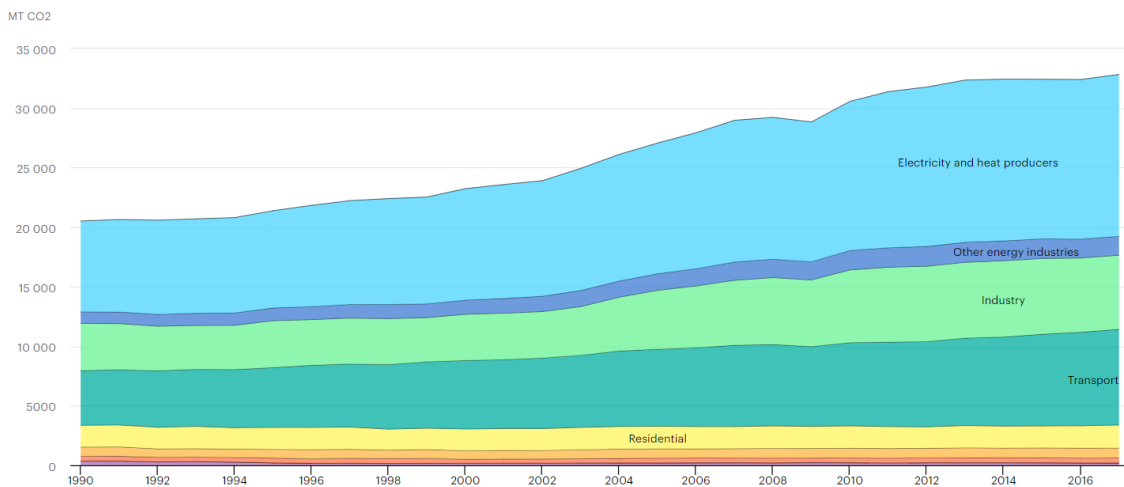
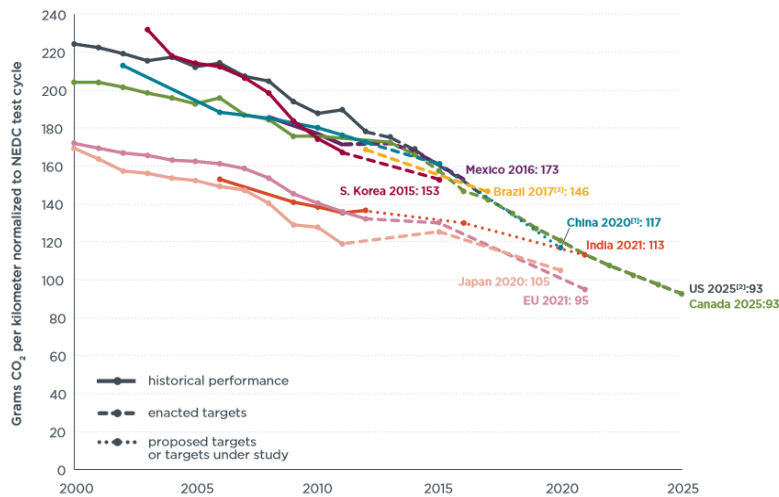


Figure 2-5 Global CO<sub>2</sub> emissions by sector in 2017 [13]

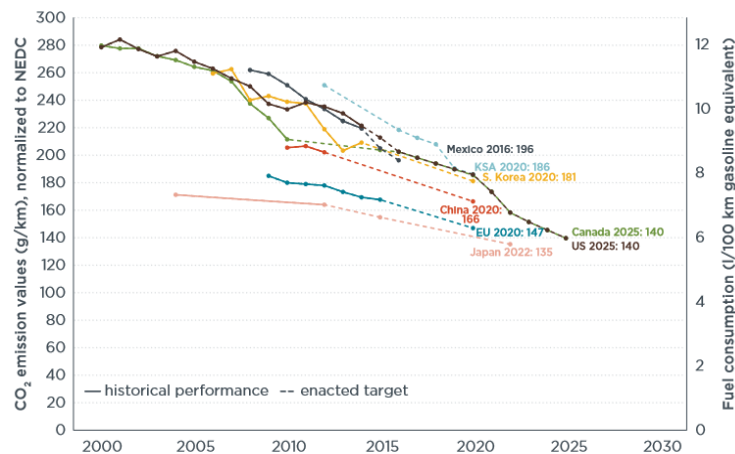
The most widely used measure of fuel efficiency has proved to be the amount of CO<sub>2</sub> emitted per travelled vehicle mile and many countries have introduced regulations that limit this by vehicle type. Figure 2-6 (a) shows a comparison of global CO<sub>2</sub> regulations for passenger vehicles in the New European driving cycle (NEDC) in 2014 [14]. It is clear that the emission limit is becoming progressively stricter; 95 g/km by 2021 in the EU, 99

g/km by 2025 in the US and 117 g/km by 2020 in China. Figure 2-6 (b) shows the CO<sub>2</sub> emission regulations for light duty vehicles in the NEDC in 2017 and shows that the regulated values are slightly higher than for passenger vehicles; 147 g/km by 2021 in the EU, 140 g/km by 2025 in the US and 166 g/km by 2020 in China [15].

These regulations are expected to be continuously tightened. Therefore, technology to improve fuel efficiency of automobiles is needed. Two main ways to improve fuel efficiency are (i) replacement of combustion engines with electric motors and (ii) reduction of mechanical losses in combustion engines.



(a)



(b)

Figure 2-6 CO<sub>2</sub> emissions and fuel consumption of (a) passenger vehicles (2014) [14] and (b) light duty vehicles (2017) [15] normalized to NEDC

### 2.4.2 Introduction of Eco-friendly Vehicles

In order to improve fuel efficiency, eco-friendly vehicles have been actively developed. These include hybrid electric vehicles (HEVs), plug-in hybrid electric vehicles (PHEVs), electric vehicles (EVs) and fuel cell vehicles (FCVs). While HEVs and PHEVs are powered by both petroleum fuel and electricity using a combustion engine and an electric motor, EVs and FCVs are powered only by electricity; thus, the latter do not emit CO<sub>2</sub> to obtain power. Recently, EU governments, for example that of Germany, decided to prohibit the supply of passenger vehicles with combustion engines by around 2030 [16]. These policies have been pushing the introduction of eco-friendly vehicles into the market. Figure 2-7 shows a light vehicle sales forecast (2017) and indicates that, as the number of combustion engine vehicles will decrease, the sales of eco-friendly vehicles, especially EVs, will increase [17].

However, to significantly accelerate the introduction of EVs into the market, several technical and infrastructural challenges must be overcome; low battery capacity to store electricity, slow charging speed of batteries and limited charging stations [18,19]. It is expected to take some years to overcome these challenges, so vehicles with a combustion engine, including HEVs and PHEVs, are likely to continue to be used for several decades. Therefore, new technology to improve the fuel efficiency of combustion engines is still required.

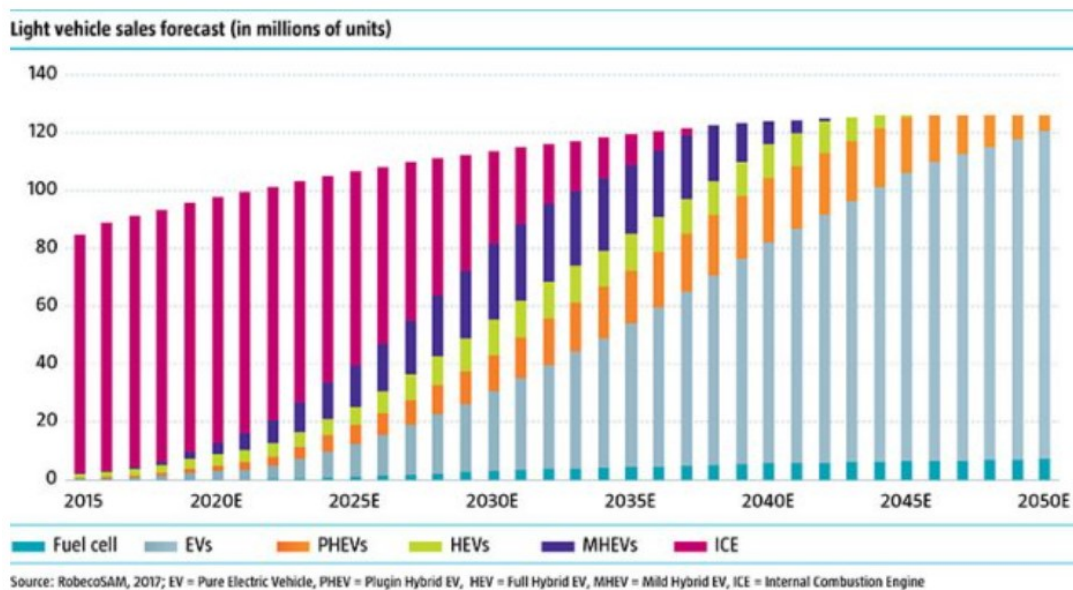


Figure 2-7 Light vehicle sales forecast (in millions of units) [17]

### 2.4.3 Reduction of Mechanical Loss

Reduction of the proportion of the energy generated from fuel combustion in internal combustion engine vehicles that is lost, *i.e.* does not directly propel the vehicle, is a main way to reduce CO<sub>2</sub> emission. Figure 2-8 (a) shows a representative energy split produced from diesel internal combustion, and shows that 4 - 15% of the overall available energy is lost due to mechanical friction, resulting in a reduction of fuel efficiency [20]. Therefore, as well as the improvements of combustion systems, technology to reduce mechanical friction inside the engine has been enthusiastically investigated. Figure 2-8 (b) shows the distribution of mechanical friction loss in a typical diesel engine and illustrates that it is important to reduce friction in all sliding parts; piston ring assembly, crankshaft and valvetrain [20,21]. Three ways to reduce friction loss of combustion engines are listed as follows; downsizing of engines, surface modification of engine components and introduction of low friction-lubricants (described later in Section 2.6).

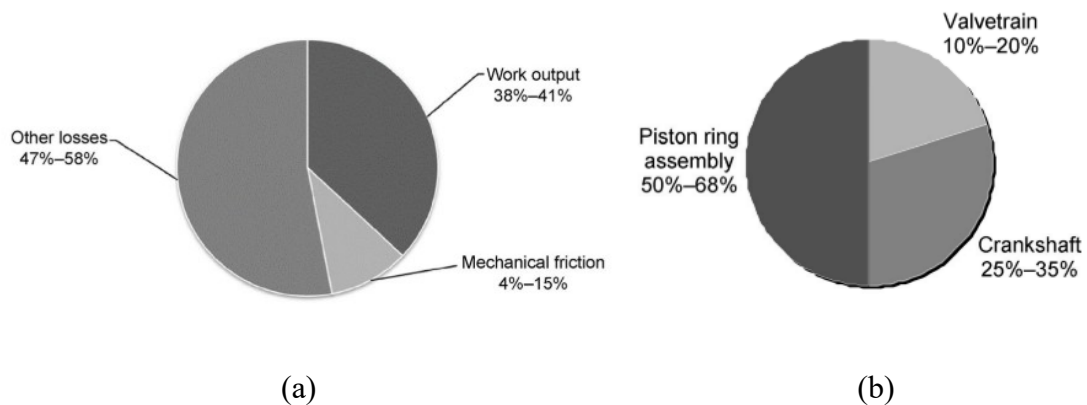


Figure 2-8 Distribution of (a) total energy in diesel combustion engine and (b) total mechanical friction losses [20]

One way to reduce total friction loss is to decrease the area of sliding parts, for example, by downsizing of engines and reduction of the number and/or volume of engine cylinders [20,22]. Figure 2-9 shows the evolution of average engine displacement of passenger vehicles, and indicates that the average engine displacement has been decreasing over the last 12 years [23]. As well as the reduction of the area of sliding parts, downsizing can lighten the weight of engine, itself increasing fuel efficiency. On the other hand, in order to maintain power output, a downsized engine is generally turbocharged, resulting in substantial increase in the power density of the engine. This severe condition in the engine

promotes thin oil films between components and also lubricant aging from high temperatures, promoting surface damage.

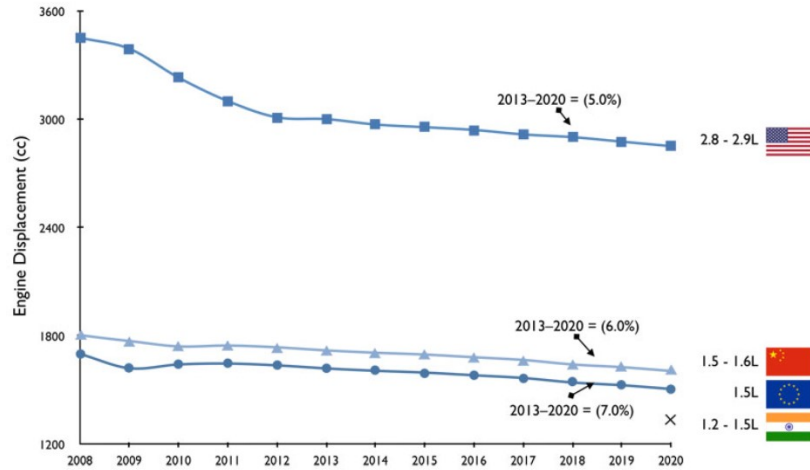


Figure 2-9 The evolution of average engine displacement of passenger vehicle (2016)  
[23]

Another way to reduce friction loss is to decrease friction coefficient in sliding components by surface modification of components, *i.e.* surface texturing and surface coating [20,24,25]. Surface texturing, for example applying dimples or pockets on surfaces such as piston-linear contacts, promote the retention of oil film, resulting in lower friction. [26,27].

Friction can also be reduced by applying surface coatings, *i.e.* diamond like carbons (DLCs) and ceramics, on ferrous surfaces. These coatings are hard and have relatively low shear strength. As such, DLC coatings have been widely applied on rocker arms, valve lifters and piston rings [28]. As shown in Figure 2-10, DLC coatings are classified into 4 types depending on the concentration of hydrogen and the  $sp^3/sp^2$  ratio of carbon; tetrahedral amorphous carbon (ta-C), hydrogenated ta-C (ta-C:H), amorphous carbon (a-C) and hydrogenated amorphous carbon (a-C:H) [29]. Also, third elements such as Ti, W, Si and Cr have been effectively doped into DLCs. These characteristics affect the mechanical and chemical properties of DLCs.

As well as DLCs, ceramic coatings such as titanium nitride (TiN), titanium carbide (TiC) and chromium nitride (CrN) have been applied to reduce friction coefficient. For example, because of its high thermal stability, high hardness and excellent wear resistance, CrN has



been applied to piston cylinders and piston rings [30–32]. Figure 2-11 shows that friction coefficient was effectively reduced by applying coatings of ceramics and DLCs on piston rings [33].

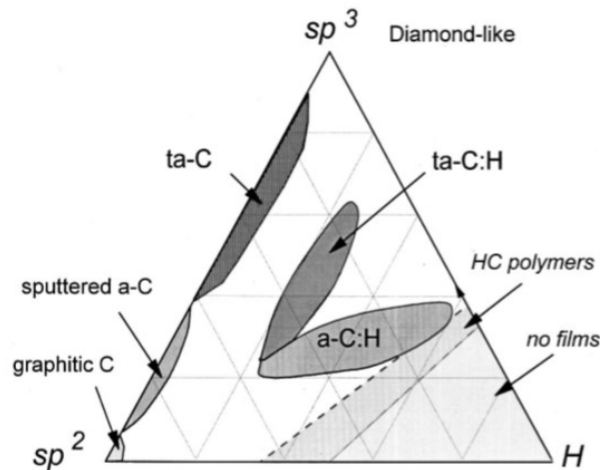


Figure 2-10 Ternary phase diagram of amorphous carbons. The three corners correspond to diamond, graphite, and hydrocarbons, respectively [29]

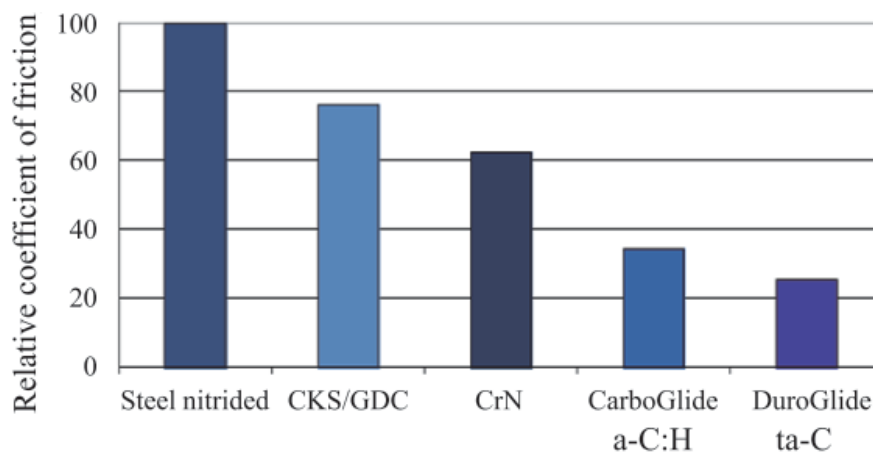


Figure 2-11 The effect of DLC and ceramic coated piston rings on friction coefficient [33]

Although these coatings can reduce friction, the resulting surfaces are generally less chemically reactive than ferrous surfaces. Therefore, to ensure surface protection, lubricants are required to be compatible with these non-metallic surfaces.

#### **2.4.4 Reduction of Pollutants**

As well as CO<sub>2</sub>, exhaust gas contains pollutants; nitrogen oxides (NO<sub>x</sub>), sulfur oxides (SO<sub>x</sub>), particle matter (PM), hydrocarbons (HC) and carbon monoxide (CO) [34]. These are undesirable, for example, NO<sub>x</sub> and SO<sub>x</sub> cause acid rain and PM results in respiratory diseases. Thus, the permitted levels of emission of these pollutants in the exhaust gas have been regulated. In order to meet these regulations, technologies to reduce these pollutant levels have been well developed since the 1980s.

Gasoline engines emit relatively low amounts of SO<sub>x</sub> and PM. Therefore, automobiles with gasoline engines are generally equipped with a quite simple exhaust aftertreatment system consisting of a three-way catalytic converter (TWC) which has a precious metal catalyst and converts NO<sub>x</sub>, HC and CO into N<sub>2</sub>, CO<sub>2</sub> and H<sub>2</sub>O [35]. However, in order to improve fuel efficiency, lean burn systems and direct fuel injection systems have also been introduced to gasoline engines, reducing HC and CO, but increasing NO<sub>x</sub> emission [36,37]. To remove this NO<sub>x</sub>, a lean NO<sub>x</sub> trap catalyst and exhaust gas recirculation systems have been adopted for automobiles with gasoline engines. EGR recirculates the combustion gas into engines, reducing NO<sub>x</sub> formation by the reduction of combustion temperature.

Unfortunately, components of the engine oils enter aftertreatment systems, where they can cause catalyst poisoning. Therefore, engine oils need to be compatible with these aftertreatment systems. For example, the catalyst, V<sub>2</sub>O<sub>5</sub>/WO<sub>3</sub>-TiO<sub>2</sub>, of the SCR system is strongly poisoned by phosphorus (P) and sulphur (S) contained in engine oil additives, decreasing NO<sub>x</sub> conversion [38,39]. This catalyst poisoning can be mitigated by reducing both the metals in engine oil additives and oil consumption [40,41]. Therefore, the properties of engine oils have been regulated in specifications as described below.

#### **2.5 Specification and Trend of Engine oils**

As described above, as well as their traditional role of surface protection, engine oils are now required to reduce friction loss and be compatible with aftertreatment systems. In order to ensure engine oil performance and properties, engine oil specifications have been developed as shown in Table 2-1. These include European Automobile Manufacturers' Association (ACEA) specifications in the EU, International Lubricant Standardization and Approval Committee (ILSAC) and American Petroleum Institute (API) specifications in the US and Japanese Automobile Standards Organization (JASO) specifications in

Japan [42–44]. Over time, the requirements for engine oils in the specifications have become increasingly strict as the regulations concerning fuel efficiency and pollutants for automobiles have tightened.

Table 2-1 The standards of gasoline and diesel engine oil in the EU, the US and Japan [42–44]

Institute	Vehicle type	Valid standard
ACEA	Passenger gasoline and diesel	A3/B3, A3/B4, A5/B5
	Passenger gasoline and diesel with DPF	C1, C2, C3, C4, C5
	Heavy duty diesel	E4, E6, E7, E9
ILSAC	Passenger gasoline	GF-5, GF-6
API	Passenger gasoline	SJ, SM, SN, SP
	Heavy duty diesel	CH-4, CI-4, CI-4+, CJ-4, CK-4, FA-4
JASO	Passenger and heavy-duty diesel	DL-0, DL-1, DH-1, DH-2, DH-2F

### 2.5.1 Fuel Efficiency Requirement

Table 2-2 and Table 2-3 show the fuel efficiency requirements of passenger car oils in ACEA, ILSAC and API [42–46]. These standards require the engine oils to have a specific value of fuel efficiency improvement (FEI) ratio measured in each engine test compared to reference oil. To ensure the retention of fuel efficiency during use, ILSAC and API also require the engine oils to meet a FEI after aging.

Table 2-2 Fuel efficiency requirement of ACEA [42,45]

	Gasoline and diesel engine oil (High *SAPS)			Catalyst compatible engine oil (Low SAPS)				
	A3/B3	A3/B4	A5/B5	C1	C2	C3	C4	C5
FEI ratio against 15W-40 reference oil (%) (CEC L-54-96)	-	-	$\geq 2.5$	$\geq 3.0$	$\geq 2.5$	$\geq 1.0$ (for xW-30 oil)		$\geq 3.0$

\*SAPS: sulfated ash, phosphorus and sulfur

Table 2-3 Fuel efficiency requirement of ILSAC and API [43]

Standard		ILSAC GF-5 and API SN			
SAE viscosity grade		xW-16	xW-20	xW-30	others
FEI ratio against 20W-30 reference oil (%) (ASTM D7589)	FEI 1+2	$\geq 2.8$	$\geq 2.6$	$\geq 1.9$	$\geq 1.5$
	FEI 2	$\geq 1.3$	$\geq 1.2$	$\geq 0.9$	$\geq 0.6$

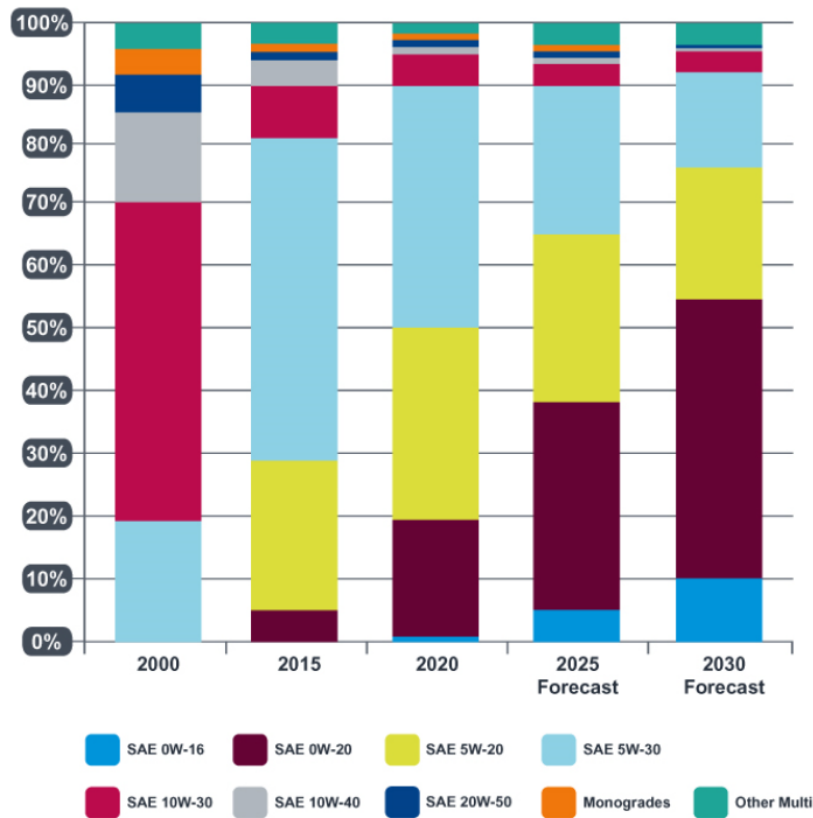
FEI 1: Tested using aged oil after 16 hours

FEI 2: Tested using aged oil after 100 hours

### 2.5.2 Technology to Improve Engine Oil Fuel Efficiency

In order to pass the tests for fuel efficiency, it is necessary for engine oils to reduce the friction coefficient of the various rubbing contacts. The technologies to achieve this have been quite thoroughly investigated. They vary across the lubrication regimes shown in the Stribeck curve (Figure 2-4).

In the HL regime, the two rubbing surfaces are completely separated by a thick fluid film [1,10] and the friction originates from the force required to shear this lubricant film. This shear force depends on the rate at which the lubricant film is sheared (the velocity gradient) and the dynamic viscosity of the lubricant in the film. Therefore, one of the main solutions to reduce shearing force is to use a lower viscosity lubricant. Figure 2-12 shows the trend of engine oil viscosity of passenger car gasoline engine oil in the US (2020) and illustrates that low viscosity engine oils with the grade of 0W-20 and 0W-16 are being more and more commonly used [47].



© 2020 Infineum International Limited. All rights reserved

Figure 2-12 The trend of engine oil viscosity of gasoline passenger vehicle in the US (2020) [47]

The effect of viscosity of engine oils has been well investigated, and it has been found that, as viscosity is decreased, in particular high temperature and high shear (HTHS) viscosity, fuel efficiency is increased, as shown in Figure 2-13 (light duty diesel engine oils) [48–51]. Considering these results, low viscosity grades of 0W-4, 0W-8 and 0W-16 were added in the viscosity standard (SAE J 300) in 2015.

As well as the increase of energy density of machines described in Section 2.5, the trends of lowering engine oil viscosity are expected to continue, resulting in thinner oil film in sliding contacts. This thin oil film can shift the lubrication regime from the HL regime to the mixed and boundary lubrication regimes, producing more and more asperity contact. Therefore, the role of additives that are able to protect component surfaces and also reduce boundary friction are becoming increasingly important.

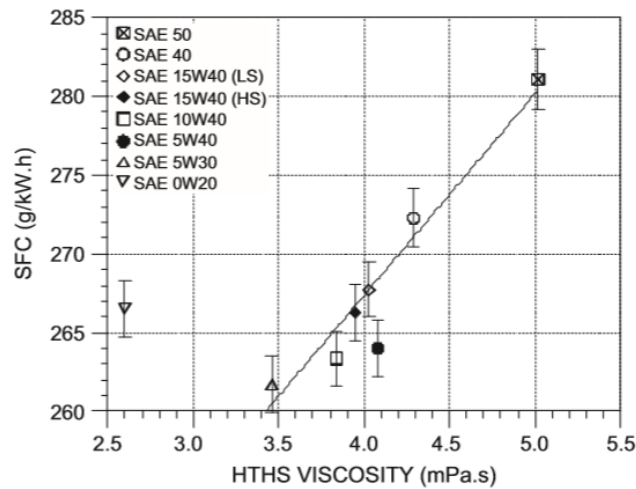


Figure 2-13 The effect of HTHS viscosity on fuel consumption measured in an diesel engine [49]

In the mixed and boundary lubrication regimes asperity contacts are present. This asperity contact increases both friction and surface damage. In order to control these, lubricant additives are employed to form protective films on the rubbing asperities. There are several different types of such film as listed below.

- Physically adsorbed films; one or several molecule-thick layers adsorb onto the surface by Van der Waal's forces.
- Chemically adsorbed films; a few nanometer thick layers form on the surface by the molecular affinity of polar molecules and interaction with metal cations.
- Chemical reaction films (tribofilms); films are formed by the chemical reaction of the surface with lubricant additives triggered by the asperity contact and high shear stress.

One common way to reduce friction is to form chemically adsorbed films or low shear strength tribofilms on the rubbing surfaces using a friction modifier (FM) additive. Two types are widely used; ashless compounds that are surfactants and form chemically adsorbed films, and organomolybdenum compounds that react with rubbing asperities to form tribofilms. Details of these additives, their structures and mechanisms of reducing friction coefficient are described in Section 2.7. Figure 2-14 shows the effect of several ashless FMs and molybdenum dialkyldithiocarbamate (MoDTC) on friction coefficient

in a ZDDP solution using a steel/steel tribopair [52]. As this study showed, the addition of FMs reduced friction coefficient in boundary and mixed lubrication regimes [52–54].

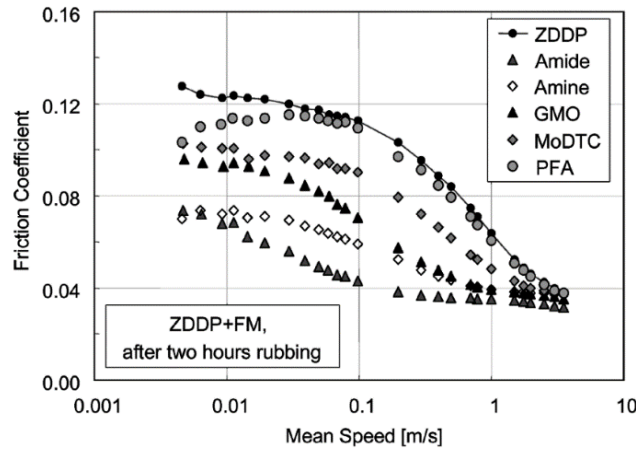


Figure 2-14 Stribeck curves for five friction modifier ZDDP blends after 2 h rubbing [52]

As presented in Section 2.5.4, non-metallic surfaces such as DLC and ceramic coatings have been commonly employed to reduce friction, primarily because they have less tendency to adhere compared to most metallic surfaces. However, these surfaces are used in engines that also contain ferrous-based contacts and are thus lubricated by conventional engine lubricants containing FMs. Therefore, the effect of FMs on non-metallic surfaces has also been investigated. Kano et al. [55] studied the effect of DLC coatings and addition of the ashless FM, glycerol monooleate (GMO), and found quite low friction coefficient (0.03) on a ta-C/ta-C tribopair with the presence of GMO, but not on an a-C:H/a-C:H tribopair (0.12 friction coefficient), as shown in Figure 2-15. This result and other studies suggest that film-forming behavior of ashless FMs is dependent on the properties of non-metallic surfaces [28,55–58]. As well as ashless FMs, a great deal of research has showed that MoDTC reduced friction coefficient on non-metallic surfaces; however, it caused abnormal wear on DLC coatings of DLC/steel tribopairs [59–64]. Although this wear mechanism has not been fully elucidated, Okubo et al. [59] have suggested that hard molybdenum carbide (MoC) tribofilm forms on steel by reaction of MoDTC with DLC, and this might cause abrasive wear of DLC coatings.

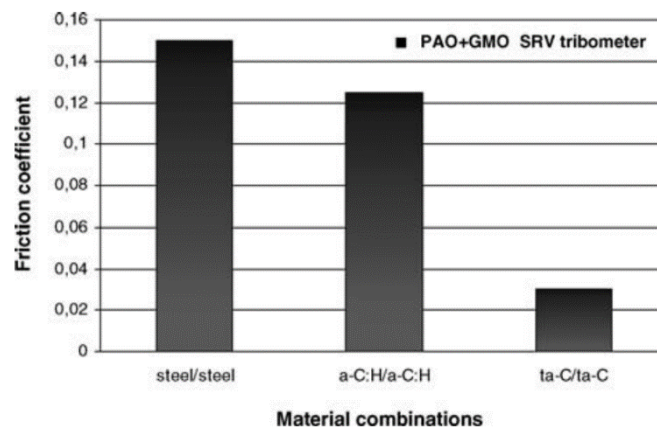


Figure 2-15 The effect of DLC coatings on friction using a SRV tribometer [55]

As shown above, lubricant additives including FMs form different films on non-metallic surfaces from those formed on ferrous surfaces, promoting different friction and wear behaviors. These mechanisms have not been fully understood, so the further study of the tribofilm formation on non-metallic surfaces is needed.

### 2.5.3 Exhaust Aftertreatment System Compatibility

As described in Section 2.5.5, harmful materials originating from the engine oil additives cause catalyst poisoning and filter plugging in exhaust aftertreatment systems such as TWC, SCR and DPF. Therefore, engine oils that limit the availability of these harmful materials are needed; this means that the concentrations of P, S and sulfated ash (S-ash) must be limited.

Table 2-4 shows the chemical limits of passenger car engine oil in ACEA, ILSAC and JASO [42–44]. P, S and S ash are controlled to small concentrations, and the amount of P that can be lost during an extended engine test (phosphorus volatility limit) is limited to a maximum of 20% in ILSAC GF-5 (Sequence IIIGB, ASTM D7320).

Table 2-4 Chemical limit of passenger car engine oil [42–44]

	ACEA		ILSAC	JASO
	C4	C5	GF-5	DL-1
Phosphorus (mass%)	≤0.09	0.07 - 0.09	0.06 - 0.08	≤0.1
Sulphur (mass%)	≤0.2	≤0.3	≤0.5*	≤0.5



Sulfated Ash (mass %)	≤0.5	≤0.8	-	≤0.6
Phosphorus volatility (%) (retention)	-	-	79≤	-

\* 0W-xx and 5W-xx: ≤ 0.5, 10W-30: ≤ 0.6

P and S mainly originates from the very widely used antiwear additive zinc dialkyldithiophosphate (ZDDP), while S-ash originates primarily from both ZDDP and Ca/Mg-based detergents. In future, the trend to reduce the amount of ZDDP and Ca/Mg detergents is expected to continue, so some research has investigated further reduction of the concentration of these additives. Shimizu and Kasai et al. [65,66] studied the performance of heavy duty diesel engine oil using ashless additives without ZDDP and Ca/Mg detergents. The authors showed that although there was no harmful effect on antiwear and detergency performance in rig tests, the ashless oil could not pass the piston detergency engine test (ASTM D6750, Caterpillar 1N engine test). Since the performance of ashless engine oils has not been investigated thoroughly in engine tests and field tests, large amounts of time and cost are likely to be needed to develop them. Therefore, additives including metals will probably to be used in engine oil for several decades. Indeed, significant further changes are becoming less likely in view of the increasing use of EVs and thus a shrinkage in the market of internal combustion engine vehicles.

## 2.6 Components in Engine Oil

Engine lubricants include a base oil and several additives. Table 2-5 lists the lubricant additives used in engine oils together with their function and representative compounds. In this section, these additives and the base oils are described.

Table 2-5 Lubricant Additives

Additive type	Function	Typical compound
Antiwear additive	- Reduce wear	- Zinc dialkyldithiophosphate (ZDDP)
Extreme pressure (EP) additive	- Prevent burning and scuffing in extreme pressure condition	- Organo sulphur compounds - Alkyl phosphate
Friction modifier (FM)	- Reduce friction - Reduce wear	- Glyceryl monooleate (GMO) - Molybdenum dithiocarbamate (MoDTC)

Detergent	- Neutralize acid - Inhibit formation of sludge and deposit	- Ca/Mg sulphonate - Ca/Mg phenate - Ca/Mg salicylate
Dispersant	- Disperse sludge and soot in engine oil	- Succinimide - Succinate
Viscosity modifier (VM)	- Increase viscosity - Control viscosity change on temperature	- Polymethacrylate - Olefin copolymer - Styrene-olefin copolymer
Pour Point Depressant (PPD)	- Reduce pour point	- Polymethacrylate
Antioxidant	- Inhibit oxidative degradation	- Hindered phenol - Aromatic amine - ZDDP
Rust Inhibitor	- Inhibit rust	- Carboxylic acid
Corrosion inhibitor	- Inhibit corrosion	- Benzotriazole - Substituted azoles
Foam Inhibitor	- Inhibit foam	- Polydimethylsiloxanes

### 2.6.1 Antiwear Additives

Engine components such as camshaft/tappet and piston ring/piston cylinder operate for parts of their cycles (when entrainment speed is low) in the mixed and boundary lubrication regime where there is asperity contact. This asperity contact can cause wear of surfaces, so an antiwear additive is added to form a protective tribofilm on the surfaces, mitigating surface damage. Without antiwear additives, serious surface failures occur; excessive wear, fatigue and seizure. Zinc dialkyldithiophosphate (ZDDP) in Figure 2-16, is by far the most widely used antiwear additive in engine oils.

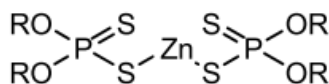


Figure 2-16 Representative antiwear additive; zinc dialkyldithiophosphate (ZDDP)

As shown in Table 2-6, the alkyl groups of ZDDPs affect both thermal stability and antiwear performance. Generally, ZDDPs with low thermal stability are most easily

decomposed to form tribofilm, resulting in better anti-wear performance than ZDDPs with high thermal stability [67]. Thus, ZDDPs are likely to show better antiwear performance in the following order: Secondary alkyl groups > Primary alkyl groups > Aryl groups. Details of tribochemical investigations of ZDDPs are described in Chapter 3.

Table 2-6 The effect of ZDDP structure on its thermal stability and antiwear performance

	Primary alkyl	Secondary alkyl	Aryl
Chemical structure	R: $R_1-CH_2-$	R: $R_1-\overset{\overset{R_2}{ }}{CH}-$	R: $R_1-\text{C}_6\text{H}_4-$
Thermal stability	good	poor	excellent
Antiwear performance	good	excellent	poor

### 2.6.2 Extreme Pressure Additives

Extreme pressure (EP) additives protect pairs of surfaces from seizing together in more severe rubbing conditions than conditions in which antiwear additives become effective [68,69]. EP additives are employed in contacts exposed to high sliding speed, high pressure and high temperature as present in cam followers and hypoid gears. Figure 2-17 shows representative sulfur type EP additives.

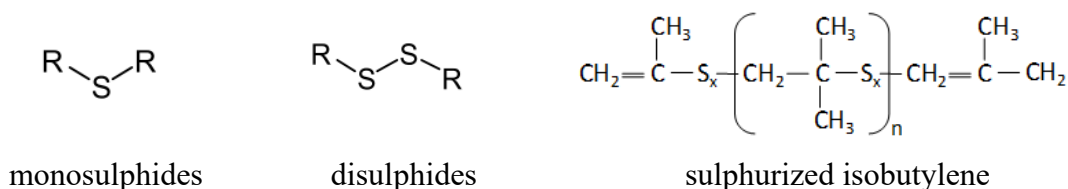


Figure 2-17 Representative EP additives

These sulfur additives react with metal surfaces very rapidly via the reactions shown in Figure 2-18. After absorbing on the metal surface, iron mercaptide undergoes a reaction to form an iron sulfide film, resulting in surface protection [70]. When EP additives have

S-S and C-S bonds that are easily broken, these reactions occur more easily. Although EP additives effectively protect surface from seizure, they may cause corrosive wear in some rubbing conditions because of their high reactivity. Because ZDDP molecules contain sulphur atoms, ZDDPs function as mild EP additives and more reactive sulfur type EP additives are not needed in engine oils.

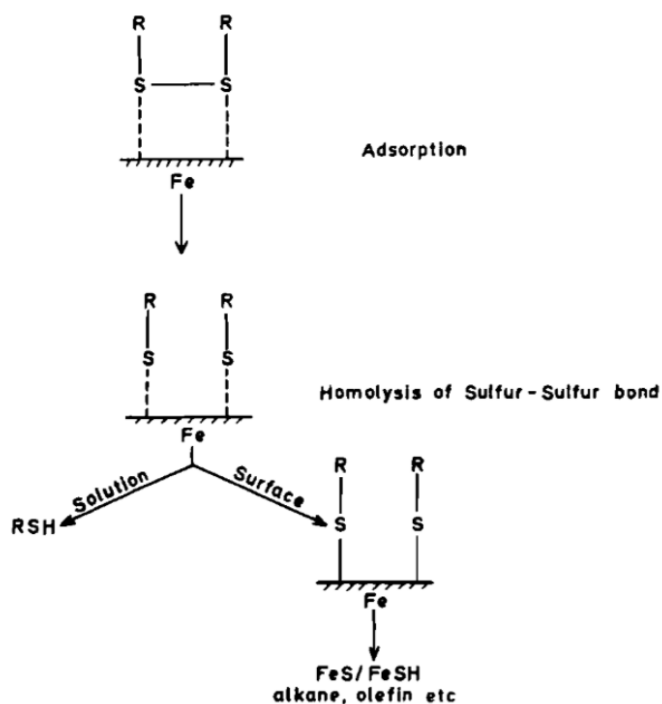


Figure 2-18 Reaction mechanism of sulphur-type EP additives [70]

### 2.6.3 Friction Modifiers

Friction modifiers (FM) were briefly discussed in Section 2.5.2. They reduce friction in mixed and boundary lubrication regimes by forming chemically adsorbed/reacted low shear strength films on rubbing surfaces. Figure 2-19 shows representative FMs including two ashless types that form chemically adsorbed layers and two organo-Mo types that form tribofilms by reacting on metal surfaces [71]. The molecular structure of ashless FMs affects friction performance and those with straight hydrocarbon chains are able to densely adsorb on surfaces, and thus prevent asperity contact [72–74]. This characteristic results in low friction coefficient.

Molybdenum dialkyldithiocarbamates (MoDTC) form tribofilms by the chemical reaction on rubbing metal surfaces. After adsorbing on surfaces, MoDTCs are decomposed by rubbing to form MoS<sub>2</sub>, which has a layer lattice structure and thus has inherently low shear strength, resulting in low friction coefficient [75].

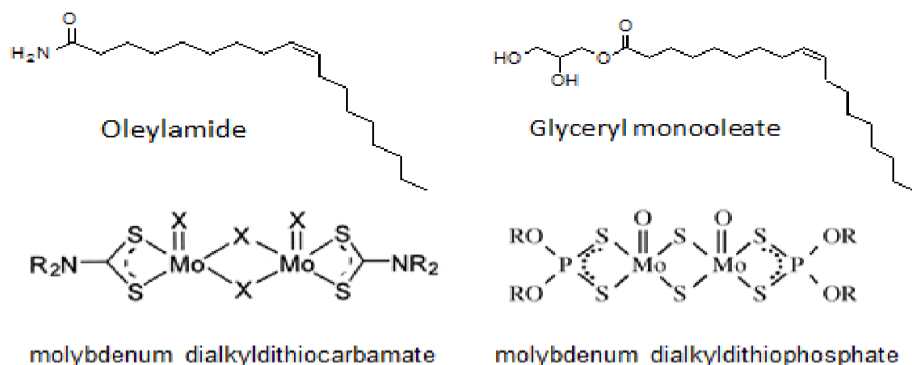


Figure 2-19 Representative friction modifiers [71]

#### 2.6.4 Antioxidants

Engine oils are exposed to high temperature and oxidizing atmosphere, resulting in the formation of sludge and varnish. These products can induce poor lubrication, causing the severe surface failure of engine components. In order to mitigate the oxidation of engine oil, antioxidants are commonly used. There are mainly two types of antioxidants, depended on their reaction mechanisms; free radical inhibitors and hydroperoxide decomposers. The free radical inhibitors, primarily hindered phenols and secondary aromatic amines as shown in Figure 2-20, react with hydroperoxy radicals (ROO·) and alkyl radicals (R·), and, as a result of this, stop oxidative chain reactions [76]. Hydroperoxide decomposers stop oxidation reactions by decomposing peroxides to non-radical compounds, again preventing further chain reactions. ZDDPs and MoDTCs react as hydroperoxide decomposers as well as antiwear additives and FMs, respectively [77–79].

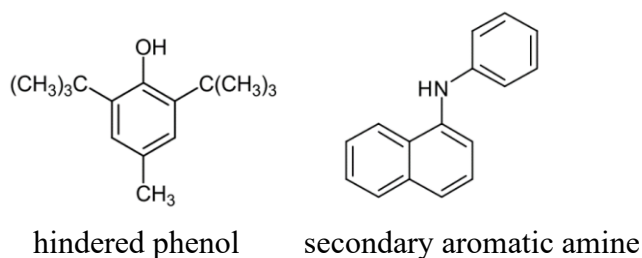


Figure 2-20 Representative antioxidants [76]

### 2.6.5 Detergents

Thermo-oxidative deteriorated products of fuel and lubricant such as carboxylic, nitric and sulphuric acid compounds cause polymerization of lubricants, resulting in the formation of sludge and deposits in engines. In order to prevent these, detergents that neutralize such acids are employed in engine oils. Detergents are composed of metal ions and oil-soluble parts, as shown in Figure 2-21 [80,81]. The oil-soluble parts are weak organic acids; salicylates, sulfonates and phenates with long chain hydrocarbons. Ca and Mg are usually used as counterion. Detergents used in engine oils are generally overbased. This means that they have a micellar form with a central solid core about 5 to 500 nm in diameter of a metal hydroxide/carbonate. This acts as a reservoir of base to neutralize acids. The structures of detergents affect their performance; acid neutralization, deposit prevention and antioxidation. Detergents also affect tribological performance in combination with antiwear additives and FMs [82–85].

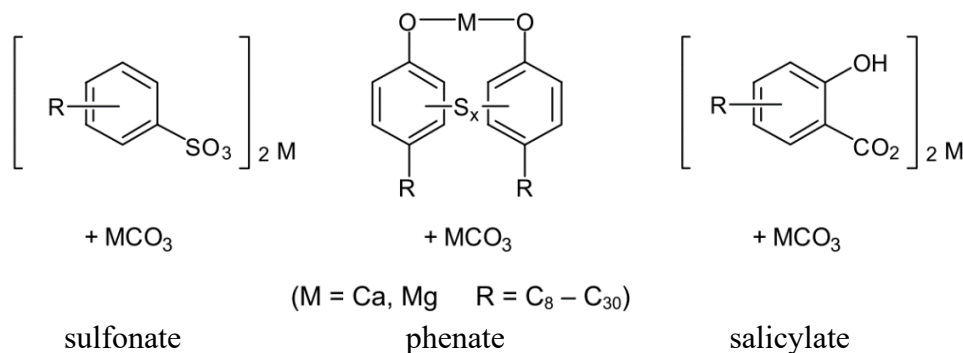


Figure 2-21 Representative detergents [80,81]

### 2.6.6 Dispersants

Sludge and soot generated through combustion accumulate in engine oils and can deposit on surfaces and in oilways, both harming lubrication and limiting oil circulation. Dispersants prevent these products agglomerating and depositing, so that they remain dispersed in engine oils, maintaining sufficient lubrication. They are composed of non-polar and polar groups as shown in Figure 2-22 [86,87]. However, while they are essential to disperse sludge and soot, dispersants may inhibit tribofilm formation of ZDDPs by competitive adsorption [88] and by lowering the adsorption capability of ZDDPs [89,90].

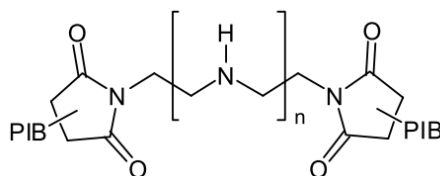


Figure 2-22 Representative dispersant; succinimide [86,87]

### 2.6.7 Viscosity Modifiers

Viscosity is one of the important properties of lubricants since it controls HL and EHL film thickness in contacts. Generally, the viscosity of viscous liquids such as lubricants falls rapidly as temperature decreases. The extent of viscosity change with temperature is defined by the viscosity index (VI); lower VI indicates a more rapid viscosity decrease with temperature. VMs are polymers and their effective molecular radii shrink at low temperature, and thus, when in solution, have relatively little effect on viscosity. However, at high temperatures VM molecular coils expand, and this effectively increases viscosity. Hence, this characteristic of VMs changes the VI of the lubricants in which they are dissolved.

Figure 2-23 shows three representative VMs; polymethacrylate (PMA), olefin copolymer (OCP) and styrene-diene copolymer (SCP) [91,92]. Since PMAs with polar groups improve VI most, PMAs are mainly used in lubricants that require high fuel efficiency. However, PMAs can absorb on surface to form boundary film, and thus negatively affect antiwear performance by inhibiting tribofilm formation [91–93]. By contrast, OCPs and SCPs do not include polar group, resulting in less VI increase than PMAs. These are mainly used to increase viscosity of lubricants which do not require high fuel efficiency.

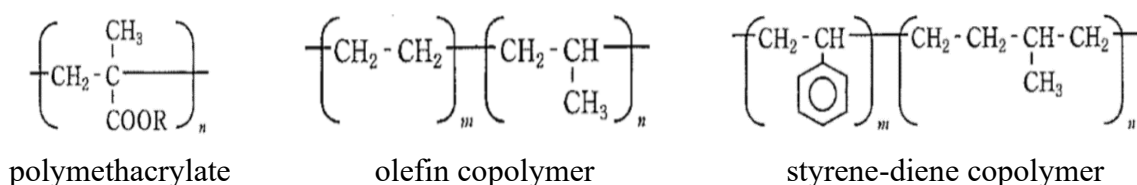


Figure 2-23 Representative viscosity modifier [91,92]

### 2.6.8 Pour Point Depressants

Mineral oils include paraffin wax which can crystalize and precipitate at low temperature, resulting in poor fluidity of lubricant. Engine oils with low fluidity at low temperature are not easily pumped and distributed round the engine, which can result in engine failure at start-up. Therefore, pour point depressants (PPD) are used in some mineral oil-based engine oils in order to prevent wax crystallization at low temperature [94]. PMAs shown in Figure 2-23 are also commonly used as PPDs.

### 2.6.9 Corrosion Inhibitors

Copper and lead in the journal bearings used in main and connecting rods in engines are susceptible to corrosion by acids and peroxides in engine oils. Corrosion inhibitors form films on metal surfaces by absorbing or reacting on them, resulting in protection of metal surfaces from acids and peroxides. Benzotriazole derivatives shown in Figure 2-24 are commonly used in engine oils [95].

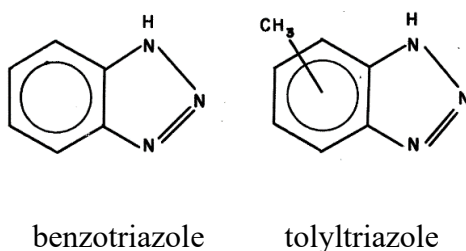


Figure 2-24 Representative corrosion inhibitor [95]

### 2.6.10 Rust Inhibitors

Rust formed in engines when water adheres to and reacts with ferrous surfaces. Rust inhibitors form close-packed adsorbed films on ferrous surfaces, protecting them from direct contact of water. Rust inhibitors are composed of lipophilic and hydrophilic groups [96,97]. Calcium sulfonates (Figure 2-21) and carboxylates are often used as rust inhibitors.



### 2.6.11 Foam Inhibitors

Foam consists of tiny bubbles of air separated by thin films of oil to form a quite stable two-phase structure. Foam in engine oils is generated by engine vibration and air/oil mixing. Since it is not easily pumped or otherwise circulated, it inhibits entrainment of oil into contacts, and thus causes starvation and consequent poor lubrication. Foam inhibitors with low surface tension break and destabilize foams by intruding into the separating thin oil films [98,99]. Polydimethylsiloxanes shown in Figure 2-25 are commonly used as foam inhibitors.

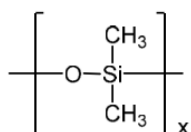


Figure 2-25 Representative form inhibitor; polydimethylsiloxane [98,99]

### 2.6.12 Base Oils

Engine oils are normally composed of 80 - 90% of base oil and 10 - 20% of additives. The composition and polarity of base oils vary, so base oil types affect oil performance. Base oils are classified in five groups based on properties as shown in Table 2-7 [100]; saturates, sulphur and VI. Base oils in Group I, II and III are mineral oils whereas base oils in Group IV and V are synthetic oils.

Table 2-7 API categories of base oils [100]

Category	Saturates, wt%	Sulphur, wt%	Viscosity Index
Group I	< 90%	0.03% <	80 - 120
Group II	90% ≤	≤ 0.03%	80 - 120
Group III	90% ≤	≤ 0.03%	120 ≤
Group IV	Polyalphaolefin		
Group V	Base oils unclassified in Group I – IV (such as ester)		

Mineral oils are refined from crude oils, which are mainly composed of three types of hydrocarbons; paraffins, naphthenes and aromatics as illustrated in Figure 2-26 [101]. Group 1 mineral oils also contain quite large proportions of sulfur-, nitrogen- and oxygen-containing molecules originating from the crude oils from which they are distilled and also retain much of the original aromatics from their crude oils. This means that they have

low VI. Mineral oils in Group II are more heavily refined and this removes much of the aromatics, sulfur and waxes. Group III oils are both heavily refined and also partially reformed into more desirable hydrocarbon structures. This makes Group II and Group III oils more suitable for use in engine oils than Group I. Thus, highly refined Group III base oils are commonly used for high tier engine oils. Exceptionally, gas to liquids (GTL) base oil synthesized from natural gas through the Fisher Tropsch reaction is used to make a Group III oil. This has higher VI and lower volatility than other Group III base oils, so GTL is becoming widely used in engine lubricants [102].

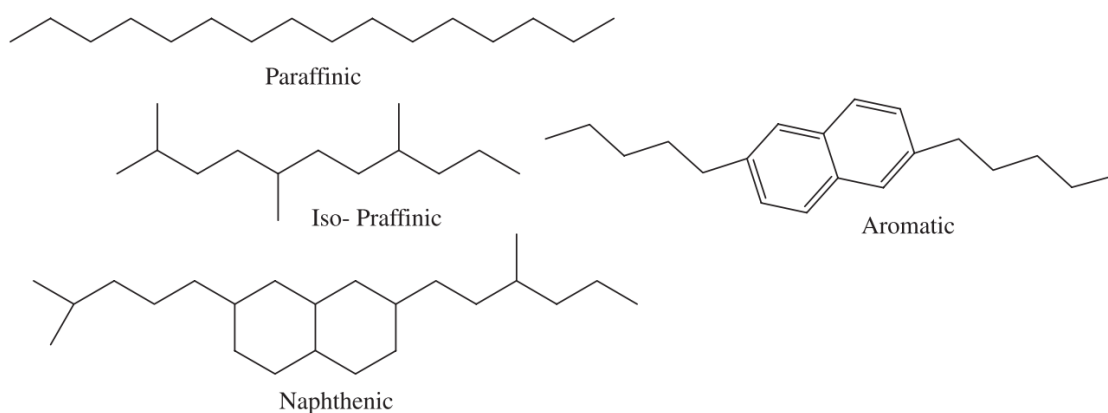


Figure 2-26 Representative mineral base oils [101]

Group IV and Group V are synthetic base oils. Polyalphaolefin (PAO) in Group IV is synthesized by the polymerization of linear alphaolefins (C6 to C18) and has an iso-paraffin structure (Figure 2-27) without any impurities such as sulfur and nitrogen [101]. PAO has excellent properties; high VI, low volatility, low pour point and high oxidation stability, and thus it is usually used for making high tier lubricants.

Representative base oils in Group V are esters (Figure 2-28) synthesized from organic acids with alcohols [101]. Esters have high polarity, and thus, as well as being used alone as base oils, they are often used blended with other base oils, especially Group III and IV in order to control solubility and reactivity of additives [103].

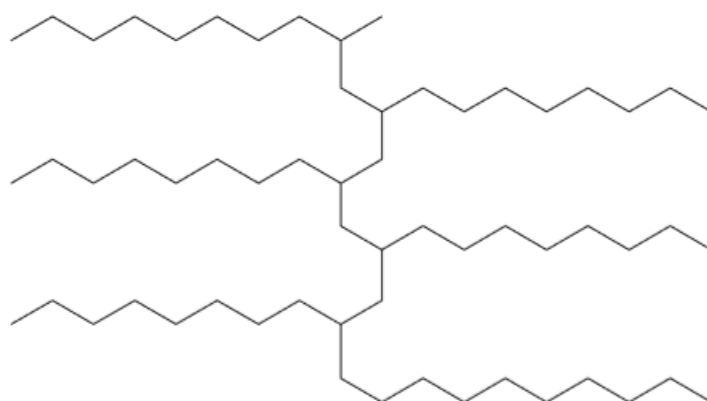
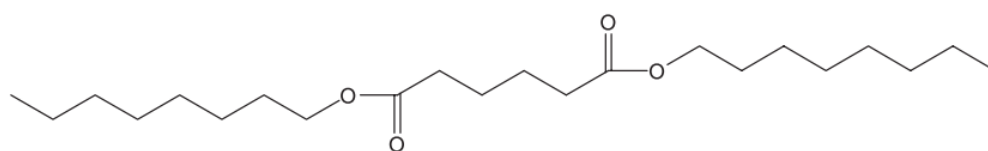
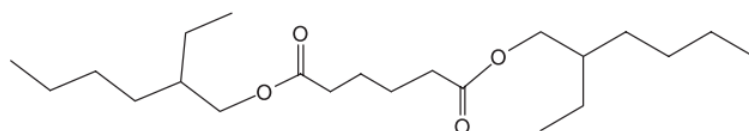


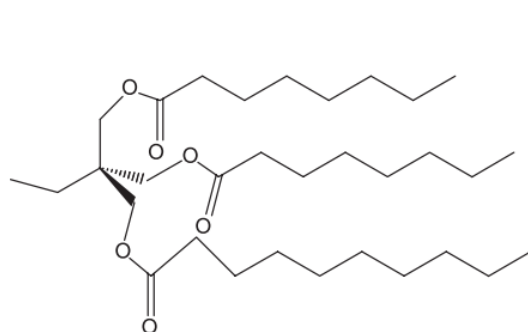
Figure 2-27 Representative poly alphaolefin [101]



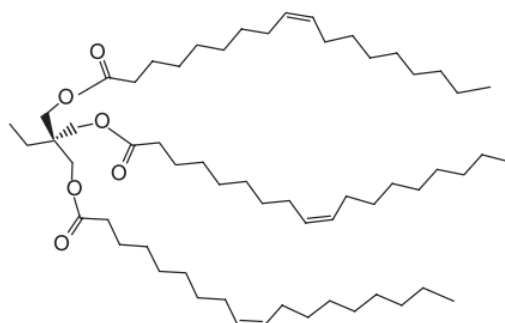
(A) bis (n-octyl) adipate



(B) bis (2-ethyl hexyl) adipate



(C) TMP C8-C10



(D) TMP Oleate

Figure 2-28 Representative esters [101]

## **2.7 Summary**

In this chapter, the trends of automobiles and engine oil development are introduced. The main current trend of engine oils is to use lower viscosity lubricants with the aim of reducing friction, and thereby improving fuel efficiency of mechanical systems. This means that machine components are required to operate for longer periods in thin oil film, mixed and boundary lubrication conditions, where the risk of surface damage is increased. This trend is observed not only in engine oils but also lubricants for other machines. This means, in turn, that technologies to protect components from surface damage in such thin oil film conditions is becoming increasingly important. For this reason, the role of tribofilms generated from zinc dialkyldithiophosphate (ZDDP) antiwear lubricant additive in providing adequate surface protection has become of growing importance. Previous studies of ZDDP tribochemical investigation are reviewed in Chapter 3.

### **3 General Introduction and Literature Review of ZDDP**

*ZDDPs have been one of the most important lubricant additives for over 70 years. Although a great deal of research has been reported, much of it with the aim of partially or wholly replacing ZDDPs by alternative, ashless antiwear additives, ZDDPs are still commonly used in engine lubricants. As described Chapter 2, the role of ZDDP tribofilms to provide adequate surface protection in thin film conditions has become increasingly important. Although extensive research on the chemical and mechanical properties, reaction mechanism of tribofilm formation, and the performance of ZDDP tribofilms have been reported, there are still several unresolved questions. This chapter discusses previous research of ZDDP tribochemical behaviour. Challenges and research questions to be addressed by new research described later in this thesis are highlighted.*

#### **3.1 Properties of ZDDP Tribofilm**

This section describes the chemical and physical characterization of ZDDP tribofilms.

##### **3.1.1 Chemical Characterization**

ZDDP tribofilms have been investigated in past research using many techniques of surface analysis. These include Infrared Spectroscopy (IR), Raman spectroscopy (Raman), X-ray Photoelectron Spectroscopy (XPS), X-ray Adsorption Near Edge Spectroscopy (XANES), Scanning Transmission Electron Microscopy Energy Dispersive X-ray Spectroscopy (STEM-EDX) and, very recently, Atom Probe Tomography (APT). Many studies have analysed the chemical properties of ZDDP tribofilms and correlated their properties to their performance.

IR and Raman spectra originate from within approximately 1  $\mu\text{m}$  from the surface and they can detect phosphorus-oxygen (P-O) bonds of tribofilms as shown in Figure 3-1 [104–109]. Piras et al. [108,109] showed the correlation between the intensity of phosphorus-oxygen (P-O) peak and friction by using a tribometer equipped with IR. In addition, Harrison et al. [105] studied the thermal stability of ZDDPs with different alkyl groups using IR and, by monitoring the development of P-O peak intensity at different

temperatures, found that ZDDP was thermally stable in the following order; n-nonyl > n-decyl > n-butyl > iso-butyl.

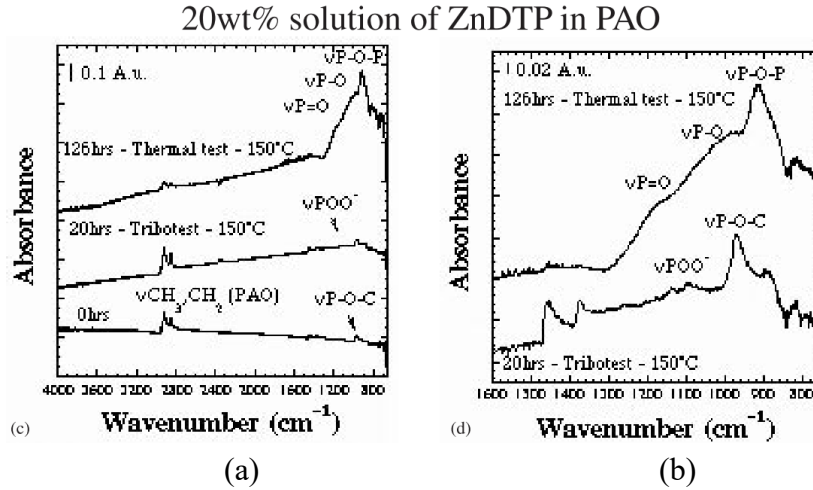


Figure 3-1 (a) IR peaks of ZDDP tribofilms and thermal films and (b) enlarged area in between 800 -1600 cm<sup>-1</sup> [108]

Raman spectra enables identifying polyphosphate types of tribofilms by detecting both P-O bond absorption (700 cm<sup>-1</sup>) and P-O-P bond absorption (970 cm<sup>-1</sup>) [110–112]. Berkani et al. [111] found that zinc orthophosphate (short chain length) was mainly formed after a friction test as shown in Figure 3-2.

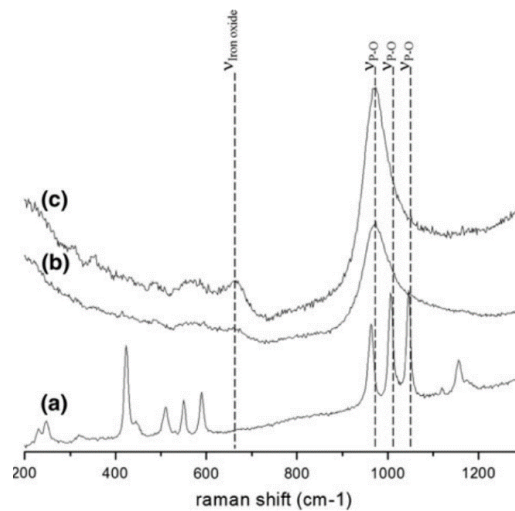


Figure 3-2 Raman spectra of (a) pure crystalline orthophosphate (a-Zn<sub>3</sub>(PO<sub>4</sub>)<sub>2</sub>), tribofilms formed after a sliding test of a steel/steel contact (b) at room temperature and (c) at 120 °C [111]

XPS gives more detailed chemical structures of ZDDP tribofilms than IR and Raman spectra [108,109,113–129], and has been able to identify Fe/Zn orthophosphate, Zn-phosphate, Zn-sulfide and Zn-oxide-containing layers [109,113,127]. It is important to note that XPS analyses only the tribofilm less than 10 nm from its surface. In particular, XPS O1s helps to understand the chemical structure of phosphates. Crobu et al. [120,121] analysed the integrated intensity ratio of bridging oxygen (P-O-P) and non-bridging oxygen (P=O and P-O-M) from XPS O1s spectra, and found that the chain length of phosphates could be estimated from the bridging oxygen/non-bridging oxygen (BO/NBO) intensity ratio. Heuberger et al. [127] showed that the BO/NBO ratio was strongly dependent on temperature as shown in Figure 3-3. Recently, Parsaeian et al. [119] also showed that BO/NBO ratio decreases with rubbing, indicating that ZDDP tribofilm depolymerizes from long chain phosphates to short chain phosphates. By using ion sputtering method, the variation with depth of the chemical composition of tribofilms can be detected [114–116,124]. Mourhatch et al. [116] showed the depth profile of Fe, C, S, O, Zn and P in ZDDP tribofilms and detected Fe in tribofilms near the steel substrate. In principle depth analysis can be carried out by progressively removing the tribofilm. However, it should be noted that ion sputtering, which usually uses Ar ions, may change the state of chemical bonding and composition of tribofilms [117,118]

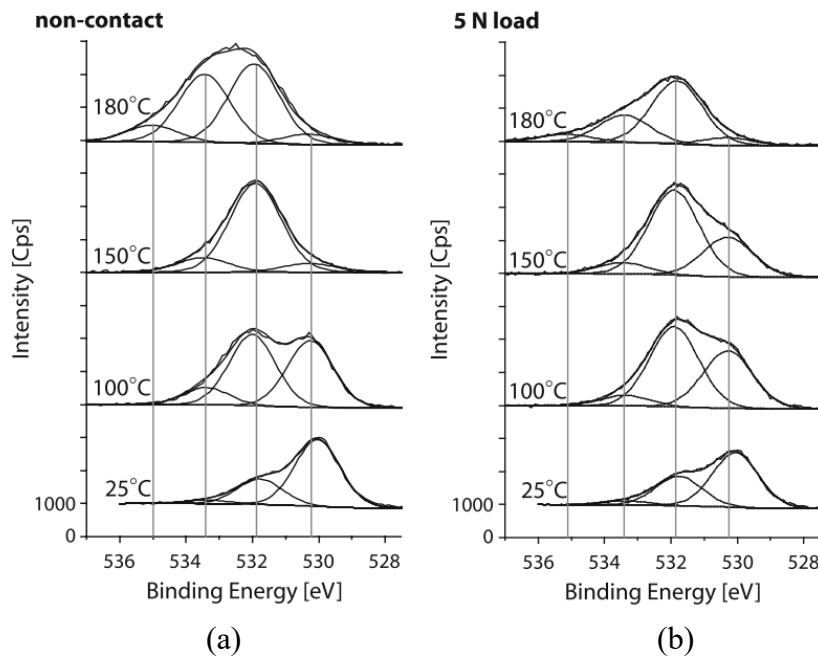


Figure 3-3 O 1s XPS spectra on (a) non-contact areas and (b) regions with 5 N tribostress at different temperatures, (NBO at 531.8 and BO at 533.4 eV) [127]

XANES analyses the upper 50 nm layer of ZDDP tribofilms in a non-destructive way with high sensitivity and obtains elemental and chemical bonding distribution [125,130–141]. While partially decomposed and unchanged ZDDPs were detected at the tribofilm surface using P and S L-edge XANES analysis, long and short chain phosphates were identified in the bulk of tribofilm. As well as XPS analysis, Fe phosphates were detected in tribofilms, resulting from the Fe ion transfer from steel substrates as shown in Figure 3-4 [116,134,138,142].

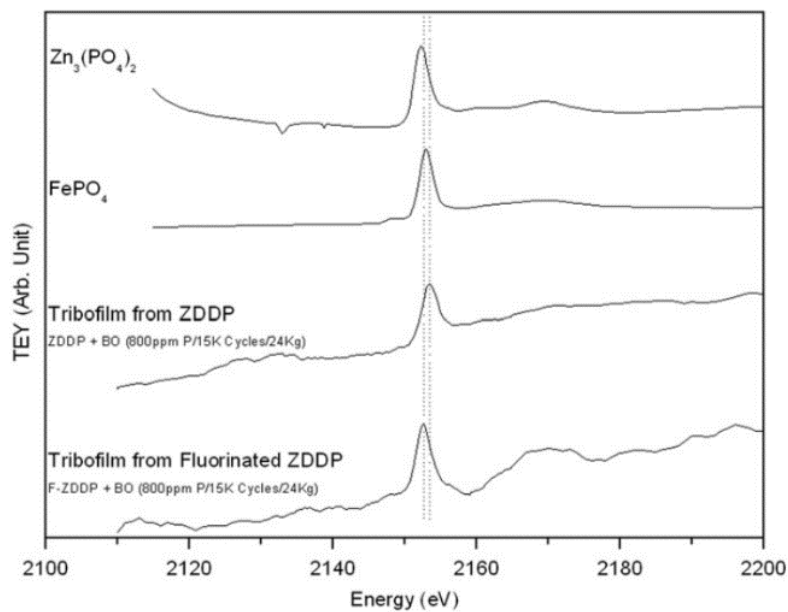


Figure 3-4 Phosphorus K-edge XANES spectra collected in TEY mode for ZDDP tribofilms and reference samples [119]

STEM-EDX allows one to obtain the precise depth profile of element distribution of ZDDP tribofilms without possible damage due to sputtering, unlike XPS [115,143,144]. Cross-sections of tribofilm need to be prepared using Focused Ion Beam milling (FIB). Ito et al. [143] found that the tribofilm on a mixed  $\text{Fe}_3\text{O}_4$  and  $\text{FeO}$  substrate consisted of a multilayer (Figure 3-5). While the 30 nm layer next to the substrate contained Zn, Fe, S, P, and O, a middle layer and an upper layer mainly consisted of carbon. Philippon et al. [144] showed that a high intensity of Fe was present near the steel substrate but not in the upper side of tribofilm as shown in Figure 3-6.



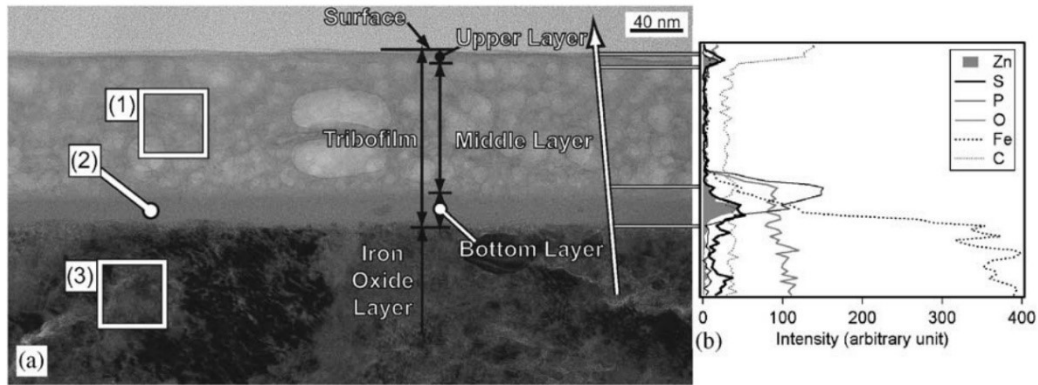


Figure 3-5 Element distribution in cross-sectional of ZDDP tribofilm on a mixed  $\text{Fe}_3\text{O}_4$  and  $\text{FeO}$  substrate using STEM-EDX [143]

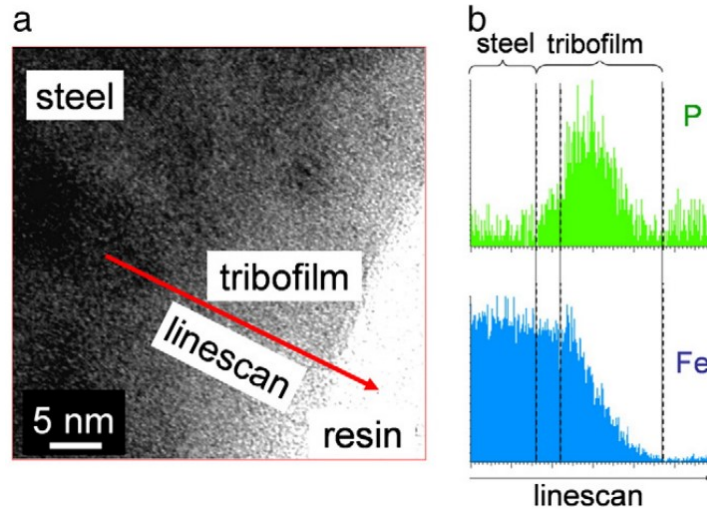


Figure 3-6 P and Fe distribution in cross-sectional of ZDDP tribofilm using STEM-EDX [144]

Recently, ZDDP tribofilms were analysed by using APT, which provides three-dimensional chemical composition at the spatial resolution limit of approximately 0.1 nm. This technique is able to give more precise element distribution in tribofilms than that provided by 2D depth profiles of XPS and STEM-EDX. Hsu et al. [145] obtained 3D chemical maps of ZDDP tribofilms with the steel substrate on the bottom and a Cr coating on the top, as shown in Figure 3-7, and found a layer with high concentration of sulfur between the main tribofilm and the steel substrate.

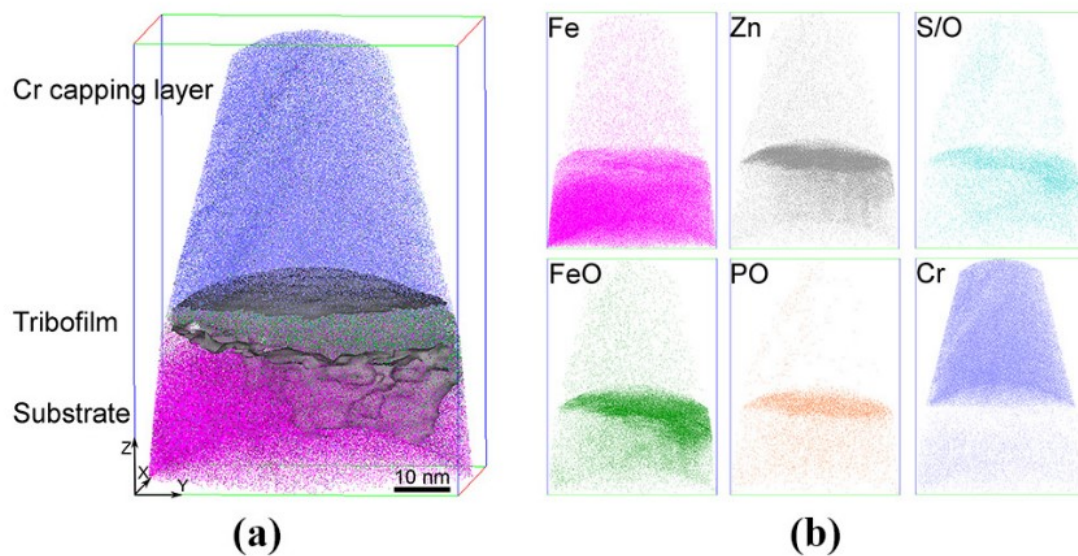


Figure 3-7 (a) 3 D APT of needle shape specimen showing the Cr capping layer, ZDDP tribofilm and steel substrate and (b) spatial distribution of Fe, Zn, S/O, FeO, PO and Cr atoms [145]

From the combination of these surface analysis methods, the chemical structure of ZDDP tribofilms has been proposed as shown in Figure 3-8 [116,123,126,146]. Overall, Zn/Fe sulphides and oxides are present near ferrous substrates. On top of these, short chain Zn/Fe phosphates are mainly found. Less Fe phosphates and more long chain Zn phosphates are present at the upper region of tribofilms than close to the substrate. At the outmost tribofilm surface is a coating of unreacted and decomposed ZDDP. Note that the chemical structures shown in this section are on ferrous substrates. In contrast to ferrous substrates, chemical analysis of ZDDP tribofilms on non-ferrous substrates is very limited.

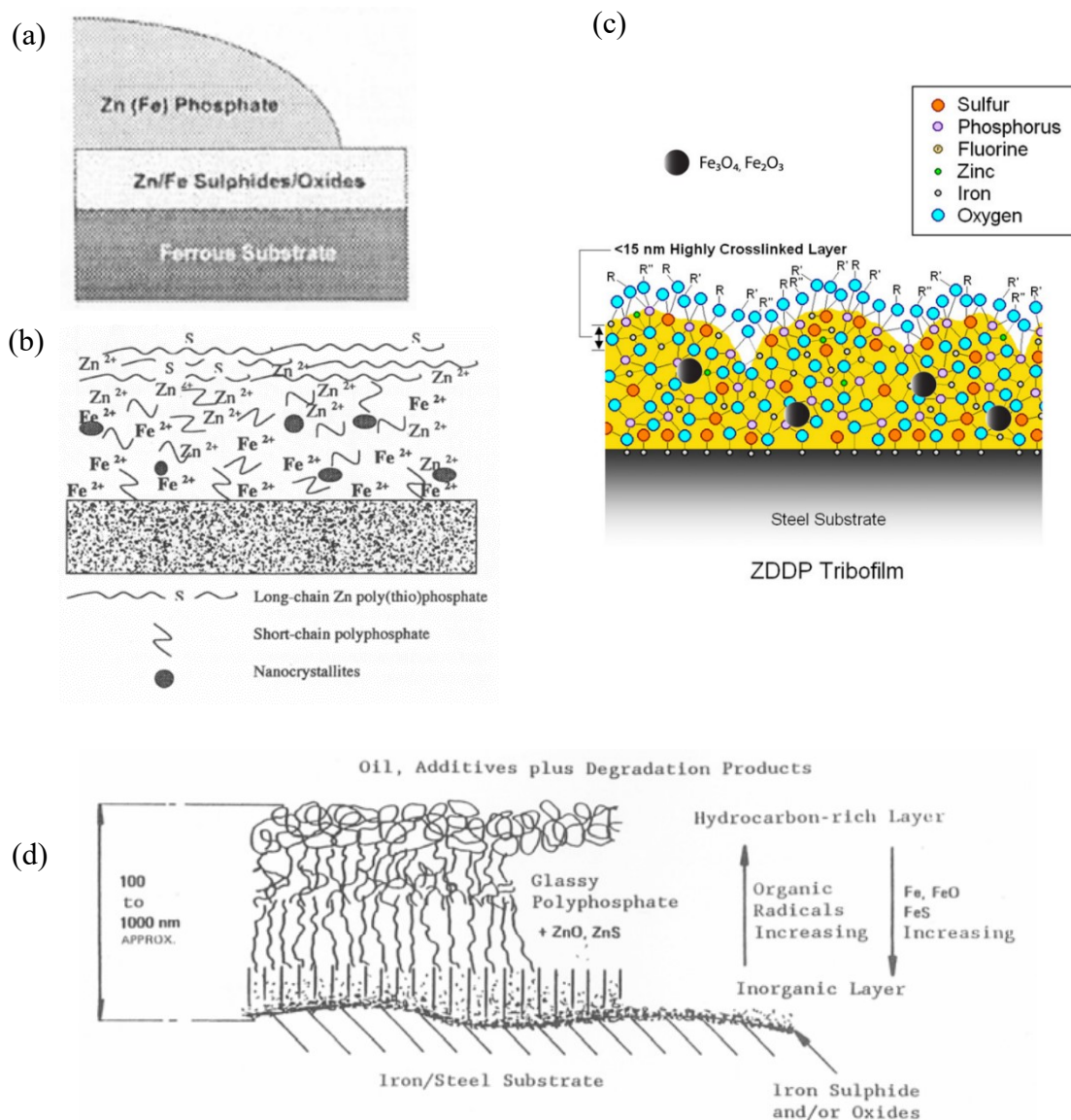


Figure 3-8 Proposed ZDDP tribofilm structures (a) [123] , (b) [146], (c) [116] and (d) [127]

### 3.1.2 Physical Characterization

The physical properties of ZDDP tribofilms have been quite thoroughly investigated, including their thickness, surface morphology, surface roughness, hardness and elasticity. These mechanical properties have been measured by several surface methods; Atomic Force Microscopy (AFM), Scanning White Light Interferometry (SWLI), Transmission Electron Microscopy (TEM), Electrical Contact Resistance (ECR), Spacer Layer Interferometry (SLIM) and Nanoindentation.

AFM measures tribofilm by scanning the tribofilm surfaces using a tiny tip at the end of a cantilever, and this provides the surface morphology and roughness with sub-micron resolution [104,147–158]. Aktary et al. [150] showed the evolution of a pad-like structure of ZDDP tribofilm with sliding time using AFM, as shown in Figure 3-9, and found that tribofilms initially form as separate patches, and that these patches then gradually develop an almost continuous structure which is separated by deep valleys. Nicolls et al. [148] investigated the difference of chemical structures in pad areas and valley areas by combining AFM and XANES, and found that, while long polyphosphates mainly formed on pad-like areas, short chain phosphates were mainly detected on valley areas. The AFM scanning size is relatively small ( $150 \times 150 \mu\text{m}^2$ ) and thus often smaller than the wear track width. In this case, in order to obtain reference planes on each side, tribofilm can be removed by using ethylenediaminetetraacetic acid (EDTA) [147,149].

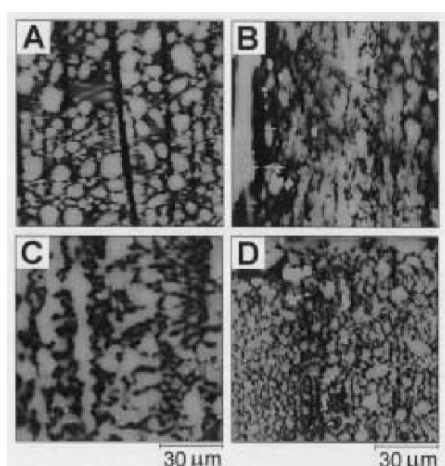


Figure 3-9 The evolution of pad-like structures of ZDDP tribofilms using AFM with rubbing time (A) 10 min, (B) 40 min, (C) 60min and (D) 120 min. [150]

SWLI allows one to measure tribofilm thickness formed on a large wear track width without EDTA treatment. However, internal reflections within the transparent tribofilms result in misleading measurements, and it is necessary to coat thin gold layers on tribofilms to make them reflective, allowing precise measurements of tribofilm thickness over large areas [149,159].

TEM measures the tribofilm thickness by observing the cross-sectional image of ZDDP tribofilms prepared using FIB [143,160–162]. Although TEM observation can precisely measure tribofilm thickness as shown in Figure 3-10, it only observes a very small area

of tribofilm (less than 1  $\mu\text{m}$ ) because of the small lamella size prepared by FIB [162]. This means that a given cross section may not be representative of the whole film. TEM also allows measurement of the crystallinity of tribofilms, and Dawczyk et al. [161] showed a crystalline structure of ZDDP tribofilms through the fast Fourier transform (FFT) spots and lattice fringes of TEM images.

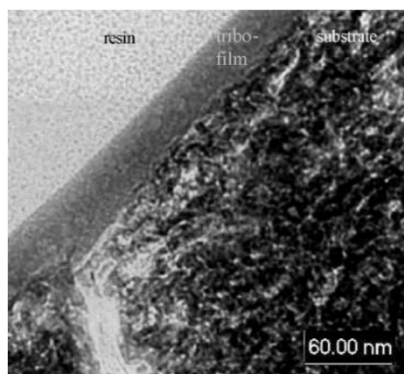


Figure 3-10 TEM observation of a FIB cross section preparation of the ZDDP tribofilm [152]

While the methods described above provide ex-situ measurements, ECR and SLIM can measure ZDDP tribofilm thickness in-situ. ECR has been widely used to study the rate of ZDDP tribofilm growth by measuring electrical resistance across contacts [129,163–166]. Georges et al. [129] showed three stages of ZDDP tribofilm growth by monitoring ECR change during a pin on disc rubbing test; 1) ECR remained low, which suggested that ZDDP tribofilm started to grow, 2) a rapid increase in ECR and then 3) high and stable ECR with thick ZDDP tribofilms. However, a direct relationship between contact resistance and tribofilm thickness has not been provided. This would require knowledge of the resistivity of the tribofilms which is likely to be very compositionally sensitive. By contrast, SLIM, which is generally designed to work with the Mini Traction Machine (MTM), can directly measure ZDDP tribofilm thickness on an MTM ball based on the principle of optical interferometry [147,153,167–170]. However, it is difficult to obtain accurate tribofilm thickness values when balls of a different reflectivity are used.

As mentioned above, there are several ways to measure tribofilm thickness. Dawczyk [171] compared the ZDDP tribofilm thickness measured by SLIM, AFM and SWLI as shown in Figure 3-11. Note that each technique provides a different thickness because of

its different principle. As shown above, each technique has advantages and disadvantages, thus they need to be properly used depending on the purpose.

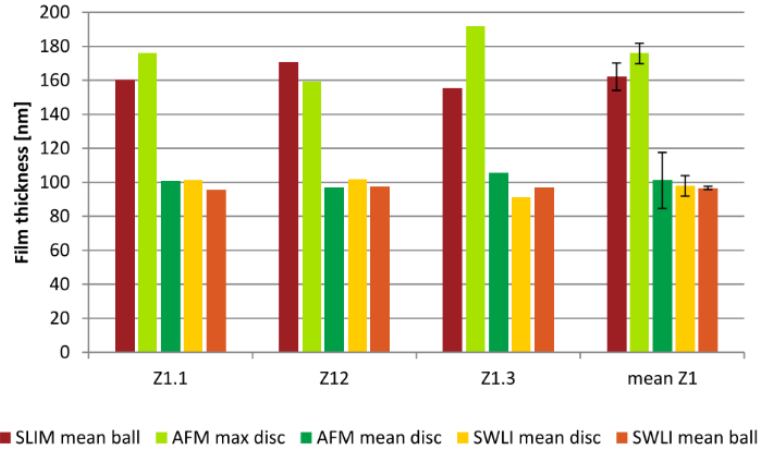


Figure 3-11 ZDDP tribofilm thickness measured by various techniques [171]

The elastic modulus and hardness of ZDDP tribofilms can be measured using nanoindentation [148,158,172–178]. These mechanical properties vary between pad areas and valley areas of tribofilms. Nicholls et al. [148] showed that a large pad area with 200 nm thickness, mainly composed of long chain phosphates, had 67.4 GPa elastic modulus; (the elastic modulus of the steel was 220 GPa). By contrast, a valley area with only 100 nm thickness, mainly composed of short chain phosphates, gave almost similar elastic modulus to the steel substrate. However, the mechanical properties of tribofilm vary with depth, so they cannot be properly measured at the point of the initial unload [174]. By comparison with a conventional one-point measurement with loading/unloading, nanoindentation in the Continuous Stiffness Measurement (CSM) mode, which allows for a measurement of the contact stiffness at any point along the loading curve, can measure mechanical properties of tribofilms more precisely. Kalin et al. [178] showed the evolution of tribofilm hardness with rubbing time as shown in Figure 3-12, and found that tribofilms became hard with rubbing time.

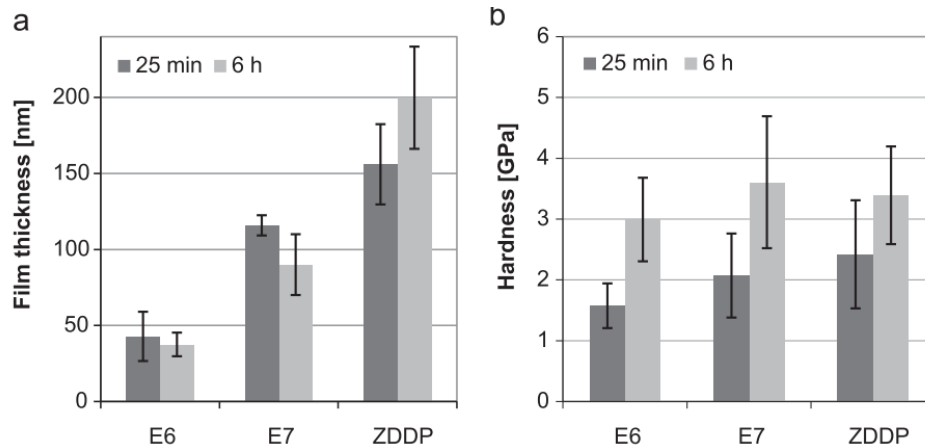


Figure 3-12 The evolution of hardness of ZDDP tribofilm measured in CSM [178]

The progressive improvements of surface analysis techniques have allowed quite detailed understanding of the chemical and mechanical properties of ZDDP tribofilms. Based on surface analyses in previous studies, Spikes [67] proposed a schematic diagram of ZDDP tribofilm structure on a ferrous surface (Figure 3-13). It is noteworthy that the scale normal to the surface is about 100 times larger than the horizontal scale.

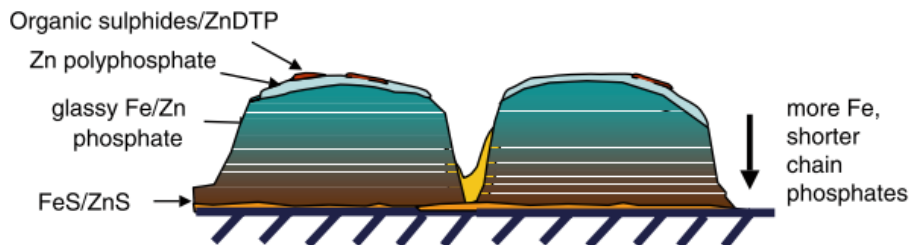


Figure 3-13 The Schematic diagram of ZDDP film structures [67]

### 3.1.3 ZDDP Tribofilm Durability

Low-viscosity oils can cause engine components to operate for long periods in thin film, mixed lubrication conditions, where wear of rubbing surfaces may occur. Although the ability of ZDDP tribofilms to survive over long rubbing times, a property usually called tribofilm durability, is an important characteristic, the factors that affect tribofilm durability have not been studied in any detail.

One way to assess the durability of a ZDDP tribofilm is to monitor changes in ZDDP tribofilm thickness after the replacement of a ZDDP-containing oil by a ZDDP-free oil



[88,119,169]. Fujita et al. [169] measured the growth of a ZDDP tribofilm in rolling-sliding contact using optical interferometry and then the effect on this pre-formed tribofilm of replacing the ZDDP solution by base oil. They found that the thickness of the ZDDP tribofilm remained almost unchanged when rubbed in base oil, indicating that it was very durable in rolling-sliding conditions. If, however, the ZDDP solution was replaced by a solution of a succinimide dispersant, about half to two-thirds of the pre-formed tribofilm thickness was rapidly removed [88,169]. They suggested that some of the tribofilm was susceptible to extraction of stabilizing Zn cations by the aminic dispersant. It thus appeared that, in the absence of specific chemical effects, ZDDP tribofilms were extremely durable.

This picture has, however, recently become more complicated since Parsaeian et al. [119] have shown that the durability of a ZDDP tribofilm appears to depend on how long it has been rubbed, as shown in Figure 3-14. Like Fujita et al. [169], they found that if ZDDP solution was replaced by base oil after prolonged rubbing, the tribofilm was not significantly removed during further rubbing and was thus durable. If, however, the ZDDP solution was replaced by base oil in the early stages of a test, and rubbing continued, some of the tribofilm was removed.

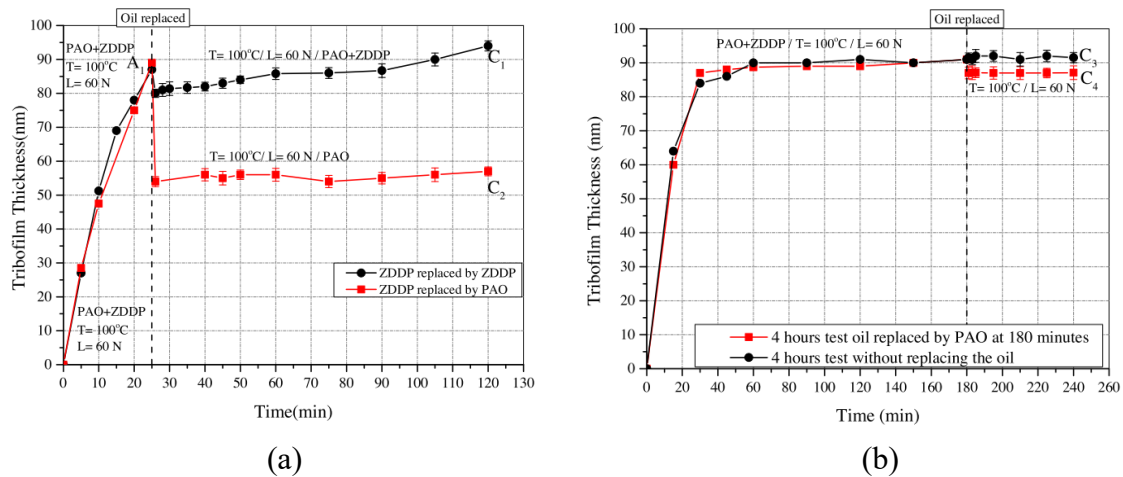


Figure 3-14 The effect of PAO rubbing on tribofilm removal after (a) 25 and (b) 180 minutes rubbing [119]

### 3.1.4 ZDDP Tribofilm Structure

Most previous research has found or assumed that ZDDP tribofilms consist primarily of amorphous and glassy zinc phosphates, based on the concept that zinc phosphates are well known to form glasses [179]. However, using high-resolution FIB-TEM it has



recently been shown that ZDDP tribofilms may have both nanocrystalline and amorphous structures as shown in Figure 3-15 [161]. Thus, the reduction in tribofilm phosphate chain length may be accompanied by the formation of a crystalline structure. Based on the above, new research described in Chapter 5 has been carried out in this project to understand the evolution of ZDDP tribofilm crystallinity during its formation and the effect of this on its durability.

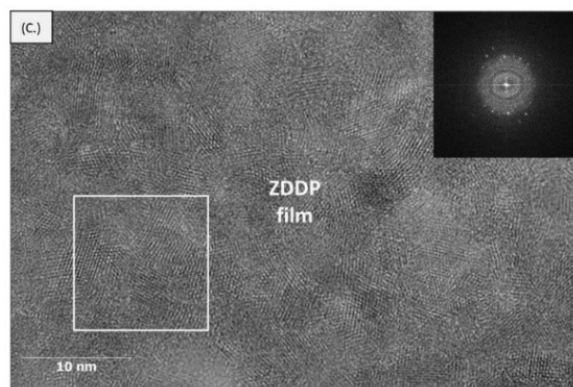


Figure 3-15 The crystalline phase of ZDDP tribofilm [161]

### 3.1.5 Properties of ZDDP Thermal Film

While a film formed through a chemical reaction caused by sliding is termed *tribofilm*, a film which is thermally formed by simply immersing metal in heated ZDDP solution is termed *thermal film*. Like tribofilm, the composition of thermal films is based on Zn phosphates. While tribofilms consist in part of Fe phosphates, thermal films are less likely to contain Fe cations transferred from steel substrates [108,134]. Also, while tribofilms are formed even at low temperature, for example 50 °C [169], thermal films are formed only when bulk temperature exceeds the temperature of ZDDP decomposition; *ca.* 120 °C. This decomposition temperature is strongly dependent on the alkyl groups of ZDDPs. The rate of thermal film growth increases with temperature as shown in Figure 3-16 [167]. Unlike tribofilms, thermal films appear to form mound-like separate islands, at least at high temperatures, with a smoother structure [180].

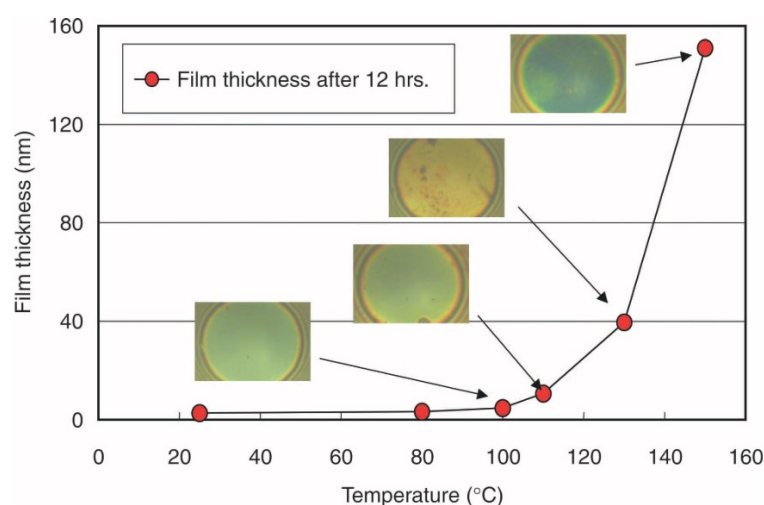


Figure 3-16 The effect of oil temperature on ZDDP thermal film developments after immersion for 12 h in a solution of 1.2 wt% ZDDP in group 2 base oil [167]

### 3.2 Reaction Mechanism of Tribofilm Formation

Although the detailed molecular reaction mechanisms of ZDDP tribofilm formation is not yet fully understood, a great deal of research has suggested general reaction schemes. In this section, the various proposed ZDDP reaction processes are reviewed; thermal decomposition, hydrolytic decomposition, thermo-oxidative decomposition and tribofilm formation.

#### 3.2.1 Thermal Decomposition

A proposed thermal decomposition process of ZDDPs is shown in Figure 3-17[181]. An initial reaction is the exchange of the alkyl groups from O to S in ZDDP molecules [182,183]. This reaction is well known for organic thiophosphates and has been confirmed by  $^1\text{H}$ - and  $^{31}\text{P}$ - nuclear magnetic resonance (NMR) [184]. Subsequently, the alkyl chains are removed as thiols and olefins followed by the formation of zinc polyphosphates. The rate of removal of alkyl chains is affected by the thermal stability of ZDDPs and varies with alkyl groups. Thermal stability of ZDDPs decreases with increase of the number of  $\beta$ -hydrogen atoms of alkyl chains, *i.e.* thermal stability decreased in the following order; secondary alkyl > primary alkyl > aryl [185]. Tertiary ZDDPs are reported to be unstable at room temperature [184,186].

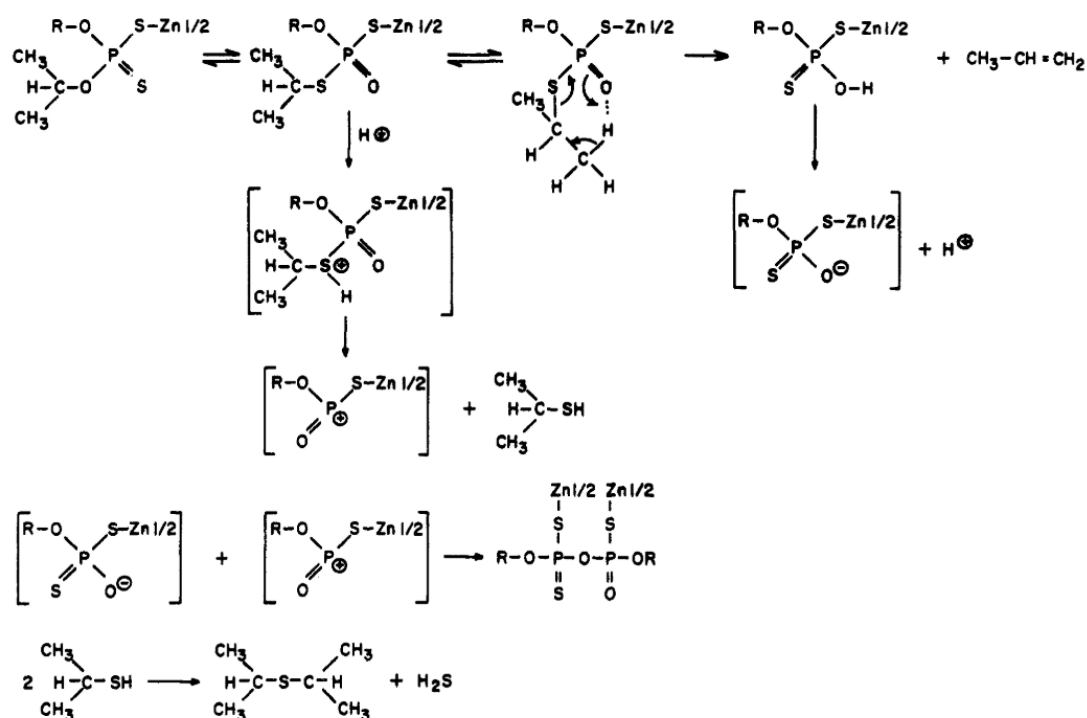


Figure 3-17 Mechanism of the thermal decomposition of ZDDPs [181]

### 3.2.2 Hydrolytic Decomposition

Water accelerates the rate of ZDDP decomposition [187]. Figure 3-18 shows a suggested mechanism of hydrolytic decomposition of ZDDPs [188]. Water reacts with ZDDPs to replace alkyl chains from molecules, forming phosphoric acid moieties. These moieties then react with each other, resulting in the formation of zinc polyphosphates. Aside from this reaction, hydrogen sulphide acid or sulphuric acid, which damage metal surfaces, may form from the reaction between ZDDPs and water [189].

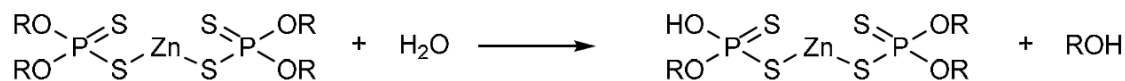


Figure 3-18 Hydrolytic reaction of ZDDPs [188]

### 3.2.3 Thermo-oxidative Decomposition

As described in Section 2.7.4, ZDDPs are thermo-oxidatively decomposed by the reaction with hydroperoxides and peroxide-radicals as shown in Figure 3-19 [106]. When ZDDPs

react with these peroxides and radicals, they form products which act as effective oxidation inhibitors, but not effective zinc phosphate antiwear films [190,191].

ZDTP: zinc dialkyldithiophosphate;  $[(RO)_2P(S)S]_2Zn$   
 HDTP: dithiolic acid;  $(RO)_2P(S)SH$   
 BZDTP: basic ZDTP;  $[(RO)_2P(S)S]_6Zn_4O$   
 DS:  $(RO)_2P(S)S-SP(S)(RO)_2$ ; DS•:  $(RO)_2P(S)S\bullet$

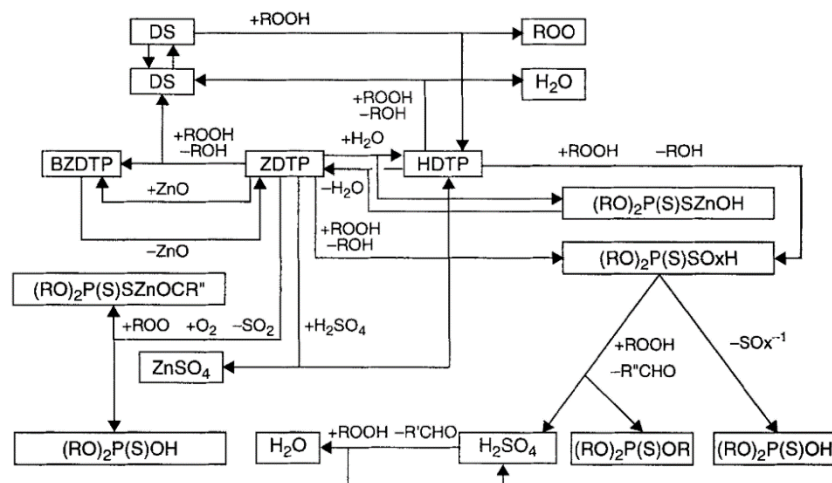


Figure 3-19 Schematic diagram of antioxidant reaction of ZDDPs [106]

### 3.2.4 ZDDP Tribofilm Formation

Considering the possible chemical reactions of ZDDPs reviewed above, tribofilm formation is believed to follow broadly the scheme indicated in Figure 3-20 [127]. Each step is described separately below.

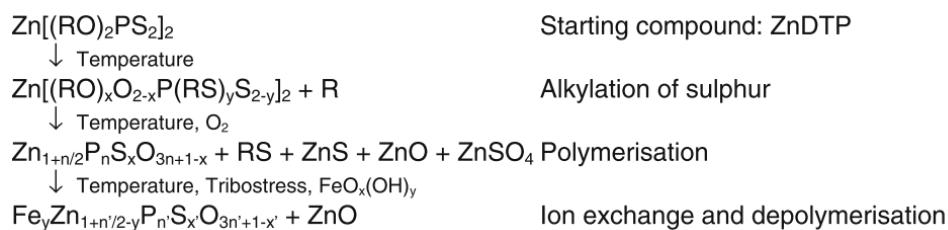


Figure 3-20 Suggested reaction sequence of tribofilm formation [127]

#### 3.2.4.1 Surface Adsorption

The first stage of ZDDP tribofilm formation must be diffusion to and adsorption of ZDDP molecules or moieties on metal surfaces. Yamaguchi et al. [192] showed that ZDDP

molecules adsorb on  $\text{Al}_2\text{O}_3$  via the sulphur atom of the  $\text{P}=\text{S}$  bond at room temperature, while Bovington and Dacre [193] found that after initial physical adsorption, when the temperature was raised above *ca.* 60 °C, a large amount of Zn was lost, and then adsorption became irreversible [194]. This resulted in the formation of Fe dithiophosphates and free dithiophosphoric acids.

Since adsorption includes the formation of bonds between ZDDPs and solid surfaces, surface composition is likely to affect the ability of ZDDP to form tribofilms. Previous studies described above have used ferrous substrates, and the effect of surface composition including non-metallic substrates on ZDDP adsorption has not been studied. This will be further discussed in Chapter 7 of this thesis.

#### 3.2.4.2 Formation of $\text{FeS}/\text{FeS}_2$

Dithiophosphoric acids are strong acids, and thus are likely to react with iron oxides rapidly to form iron salt [195]. Subsequently, the reaction of nucleophilic displacement of sulphur occurs, resulting in the formation of  $\text{FeS}$  and/or  $\text{FeS}_2$  [193,196]. The formation of  $\text{FeS}/\text{FeS}_2$  films have been confirmed at the initial stage of rubbing [197,198]. Another mechanism of forming them has been proposed through a ligand exchange reaction [199] with dithiophosphates exchanging from Zn cation to Fe cation. Subsequently, Fe dithiophosphates, which are less stable than ZDDPs, are decomposed by heat and stress, resulting in the formation of  $\text{FeS}$  and  $\text{FeS}_2$ .

Dithiophosphates  $(\text{RO})_2\text{PSS}^-$  are strong alkylating agents, and thus a self-alkylation can occur even at room temperature in the presence of some Lewis acids [200]. Although it is still not confirmed with respect to tribofilm formation, this may involve the initial transfer of alkyl groups from O to S, to convert the dialkylthiophosphate to dithionylphosphate  $(\text{RS})_2\text{POO}^-$  as shown in Figure 3-21 [67,201]. In addition to the formation of dithionylphosphate, intermolecular alkylation provides a wide range of thiophosphates such as  $(\text{RO})_2(\text{RS})\text{PS}$  and  $(\text{RS})_3\text{PS}$  [183].

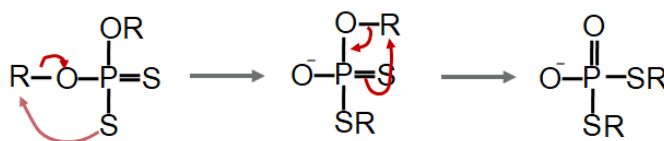


Figure 3-21 Conversion of dialkylthiophosphates to dothionylphosphates [67,201]

### 3.2.4.3 Polymerisation

Phosphates are a strong nucleophiles, while thionyls, and to a lesser extent alkoxy groups, are easy leaving groups, so an intermolecular reaction between thionylphosphate species should lead to rapid polymerization to form polyphosphate chains as shown in Figure 3-22 [67,183]. These first two processes are accelerated by both temperature and stress and lead to a formation of polyphosphate tribofilms.

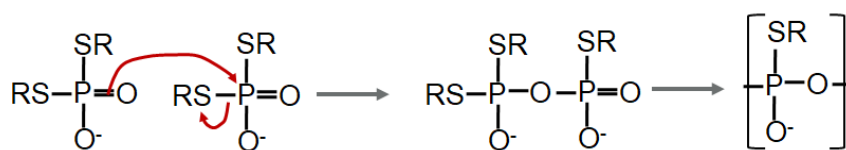


Figure 3-22 Polymerisation to polyphosphates [67,183]

### 3.2.4.4 Ion Exchange and Depolymerisation

The final stage is subsequent depolymerization of this long chain polyphosphates to short chain phosphates by losing thionyl or alkoxy groups as shown in Figure 3-23 [67]. This reaction increases ionic charge in phosphates which must be balanced by cations. Aside from Zn cation, one of the possible way to balance charge is the transfer of Fe cation into tribofilms from a steel substrate, resulting in the formation of iron phosphates [116,127,134,138,142,144].

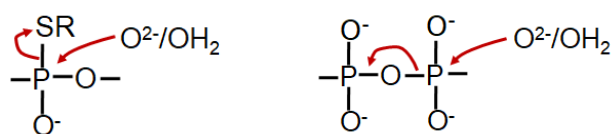


Figure 3-23 Depolymerisation to Zn/Fe phosphates [67]

The processes of polymerisation and depolymerisation form phosphates which have varied chain length ranging from rings (metaphosphates) to long chains (polyphosphates), to very short chain ones (pyrophosphates) and ultimately orthophosphates, as shown in Figure 3-24 [67]. Although these changes of phosphate structures have been investigated, the change of tribofilm properties from depolymerization is still unclear. The effect of the reactions of ion exchange and depolymerization on tribofilm properties are discussed in Chapter 5.

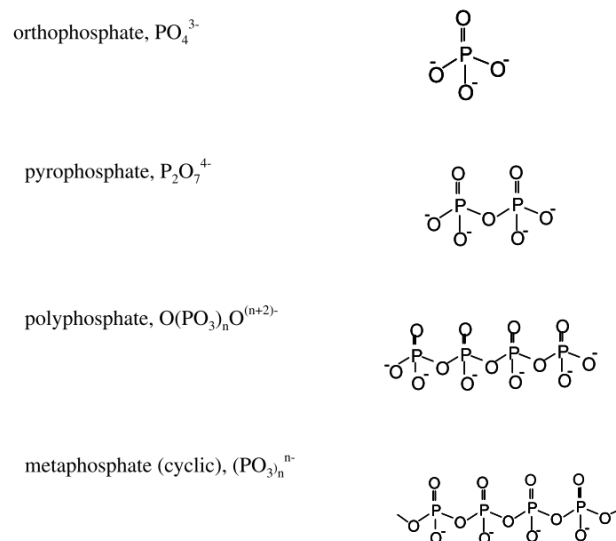


Figure 3-24 Phosphates formed from ZDDPs [67]

### 3.2.5 Influence of Steel Surface Composition on ZDDP Tribofilm Growth using Ion Implantation

Effective tribofilm formation relies on the interaction of ZDDP with a rubbing, solid surface, so to understand and improve the anti-wear performance it is essential to consider the additive and surface in combination. Previous investigations have shown that ZDDP tribofilm formation is influenced by the solid surface properties, including hardness [202–204] and roughness [205–207], as well as chemical composition [152,208]. All these surface properties must be taken into account when studying mechanisms of tribofilm formation. Of these, the least well understood is the influence of chemical composition since it is quite difficult to vary this independently of hardness and roughness.

Pagkalis et al. [208] have recently shown that the growth and performance of antiwear tribofilms are different on different steel types. In the case of ZDDP, the rate of tribofilm formation was slower on AISI M2 steel than on AISI 52100, 16MnCr5 and 440C steels. Jelita Rydel et al. [152] found that thinner ZDDP tribofilms formed locally on residual carbides than on the surrounding martensite matrix of steel. From the above, it appears that steel composition, including the presence of different non-metallic compounds in steels, may chemically play a role in antiwear tribofilm formation.

Research to date on the effect of steel composition on tribofilm formation, and also on friction and wear performance, is constrained by the fact that only a limited range of steels of different composition are commercially available for testing and these do not have

compositions that differ in a systematic fashion. Also, very few steels are available in the ball form needed in most tribotesters, for example in the 4-ball, MTM and HFRR. To address this, a novel approach was developed in this project and is described in Chapter 6 in which the impact of alloying elements in steel on antiwear performance is investigated by using ion implantation to dope surfaces of steel specimens with a series of non-ferrous, metallic elements. This has the advantage of causing relatively little change in roughness from the original surface and not altering the dimensions of the original sample, although, depending on the implanted element, it may increase the hardness. Another practical advantage is that it can be used as easily on steel balls as on flats, so enabling rolling-sliding tests to be carried out with materials not generally available in ball form.

### **3.2.6 Effect of Non-metallic Material on Tribofilm Formation**

In recent years, non-metallic materials, both bulk materials and coatings, have become widely used in lubricated machine components, both to reduce wear and, in the case of bulk lightweight materials, to reduce vehicle mass to increase fuel efficiency. Therefore, understanding the behaviour of ZDDP tribofilm formation on non-metallic surfaces is increasingly important.

Our current understanding of the overall process by which ZDDP forms tribofilms on ferrous surfaces was described above in Section 3.2.4 and from this it was clear that interactions of ZDDP with the metal or metal ions are important at various stages of film formation; in adsorption, formation of iron sulphide and in polyphosphate depolymerization. It is not, however, at all clear whether similar processes can occur on non-metallic surfaces, where metal cations other than Zn are either absent or present in only small doping concentrations.

There have been some studies of the formation of ZDDP tribofilms on non-metallic surfaces, but the majority of these have used a non-metallic on ferrous tribopair combination, where transfer of tribofilm or of ferrous or ferric ions from ferrous surfaces may take place. A few researchers have investigated ZDDP tribofilm formation on non-metallic/non-metallic tribopairs, including DLC/DLC,  $\text{Si}_3\text{N}_4/\text{Si}_3\text{N}_4$  and  $\text{Al}_2\text{O}_3/\text{Al}_2\text{O}_3$ . In most of these studies, ZDDP tribofilm was identified on non-metallic surfaces, but some tribofilm properties and particularly adhesion to substrate surfaces, were found to be different from those of ZDDP tribofilms present on ferrous surfaces.



Chapter 7 of this thesis describes a systematic study of the extent to which ZDDP forms a tribofilm on non-metallic surfaces and the composition of these films when they are formed.

### **3.2.7 Driving Force of ZDDP Tribofilm Formation**

Various factors that might influence tribofilm formation on surfaces have been suggested, including temperature, pressure, triboemission, surface catalysis and shear stress.

#### **3.2.7.1 Temperature**

Many studies have shown that high bulk temperatures promote tribofilm growth [169]. However, heat is also generated when surfaces are rubbed together, and this can result in a local transient contact temperature rise termed “flash temperature”. The magnitude of this flash temperature rise depends on the rate of heat generation and this depends primarily on sliding speed and friction [209]. This flash temperature may promote tribofilm formation. However, although flash temperature rises may be significant at high sliding speeds, tribofilms can form even at very low sliding speeds when flash temperature rise is negligible. This suggests flash temperature is not generally a key driver for ZDDP tribofilm formation [167], though bulk temperature is certainly an important factor.

#### **3.2.7.2 Pressure**

High pressure in non-conforming contacts may be a driving force of tribofilm formation [210]. Mosey et al. [210] used computational modelling to show that very high pressures can lead to a modification of the coordination number of Zn atoms that induce a cross-linking in phosphates, resulting in a formation of phosphate tribofilms. However, the pressures required were far in excess of the yield pressures of most materials, and thus the tribofilm formation caused by high pressures may not occur in normal rubbing contacts. For example, Tse et al. [211] showed ZDDP structures did not change up to 21 GPa contact pressure.

### 3.2.7.3 Triboemission

Triboemission is a term used for the emission of electrons, ions, radicals and photons caused by sliding. It is well known that plastic deformation and fracture processes that can occur when solid surfaces rub together generate localized charged regions, resulting in the emission of energetic particles; photons, electrons and ions [212–214]. Puhan [215] observed that ultraviolet (UV) irradiation onto ZDDP-coated substrates resulted in a formation of phosphate tribofilms. However, as emitted particles are likely to be captured by the lubricants, it is difficult to confirm the impact of triboemission on a tribofilm formation.

### 3.2.7.4 Surface Catalysis

Plastic deformation of metals forms oxide-free and dislocation-rich surfaces. These surfaces are reactive and may help in surface catalysis of ZDDP tribofilm formation. As described in Section 3.2.4, Yamaguchi et al. [192] showed that ZDDP molecules adsorb on Al via the sulphur atom of the P=S bond. Martin et al. [179] suggested that the S in ZDDPs is likely to react with iron oxide particles freshly formed by wear to form iron sulphides. These studies suggest that fresh metal surfaces may act as a catalyst to form tribofilms.

### 3.2.7.5 Shear Stress

Recently, a few studies have suggested that the shear stress or other asymmetric stresses in sliding contacts can act on molecular bonds in ZDDP to promote mechanochemical reactions. When an atomic-scale force ( $f$ ) or shear stress ( $\tau$ ) are applied to a molecule, temperature and stress couple to determine the probability of the molecule undergoing many physical and chemical processes;

$$Probability = Ae^{-(E_0 - f\Delta x)/k_B T} \text{ or } Ae^{-(E_0 - \tau\Delta v)/k_B T}$$

where  $A$  is a pre-factor,  $E_0$  is the activation energy for the process,  $\Delta x$  is the activation length,  $\Delta v$  is the activation volume,  $k_B$  is the Boltzmann constant and  $T$  is the absolute temperature. In this *stress-promoted thermal activation model*, the activation energy characteristic of the Arrhenius equation is effectively reduced by a work term applied to the molecule, the product of an applied force and a displacement known as the activation

length. The activation volume is then the product of this activation length and the area of the molecule over which the stress,  $\tau$ , acts.

Gosvami et al. [216] investigated the influence of force and temperature on ZDDP tribofilm formation on a silicon using a liquid-cell AFM, and showed that the growth rate of ZDDP tribofilm exponentially increased with applied pressure, as shown in Figure 3-25. This increase is in agreement with the stress-promoted thermal activation model in the above equation although, since shear stress is generally proportional to pressure, it did not establish whether pressure or shear stress was the controlling factor. Although the growth rate of ZDDP tribofilm was consistent with the stress-promoted thermal activation model, there was a considerable practical problem to prove that ZDDP tribofilm formation is directly controlled by the model because all the other possible influencing factors mentioned above can occur in rubbing contacts. To solve this limitation, Zhang et al. [217,218] studied how the shear stress controlled the rate at which ZDDPs form tribofilms on rubbing surfaces using a novel approach to form films in full film EHD conditions. The authors showed that tribofilm formation does not require a solid-solid rubbing contact, and that the rate of tribofilm formation depends on shear stress rather than the pressure, consistent with the stress-promoted thermal activation model. This suggests that shear stress can reduce the thermal activation barrier to ZDDP tribofilm formation.

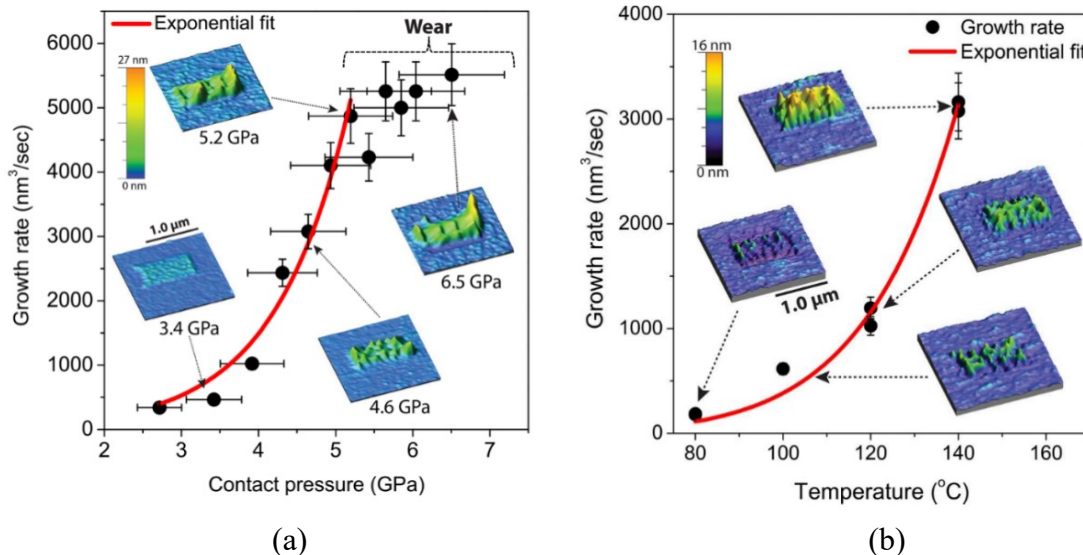


Figure 3-25 Tribofilm volumetric growth rate dependence on (a) contact pressure and (b) temperature [232]

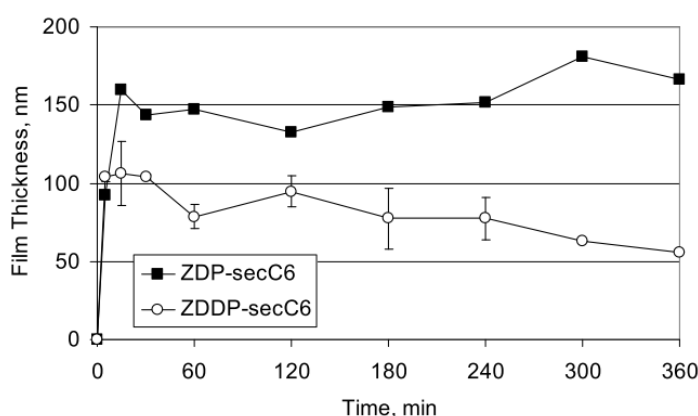
### 3.2.8 Comparison of the Reaction Mechanism of ZDP Tribofilm Formation

Although the S atoms in ZDDPs play an important role in forming initial tribofilms as shown in Section 3.2.4, study of zinc dialkyldiphosphates (ZDP) which do not include S (Figure 3-26) showed that ZDPs also form antiwear phosphate tribofilms [219–221]. Hoshino et al. [220] compared the growth of ZDDP and ZDP tribofilms in boundary lubrication condition, and found that ZDPs formed thick tribofilms similar to ZDDPs (Figure 3-27). Like ZDDP tribofilms, these ZDP tribofilms reduced wear and increased friction.

One of the possible process of ZDP tribofilm formation has been proposed as Figure 3-28 [221]. As the initial step, ZDPs may adsorb on metal surfaces through O atoms instead of S as with ZDDPs. Subsequently, intermolecular nucleophilic attack catalysed by ferrous substrates may occur in two ways; the reaction between two adsorbed ZDP molecules (Figure 3-28 left), and the reaction between an adsorbed ZDP molecules and molecules in bulk solution (Figure 3-28 right). In both cases, the reaction might be initiated by the cleavage of Zn-O, followed by the removal of alkyl chains along with the pyrophosphate formation. These studies suggest that S is not necessary to form surface-protective phosphate tribofilms and that the alkylation stage described in section 3.2.4.3 may not necessarily occur in tribofilm formation.



Figure 3-26 Chemical structure of (a) ZDDP and (b) ZDP [220]



(a)

(b)

Figure 3-27 Tribofilm thickness growth of ZDP-secC6 and ZDDP-sec C6 at 100 °C [220]

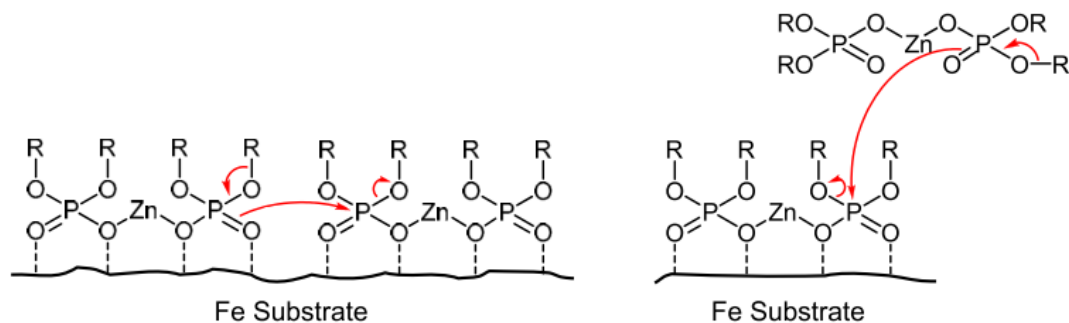


Figure 3-28 Proposed reaction mechanism of ZDP tribofilm formation [221]

### 3.2.9 ZDDP Thermal Film Formation

The study of reaction mechanisms of thermal film formation is quite limited. Fuller et al. [130] used XPS to suggest that S/O exchange isomer (see in Section 3.2.4) formed on metal surfaces immersed in pre-heated ZDDP solutions. Possibly, thermal films may form on metal surfaces by the S/O exchange mechanism shown in Figure 3-21.

## 3.3 Studies of ZDDP Tribofilm Performance

ZDDPs function as both an antiwear additive and an antioxidant. In this section previous studies of the effect of ZDDPs on wear and friction are outlined.

### 3.3.1 Antiwear Performance

It has been proposed that ZDDPs may function as an antiwear additive in three main ways [67]; (i) by forming mechanically protective tribofilms; (ii) by removing corrosive peroxides or peroxy-radicals; (iii) by digesting hard and thus abrasive iron oxide particles. Generally, forming a mechanically protective tribofilms (i) is the most accepted view of ZDDP antiwear discussed in this section [222]. Tribofilms prevent direct contact and thus adhesion between metal surfaces. They may also reduce the stresses caused by direct asperity contact. ZDDP performance has been studied using various tribometers. The effect of influential factors of ZDDPs on antiwear performance has been well investigated; *i.e.* alkyl groups, P concentration, contaminants, coexisting lubricant additives, rubbing conditions and tribofilm properties.

### 3.3.1.1 Alkyl Groups

The alkyl groups of ZDDPs affect thermal stability of ZDDPs, and thus tribofilm development. Generally, antiwear performance of ZDDPs is considered to be in inverse proportion to thermal stability, as Sheasby et al. [223] showed that some primary ZDDPs caused more wear than secondary ZDDPs. This is because ZDDPs with lower thermal stability are easily decomposed, and thus quickly form tribofilms [224].

### 3.3.1.2 Phosphorus Concentration

In order to study the effect of P concentration on antiwear performance, Fan et al. [225] monitored the Fe concentration in lubricants as an indicator of wear as shown in Figure 3-29. The authors found that, while ZDDP solutions with 0.005 to 0.01 wt% of P generated large amount of wear like a base oil, ZDDP solutions with 0.02 to 0.05 wt% of P reduced wear. This result shows that certain amount of ZDDP is needed to protect surfaces from wear.

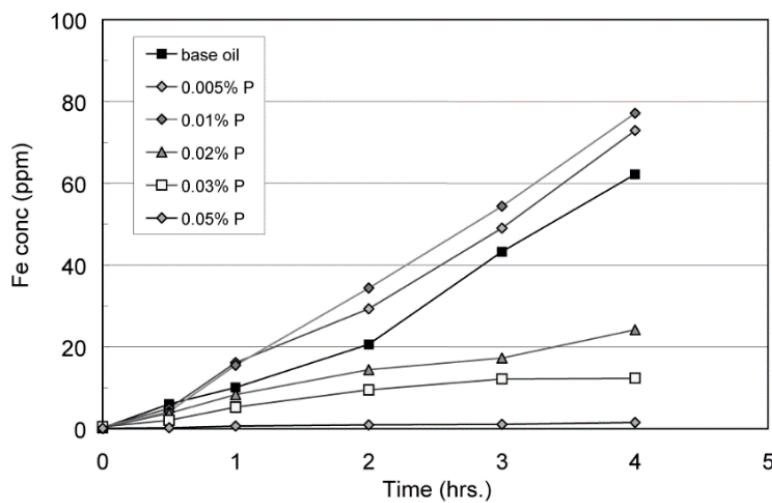


Figure 3-29 The effect of ZDDP concentration on wear [225]

### 3.3.1.3 Contaminants

Contaminants such as water and soot are mixed into engine oils during engine operation. Generally, these contaminants deter tribofilm formation and promote wear. Parsaeian et al. [226] studied the effect of relative humidity on ZDDP antiwear performance and found that more wear occurred with high humidity (Figure 3-30). Cen et al. [227] showed that water could lead to the formation of sulphate on wear track rubbed in a ZDDP-containing

oil, resulting in more wear. Like water, it has been reported that soot and soot surrogate carbon blacks (CB) in ZDDP solutions gave higher wear than when ZDDP was not present [228]. Kontou et al. [198] suggested that CB might remove thin FeS<sub>2</sub> films formed by ZDDPs at the initial stage, so that thick ZDDP tribofilms could not form. The authors showed that the addition of some dispersants into ZDDP and CB solutions reduced wear by dispersing CB in lubricants.

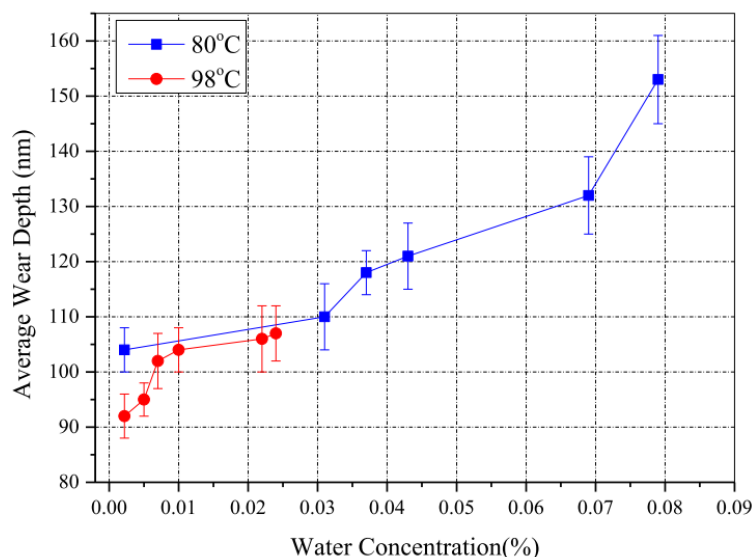


Figure 3-30 The effect of relative humidity on wear [226]

### 3.3.1.4 Coexisting additives

Formation of ZDDP tribofilms can be deterred by the presence of other lubricant additives; dispersants, friction modifiers and detergents. Zhang et al. [88] found that dispersants reduced ZDDP tribofilms to an extent dependent on the dispersant concentration. This tribofilm reduction resulted in an increase of wear rate in proportion to dispersant concentration. Several mechanisms by which the presence of dispersants in ZDDP oils increases wear have been suggested; in particular, competitive adsorption on surfaces with ZDDPs and the reduction of ZDDP activity to adsorb on surfaces by a complex formation [229,230]. These behaviors result from the interaction with polar compounds, so some FMs and detergents provide similar negative effects on antiwear performance of ZDDPs [52,73].

### 3.3.1.5 Rubbing Conditions

The rubbing conditions including temperature, slide-roll-ratio (SRR) and oxidation have significant effects on ZDDP antiwear performance. Fujita et al. [231] showed that wear increased as oil temperature increased over 135 °C because of the precipitation of decomposed ZDDPs. Shimizu et al. [197] showed that while thick tribofilms were formed up to 198% of SRR and resulted in no wear, in the condition of 199% and 200% of SRR (pure sliding) they were not uniformly formed on a wear track, providing severe wear. Masuko et al. [232] studied the ZDDP antiwear performance in oxidative atmosphere and found that wear increased with ZDDP oxidation through the reaction with cumene hydroperoxide, resulting from less phosphate tribofilms as shown in Figure 3-31.

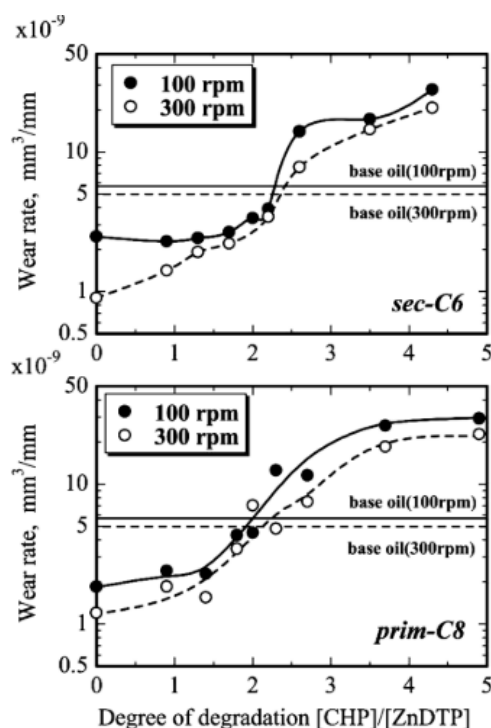


Figure 3-31 Antiwear characteristics of oxidatively degraded ZDDPs [232]

### 3.3.1.6 Tribofilm Properties

As described above, tribofilm thickness, especially in the running-in stage, may play an important role to protect surfaces from wear. On the other hand, Zhang et al. [233] compared the antiwear performance of ZDDPs with ashless dialkyldithiophosphates (DDPs) and found that ZDDPs provided less wear than DDPs, though they formed the tribofilms with the same thickness. Tribofilms of ZDDPs had a pad-like structure whereas DDPs formed much smaller pads and more “streaky” tribofilms. Landauer et al. [234]



found tribofilms with high elastic modulus were associated with the superior antiwear performance. It is not fully understood, but these tribofilm properties in addition to thickness may affect antiwear performance.

### **3.3.2 Effect of ZDDP on Friction**

The effects of ZDDP on friction have been well investigated and it has been shown that ZDDP generally increases friction coefficient in mixed and boundary lubrication conditions compared to the base oil alone [235]. This friction increase was correlated with the thickness of the ZDDP tribofilms and it was proposed that it originated from the roughness of tribofilms [153,170]. Recently, Dawczyk et al. [149] proved that increase in friction in mixed lubrication condition is caused by the increase in effective roughness of the rubbing surfaces due to the formation of ZDDP tribofilms. Figure 3-32 (a) shows the effect of entrainment speed on friction coefficient (Stribeck curves). The shape of the curve before rubbing (0 min) indicated that the contact was in mixed and boundary lubrication regime at the lowest speed and reached full film lubrication regime at high entrainment speed, greater than 500 mm/s. After 2 hours rubbing, a thick ZDDP tribofilm formed, resulting in the increase of boundary lubrication regime at slow speeds up to 100 mm/s, and no full film lubrication even at the highest entrainment speed of 3 m/s. This indicates that increase of boundary and mixed lubrication regimes with rubbing time is due to the formation of rough, solid tribofilm surfaces that prevent fluid entrainment. Tribofilms became thick and rough with rubbing, and the authors determined lambda ratio using the measured roughnesses of the tribofilms. As shown in Figure 3-32 (b), all the friction curves overlapped in a single friction coefficient curve against lambda ratio. This indicates that the evolution of friction was mainly influenced by the surface roughness development of ZDDP tribofilms.

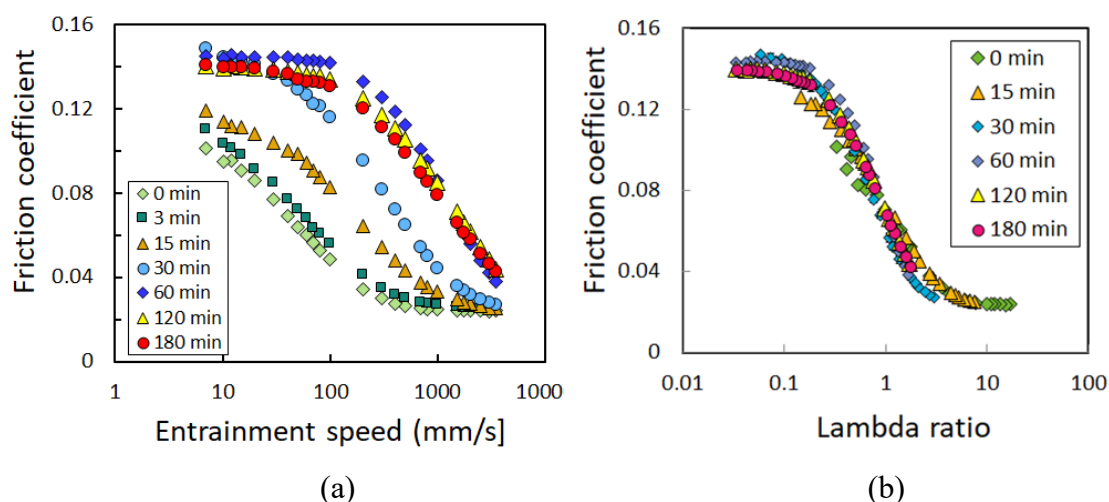


Figure 3-32 Friction -speed curves using a ZDDP solution and (b) collapse of friction curves when plotted against lambda ratio [149].

There has been limited research on the boundary friction properties of ZDDP tribofilms [73,107,221,236]. Studt [73] studied the effect of ZDDP alkyl group on friction in boundary lubrication regime and found that friction coefficient decreased with the increase of chain length of linear alkyl ZDDPs (Figure 3-33), while high friction coefficient was obtained from ZDDPs with branched alkyl chain. The author suggested that the ZDDP molecules adsorbed to form close-packed monolayers in a similar way to organic friction modifiers.

Recently, Zhang et al. [236] studied the boundary friction coefficients of tribofilms formed in the MTM by ZDDPs having a range of different alkyl structures. They found that boundary friction depended strongly on alkyl structure, broadly in line with Studt's findings. XPS analysis of the residual tribofilm indicated the presence of a considerable proportion of C-O bonds, which showed that some alkoxy groups remains within the tribofilm to influence boundary friction properties when the film was partially removed.

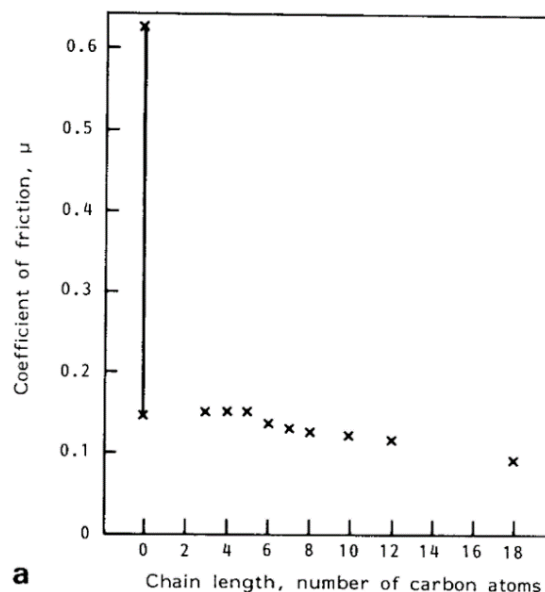


Figure 3-33 The effect of ZDDP alkyl groups on boundary lubrication friction [73]

### 3.3.3 Studies of Effect of MoDTC on ZDDP Properties

Most studies reviewed above have studied lubricants with ZDDP in base oil, without any other additives present. In practical use, ZDDPs are used with other additives, especially FMs, VMs, dispersants and detergents. These additives can interact with ZDDPs, resulting in synergetic or antagonistic effects on ZDDP performance. Recently, because of the requirement to improve mechanical efficiency, the effect of FMs, and especially MoDTC, on ZDDP properties has been increasingly studied. In this section, the effects of MoDTC on the properties and performance of ZDDP tribofilms are reviewed.

#### 3.3.3.1 Tribofilm Formation and Properties of Tribofilms

Generally, the addition of MoDTC into ZDDP solution retards ZDDP tribofilm growth [52,237–240], due to the competitive adsorption of ZDDPs and MoDTCs on metal surfaces. The properties of the resulting tribofilms have been well investigated and it has been found that  $\text{MoS}_2$  and  $\text{MoO}_3$  are formed on phosphates (Table 3-1) [237–241]. Topolovec Miklozic et al. [242] showed that an oil containing both ZDDP and MoDTC

formed a broad pad structure like ZDDP tribofilms, but it was rather more uneven than with ZDDP alone.

Table 3-1 Tribofilm composition in wt.% measured using EDX on wear scar after 6 h tests. 002A: ZDDP, 003A: MoDTC, 004A: ZDDP + MoDTC solutions [238]

	EDX (wt%)									
	P	S	Zn	Fe	O	C	Cr	Si	Mn	Mo
002A	1.2	0.5	2.4	83.8	5.9	0	4.0	0.5	1.6	–
003A	–	0.6	–	80.5	5.0	3.4	5.1	0.7	2.3	2.3
004A	0.3	0.3	0.7	82.5	4.6	3.7	4.7	0.5	2.1	0.4

### 3.3.3.2 Friction Behaviour

Blends of ZDDPs and MoDTCs give lower friction coefficient than when ZDDP alone is present. Muraki et al. [237] studied the effect of concentration of MoDTC in a ZDDP-containing oil on friction coefficient, and found that friction decreased and the rate of friction reduction became faster as the concentration of MoDTC increased (Figure 3-34). Morina et al. [238,239] found that while friction coefficient in a MoDTC oil was similar to that of a MoDTC + ZDDP blend, it became more stable at a lower level when ZDDP and MoDTC were present together (Figure 3-35). Xu et al. [243] showed a good correlation between the reduction of friction coefficient and the intensity of  $A_{1g}$  Raman spectra peak ( $412\text{ cm}^{-1}$ ) attributed to  $\text{MoS}_2$ , so that this low friction coefficient was believed to result from the formation of  $\text{MoS}_2$  on the surfaces of phosphate tribofilms. This  $\text{MoS}_2$  layer has low shear strength [173,244]. It has been reported that the ratio of  $\text{MoS}_2$  to  $\text{MoO}_3$  was increased when ZDDP and MoDTC were present together, resulting in lower friction coefficient [238,241].

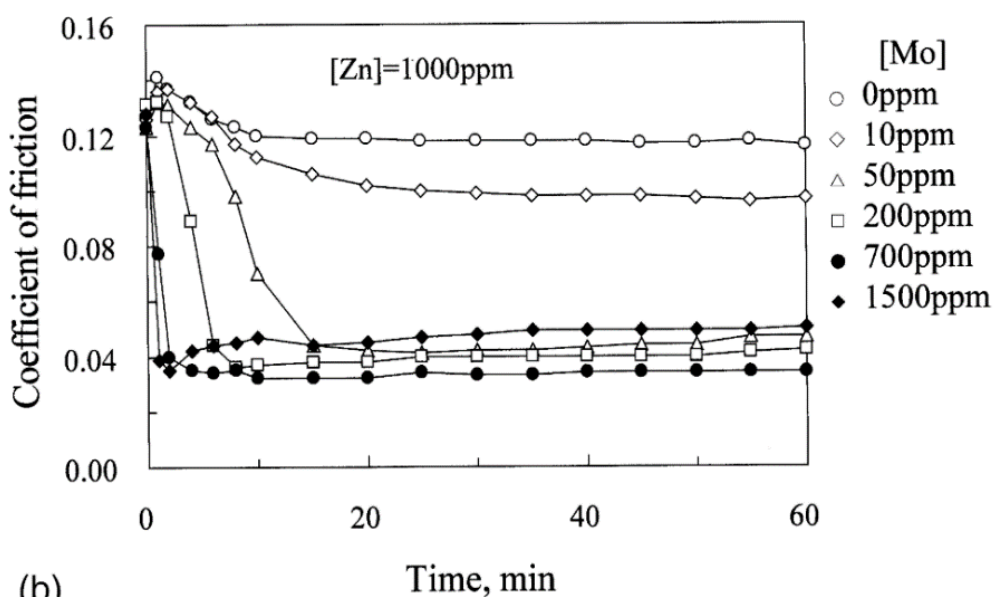


Figure 3-34 Effect of MoDTC concentration in a ZDDP oil on friction coefficient [237]

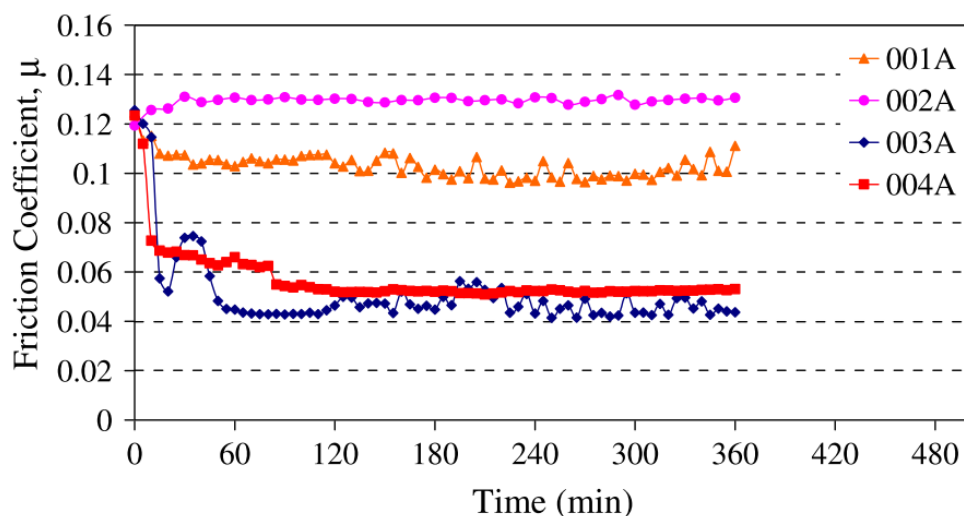


Figure 3-35 Friction behaviour of MoDTC containing oil. 001A: PAO6, 002A: PAO6 + ZDDP, 003A: PAO6 + MoDTC, 004A: PAO6 + ZDDP + MoDTC. [238,239]

Various mechanisms by which the co-existence of MoDTC and ZDDP promote  $\text{MoS}_2$  formation have been proposed. Sogawa et al. [245] showed by using  $^{34}\text{S}$ -labelled ZDDP that 40% of the sulphur in  $\text{MoS}_2$  was derived from ZDDP, and De Barros Bouchet et al. [244] suggested that ZDDP might supply S to form  $\text{MoS}_2$  from  $\text{MoS}_{2-x}\text{O}_x$  as shown in Figure 3-36, resulting in the increase of  $\text{MoS}_2$  formation rather than  $\text{MoO}_3$ . In addition, it

has been suggested that ZDDPs might digest the high friction compounds such as sulphate [240] or  $\text{MoO}_3$  [246], and also that ZDDPs may extend the useful life of  $\text{MoS}_2$  [238,247].

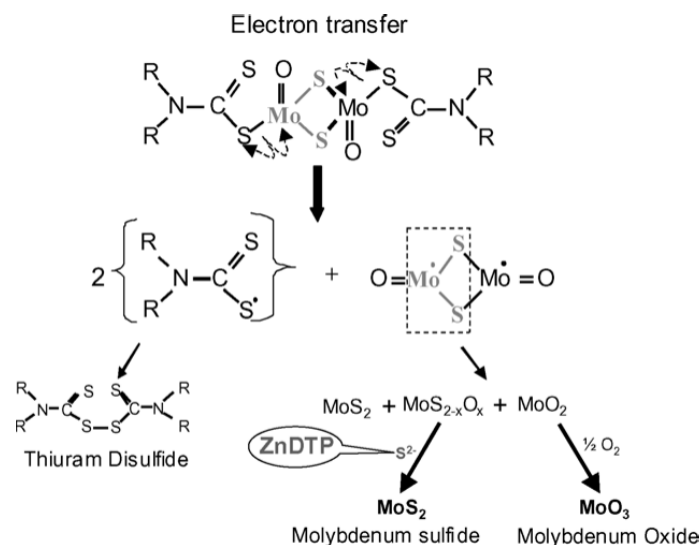


Figure 3-36 Chemical process of the  $\text{MoS}_2$  formation from MoDTC in the presence of ZDDP [244]

### 3.3.3.3 Antiwear Performance on Steel Tribopairs

Although the extent of influence of MoDTC on ZDDP antiwear performance may vary with test conditions, the addition of MoDTC to a ZDDP solution generally gives higher wear than ZDDP alone [239–241]. Morina et al. [239] suggested that MoDTC deters the formation of phosphate tribofilms, resulting in more wear, as shown in Figure 3-37.

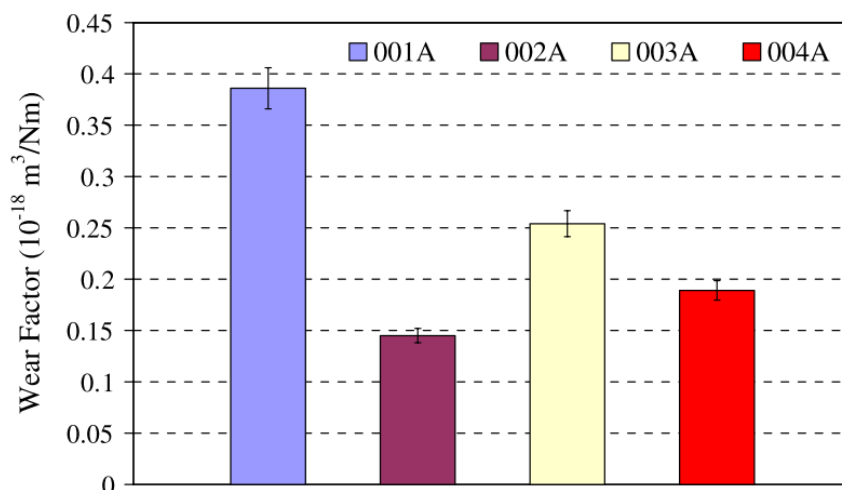


Figure 3-37 Wear factors tested in 6 hours using a reciprocating pin-on-plate tests, 001A: PAO6, 002A: PAO6 + ZDDP, 003A: PAO6 + MoDTC, 004A: PAO6 + ZDDP + MoDTC [239]

### **3.3.3.4 Wear of Hydrogenated DLC in MoDTC-containing Oils**

As described in Section 2.3.5.1, Diamond-like carbon (DLC) coatings on steel substrates have been widely applied to machine components to reduce friction. Engine components so coated include rocker arms, valve lifters and piston rings. An obvious approach to achieving even larger reductions in friction is to combine DLC coatings with friction modifier additives and indeed the two appear to be complementary [242]. Unfortunately, while MoDTCs can greatly reduce boundary friction with DLC, many studies have reported that MoDTC can cause high wear of some types of DLC coatings, especially of the hydrogenated amorphous carbon (a-C:H) type.

The precise mechanism of MoDTC promotes high wear of a-C:H DLC coating has not been unambiguously determined, but several studies have suggested that this wear is related to the formation of MoO<sub>3</sub> from MoDTC in the DLC/steel tribocontact [62].

Some researchers have reported that the harmful effect of MoDTC on a-C:H DLC wear can be prevented by including ZDDP together with MoDTC in the oil and several possible origins of this response have been suggested. However, the precise mechanism by which both the chemical properties of MoDTC tribofilms affect DLC wear and the way that ZDDP partially alleviates this wear are not fully proven, while there appears to have been no published work on the impact of other surface-active additives used in engine lubricants on MoDTC/DLC wear.

Based on this, Chapter 8 describes new research that aims to determine whether informed lubricant formulation can control the deleterious impact of MoDTC on a-C:H DLC wear and to identify the mechanisms involved.

## **3.4 Influence of ZDDP on Micropitting**

### **3.4.1 Effect of ZDDP Tribofilm Growth on Micropitting**

As described in Section 2.3.6, micropitting is a type of surface fatigue damage caused by stress fluctuations due to asperity interactions in rolling-sliding contacts. It occurs in thin oil film and thus low lambda ratio conditions where such asperity interactions are prevalent. Because of this, boundary film-forming lubricant additives significantly affect micropitting.

Since the number and severity of asperity interactions increase at low lambda ratios, micropitting should also increase at low lambda. However, in practice, the occurrence of mild adhesive or abrasive wear at very low lambda ratio often means that this simple relationship between lambda and micropitting does not hold. Morales Espejel et al. [248] have shown that in the presence of mild wear, micropitting may have a maximum value at a critical, intermediate lambda ratio. Above this lambda ratio, micropitting decreases as there are fewer asperity interactions. Below this lambda ratio, micropitting decreases as shown in Figure 3-38 due to increased mild wear and thus removal of microcracks. This trend is a direct result of the continuous competition between micropitting and mild wear, the outcome of which is heavily dependent on the prevailing contact conditions and especially lambda. The key aspect to note here is that it is the combined action of low lambda ratio and minimal surface wear, particularly of the rougher and harder counterface, that promotes the accumulation of asperity contact cycles and consequently increases microcrack growth and micropitting.

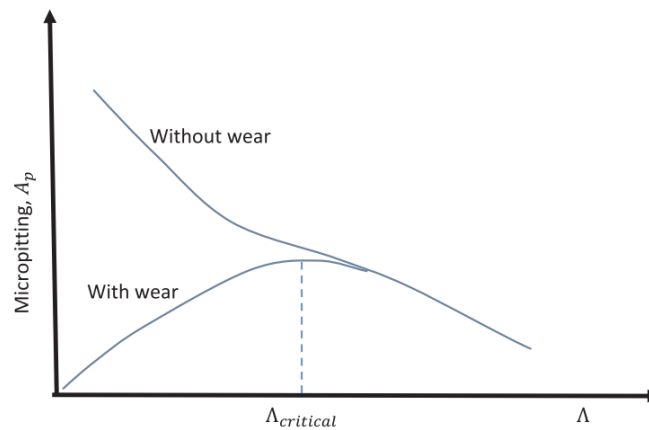


Figure 3-38 The expected trends in micropitting behaviour with specific film lambda for cases with and without the presence of mild wear [248]

ZDDPs affect the above competition between surface fatigue and mild wear by forming tribofilms, and hence influence the type and extent of surface damage. It has been shown that the excellent performance of ZDDP in reducing mild wear originates from its ability to form protective tribofilms very rapidly. On the other hand, several studies have shown that ZDDPs promote micropitting. Olver and co-workers [249–251] demonstrated the significance of ZDDPs on micropitting using a micropitting rig (MPR). They found that, while a solution of ZDDPs in PAO produced significant micropitting on the test roller, pure PAO base oil did not produce any appreciable micropitting. However, when surfaces



were initially lubricated with PAO alone and then ZDDPs were added after 73000 cycles, no micropitting progressed, as shown in Figure 3-39 [251]. This, coupled with measurement of the evolution of surface roughness during tests, demonstrated that the rapid formation of ZDDP tribofilms protected the roughness asperities of the harder counterface rings from wear, so that the test roller continued to be subjected to high asperity stresses throughout the test, which caused severe micropitting. In effect, ZDDP prevented beneficial running-in. By contrast, the pure PAO base oil offered no such wear protection, so that the counterface roughness was drastically reduced in the initial stages of the test, reducing subsequent asperity stress cycles and thus micropitting.

Clearly, a lubricant that minimises micropitting by producing excessive amounts of adhesive or abrasive wear is unacceptable as the component is condemned to failure either way: the optimum lubricant formulation needs to be able to control both of these failure modes. In Chapter 9, the influence of ZDDP on preventing running-in and thereby promoting micropitting is investigated using a novel method in which micropitting and tribofilm formation are monitored in parallel in the same test. This shows very clearly the linkage between running-in and tribofilm formation and the role played by ZDDP in controlling this linkage.

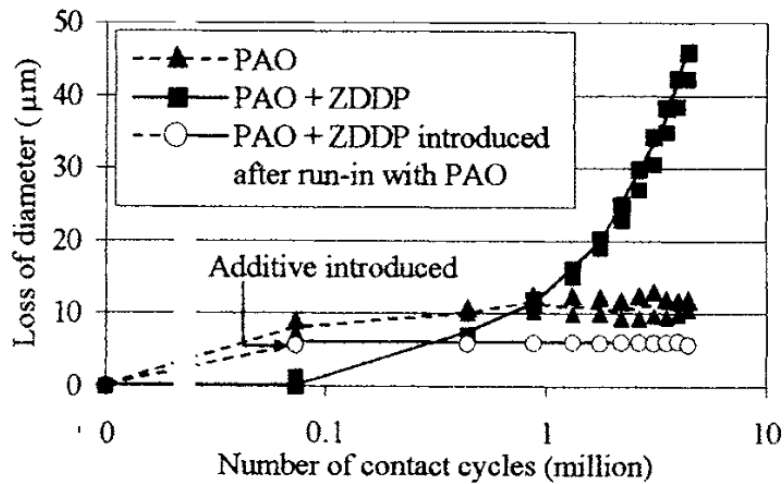


Figure 3-39 Evolution of micropitting as a function of contact cycles during the test with different lubricants [251]

### 3.4.2 Influence of Black Oxide Coating on Micropitting and ZDDP Tribofilm

Ways to mitigate micropitting have been widely investigated and include reducing counterface roughness [251], reducing friction [252], slowing initial tribofilm growth rate (Chapter 9) and application of surface coatings. Of these, the application of surface coatings, particularly black oxide (BO) coating, is currently believed to be one of the most practical approaches to alleviate micropitting.

Black oxide (BO hereafter) coating is a surface treatment that chemically converts the surface of ferrous alloys to magnetite ( $\text{Fe}_3\text{O}_4$ ). To apply the BO coating, steels are blackened in an alkaline aqueous salt solution operating at 130 - 150 °C [253]. The process is relatively cheap and fast although care must be taken not to generate unfavourable near-surface stress distributions and/or cause unwanted surface damage by aggressive solution treatment. BO coatings were originally used primarily for corrosion protection, but nowadays they are also employed to mitigate against other types of damage in machine elements such as smearing in rolling bearings [254–256], and more recently, fatigue failures associated with white etching cracks in wind turbine bearings [257–259]. Generally, BO coating has only about a quarter of the hardness of typical bearing and gear steels, so that it is easily worn off in operation. This has been suggested to enable fast running-in of rubbing surfaces [254–260]. This can reduce friction and in particular, asperity stresses in rolling-sliding contacts.

Recently, Brizmer et al. [260] reported that BO coating can reduce micropitting damage when it is applied on the rougher of the two bodies in rolling-sliding contact. Based on the evolution of friction and roughness during tests lubricated with a ZDDP-containing oil, they suggested that the mechanism by which BO reduces micropitting is related to enhanced running-in of the BO-coated surfaces that is at least partly brought about by BO suppressing the formation of ZDDP antiwear tribofilms. It has also been reported that the reaction mechanism of ZDDP tribofilm formation and tribofilm properties on a surface containing  $\text{Fe}_3\text{O}_4$  may be different from that on steel surface [143,261].

From the above it appears that BO coating may influence micropitting in several different ways; by promoting running in due to its low hardness, by inhibiting ZDDP tribofilm formation and also, as described in the next section, by influencing boundary friction. Chapter 10 of this thesis describes new research to identify the primary mechanism by which BO alleviates micropitting.

### 3.4.3 Effect of Friction on Micropitting in ZDDP-Containing Oils

Because micropitting is a fatigue process, it will depend strongly on the asperity stresses that promote crack development. In a rubbing, rough surface contact, these stresses arise from applied normal load and friction, so boundary friction coefficient should influence crack development and thus micropitting.

Our understanding of the ways that friction influences crack growth originates largely from studies of macro-scale fatigue but the mechanisms involved are likely to be similar in both macro-scale fatigue and micro-scale micropitting. Since it contributes to the overall contact stress levels, friction will promote plasticity within the contact, and hence increases the risk of crack initiation. Once initiated, surface cracks can propagate under the action of tensile (mode 1) and/or shear stress (mode 2). Hamilton et al. [262] have shown that the magnitude of the tensile stress at the rear of a point contact depends on a factor  $(1 + A\mu)$ , where  $A = 3\pi(4 + \nu) / 8(1 - 2\nu)$ ,  $\nu$  is Poisson's ratio and  $\mu$  is friction coefficient. When  $\nu$  is 0.3, as is the case for steels,  $A$  is about 12, so that according to this relationship, the magnitude of tensile stress at the rear of the point contact will increase by about 65% when friction coefficient increases from  $\mu = 0.04$ , typical of a well lubricated, elastohydrodynamic contact, to  $\mu = 0.12$ , typical of a contact operating in a boundary regime with a ZDDP-containing oil without an FM. As well as increasing tensile stresses, higher friction will increase contact shear stresses that are widely recognized to promote fatigue damage [263–266], with the orthogonal shear stress amplitude being commonly used as the critical stress value in rolling bearing fatigue life predictions [267]. Growth of surface cracks under rolling-sliding contact is believed to be further promoted by the hydraulic action of oil that is able to enter a surface breaking crack and is then pressurized during subsequent over-rolling [268–271]. Friction probably plays a crucial role in this mechanism also, by opening the mouth of the surface breaking crack ahead of the contact which aids oil entry into the crack.

A few researchers have used friction modifier additives to investigate the role of friction on micropitting. Lainé et al. [252] compared micropitting performance of ZDDP-containing oils with and without the friction modifier MoDTC. They showed that MoDTC reduced friction coefficient from 0.08 to 0.04 and also significantly reduced micropitting damage compared to the oils containing only ZDDP. Recently Soltanahmadi et al. [272] showed that the addition of ashless amine friction modifier to a ZDDP-containing oil also reduced micropitting in a similar general manner to that of MoDTC. They ascribed this

effect both to the impact of friction on asperity stresses and also the effect of the friction modifier additive on partially suppressing ZDDP tribofilm formation. This raises the important question of whether the effect of friction modifier additives on micropitting originates primarily from their effect on friction or on their effect on running-in via their interaction with ZDDP. To address this question, Chapter 11 describes a study in which the friction and running-in effects are decoupled by running-in with a ZDDP-containing oil and then adding MoDTC to reduce friction.

### **3.5 Summary and Research Questions**

As described above, a great deal of tribochemical investigation of ZDDP tribofilms has been carried out and we understand a great deal about the formation, nature and properties of these tribofilms. There are, however, several important issues remaining unresolved and some of these have been investigated by the author as described in this thesis. These research questions are addressed in Chapters 5 to 11 as summarized below.

**Chapter 5:** The chemical and mechanical properties of ZDDP tribofilms have been quite thoroughly investigated and it has been found that these tribofilms have a layered structure composed of mainly Zn and Fe phosphates with a patchy morphology. However, the properties of the tribofilms have not yet been fully elucidated, especially in terms of crystallinity and durability. This chapter describes new research into the evolution of ZDDP tribofilm crystallinity during its formation and the effect of this on the tribofilm durability. Reaction mechanisms of tribofilm crystallinity formation are also suggested.

**Chapter 6:** Most research on ZDDP has used bearing steels but many important machine components such as gears and cams employ quite different alloy steels, and it has recently been shown that tribofilm formation on such alloys is not the same as that on conventional bearing steel. This difference might originate from differences in mechanical properties, such as hardness or topography, and/or differences in surface chemical composition. To explore this further, this chapter examines the influence on ZDDP tribofilm formation of ion-implanting various alloying elements, Ni, Mo, Cr, V and W, into bearing steel surfaces.

**Chapter 7:** Although the precise reaction equations of ZDDP tribofilm formation have not been directly demonstrated, plausible reaction sequences on ferrous surfaces have been proposed. However, these proposed reaction sequences are based almost entirely on

studies using ferrous surfaces; reaction mechanisms on non-metallic surfaces are not yet much investigated or understood. This chapter describes research to understand the extent to which ZDDP tribofilms form on non-metallic surfaces in rubbing contacts and, if they do form, the chemical properties of these tribofilms. Of particular interest is the impact of different materials on the mechanism of tribofilm formation compared to its formation mechanism on steel substrates.

**Chapter 8:** Severe wear of hydrogenated DLC rubbed against steel in an MoDTC solution has been reported. The possible ways to reduce such wear and the mechanisms of how this wear is reduced have not been well examined. In this chapter the effect on MoDTC-promoted a-C:H DLC wear of adding various surface-active additives used in engine lubricants, including ZDDP, an ashless EP additive, Ca detergents, dispersants, an OFM and a PAMA, to an MoDTC solution has been studied. Relevant mechanisms by which these additives reduce the impact of MoDTC on DLC wear are also suggested.

**Chapter 9:** Thick phosphate tribofilms generated from ZDDPs can prevent asperity contact, resulting in excellent antiwear performance. However, ZDDPs may promote micropitting wear. Although this increase of micropitting may result from an inadequate running-in due to the formation of antiwear tribofilms, the direct effects of ZDDP tribofilms on micropitting have not been studied. This Chapter correlates ZDDP tribofilm growth rates and the evolution of micropitting by developing a new technique based on the MTM to observe the evolution of ZDDP tribofilm in-situ and any accompanying micropitting during the same test.

**Chapter 10:** To alleviate micropitting, one known solution is to apply black oxide coating,  $\text{Fe}_3\text{O}_4$ , on steel surfaces. It has been reported that black oxide has considerably lower hardness than steel, resulting in fast running-in, and thereby the reduction of asperity stress on surfaces. Thus, little micropitting occurs on such surfaces. However, the relevant mechanisms by which black oxide coating mitigates micropitting has not been fully understood, especially the effect of black oxide coating on antiwear tribofilm formation and its effect on micropitting. This chapter uses the MTM-based technique developed by the author to monitor both ZDDP tribofilm formation and micropitting to understand the impact of black oxide coating on ZDDP tribofilm formation and micropitting.

**Chapter 11:** It has been found that the addition of MoDTC to a ZDDP oil can mitigate micropitting. This may result from MoDTC producing low friction and/or MoDTC

promoting adequate running-in with ZDDP-containing oils. However, the relative contribution of these two factors on micropitting have not been isolated, so that the simple impact of friction reduction on micropitting is still unclear. This research aims to understand the effect of friction on micropitting and the relative mechanisms by which friction influences micropitting by isolating the friction from other influential factors.

## 4 Test Methods

*In this chapter, materials, equipment and test procedures used in this study are described.*

### 4.1 Test Materials

Materials used throughout this research, including base oils, some lubricant additives and test specimens are described below. Those used in just one area of research are described in the relevant chapter. All lubricant components were provided by Shell Lubricant Japan K.K..

#### 4.1.1 Base Oils

In this research, the main base fluids employed were a range of polyalphaolefins (PAOs) with different kinematic viscosities, as shown in Table 4-1. For high entrainment speed, high load Extreme Pressure Traction Machine (ETM) tests described in Chapter 7, a relatively high viscosity polyisobutene (PIB) was used in order to provide a sufficiently high shear stress in a full-film elastohydrodynamic lubrication (EHL) [218]. Unlike some mineral oils, PAOs and PIB do not include any impurities such as sulphur-based and unsaturated compounds so possible effects these impurities on tribological phenomena are avoided.

Table 4-1 Base oils used in this study

Base oil type	Kinematic Viscosity 40 °C, mm <sup>2</sup> /s	Kinematic Viscosity 100 °C, mm <sup>2</sup> /s	Viscosity Index	Density 15 °C, g/cm <sup>3</sup>
PAO2	5.5	1.8	-	0.80
PAO4	18.5	4.1	124	0.82
PAO10	62.8	9.9	142	0.83
PAO40	389.7	40.3	154	0.85
PAO100	1182.0	99.3	172	0.85
PIB	156.8	15.3	98	0.86

#### 4.1.2 ZDDPs

Three types of ZDDP were used throughout this research, as listed in Table 4-2. The concentration of alkyl group types in ZDDPs was determined by H-NMR. ZDDP1 is predominantly based on the primary 2-ethylhexyl group, but, being commercially produced also contains 12% of a secondary alkyl group of unknown structure. ZDDP2 is a pure secondary while ZDDPM is a mixture of primary and secondary, made from mixed alcohols.

Table 4-2 ZDDPs used in this study

Code	ZDDP type	Alkyl structure	P, wt%	Concentration of alkyl group type in ZDDPs, wt.%	
				Primary	Secondary
ZDDP1	Primary	2-ethylhexyl (C8)	6.1	88	12
ZDDP2	Secondary	1,3-dimethylbutyl (C6)	7.1	100	0
ZDDPM	Primary- Secondary mixed	6-methylheptane (C8) 1-methylpropyl(C4)	8.0	25	75

#### 4.1.3 MoDTC

Molybdenum dialkyldithiocarbamate (MoDTC) was used to study the impact of other additives on MoDTC-promoted wear in Chapter 8 and also in the study of the effect of friction on micropitting in Chapter 10. ADEKA Sakura-lube 165 (4.5 wt.% of Mo) was employed in these studies.

#### 4.1.4 MTM and ETM Test Specimen

In this study, a range of ferrous and non-metallic materials were used for balls (19.05 mm diameter) and discs of the MTM and ETM; AISI 52100 steel, ion implanted AISI 52100 steels, a-C:H coated AISI 52100 steel, black oxide coated AISI 52100 steel and ceramics. The details of mechanical and chemical properties of specimens are described in the relevant chapters.



## 4.2 Tribometers

Throughout this study, two types of tribometer were used to investigate ZDDP tribofilm growth and its performance.

### 4.2.1 Mini Traction Machine - Spacer Layer Interferometry (MTM-SLIM)

An MTM ball on disc tribometer with SLIM was employed to obtain and observe ZDDP tribofilm growth and also, in Chapters 9 to 11, its effect on micropitting. The rig is shown in Figure 4-1. A ball is loaded against a disc which is immersed in lubricant. The ball and the disc are driven by separate electric motors at specified rolling/sliding conditions. In this study in Chapters 5 to 8, the entrainment speed was kept low with smooth specimens so as to provide thin lubricant film conditions (boundary and mixed lubrication regimes). By contrast, in research in Chapters 9 to 11, the entrainment speed was high at 3 m/s, but rough steel discs were employed to provide thin lubricant film conditions.

To capture SLIM images, the rubbing test is paused and the ball is raised and loaded against a glass flat. The glass flat surface is coated with a semi-reflective chromium layer on top of which is a transparent silica spacer layer. Light waves reflected from the chromium layer and the ball surface undergo optical interference upon recombination, generating an interference image of the contact between the ball and the glass surface which is then captured by an RGB camera. Tribofilm thickness is calculated from this interferometry image using calibrated RGB values.

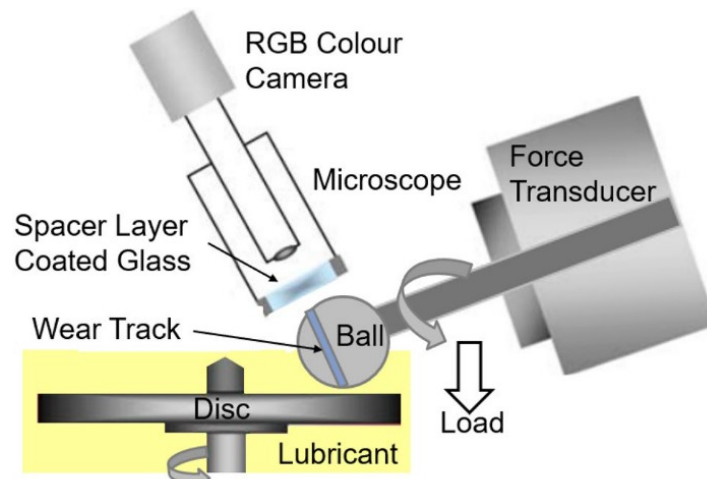


Figure 4-1 Schematic image of the MTM–SLIM set-up

#### **4.2.2 Extreme Pressure Traction Machine (ETM)**

The ETM rig has a similar configuration to the MTM as shown in Figure 4-1, but can apply much higher loads (up to 1650 N, compared to a maximum of 75 N for the MTM). This means that it can produce rolling-sliding contacts with much higher contact pressures than in the MTM. For the study in Chapter 6, ETM was employed in full film EHL condition without any asperity contact to evaluate the ability of ZDDP to react to form tribofilms in such conditions. Ferrous and non-metallic materials were tested. SLIM was not used to measure tribofilm thickness because of difficulties in obtaining accurate thickness values using SLIM from non-metallic balls of a different reflectivity.

### **4.3 Chemical Characterization of Tribofilm and Material**

Tribofilms formed after rubbing using MTM and ETM and test specimens were chemically analysed by a wide range of techniques as described below.

#### **4.3.1 X-ray Photoelectron Spectroscopy (XPS)**

A Thermo Fisher K-Alpha spectrophotometer was used for X-ray photoelectron spectroscopy (XPS) to analyse tribofilms in Chapter 5 to 8 and test specimens in Chapter 6. A monochromatic Al-K $\alpha$  X-ray source (energy = 1486.6 eV) was employed. The X-ray source was operated at 6 mA emission current and 12 kV anode bias. The calibration of the spectrometer was performed using Au (4f<sup>7/2</sup>), Cu (2p<sup>3/2</sup>) and Ag (3d<sup>5/2</sup>) signals. The spot size was an elliptical shape with a long axis of 200  $\mu\text{m}$  for tribofilm on steel and Si<sub>3</sub>N<sub>4</sub> and 40  $\mu\text{m}$  for tribofilm on WC to make sure that analysis area was within the wear track. In Chapter 8 wear tracks on steel balls were analysed. In other studies, all analysis was carried out on disc specimens. Samples were positioned at 0-degree emission angle. Base pressure in the main chamber of the spectrometer was  $2 \times 10^{-9}$  mbar. A survey spectrum was acquired in a high-pass energy (200 eV) scanned mode. A narrow scan, used to determine the relative atomic composition, as well as for determination of chemical information, was then acquired in a low-pass energy (20 eV). The charging of the specimen was corrected by referring aliphatic carbon binding energy to 284.8 eV (C 1s signal). The XPS analyses were carried out on the tribofilm surfaces on the discs without any sputtering. When relevant the O 1s peak was curve-fitted to non-bridging bond (NBO) at  $531.2 \pm 0.5$  eV and bridging oxygen (BO) at  $532.6 \pm 0.5$  eV [120,121],

### 4.3.2 Raman Spectroscopy

Raman spectroscopy was performed to examine both the chemical composition of DLC discs and tribofilms formed on steels in Chapter 8. This used a WiTec Confocal Raman spectrometer alpha 300 equipped with multiple objectives and a charge-coupled device detector. A laser with 532 nm wavelength was employed and Raman spectra was collected from a  $20\text{ }\mu\text{m} \times 20\text{ }\mu\text{m}$  area. For DLC-coated discs, the D band and G band peaks attributed to carbon were fitted with Lorentzians and the area ratio of D peak to G peak ( $I_D/I_G$ ) was estimated.

### 4.3.3 Focused Ion Beam (FIB)

To investigate tribofilm crystallinity using transmission electron microscopy (TEM) and element distribution using scanning transmission electron microscopy and energy-dispersive X-ray spectroscopy (STEM-EDX), lamellae of ZDDP tribofilm cross sections were extracted using a Helios 600 NanoLab Focused Ion Beam (FIB) instrument. Before this, the ZDDP tribofilms were coated with a 50–70 nm gold or chromium layer to protect them from damage during Pt deposition and gallium ion milling [161]. Au was used normally but Cr was generally preferred when EDX was to be carried out on the lamellae since the Au peak overlapped with those of Zn and P that were present in ZDDP tribofilms Table 4-3 shows the conditions used in the FIB process. After the specimens were installed in a vacuum chamber, a Pt layer was deposited in an atmosphere of Ga. After bulk-out and U-cut milling processes using Ga ions, lamellae with tribofilm (width 10  $\mu\text{m}$ , depth 7  $\mu\text{m}$ , thickness 100 nm) were lifted out using a tungsten omniprobe. These lamellae were then mounted on copper grids and thinned down and cleaned

Table 4-3 Focused ion beam conditions for ZDDP tribofilm cross section preparation

Step	Acceleration voltage, kV	Beam current, nA
Pt deposition	30	0.46
Bulk-out	30	21
Cleaning of cross section	30	6.5
U-cut	30	6.5
Thinning	30	0.46
Cleaning	2	28

#### **4.3.4 Transmission Electron Microscopy (TEM) and Scanning Transmission Electron Microscopy and Energy-Dispersive X-ray Spectroscopy (STEM-EDX)**

To observe tribofilm crystallinity in these FIB lamellae, TEM images were captured using a TEM (JEOL 2100 F) with 200 kV accelerating voltage. Fast Fourier transform (FFT) of the TEM images was also obtained. Scanning TEM (STEM) was then performed on JEOL-2100 F operated at 200 kV, equipped with an Oxford Instruments energy-dispersive X-ray spectroscopy (EDS) detector to observe the elemental distribution of tribofilms. Elemental maps of tribofilm were collected on the samples tilted to 15° using the Oxford Instruments X-ray System INCA.

#### **4.3.5 Scanning Electron Microscope and Energy-Dispersive X-ray Spectroscopy (SEM-EDX)**

An SEM, HITACHI S-3400N, was used to capture high-resolution images of tribofilm surface topography and for EDX, an Oxford X-ray System, INCA was used to analyse the chemical composition of materials.

### **4.4 Mechanical Characterization of Tribofilm and Material**

The mechanical properties of tribofilms formed on MTM and ETM test specimens were observed using the techniques below.

#### **4.4.1 Atomic Force Microscope (AFM)**

The thickness and topography of tribofilms after MTM and ETM tests were observed using atomic force microscopy (AFM) in Chapter 7. A confocal AFM-Raman alpha300 RA supplied by WiTec was employed for this study. A V-shaped Silicon Nitride AFM cantilever with spring constant 0.2 N/m was used in contact mode. Although tribofilm thickness during MTM and ETM tests is generally measured by spacer layer interferometric method (SLIM) [167,169], AFM was used in this study because of difficulties in obtaining accurate thickness values using SLIM from non-metallic balls of low reflectivity. Dawczyk et al. [149] showed that the maximum tribofilm thickness measured by AFM was similar to the mean the tribofilm thickness measured by SLIM. Therefore, to plausibly compare tribofilm thickness with previous studies that quantify tribofilm thickness by using SLIM, the maximum tribofilm thickness from AFM was used

to describe the tribofilm thickness for this study. To facilitate AFM tribofilm measurements, a method described in [147] was used where one small region of the wear track was selected and strips on both sides of the track were treated with 0.05 M ethylenediaminetetraacetic (EDTA) solution for 60 seconds to remove ZDDP tribofilm from the edges and leave a thin, central strip of tribofilm untouched. This approach is illustrated in Figure 4-2. The strips where the film was removed provide reference substrate planes close to the centre of the track so that the AFM scans were able to encompass both the tribofilm in the central region and the substrate planes on the sides, allowing the thickness of the film to be determined. AFM topography images covered the  $150 \times 150 \mu\text{m}^2$  square spanning the central region of the wear track and the edges of the said strips.

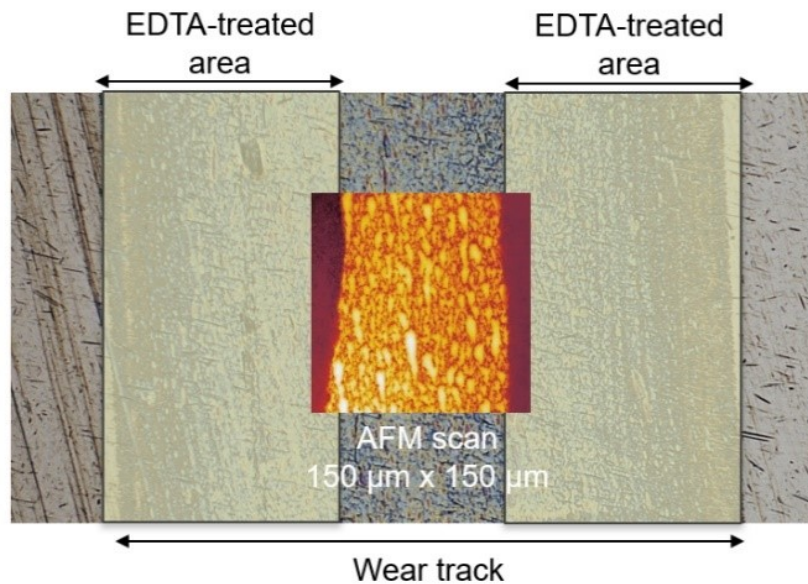


Figure 4-2 Procedure to measure ZDDP tribofilm thickness and morphology using AFM

#### 4.4.2 Optical Microscopy

The morphology of tribofilms after rubbing tests and surface cracks and micropitting on the ball obtained were observed using an optical microscope (HIROX RH 2000).

#### **4.4.3 Stylus Profilometer**

A stylus profilometer (Taylor Hobson Talysurf) was used to obtain roughness profiles of test specimens and the wear depth on the ball. Lower and upper cut-off length was 0.0025 mm and 0.25 mm, respectively.

#### **4.4.4 White Light Interferometry**

Wear tracks on DLC discs were observed by an optical white light interferometer (WLI, WYKO NT 9100) in Chapter 8. Wear depth and wear volume were measured.

#### **4.4.5 Nanoindentation**

To determine the properties of ZDDP tribofilms in Chapter 11, and MTM test specimens in Chapters 6 and 10, a Nano Indenter G 200 with a Berkovich tip manufactured by Keysight Technologies was employed. The mechanical properties of tribofilm vary with depth, so they cannot be properly measured at the point of the initial unload [158]. Therefore, ZDDP tribofilm and surface treated steels were measured in the Continuous Stiffness Measurement (CSM) mode, which allows measurement of the contact stiffness at any point along the loading curve [273]. The elastic modulus at each indentation depth was determined by analyzing the amplitude and phase response. The frequency and displacement amplitude values were 45 Hz and 2 nm, respectively. Surface approach velocity was 10 nm/s. Under a load range of 50 mN, a target depth of 500 nm and a strain rate of  $0.01 \text{ s}^{-1}$ , 25 points at 25  $\mu\text{m}$  intervals inside and outside of the wear track were measured. All surfaces were measured at room temperature.

#### **4.5 Adsorption: Quartz Crystal Microbalance with Dissipation Monitoring (QCM-D)**

A quartz-crystal microbalance with dissipation monitoring (QCM-D, Biolin Scientific) was used to monitor the adsorption of ZDDP from PAO solution on to quartz sensors with various coatings. QCM monitors shifts in frequency ( $\Delta f$ ) and dissipation ( $\Delta D$ ) versus time as the liquid in contact with the sensor is successively changed. An AC voltage is applied to the quartz sensor, causing an oscillation at its fundamental resonance frequency of 5 MHz. Intermittently, the driving voltage is switched off and the oscillation observed to decay exponentially. Dissipation (D) is given by equation 1.

$$D = E_{dissipated} / 2\pi E_{stored} \quad (1)$$

where  $E_{dissipated}$  is the energy dissipated during one oscillation period and  $E_{stored}$  is the total energy stored in the oscillation crystal. The crystal is oscillated at odd overtones ( $n$ : 1-13) of the fundamental frequency. Considering the effect of changing PAO4 to ZDDP solution, which has different viscosity and density from PAO4 (liquid loading), frequency and dissipation data were corrected by using liquid loading shifts,  $\Delta f_{liquid\ loading}$  and  $\Delta D_{liquid\ loading}$  in equations 2 and 3:

$$\Delta f_{liquid\ loading} = -\sqrt{\frac{n}{\pi}} \frac{f_0^{3/2}}{\rho_q v_q} (\sqrt{\rho_l \eta_l} - \sqrt{\rho_s \eta_s}) \quad (2)$$

$$\Delta D_{liquid\ loading} = \frac{1}{\sqrt{n\pi}} \frac{2f_0^{1/2}}{\rho_q v_q} (\sqrt{\rho_l \eta_l} - \sqrt{\rho_s \eta_s}) \quad (3)$$

where  $\rho_q$  is the specific density of quartz,  $v_q$  is the shear wave velocity in quartz,  $\rho_l$  is the density of the liquid containing the adsorbing species,  $\eta_l$  is the viscosity of the liquid containing the adsorbing species,  $\rho_s$  is the density of the solvent and  $\eta_s$  is the viscosity of the solvent [274,275]. The liquid trapping effect was assumed to be zero because of the use of sensors with a smooth surface.

The adsorbed ZDDP mass ( $\Delta m$ ) was calculated from the Sauerbrey equation (equation 4) by using corrected  $\Delta f$  where  $C$  is related to the properties of the quartz crystal since  $\Delta D$  was close to zero and  $\Delta f$  overlapped on each odd overtone. This equation assumes that the adsorbed layer is relatively rigid and the adsorbed layer is uniform over the surface of the crystal.

$$\Delta m = C \Delta f_n / n \quad (4)$$

All QCM-D experiments were conducted in a flow cell at 60 °C, which was the highest temperature available, and the liquid flow rate was 0.12 mL/min. Before the tests, quartz sensors were cleaned by rinsing in toluene and isopropanol, followed by oxygen plasma cleaning for 1 minute in order to ensure that no adsorbents were left on the sensors, and to avoid damage on coated surface [276]. Before flowing ZDDP solutions with PAO4, baselines were monitored in a flow of PAO4. Once these baselines became stable, the

liquid was changed from PAO4 to ZDDP (P: 800 ppm) in PAO4, and then ZDDP solution was flowed for 1.5 hours to allow ZDDP adsorption on coated quartz sensors. Finally, ZDDP solutions were replaced with PAO4, and PAO4 was flowed into the cell until new baselines of frequency became stable. Tests were also run at a faster flow rate, which gave similar results, confirming that ZDDP adsorption was not transport-limited. For the study in Chapter 7, quartz sensors with coating of  $\text{Fe}_2\text{O}_3$ ,  $\text{Si}_3\text{N}_4$ , WC, SiC and carbon were used. For the study in Chapter 10, those with coating of  $\text{Fe}_2\text{O}_3$  and  $\text{Fe}_3\text{O}_4$  were used.



## 5 Crystallinity and Durability of ZDDP Tribofilm

*This chapter describes a study of the durability of pre-formed ZDDP tribofilms and relates this to an evolution of tribofilm structure during rubbing and, in particular, to the conversion of an initial amorphous phosphate structure to one that is nanocrystalline during extended rubbing. Reaction mechanisms of tribofilm crystallinity formation are also suggested. The research described in this chapter has already been published in Tribology Letters with an open access [277].*

### 5.1 Introduction

In chapter 3 it was reported in section 3.1.3 that, while ZDDP tribofilms are normally quite durable and able to withstand prolonged rubbing in base oil where there is no possibility of the film being chemically regrown [88,119,169], some recent work by Parsaeian et al. [119] has indicated that this durability appears to depend on how long it has been rubbed, as was shown in Figure 3-14. Parsaeian et al. found that if ZDDP solution was replaced by base oil after prolonged rubbing, the tribofilm was not significantly removed when rubbing resumed, but if the ZDDP solution was replaced by base oil in the early stages of a test and rubbing continued, some of the tribofilm was removed. Partial tribofilm removal was also observed when the applied load or temperature was increased in the early stages of a test. The authors also used XPS to show that, while durable tribofilm was composed of shorter polyphosphates, the tribofilm that could be partially removed by rubbing in base oil was composed of longer polyphosphates.

Parsaeian et al.'s work suggests that the strength/durability of ZDDP tribofilm correlates with and may depend on its phosphate chain length as the latter changes with rubbing time. It should be noted that many studies have shown that the chain length of zinc polyphosphate reduces with rubbing time [119,127,138,179,226] though a few have proposed precisely the opposite [210,278]. Parsaeian et al.'s work [119] thus suggests that the strength/durability of ZDDP tribofilm may depend on its phosphate chain length and thus change with rubbing time.

One way that phosphate chain length might influence the mechanical properties of as ZDDP tribofilm is by influencing its structure and, in particular, its crystallinity. As stated in Section 3.1.4, most previous research has found or assumed that ZDDP tribofilms consist primarily of an amorphous, glassy structure, perhaps based on the knowledge that

zinc phosphate can form glasses. Such phosphate glasses have been proposed for use in, for example the storage of radioactive waste. However, in a recent study using high-resolution FIB-TEM, it was shown that ZDDP tribofilms may have both nanocrystalline and amorphous structures [161]. Crobu et al. [121] determined the structures of synthesized metaphosphate and orthophosphate using X-Ray Diffraction (XRD) analysis. While pure metaphosphate showed amorphous peak patterns, pure orthophosphate showed crystalline XRD patterns. Thus, it is possible that the increase in durability that occurs when a ZDDP tribofilm experiences prolonged rubbing may result from it converting to a crystalline structure as a consequence of a decrease in polyphosphate chain length. This may also explain the increase in hardness of ZDDP tribofilms observed by Kalin as reported in Section 3.1.2.

The current chapter describes experimental work to test this conjecture. ZDDP tribofilm tests of different duration, similar to those of Parsaeian et al., have been carried out and these have been combined with FIB-TEM analysis of the films to determine their amorphous or crystalline structure and XPS measurements to determine polyphosphate chain length

## **5.2 Test Method**

For this research on the crystallinity and durability of ZDDP tribofilm, experiments were carried out using MTM-SLIM as detailed below.

### **5.2.1 Test Lubricants and Materials**

Solutions of two ZDDPs (ZDDP1 and ZDDP2) in PAO4 were studied. Both were used at a concentration of 0.08 wt% P. MTM-SLIM was employed to observe ZDDP tribofilm growth in tests using tribopairs of AISI 52100 steel ball and disc.

### **5.2.2 Test Procedure and Condition**

ZDDP tribofilm durability was evaluated by measuring the evolution of tribofilm thickness after the replacement of the ZDDP solution by PAO base oil. Most MTM-SLIM tests thus consisted of two stages, stage 1 in which the ball and disc were rubbed in ZDDP solution and stage 2 in which the ball and disc, now having pre-formed ZDDP tribofilms, were rubbed in PAO4. Before this second stage, the ball and discs were removed from the

test rig and rinsed in toluene to remove all ZDDP solution and then three times in PAO4. They were then returned to the rig to be rubbed in PAO4. Table 5-1 lists the invariant conditions used throughout all tests, while Table 5-2 lists the conditions that varied from test to test for all 16 tests carried out. Two test temperatures were studied, 60 °C and 100 °C. At these two temperatures, the calculated to 5 nm and 3 nm of minimum oil film thicknesses were to 5 nm and 3 nm, resulting in lambda ratios of 0.4 and 0.2 respectively. To investigate the tribofilm properties, some rubbed discs were cleaned by toluene in an ultrasonic bath for 10 min followed by analysis (Tests 1, 3, 4, 6, 9, 12 and 14). Test 4 was stopped after 5 min rubbing in stage 2, and tribofilm on the disc was then analysed after cleaning to evaluate the property changes in tribofilm before and after the replacement of ZDDP solution with base oil. The effect of temperature (100 °C and 60 °C) and ZDDP alkyl structure (secondary type and primary type) was studied to understand the mechanism of tribofilm crystallinity formation.

Table 5-1 General MTM test conditions

Mean (entrainment) speed; $U = (U_{ball} + U_{disc})/2$	50 mm/s
Slide-roll-ratio (SRR); $SRR = 100 * (U_{disc} - U_{ball}) / U$	50%
Applied load	31 N (max Hertz pressure 0.95 GPa)
Ball	19.05 mm diameter, AISI 52100, 855 HV, ~0.012 $\mu$ m Ra
Disc	AISI 52100, 825 HV, ~0.010 $\mu$ m Ra

Table 5-2 Specific test conditions

Test #	Stage 1 conditions			tribofilm analysis on the disc	Stage 2 conditions			tribofilm analysis on the disc
	Oil	Temp (°C)	Rubbing time (min.)		Oil	Temp (°C)	Rubbing time (min.)	
1	ZDDP2	100	30	✓	no stage 2			
2	ZDDP2	100	30		PAO4	100	210	
3	ZDDP2	100	60	✓	no stage 2			
4	ZDDP2	100	60		PAO4	100	5	✓
5	ZDDP2	100	60		PAO4	100	180	
6	ZDDP2	100	180	✓	no stage 2			
7	ZDDP2	100	180		PAO4	100	60	
8	ZDDP2	100	240		no stage 2			
9	ZDDP2	60	180	✓	no stage 2			

10	ZDDP2	60	180		PAO4	100	60	
11	ZDDP2	60	240		no stage 2			
12	ZDDP1	100	180	✓	no stage 2			
13	ZDDP1	100	180		PAO4	100	60	
14	ZDDP1	100	360	✓	no stage 2			
15	ZDDP1	100	360		PAO4	100	60	
16	ZDDP1	100	420		no stage 2			

### 5.3 Tribofilm Analysis

To investigate tribofilm crystallinity using TEM, lamellae of ZDDP tribofilm cross sections were extracted using a FIB instrument. Before FIB preparation, ZDDP tribofilms were coated with a 50-70 nm Au or Cr layer to protect them from damage during gallium ion milling. Au was used normally but Cr was preferred when EDX was to be carried out since the Au peak overlapped with those of Zn and P. Chemical properties of ZDDP tribofilms were analysed using XPS.

## 5.4 Results

### 5.4.1 Evolution of ZDDP Tribofilm Durability

Figure 5-1 shows the effect of sliding time on ZDDP2 tribofilm durability at 100 °C. In the case of rubbing for 240 min in ZDDP2 solution (Test 8), tribofilm thickness increased to 170 nm over the first 120 min of rubbing and subsequently remained stable until the end of the test. Tribofilm growth was relatively linear with time and negligible induction period was observed. In the case of replacement of the ZDDP2 solution by PAO4 after 180 minutes rubbing, none of the ZDDP tribofilm was removed (Test 7). However, in the case of replacement of the ZDDP2 solution by PAO4 after only 30 and 60 minutes rubbing, ca. 20 and 40 nm tribofilm, respectively, was removed from the ball after just 5 minutes rubbing in PAO (Tests 2 and 5). These results confirm that ZDDP tribofilms become more durable with rubbing time. All tests were repeated one time, and the film thickness spread is shown in Figure 5-1 and Figure 5-2. To further illustrate repeatability, Figure 5-2 shows the results for Tests 3, 4 and 5, in all of which the test oil was either replaced by PAO after 60 minutes or the test ended at this stage. It is evident that the rate and thickness of tribofilm formation are similar in each test.

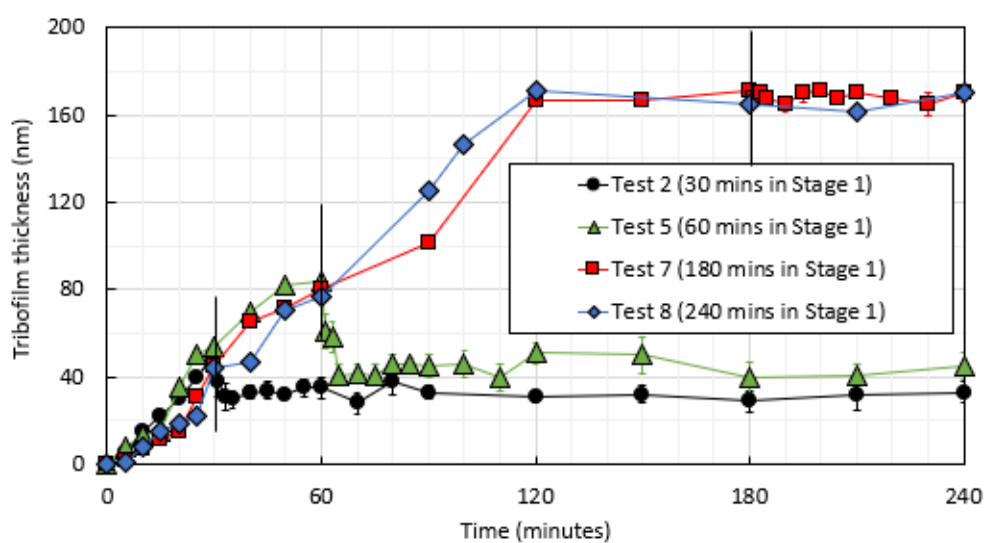


Figure 5-1 ZDDP2 tribofilm evolution and its durability after different Stage 1 rubbing times at 100 °C (Tests 2, 5, 7 and 8)

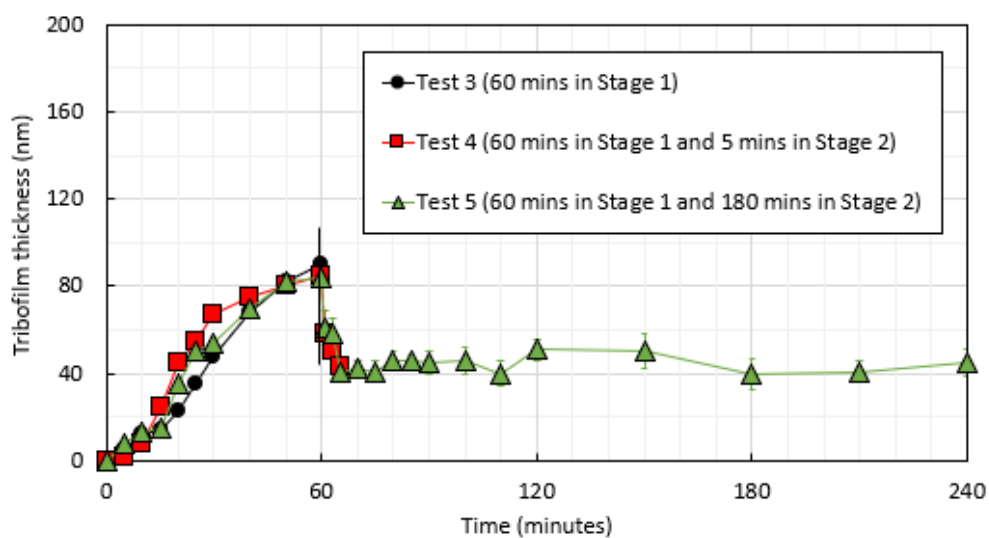


Figure 5-2 ZDDP2 tribofilm evolution and its durability after 60 minutes in Stage 1 and different Stage 2 rubbing times at 100 °C (Tests 3, 4 and 5)

## 5.4.2 ZDDP Tribofilm Crystallinity

### 5.4.2.1 Tribofilm Crystallinity after Rubbing in ZDDP Solution

Figure 5-3 shows cross-sectional TEM images of ZDDP tribofilms after 30, 60 and 180 minutes rubbing in ZDDP2 solution at 100 °C (Tests 1, 3 and 6). FFTs taken from inside the black and white squares in the TEM images are also shown. In these TEM images, the black regions on the top of tribofilm represent the gold coating, while the grey regions on the bottom of tribofilm are the steel substrate. For the thick tribofilms formed after 60 and 180 min, separate TEM images are shown of the lower side (closest to steel) and the upper side of tribofilm. For the thin tribofilm formed after 30 min, just one TEM image is shown, with FFT taken from the lower and upper sides of the tribofilm as indicated.

In all of the lower-side regions closer to the substrate, *i.e.* after 30, 60 and 180 minutes rubbing, lattice fringes are observed; also, FFTs indicate that the tribofilms have periodic structure. These results show the presence of crystalline structures in the lower-side tribofilms. By contrast, the upper-side regions after 30 and 60 minutes rubbing do not show any lattice fringes, suggesting that the tribofilm in these regions consists of amorphous structures. However, after 180 minutes rubbing (Test 6), lattice fringes are observed in the upper-side tribofilm. Figure 5-4 is a close-up image of a region in the upper side of the tribofilm after 180 minutes rubbing extracted from Figure 5-3 to more clearly show the nanocrystallinity. The tribofilm consists of packed crystalline domains of diameter *ca.* 3–5 nm. The d-spacings (distances between planes of atoms giving rise to the diffraction peaks) were calculated from the FFTs to compare with known crystal structures. The main spacings found were 0.289, 0.263 and 0.168 nm. This does not give a clear match to zinc ortho- or pyrophosphate although there is some similarity with zinc oxide. This suggests that the nanocrystals may have mixed composition.

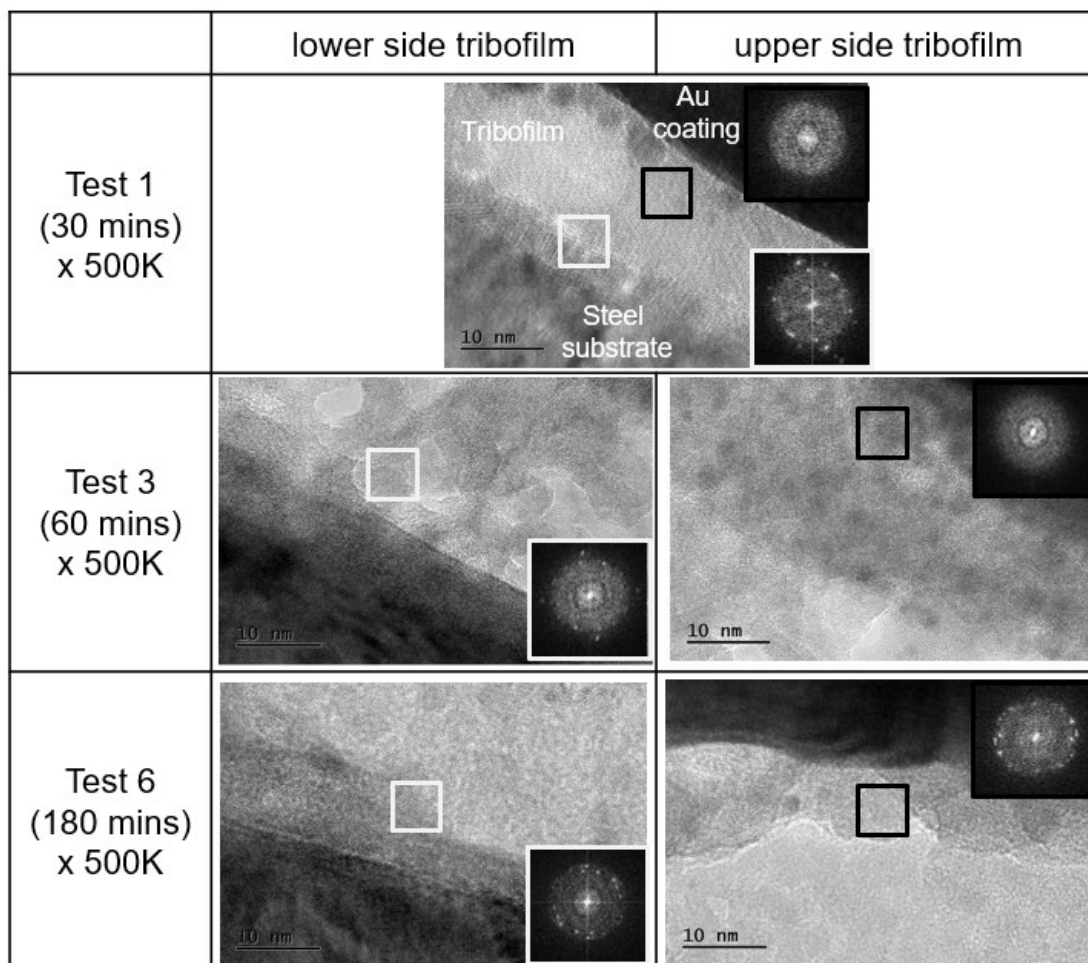


Figure 5-3 TEM images and FFTs of the upper and lower side of tribofilms after 30, 60 and 180 minutes rubbing in ZDDP2 solution (Tests 1, 3 and 6). Steel substrate is the dark gray region at the bottom of these images while the upper black regions are gold layer.

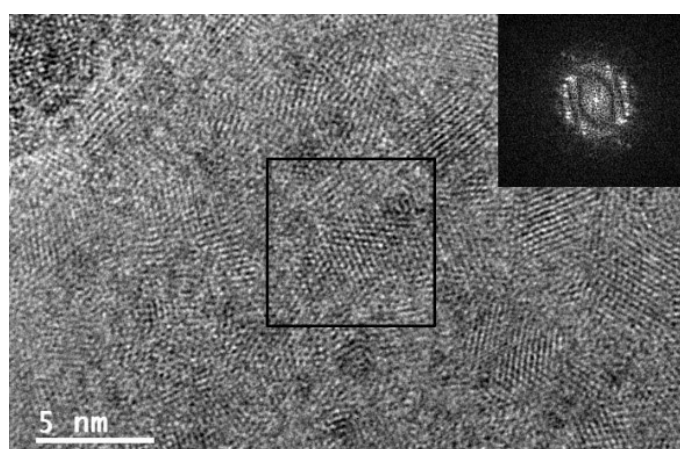


Figure 5-4 Magnified view of crystalline region of ZDDP tribofilm in upper side (Test 6)

#### 5.4.2.2 Tribofilm Crystallinity after Rubbing in PAO

Tribofilm crystallinity before and after the replacement of ZDDP2 solution by PAO was compared to investigate the effect of tribofilm crystallinity on durability. Figure 5-5 shows the cross-sectional TEM images of ZDDP tribofilm after 60 minutes rubbing in ZDDP2 (Test 3) and after 5 minutes of further rubbing in PAO (Test 4). The TEM image of the tribofilm after 60 minutes rubbing was obtained at low magnification (Test 3) to enable the entire tribofilm to be seen. FFTs of three regions, between 0 and 20 nm, 20 and 40 nm, and 40 and 70 nm from the steel substrate, are shown. While the crystalline structures are observed between 0 and 20 nm and 20 and 40 nm from the steel substrate, amorphous structures are confirmed in the uppermost 40–70 nm region. After 5-min rubbing in PAO, the TEM images show that 30 to 40 nm of tribofilm has been removed, which agrees with the SLIM measurement in Figure 5-2. Now all the remaining tribofilm has a crystalline structure, suggesting that the 30 to 40 nm tribofilm removed consisted mainly of amorphous material.

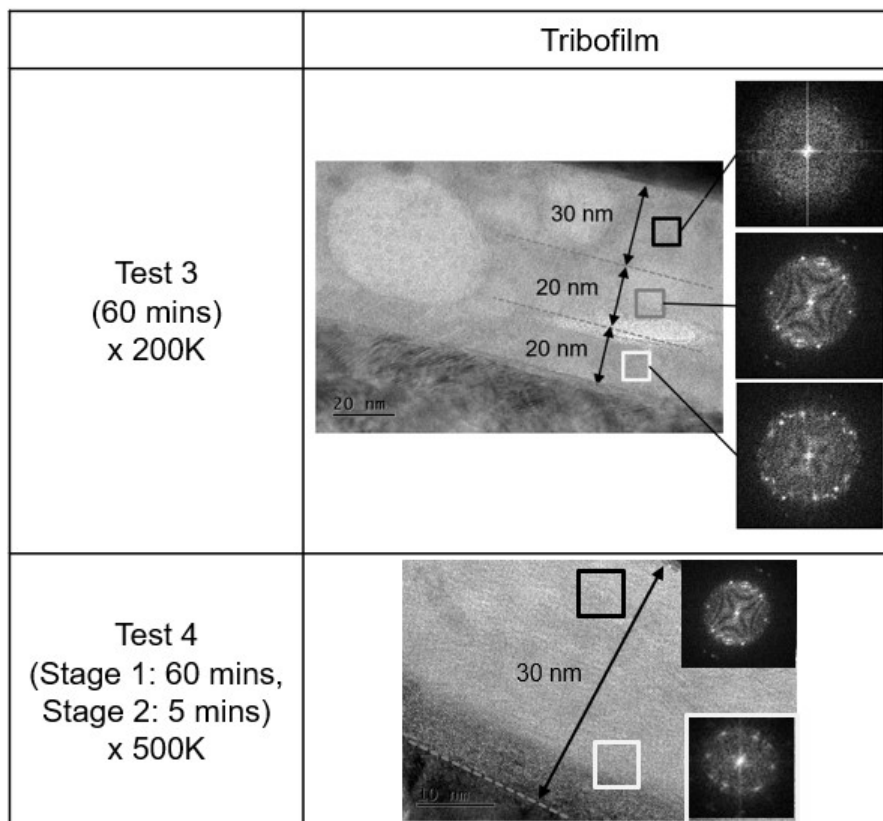


Figure 5-5 TEM images and FFTs of ZDDP tribofilm formed after 60 minutes rubbing in ZDDP2 solution (Test 3) and after additional 5 minutes rubbing in PAO (Test 4)



### 5.4.3 Tribofilm Chemical Structure

Tribofilm on rubbed MTM discs was analysed using XPS to correlate the tribofilm crystallinity and chemical structure. Figure 5-6 shows the O 1s XPS spectra of ZDDP tribofilm in Tests 1, 3, 4 and 6. The ratios of bridging oxygen (BO) to non-bridging oxygen (NBO) were calculated from the O 1s BO bond peak area ( $532.6 \pm 0.5$  eV in the red line) and NBO peak area ( $531.2 \pm 0.5$  eV in the blue line) [120,121]. A higher BO/NBO ratio indicates the longer polyphosphate chains, while a lower BO/NBO ratio indicates shorter polyphosphate chains and orthophosphate. The BO/NBO ratio was 0.56, 0.48 and 0.30 after 30, 60 and 180 minutes rubbing with ZDDP2, respectively (Tests 1, 3 and 6). These BO/NBO ratios suggest that zinc polyphosphate chains convert from longer chains to shorter chains during rubbing. It is important to note that the XPS signals originate almost entirely from within approximately 10 nm of the surface. In addition, the effect on tribofilm chemical structure of rubbing in PAO subsequent to rubbing in a ZDDP2 solution was evaluated (Tests 3 and 4). After rubbing in PAO for 5 min, the BO/NBO ratio decreased from 0.48 to 0.31, suggesting that longer-chain polyphosphates are removed after 5 minutes rubbing in PAO to expose shorter-chain polyphosphates.

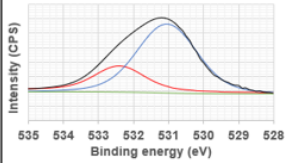
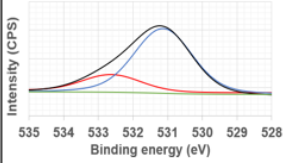
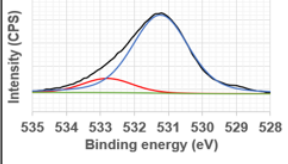
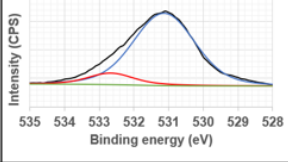
	O 1s Spectra	BO/NBO
Test 1 (30 mins)		0.56
Test 3 (60 mins)		0.48
Test 4 (Stage 1: 60 mins, Stage 2: 5 mins)		0.31
Test 6 (180 mins)		0.30

Figure 5-6 O 1s XPS spectra of ZDDP tribofilm in different rubbing time with the BO/NBO ratio (Tests 1, 3, 4 and 6)

#### 5.4.4 Influence of Temperature and ZDDP Alkyl Structure on Tribofilm Properties

To better understand the mechanism of polyphosphate crystallinity growth, the influencing factors on tribofilm growth and their effects on the evolution of tribofilm properties were evaluated at different temperatures and for different ZDDP alkyl structures.

##### 5.4.4.1 Tribofilm Durability

Figure 5-7 shows the effect of rubbing temperature (100 °C and 60 °C) on ZDDP tribofilm growth and durability. The ZDDP tribofilm grew more slowly at 60 °C than at 100 °C and stabilized at a lower thickness of ca. 60 nm. When the ZDDP2 solution was replaced by PAO after 180 minutes and rubbing continued, some of the ZDDP tribofilm formed at 60 °C was removed (Test 10), unlike that formed at 100 °C (Test 8). These results show that ZDDP tribofilm becomes durable faster at higher temperature.

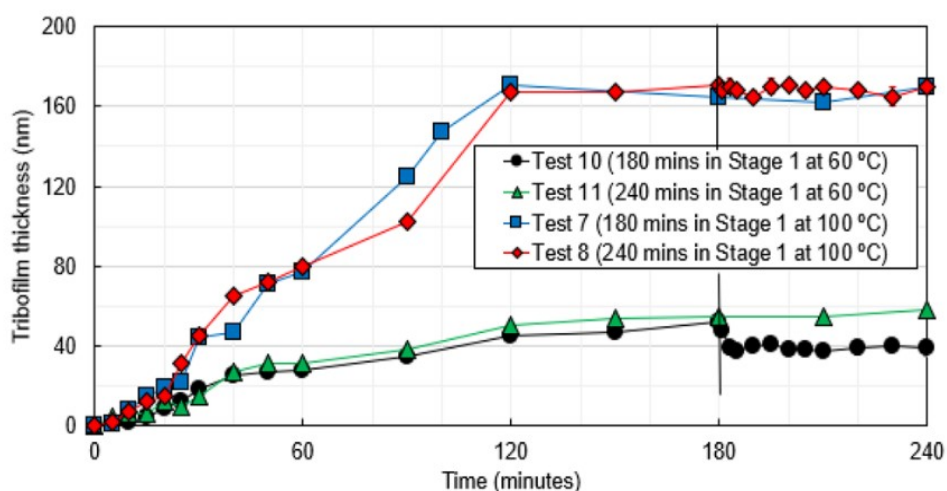


Figure 5-7 ZDDP tribofilm evolution and its durability at 100 °C (Tests 7 and 8) and 60 °C (Tests 10 and 11)

Figure 5-8 shows the effect of ZDDP alkyl structure on tribofilm durability. The tribotests using ZDDP1 were conducted for up to 420 minutes to stabilize tribofilm growth. It is evident that ZDDP1 forms a tribofilm at a slower rate than ZDDP2 although the final tribofilm thickness is very similar. Although ZDDP2 tribofilm is not removed after 180 minutes when rubbed in PAO, 40 nm of ZDDP1 is removed after 180 minutes. In contrast,

when ZDDP1 is replaced with PAO after 360 minutes, tribofilm is not removed. These results show that tribofilm from ZDDP1 needs a longer rubbing time than ZDDP2 to become durable.

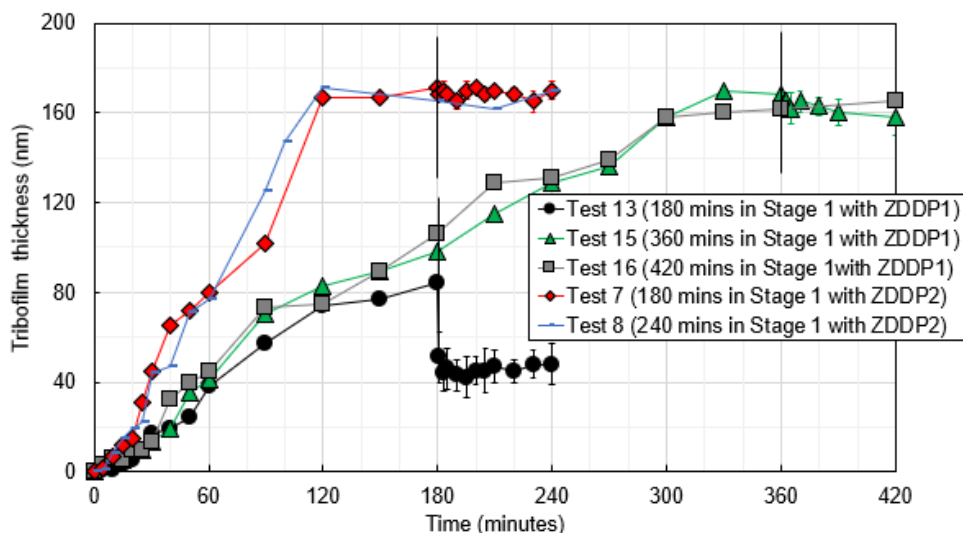


Figure 5-8 The effect of ZDDP alkyl structure on tribofilm durability after different Stage 1 rubbing times (ZDDP1: Tests 13, 15 and 16, ZDDP2: Tests 7 and 8)

#### 5.4.4.2 Tribofilm Crystallinity

Figure 5-9 shows the TEM images of ZDDP tribofilms with FFT after 180 minutes rubbing at 60 °C and 100 °C test with ZDDP2 solution (Tests 6 and 9). TEM images of tribofilms after 180 minutes and 360 minutes rubbing at 100 °C using ZDDP1 solution are also shown (Tests 12 and 14). For each tribofilm, the lower region close to the steel substrate is crystalline-based. However, ZDDP2 tribofilm after 180 minutes at 60 °C shows an amorphous layer in the upper regions, suggesting that crystallinity develops faster as rubbing temperature is increased. In the case of ZDDP1, amorphous layer formed in upper region after 180 minutes rubbing at 100 °C, but crystalline structures are then observed in upper region after 360 minutes. These results suggest that ZDDP2 forms a crystalline structure faster than ZDDP1.

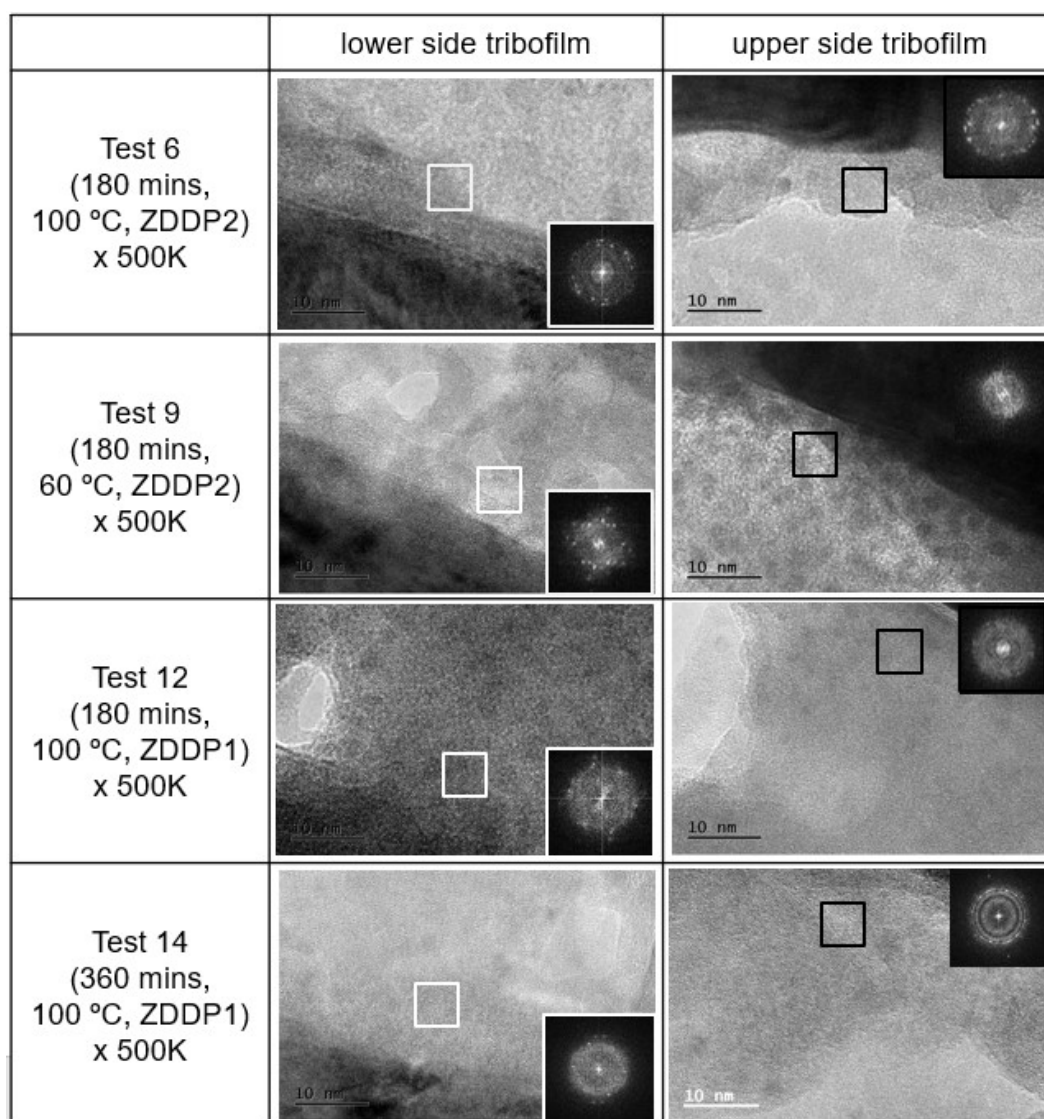


Figure 5-9 TEM images and electron FFTs of ZDDP tribofilm at 60 °C and from primary ZDDP1

#### 5.4.4.3 Tribofilm Polyphosphate Structure

Figure 5-10 shows the XPS O 1s spectra of ZDDP tribofilm after 180 minutes rubbing at 60 °C in ZDDP2 solution (Test 9) and at 100 °C in ZDDP1 solution after 180 minutes and 360 minutes (Tests 12 and 14). Spectra are compared with those from a tribofilm formed at 100 °C from ZDDP1 solution (Test 6). While the BO/NBO ratio after 180 minutes rubbing in ZDDP2 at 100 °C is 0.30, the BO/NBO ratio is 0.57 at 60 °C. This suggests that ZDDP2 tribofilms consist of longer polyphosphate chains after 180 minutes rubbing at 60 °C than at 100 °C. In the case of ZDDP1, polyphosphates are present after

180 minutes rubbing compared to ZDDP2, and tribofilm chain length then shortens after 360 minutes, suggesting that zinc polyphosphate chains from ZDDP1 convert more slowly from longer chains to shorter chains with rubbing time than from ZDDP2.

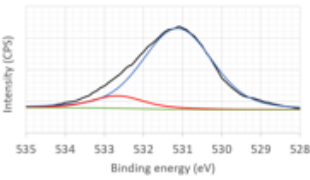
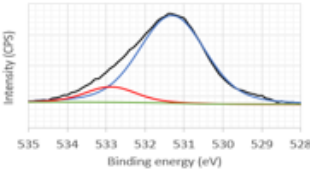
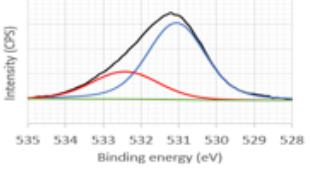
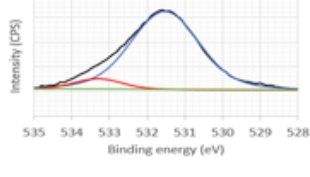
	O 1s Spectra	BO/NBO
Test 6 (180 mins, 100 °C, ZDDP2)		0.30
Test 9 (180 mins, 60 °C, ZDDP2)		0.57
Test 12 (180 mins, 100 °C, ZDDP1)		0.52
Test 14 (360 mins, 100 °C, ZDDP1)		0.31

Figure 5-10 O 1s XPS spectra of ZDDP tribofilm at 60 °C from primary ZDDP1

## 5.5 Discussion

This study provides clear evidence that a ZDDP tribofilm initially has an amorphous, glassy structure but that this converts to a nanocrystalline structure during prolonged rubbing. This conversion to nanocrystallinity begins in the tribofilm material adjacent to the ferrous substrate but later extends throughout the tribofilm. Tests in which an existing tribofilm is rubbed in base oil indicate that the amorphous tribofilm is relatively weak, but that once it converts to a nanocrystalline structure, it is highly durable and able to withstand extended rubbing in a ZDDP-free lubricant. Kalin et al. [178] measured the

evolution of ZDDP tribofilm hardness with rubbing time using a nanoindenter. After 25 minutes rubbing in his test conditions, the hardness of ZDDP tribofilm was 2.4 GPa, whereas after 6 hours rubbing, the hardness reached was 3.3 GPa, *i.e.* ZDDP tribofilm became harder with rubbing. Nanocrystalline structures are known to exhibit higher strength relative to amorphous or macro-crystalline ones since they combine lattice energy with effective obstruction of dislocation movement [279–281]. This evolution of ZDDP tribofilm properties during rubbing may also help explain the finding that ZDDP tribofilms appear to adapt to applied stress by becoming stronger [126,174].

The study also suggests that the evolution of ZDDP tribofilm to a durable, nanocrystalline structure results from a conversion of the molecular structure of the tribofilm from an initially formed polyphosphate to shorter chains and possibly primarily orthophosphate. In confirmation of previous studies, it finds that longer-chain polyphosphates in ZDDP tribofilms are converted to shorter-chain ones during extended rubbing [127,136,282]. A recent study of a ZDDP tribofilm using XANES has suggested that after a 2 hour test at 100 °C the bulk of the tribofilm formed was almost entirely orthophosphate [171]. Crobu et al. [121] synthesized several types of zinc phosphate and found that zinc orthophosphate had a crystalline structure but that metaphosphate, polyphosphate and pyrophosphate were amorphous. When bulk metaphosphate and polyphosphate discs were rubbed against a steel ball counterface, the transferred material contained only short polyphosphates, while the discs also experienced a reduction in polyphosphate chain length. Berkani et al. [110] also studied the behaviour of meta- and orthophosphate in a tribocontact and found that at 120 °C the metaphosphate was converted almost entirely to orthophosphate, while it became primarily pyrophosphate when rubbed against a steel counterface at room temperature.

The sequence of reactions that occurs during the formation of a ZDDP tribofilm is still not entirely understood, but, as outlined in Section 3.2.4 in Chapter 3, after surface adsorption and initial formation of iron disulphide, is believed to follow broadly the scheme indicated in Figure 3-20 [127]. The phosphate is a strong nucleophile, while thionyl is an easy leaving group, so intermolecular reaction between thionyl phosphate species leads to rapid polymerization to form polyphosphate chains. These first two processes are accelerated by both temperature and stress and lead to formation of an amorphous polyphosphate tribofilm. The final stage, which is of particular interest in the current study, is subsequent depolymerization of this amorphous polyphosphate to primarily nanocrystalline orthophosphate.

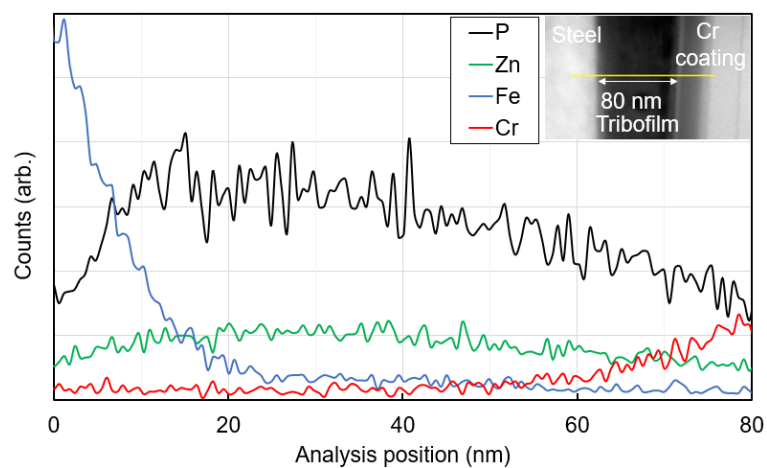
These results suggest that the depolymerization step is driven by prolonged rubbing at elevated temperature and thus by shear and heat. Berkani et al. [110] studied the properties of tribofilms formed by dispersed zinc metaphosphate powder and found that its depolymerization during rubbing was much less at room temperature than at 120 °C, while Crobu et al. [120] showed that the extent of depolymerization of meta- and polyphosphates was greater at higher load than lower load. It has been suggested that applied pressure alone may influence zinc phosphate chain length [283], but Berkani et al. [110] found no significant polymerization of orthophosphate or depolymerization of metaphosphate at high hydrostatic pressure. It is thus much more likely that asymmetric stresses such as shear and tensile stress, which increase proportionately with hydrostatic pressure in rubbing contacts, help drive depolymerization.

Along with heat and stress, depolymerization requires an oxygen-based nucleophile to break a P–O–P into two P–O bonds and provision of a cation to balance the anionic charge generated. The nucleophile is likely to be water and/or oxide ions, while the cation might be Zn or Fe. Martin et al. [179] proposed that zinc polyphosphates reacted with iron(III) oxide in a hard acid/soft base reaction to form shorter-chain phosphates and ZnO, while Heuberger et al. [127] also suggested that Fe ion from the steel substrate was the driving force to depolymerization. They found that while ZDDP thermal film was composed of longer polyphosphate, ZDDP tribofilm was composed of shorter polyphosphate, and XPS analysis showed larger amounts of Fe cations in tribofilm than thermal film, suggesting that Fe was released into the tribofilm during rubbing. Crobu et al. [121] rubbed a steel ball against a bulk zinc metaphosphate disc and found evidence of Fe transferred into the zinc phosphate, accompanied by reduction in the phosphate chain length. Berkani et al. [111] showed that addition of FeOOH to the lubricant promoted rapid depolymerization of tribofilms formed from zinc meta-phosphate powder during rubbing. However, some depolymerization has also been observed in the absence of Fe, in which case water and Zn cations are the most likely participants. Thus, Crobu et al. [121] found that some depolymerization of zinc metaphosphate and polyphosphate occurred when this was rubbed against a glass sphere, though much less than when rubbed against steel. These changes were ascribed to the action of adventitious water, and recently Parsaeian et al. [226] have shown that the deliberate addition of water does reduce the chain length of ZDDP tribofilms.

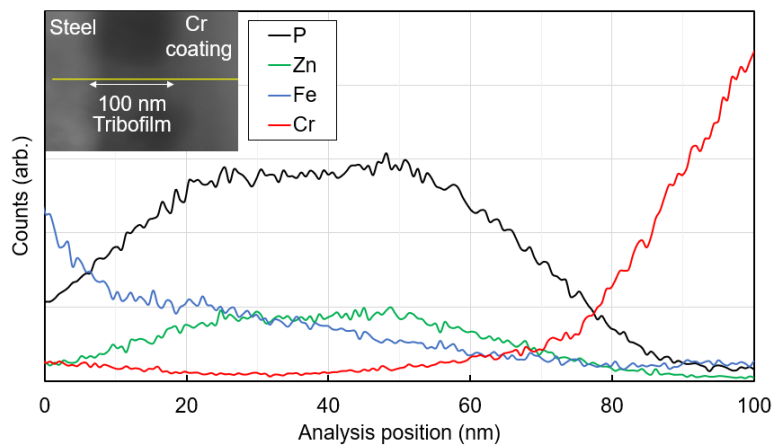
To investigate the effects of Fe cation distribution with rubbing time on depolymerization, element distribution in the cross-sectional tribofilm was analysed using EDX. While a protective Au coating was employed to protect tribofilm surface from Ga ion during the FIB preparation, a protective Cr coating was used prior to FIB for the EDX analysis. This is because EDX peaks of Au overlap with those of Zn and P, but peaks of Cr do not, facilitating more precise analysis. Figure 5-11 shows the EDX line spectra and Fe/P atomic ratio of tribofilm after Test 5 and Test 7. It can be seen that, while Fe cation is only present in the lower and middle regions of the tribofilm after 60-min rubbing, Fe cation is also present in upper tribofilm after 180-min rubbing. These results showed that Fe cations from the steel substrate transfer to tribofilm with rubbing time. This transfer is most likely to be responsible, at least in part, for the depolymerization of polyphosphate and consequent development of crystallinity of the tribofilm. These results agree and support the ion exchange and depolymerization stage in Figure 5-11.

The results for ZDDP1 solution show that the rate of tribofilm is slower for the primary ZDDP than for the secondary one tested, as generally reported in the literature [169]. However, the results also show that the conversion from amorphous to durable nanocrystalline structure is slower for primary than for secondary ZDDP. The faster reaction rate of secondary ZDDPs is generally ascribed to the fact that the C–O bonds in secondary ZDDPs are weaker than in primary ones, facilitating transfer of the alkyl to sulphur, together with the fact that the P–OR and P–SR bonds in, or formed by, secondary ZDDPs are weaker due to the greater stability of the secondary OR and SR anions. This does not explain why the rate of depolymerization is slower for the primary ZDDP tribofilm, as evident in Figure 5-7 since the depolymerization is driven by shear, heat, metal cations and water or oxide, which should be the same for both. It is possible that the primary ZDDP tribofilm retains more alkoxy or thionyl groups attached to the polyphosphate chains than the secondary ZDDP where these groups are lost more easily and that this retards depolymerization compared to the secondary ZDDP2 tribofilm.

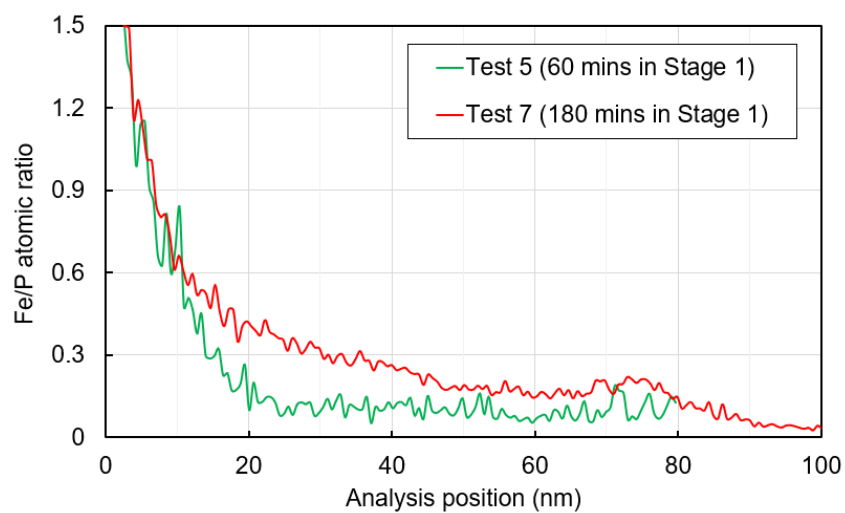




(a)



(b)



(c)

Figure 5-11 EDX line profiles in (a) Tests 5 and (b) 7 and (c) Fe/P atomic ratio of the tribofilm

The discovery that ZDDP tribofilms are initially amorphous and relatively weak and only become mechanically durable after depolymerization and crystallization has several important implications. One concerns research into ZDDP tribofilm kinetics. In the past, because the tribofilms tested after prolonged rubbing appeared to be very durable, it was assumed that there was negligible tribofilm removal during formation [169]. This allowed the rate of tribofilm thickness growth to be equated to the rate of ZDDP reaction, as the starting point for quantifying ZDDP tribofilm models [284]. However, it now appears that measured rates of ZDDP tribofilm growth may actually represent the difference between tribofilm formation and removal during the tribofilm development process. Development of useful kinetic models must thus find experimental ways to quantify each process separately.

The fact that tribofilm formation and removal processes both occur during ZDDP tribofilm growth also has practical implications since in some conditions tribofilm removal rate may exceed tribofilm formation rate. For example, ZDDP concentration should affect tribofilm formation rate but not removal rate, so at very low concentrations it may not be possible for protective ZDDP tribofilms to develop. High wear rates, in excess of those of the ZDDP-free base oil, have indeed been observed at very low ZDDP concentrations [225]. Although it appears that increase in contact pressure increases both tribofilm formation and removal rate [217], this is not likely to be the case at very high loads, where removal rate may well exceed formation rate; if this is the case there may be conditions in which ZDDP becomes no longer effective at reducing wear. Further work at high applied loads is needed to explore this. Finally, if, as seems very likely, Fe ions play an important role in tribofilm depolymerization and thus crystallization, it is likely that in the absence of such ions, tribofilm material might form but be very easily lost by rubbing. This may explain the apparent inability of ZDDP to form stable tribofilms on some DLCs and this will be investigated in Chapter 7 [285].

## **5.6 Conclusions**

The work described in this chapter has shown using the MTM-SLIM tribometer and FIB-TEM, that ZDDP tribofilms undergo a structural transformation during rubbing from a predominantly amorphous structure to one that is nanocrystalline. This occurs due to the depolymerization of initially formed polyphosphate chains to much shorter phosphates, possibly predominantly the orthophosphate, driven by temperature, applied stress and diffusion into the tribofilm of depolymerizing agents including iron cations. Importantly,

this amorphous to nanocrystalline structural transformation results in the tribofilm becoming much stronger and more durable after extended rubbing. The results also show that primary ZDDP tribofilms convert from amorphous to nanocrystalline structure more slowly than those of secondary ZDDP.

## 6 Influence of Steel Surface Composition on ZDDP Tribofilm Growth using Ion Implantation

*This chapter examines the influence of steel surface composition on antiwear tribofilm formation by ion-implanting typical steel alloying elements, Ni, Mo, Cr, V and W, into AISI 52100 bearing steel surfaces. Such implantation changes the chemical composition of the steel surface but has relatively little effect on its mechanical properties or topography. The behaviour of zinc dialkyldithiophosphate (ZDDP) antiwear additive was studied. The study employs a ball on disc tribometer with the ability to monitor tribofilm development and a range of analytical tools including STEM-EDX, XPS and FIB-TEM to analyse the formed tribofilms. The research described in this chapter has already been published in Tribology Letters with an open-access [286].*

### 6.1 Introduction

As described in section 3.2.5, research indicates that steel composition, including the presence of different metallic metals in steels, may play a role in antiwear tribofilm formation. However, research has been limited by the few steel types available in ball form, as needed for most tribotests. One approach to address this might be to examine the formation of ZDDP tribofilms on a range of pure metals. However, a problem that arises is that different metals have very different hardnesses and hardness itself influences tribofilm formation. For example, Gosvami et al. [287] found that sliding promoted strain-hardening of Al with the counterface of  $\text{Al}_2\text{O}_3$  in a ZDDP solution, resulting in ZDDP tribofilm formation on the hardened surface. This makes it difficult to isolate the effect of the relevant metal on ZDDP tribofilm formation. An alternative approach would be to manufacture a range of steels with systematically-varied alloying elements and prepare from these suitable tribological test specimens. Unfortunately, this is currently impractical in terms of cost, especially when ball specimens are needed. The use of specimens with a thin coating of the metal of interest on steel substrate is also problematic as such coatings often cannot survive the contact conditions imposed in typical sliding-rolling tribological tests [288].

A novel approach described in this chapter is to investigate the impact of alloying elements in steel on antiwear performance by using ion implantation to dope surfaces of

steel specimens with a series of different metallic elements. This has the advantage of causing relatively little change in roughness from the original surface and not altering the dimensions of the original sample, although, depending on the implanted element, it may increase the hardness. Another practical advantage is that it can be used as easily on steel balls as on flats, so enabling rolling-sliding tests to be carried out with materials not generally available in ball form.

Ion implantation to steel has been studied and applied quite extensively to control friction, wear and corrosion performance. Ions can be implanted up to a few nm to  $\mu\text{m}$  depending on implantation conditions [289–292]. Most ion implantation research in tribology has studied the effect of implanting non-metallic elements, particularly N, but also C and B, with the aim of improving the physical properties of the rubbing surfaces. While the effect of ion implantation on hardness of surfaces is dependent on the type of ions, non-metallic elements such as N and B are likely to harden surfaces by forming ceramic compounds, for example CrN, or interstitials, resulting in the improvement of wear performance [289,293].

Very few researchers have studied the effect of implanting metal ions on tribofilm formation. Yang et al. [114,294,295] showed that Ni, Mo and Al implantation in pure iron deterred the formation of ZDDP tribofilms. However, ion implantation into pure iron might have caused lattice distortion of iron, which could create residual compressive stresses and hence increase hardness of the near substrate region [296]; this means that both chemical and mechanical properties of the surfaces were potentially changed. More recently, Pagkalis [288] studied the effect of ion implantation of AISI 52100 steel on ashless dithiophosphate additive tribofilm growth, and found that some ashless tribofilms could form faster and reach higher thickness on Ni-implanted steel discs than on unimplanted steel, while Cr-implantation deterred tribofilm growth. Pagkalis did not study the behaviour of ZDDP on ion-implanted surfaces and the effect of chemical composition of steel on ZDDP tribofilm formation is not yet well understood.

The study applies ion implantation in steel to investigate systematically the effect of a series of alloying metals commonly present in steels used in tribological components on ZDDP tribofilm formation and the chemical properties of formed tribofilms. Possible mechanisms by which implanted metals affect ZDDP tribofilm growth are then suggested based on tribofilm analysis using STEM-EDX, XPS and TEM.

## **6.2 Test Materials**

### **6.2.1 Test Lubricants**

In most tests, a solution of ZDDP2 at a concentration of 800 ppm P in a PAO4 base oil was studied. A few tests were performed at ZDDP concentrations of 200, 400 and 1600 ppm as indicated in the relevant figures.

### **6.2.2 MTM Test Specimens**

Standard and ion-implanted AISI 52100 steel discs and balls were studied. The following metals were implanted in steel discs and balls; nickel (Ni), molybdenum (Mo), chromium (Cr), vanadium (V) and tungsten (W). These implanted metals were chosen as they are present in many steels that are widely used for tribological components including case-carburising gear steels, stainless steels, high speed steels and bearing steels, including aerospace grades M50 and M50NiL. A metal vapor vacuum arc (MEVVA) ion source was used to generate ions. Doses of ions were  $3 \times 10^{17}$  ions/cm<sup>2</sup> with an extraction voltage of 45 kV. Implantation was carried out at Beijing Institute of Technology, China.

### **6.2.3 Mechanical Properties of Disc and Ball Specimens**

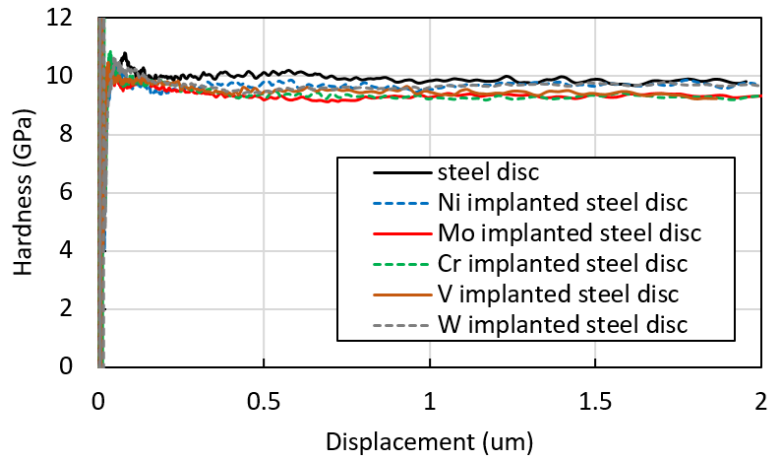
Table 6-1 shows roughness values of the implanted balls and discs measured using a stylus profilometer. Also, shown are two sets of specimen hardness values measured using a standard Vickers indenter and a nano-indenter. In all cases, the values shown in the table are the average of at least four measurements in different locations on each specimen, and tolerances show variation of measurements. Vickers Hardness values were measured using 1 N force, corresponding to approximately 7  $\mu\text{m}$  of indentation depth. Since ion-implanted depth is *ca.* 0.1  $\mu\text{m}$  (see Figure 6-2), these hardness values reflect the hardness of the bulk, implant-free steel.

To determine the effect of ion implantation on hardness close to the surface, and thus relevant to tribological behaviour and tribofilm formation, nano-scale depth profiles of hardness of the ion-implanted steel discs were measured using nanoindentation in CSM method. Details of the test method are given in Section 3.4. Figure 6-1 (a) shows the hardness depth profiles over the 2  $\mu\text{m}$  target depth and Figure 6-1 (b) shows the profile in the enlarged area up to 0.2  $\mu\text{m}$ . Generally, the true mechanical properties of surface-

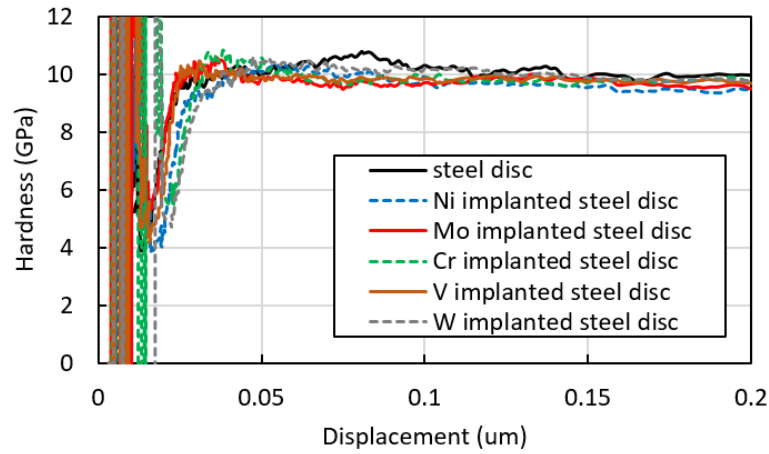
treated materials can only be determined from indentation data originating from the outermost 10% of the surface treatment because of the well-known substrate effect [297]. Since implanted ion penetration depth is about 50 nm as shown in Figure 6-2, hardness values should be obtained in the range of less than 5 nm from the surfaces. Unfortunately, as illustrated in Figure 6-1 (b), hardness profiles below 0.05  $\mu\text{m}$  are unstable due to an indentation size effect. Therefore, the outermost surface hardness of implanted discs could not be measured.

Table 6-1 Measured properties of MTM discs and balls.

Material		Surface roughness Rq (nm)	Vickers hardness (HV)
AISI 52100 steel	disc	$9 \pm 3$	$730 \pm 30$
	ball	$7 \pm 2$	$820 \pm 30$
Ni-implanted	disc	$8 \pm 3$	$750 \pm 25$
	ball	$7 \pm 2$	$810 \pm 30$
Mo-implanted	disc	$10 \pm 3$	$715 \pm 5$
	ball	$8 \pm 3$	$800 \pm 30$
Cr-implanted	disc	$9 \pm 3$	$700 \pm 5$
	ball	$6 \pm 2$	$810 \pm 30$
V-implanted	disc	$7 \pm 2$	$720 \pm 10$
	ball	$8 \pm 3$	$840 \pm 40$
W-implanted	disc	$10 \pm 3$	$740 \pm 20$
	ball	$7 \pm 2$	$830 \pm 30$



(a)



(b)

Figure 6-1 Depth profile of nano-indentation hardness of ion-implanted steels (a) up to 2  $\mu\text{m}$  and (b) up to 0.2  $\mu\text{m}$

#### 6.2.4 Chemical Composition of Disc and Ball Specimens

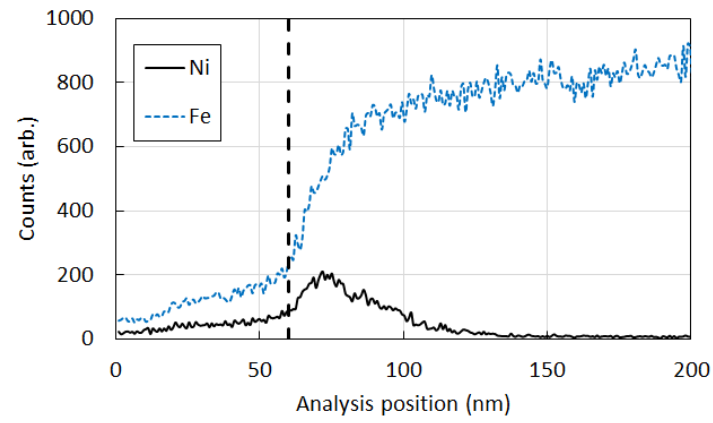
Table 6-2 shows the chemical composition of the specimens measured by SEM-EDX. Ion implantation increased the concentration of implanted ions in the discs and balls by approximately 1.5 atomic % and 1.3 atomic %, respectively. To determine the penetration depth of ions, the depth profile of elemental distribution in the unrubbed Ni-implanted steel disc and the rubbed Mo-implanted steel disc in ZDDP solution were measured using STEM-EDX as shown Figure 6-2. These indicate that implanted metal is distributed within 40-60 nm of the surface, with a maximum implanted metal-iron ratio of about 30%.



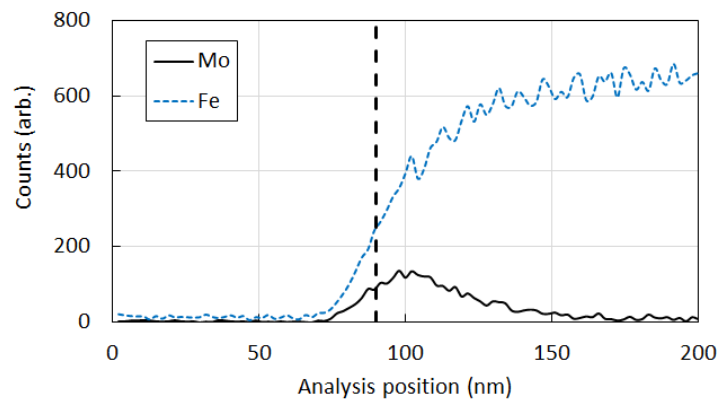
It should be noted that the distributions appear to have a maximum slightly beneath the surface, but this is believed to be an artefact from the finite width resolution of the measurement method due to the size of the X-ray excitation volume in the lamellae [298]. In fact, the maximum implanted metal concentration is believed to be at or very close to the surface, with a roughly exponential decay into the bulk. To determine the chemical state of ions at the surface, Ni-, Mo-, Cr-, V-, W-implanted discs were analysed by XPS as shown Figure 6-3. From the peak areas, Ni, Mo, Cr, V, and W on steel discs are mainly present as metal and the oxides NiO, MoO<sub>3</sub>, Cr<sub>2</sub>O<sub>3</sub>, V<sub>2</sub>O<sub>5</sub>, and WO<sub>3</sub> respectively [299–303]. Table 6-3 lists the surface compositions based on XPS and indicates that the ratio of implanted metal ions to iron at the surface was between 10 and 30%. This is consistent with the maximum ratios shown in Figure 6-2.

Table 6-2 Measured chemical composition of MTM discs and balls (atomic %)

Material		Fe	Mn	Si	Cr	Ni	Mo	V	W
AISI 52100 steel	disc	96.4	0.7	0.8	2.1				
	ball	96.4	0.6	1.1	1.9				
Ni-implanted	disc	95.1	0.6	0.8	2.0	1.5			
	ball	95.4	0.7	1.0	1.7	1.2			
Mo-implanted	disc	95.3	0.7	0.8	1.6		1.6		
	ball	95.5	0.7	1.0	1.5		1.3		
Cr-implanted	disc	95.0	0.7	0.8	3.5				
	ball	95.0	0.8	1.0	3.2				
V-implanted	disc	94.6	0.8	0.9	2.2			1.5	
	ball	94.7	0.8	1.1	2.1			1.3	
W-implanted	disc	94.7	0.7	1.2	1.9				1.5
	ball	95.0	0.7	1.1	1.9				1.3

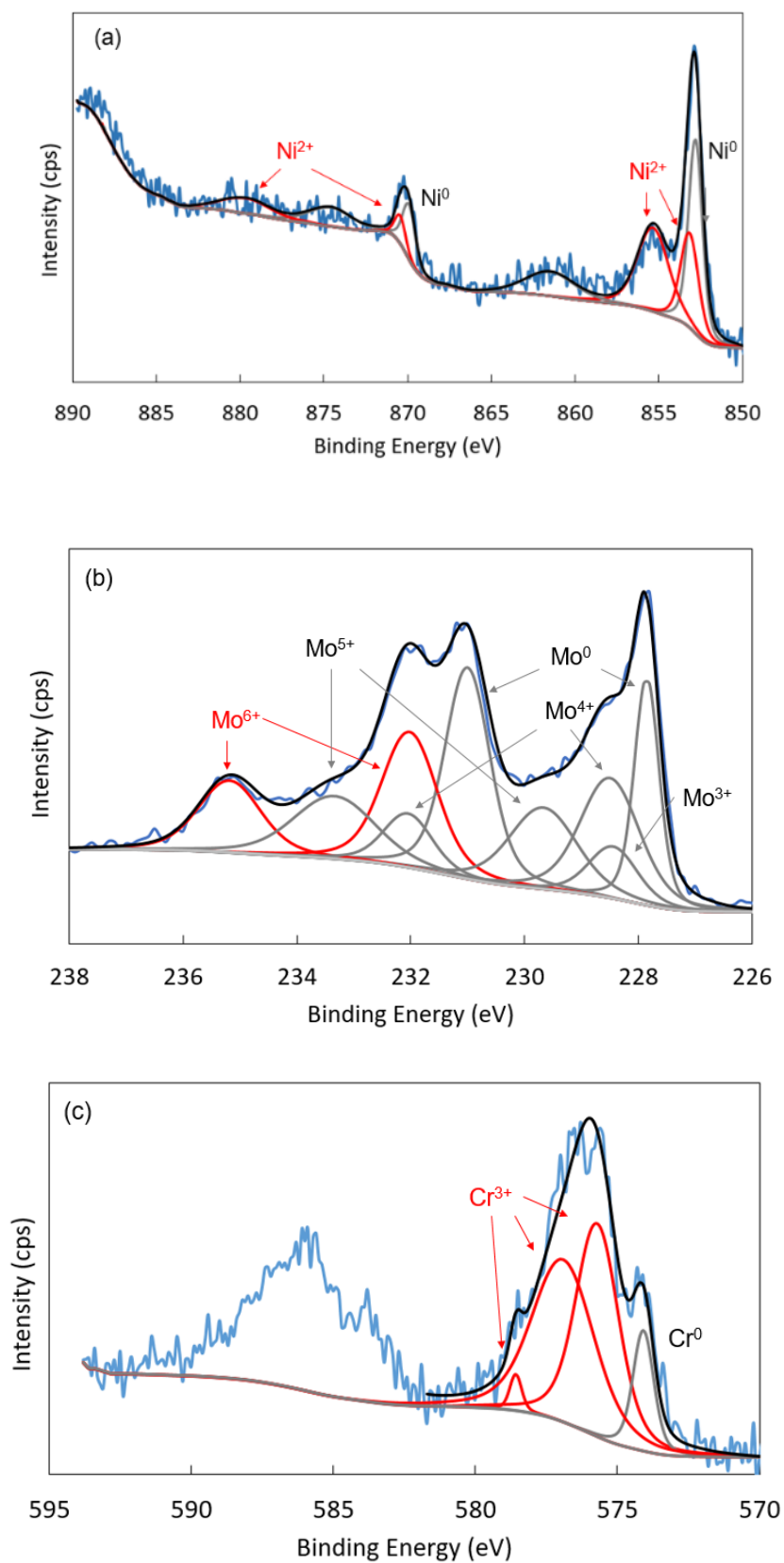


(a)



(b)

Figure 6-2 STEM-EDX analysis of a cross section of (a) an unrubbed Ni-implanted disc and (b) rubbed Mo-implanted disc in ZDDP solution. Approximate position of each surface is marked with a dashed line.



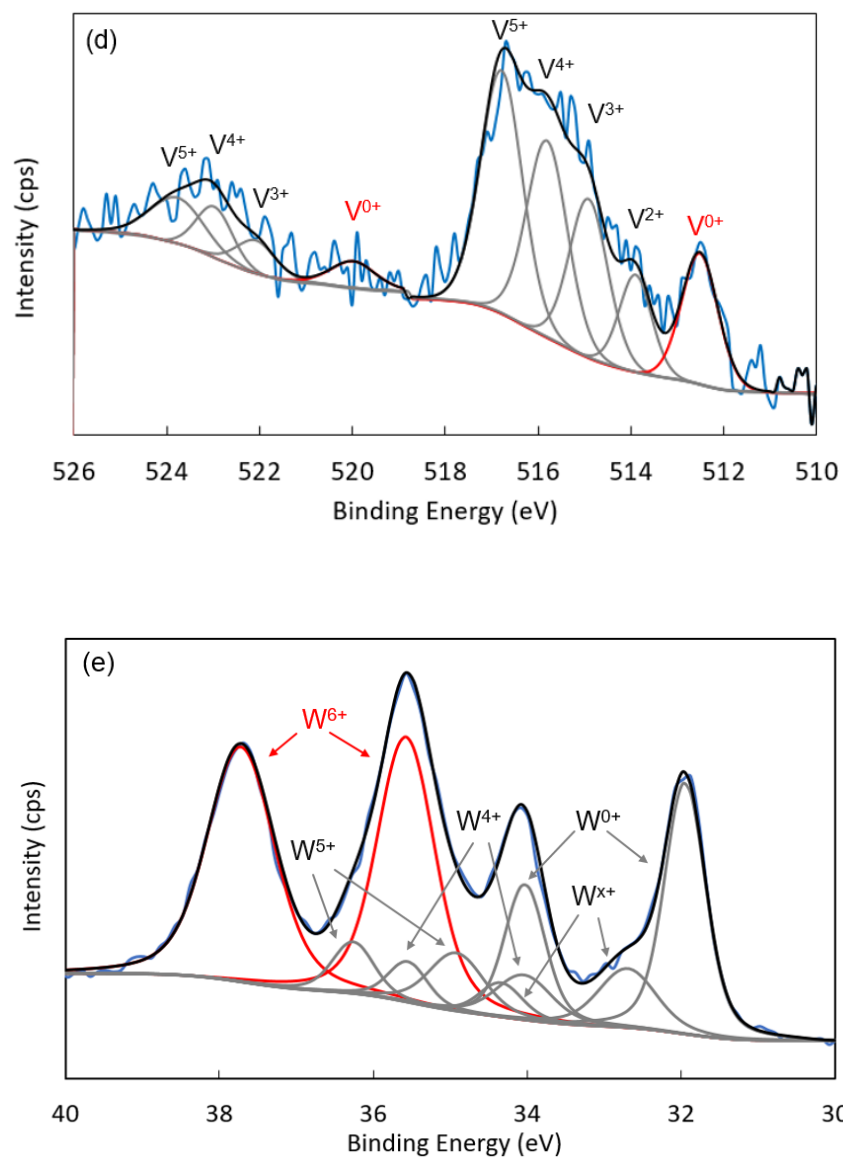


Figure 6-3 Example XPS spectra of (a) Ni-, (b) Mo-, (c) Cr-, (d) V-, (e) W-implanted disc

Table 6-3 Chemical composition of MTM discs using XPS (atomic %)

Atomic %	Cr- implanted	Mo- implanted	Ni- implanted	V- implanted	W- implanted
C 1s	45.17	33.83	40.97	39.76	38.46
N 1s	1.97		2.01		
O 1s	41.7	48.22	44.67	47.06	41.5
Fe 2p	9.06	13.72	10.21	11.67	16.8
Ni 2p			2.14		
Mo 3d		4.23			
Cr 2p	2.10				
V 2p				1.51	
W 4f					3.24
Implant : Fe ratio	0.23	0.31	0.21	0.13	0.19

### 6.3 Test Methods

#### 6.3.1 MTM Test Rig

MTM-SLIM was employed to observe ZDDP tribofilm growth.

#### 6.3.2 Test Conditions and Procedures

The contact conditions used in the MTM-SLIM tests are shown in Table 6-4. Under these conditions, the minimum oil film thickness was calculated to be 3 nm, resulting in a lambda ratio (ratio of EHD film thickness to composite surface roughness) of 0.2, *i.e.* rubbing conditions in the boundary lubrication regime. The development of ZDDP tribofilm on balls was monitored by SLIM measurements performed at set intervals throughout the 4-hour test.

Table 6-4 MTM test conditions

Mean (entrainment) speed; $U = (U_{ball} + U_{disc})/2$	35 mm/s
Slide-roll-ratio (SRR); $SRR = 100 * (U_{disc} - U_{ball}) / U$	100%
Applied load	34.6 N (max Hertz pressure 1.0 GPa)
Temperature	80 °C
Rubbing time	4 hours

---

Lambda (minimum EHD film thickness / composite Rq roughness)	0.2
--	-----

---

### 6.3.3 Tribofilm Analysis

At the end of the 4-hour rubbing test, tribofilms on the discs were analysed using XPS, TEM and STEM-EDX. Before analysis, discs were lightly rinsed in toluene without any wiping, to remove supernatant liquid but avoid removing tribofilm from the surfaces.

## 6.4 Results

### 6.4.1 Effect of Ion Implantation on Tribofilm Formation

Figure 6-4 shows the evolution of ZDDP tribofilm thickness on the original and ion-implanted steel balls over 4 hours rubbing time, determined using SLIM. Tribofilms on unimplanted steel gradually grew to approximately 150 nm over the first 3 hours and then remained stable at this thickness for the remaining hour. Interestingly, implanted Ni ions considerably promoted tribofilm growth, with tribofilm in this case reaching 150 nm after only 1 hour of rubbing, and then stabilizing. By contrast, implanted Mo and Cr ions deterred tribofilm growth; tribofilms grew much more slowly and reached only about 50 nm at the end of the 4-hour tests. W implantation did not significantly affect ZDDP tribofilm growth while V implantation slowed it slightly. These results suggest that the chemical composition of steel can have a significant influence on ZDDP tribofilm growth. The observed impact of implanted metals on ZDDP tribofilm growth broadly agrees with a previous study using an ester-functionalised ashless dithiophosphate additive, except for the behaviour of Mo-implanted steel [288].

Figure 6-5 shows optical micrographs of tribofilms on the discs and balls after 4 hours rubbing. While ZDDP tribofilms were formed on all specimens, the absence of blue interference colours on Mo- and Cr-implanted steels indicates thinner films in these cases in line with the above SLIM measurements on balls.

Figure 6-6 shows how MTM friction coefficient *versus* entrainment speed evolves with rubbing time on steel, Ni- and Cr-implanted steels. The two characteristic features of friction behaviour with ZDDP tribofilm growth can be seen; (i) a shift of the mixed lubrication region of the friction curves to higher entrainment speed, and (ii) an increase in slow speed boundary friction. For a steel/steel tribopair, friction coefficient increases

predominantly in the mixed lubrication regime up to 60 minutes rubbing, and then slightly decreases. On Ni-implanted steel, friction coefficient initially increases rapidly across the whole range of lubrication regimes to reach a maximum value after 30 minutes rubbing. After 30 minutes rubbing, friction coefficient then decreases to the end of the test. By contrast, with Cr-implanted steel tribopairs, friction coefficient slightly increases, mainly in the mixed lubrication regime, up to 60 minutes rubbing, followed by a relatively stable friction coefficient over the whole range of speeds. Recently, Dawczyk et al. [149] proved that the increase in MTM friction in mixed lubrication condition originates from the increase in effective roughness of the rubbing surfaces due to the formation of ZDDP tribofilms. Generally, the trends in increasing friction coefficient followed the tribofilm growth shown in Figure 6-4. However, unlike with steel and Cr-implanted steel, tribofilms on Ni-implanted steel might be partially smoothed during rubbing, resulting in the reduction of friction coefficient after 60 minutes rubbing.

Figure 6-7 shows surface profiles of four implanted discs at the end of rubbing tests obtained using a Talysurf stylus profilometer. Profiles are shown before and after EDTA treatment since it is well known that EDTA treatment removes ZDDP tribofilm from surfaces [159]. The results show that there was negligible wear occur of the implanted discs after rubbing. This suggests that implanted metals were present on the surfaces and thus available to affect ZDDP tribofilm formation throughout the tests.

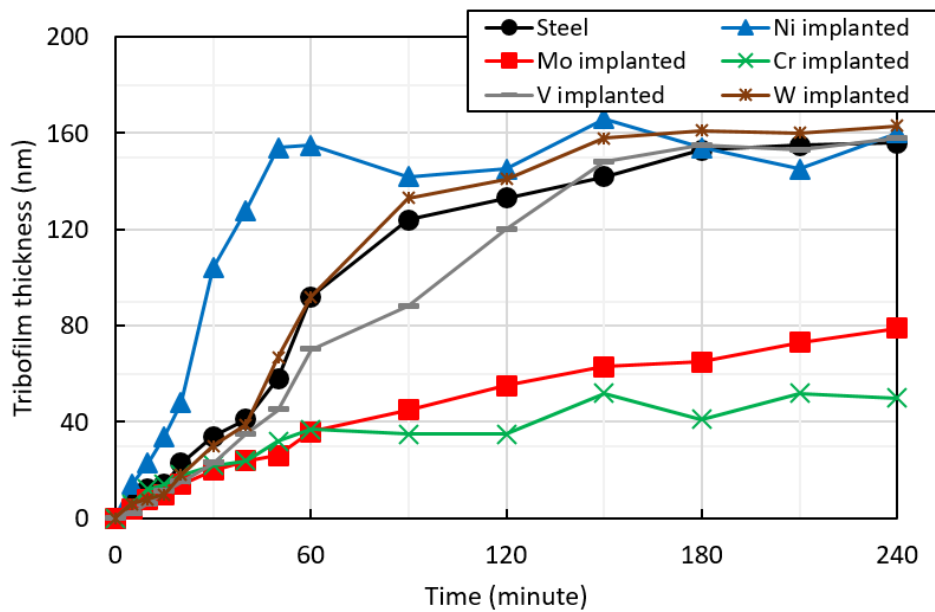


Figure 6-4 The evolution of ZDDP tribofilm thickness on the original unimplanted and ion-implanted steel balls during rubbing.

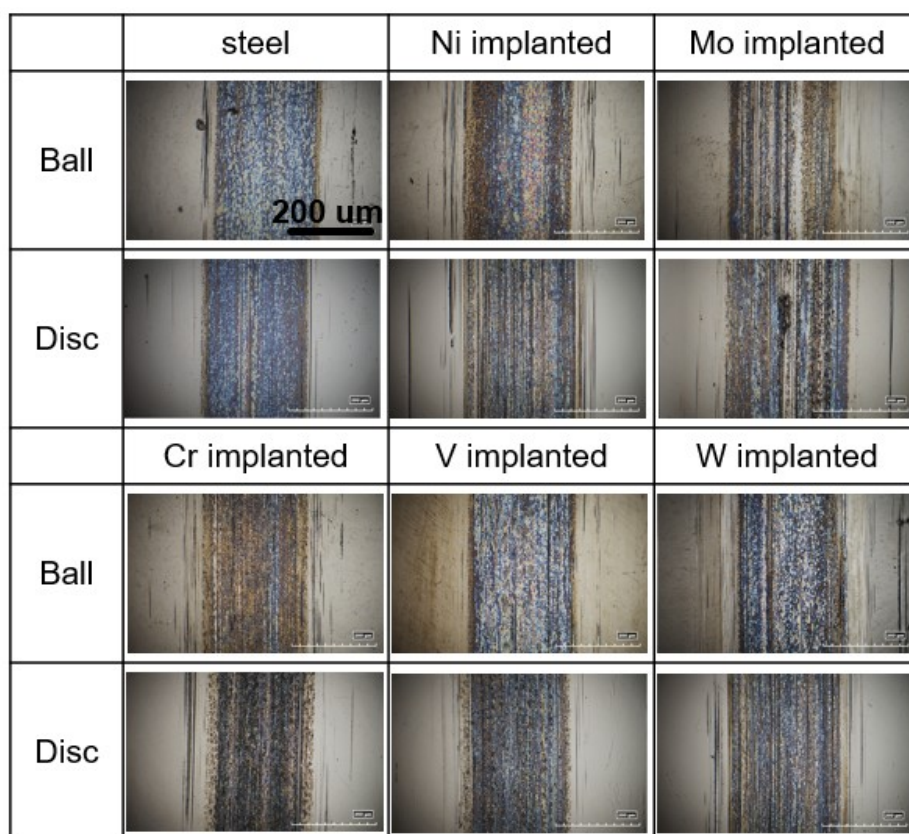
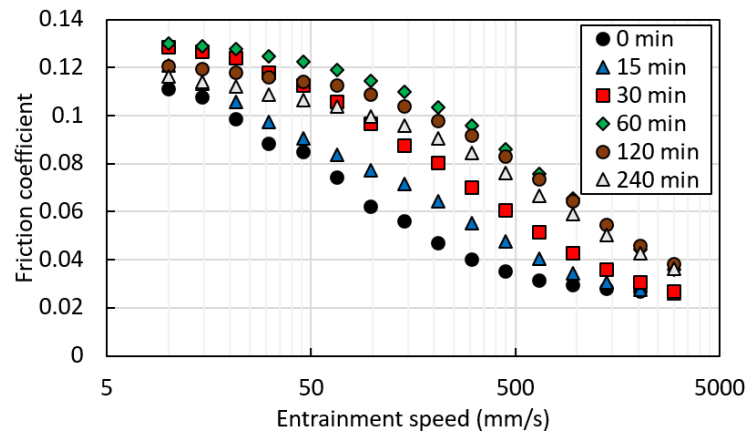
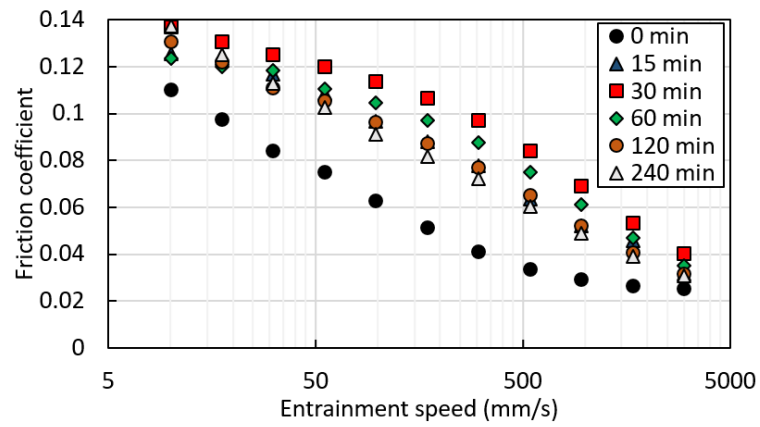


Figure 6-5 Optical micrographs of ZDDP tribofilm on the MTM balls and discs after 4 hours rubbing. The scale bar shown in upper left image is applicable to all images.

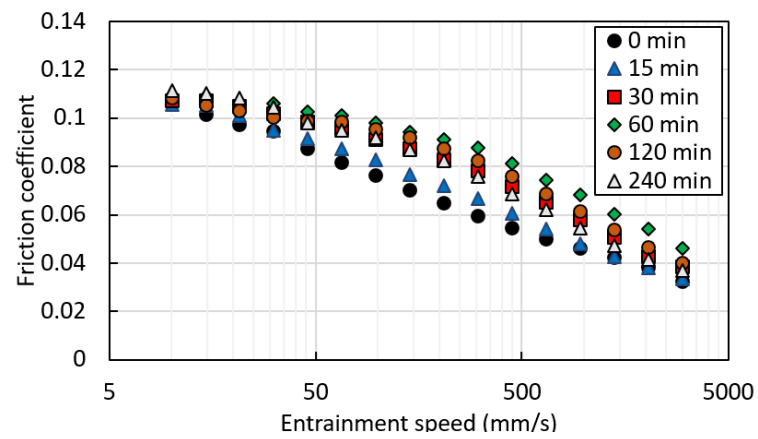




(a)



(b)



(c)

Figure 6-6 Evolution of MTM friction coefficient versus entrainment speed curves during 4 hours rubbing on (a) original 52100 steel, (b) Ni-implanted steel and (c) Cr-implanted steel

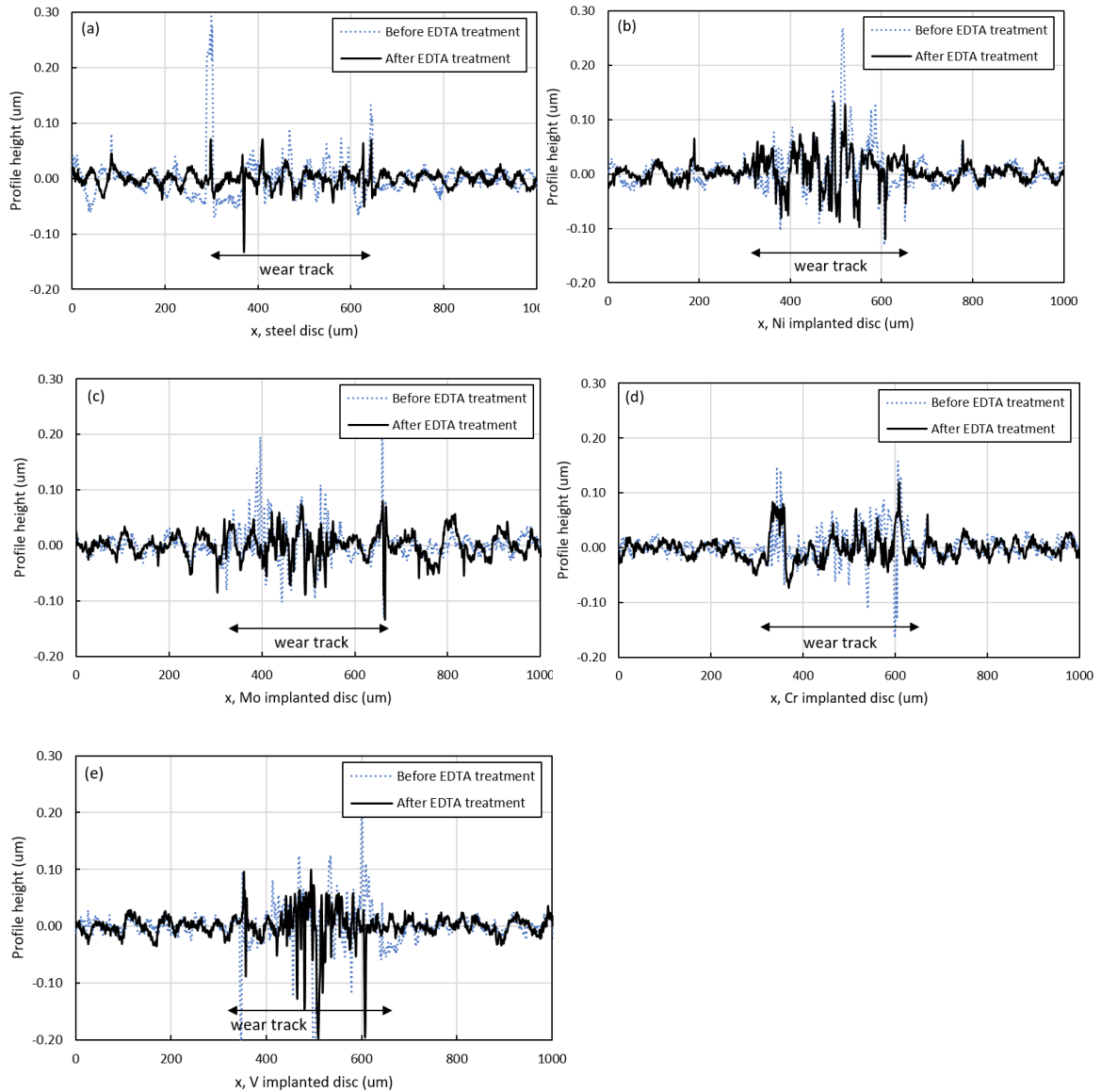


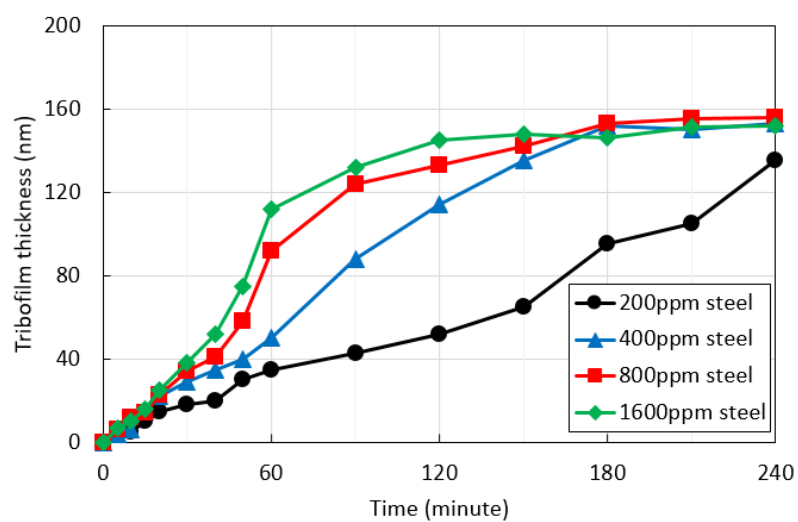
Figure 6-7 Surface profiles after rubbing of (a) steel disc, (b) Ni implanted disc, (c) Mo-implanted disc, (d) Cr implanted disc and (e) V implanted disc

#### 6.4.2 Effect of ZDDP Concentration on Tribofilm Formation

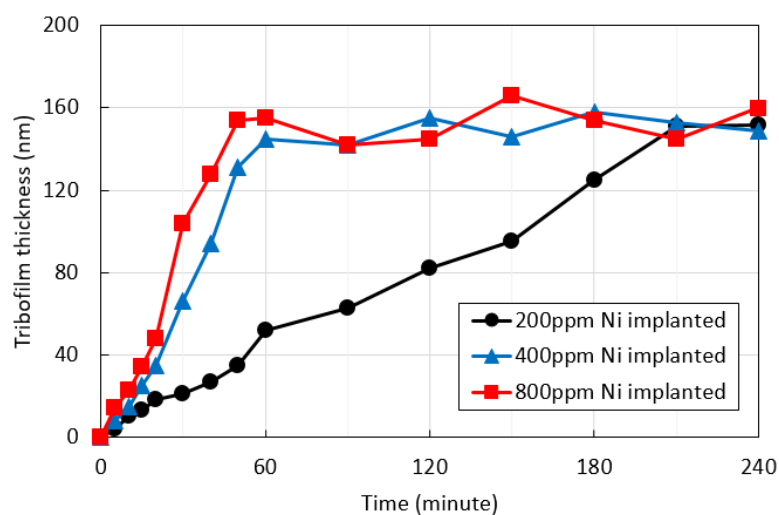
To examine the ability of ZDDP to adsorb on ion-implanted steels, the effect of varying ZDDP concentration on tribofilm formation on (a) steel, (b) Ni-, (c) Mo-, and (d) Cr-implanted steels was studied. Results are shown in Figure 6-8. On 52100 steel, tribofilm formation rate increases with P concentration from 200 ppm to 800 ppm, with 135 nm and 155 nm maximum tribofilm thickness, respectively, after 4 hours rubbing. However,

1600 ppm of P forms a tribofilm at a similar rate and to a similar thickness as 800 ppm P. This saturation of tribofilm growth with increased ZDDP concentration was previously observed by Fujita et al. [169]. On Ni-implanted steel, while tribofilm forms faster at 400 ppm P than at 200 ppm P, behaviour at 800 ppm P is similar to that at 400 ppm P. On Mo- and Cr-implanted steels, tribofilms grew faster and thicker as P concentration increased from 800 ppm to 1600 ppm.

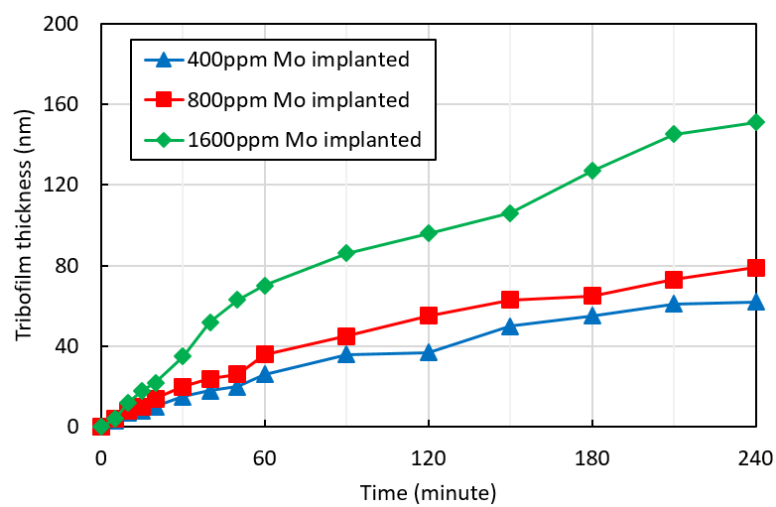
These results show that the concentration of ZDDP above which tribofilm formation saturates varies with the presence of different elements in the surface, being no more than 800 ppm P for unimplanted steel, 400 ppm P for Ni-implanted steel, and greater than 1600 ppm P with Mo- and Cr-implanted steels. This suggests that ZDDP may adsorb most easily on Ni-implanted steel, and least easily on Mo- and Cr-implanted steels.



(a)



(b)



(c)

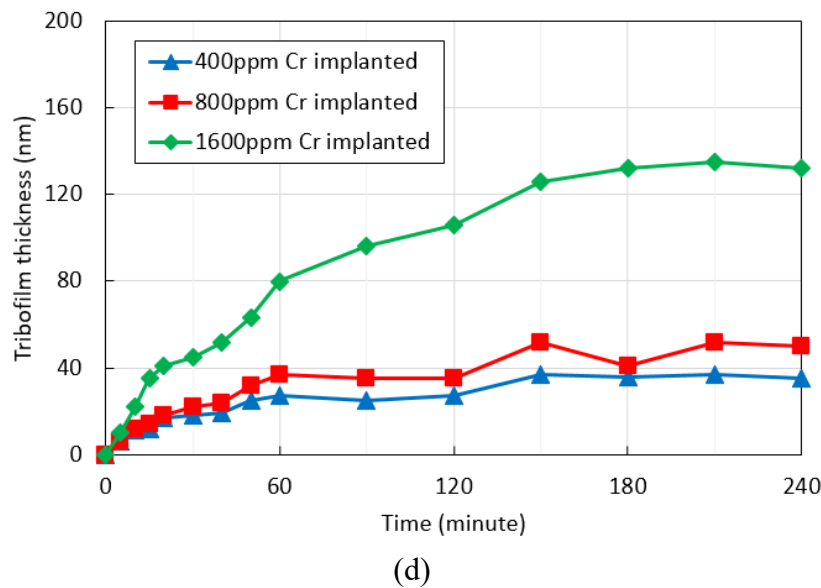


Figure 6-8 The effect of ZDDP concentration on tribofilm thickness on (a) original 52100 steel, (b) Ni-implanted steel (c) Mo-implanted steel and (d) Cr-implanted steel (Note that values quoted in the legend are ppm of P)

### 6.4.3 Chemical Analysis of Tribofilms

To understand the effect of ion implantation on ZDDP tribofilm properties, the tribofilms on steel, Ni-, Mo- and Cr-implanted steels were analysed using a range of analytical techniques.

### 6.4.4 Elemental Distribution in Tribofilms (STEM-EDX)

Cross-sections of tribofilms on Ni- and Mo-implanted discs were analysed using STEM-EDX. Tribofilms on Cr-implanted discs were not analysed because of EDX peak overlap between Cr in the steel disc and implanted Cr. Figure 6-9 shows the EDX line spectra of tribofilms on Ni- and Mo-implanted steels after 4 hours rubbing tests. The peak intensity was adjusted by scaling to the same phosphorus peak intensity to easily compare the ratio of other elements to phosphorus. Although the tribofilm thickness on Ni-implanted disc as shown in Figure 6-4 was about 160 nm, *ca.* 80 nm of thickness is observed in the STEM image. It is well known that ZDDP tribofilms have a patchy structure [33], and this discrepancy is probably because the FIB lamella was lifted out from a region with thin tribofilm thickness, such as the edge of a pad structure. Also it has been reported that different techniques give varied thickness values and that SLIM measures a thickness close to the maximum value present [171]. Note that the vertical dashed lines in the figure

show only approximate extent of the tribofilm since the exact boundaries are difficult to ascertain in the EDX spectra. Zn and P were detected in both tribofilms, suggesting the formation of zinc phosphates. The peak of Fe was present in the tribofilm near the steel substrate, and this decreased towards the tribofilm surfaces. This suggests that Fe was transferred into tribofilms from steel substrates. The peaks of implanted Ni and Mo were clearly detected in both substrates while within the tribofilm, they only appear to be present in the immediate vicinity of the tribofilm-substrate interface and at relatively low concentrations.

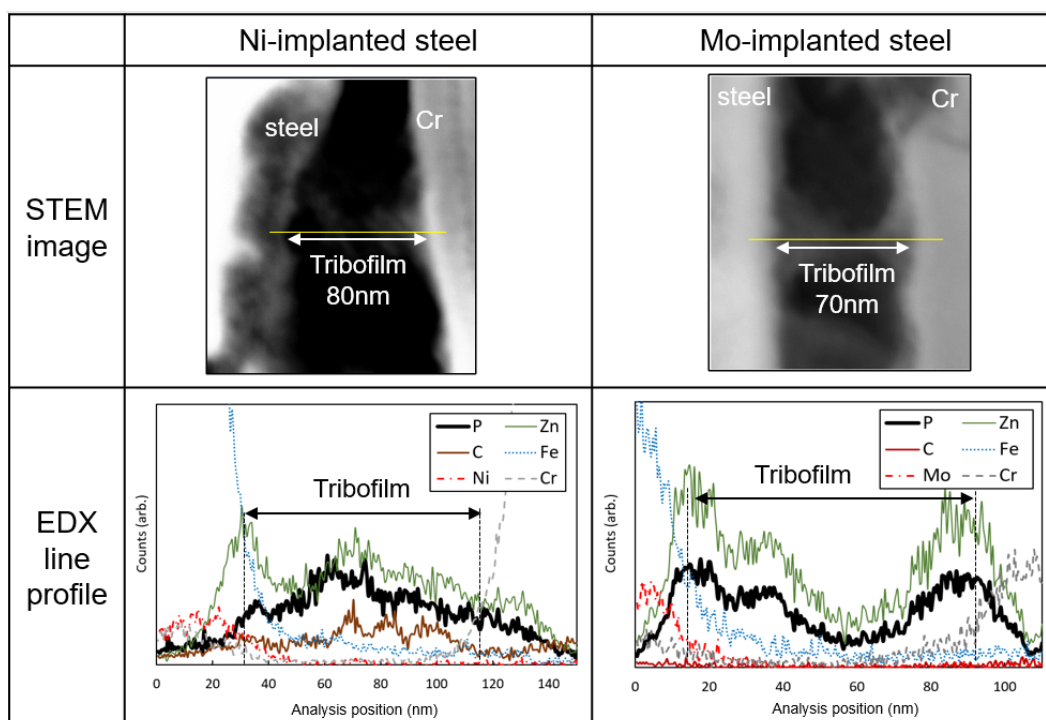


Figure 6-9 STEM images and EDX line profiles of the tribofilms on Ni- and Mo-implanted steels

#### 6.4.5 Chemical Bonds in Tribofilms (XPS)

The chemical environment of oxygen in the tribofilm surfaces was analysed using XPS. Figure 6-10 shows the O 1s XPS spectra of tribofilms on Ni-, Mo- and Cr-implanted steels after 4 hours rubbing. All spectra were normalized to their maximum peaks to aid comparison. BO and NBO ratio was determined as described in chapters 4 and 5 and this ratio was the same for the tribofilms on each substrate, *i.e.* 0.38, 0.33, 0.31 and 0.33 on steel, Ni-, Mo- and Cr-implanted steels, respectively. Given that XPS signals generally originate from within *ca.* 10 nm of the surface, these results suggest that in all four cases

the outermost regions of the tribofilms consisted of short chain phosphates such as orthophosphate.

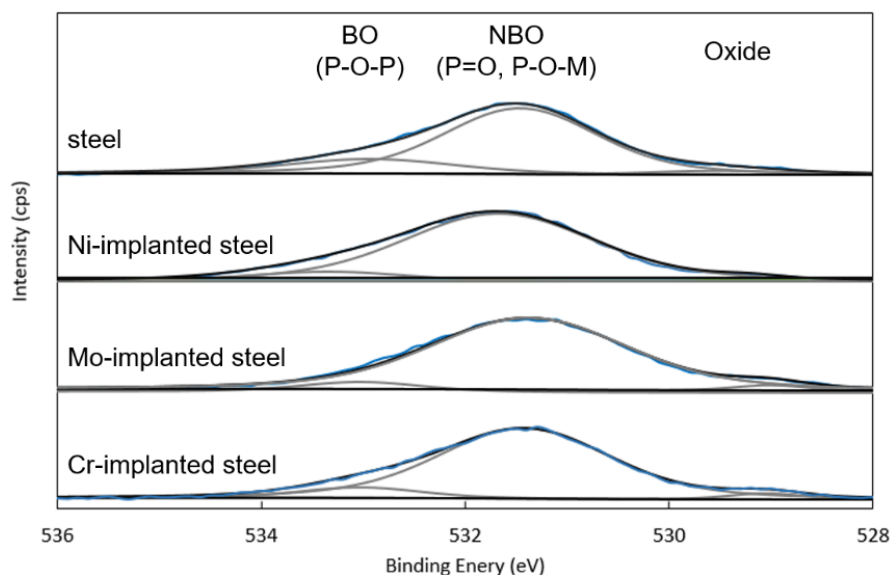


Figure 6-10 O 1s XPS spectra of ZDDP tribofilms on Ni-, Mo- and Cr-implanted steels

#### 6.4.6 Crystallinity of Tribofilms (TEM)

The nanocrystallisation of phosphate structure was investigated using TEM. Figure 6-11 shows TEM images of cross sections of ZDDP tribofilms on Ni- and Mo-implanted steels after 4 hours rubbing, together with FFT images captured from a white square. Given the lattice fringes and FFT spots, both tribofilms were crystalline both near the substrate and close to the surface. These results suggest that the ZDDP tribofilms formed on these specimens are nanocrystalline throughout. This is similar to behaviour on non-implanted bearing steel, as described in the previous chapter.

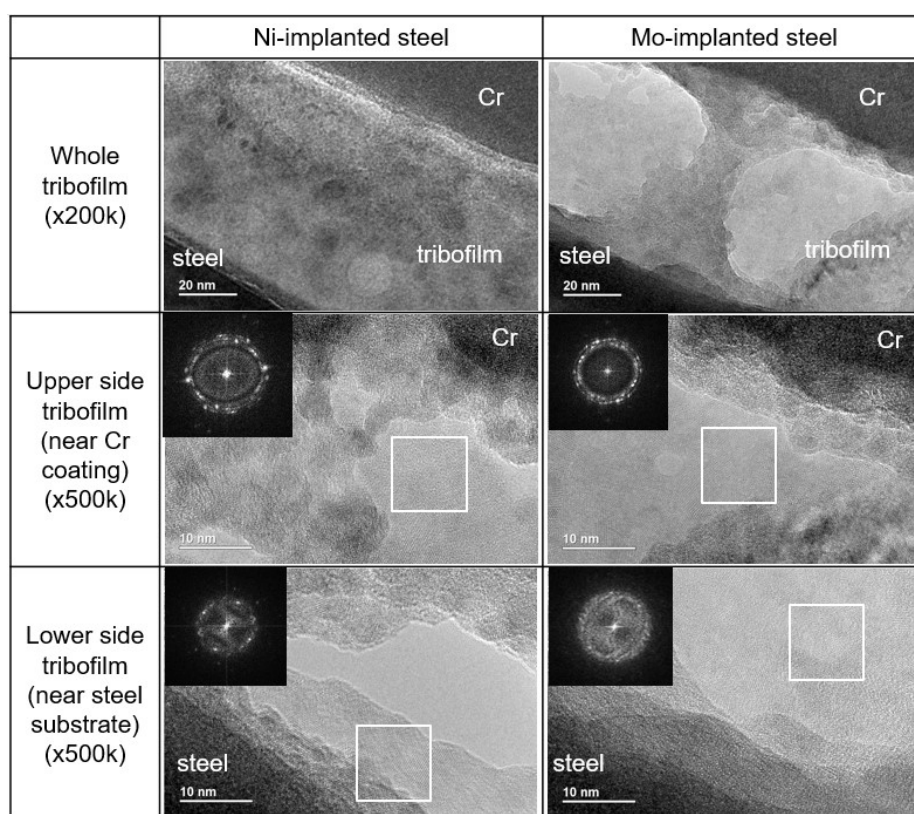


Figure 6-11 TEM images and FFTs of ZDDP tribofilms on Ni-and Mo-implanted steels

## 6.5 Discussion

The results presented here indicate that the ion implantation of relatively low concentrations of selected transition metals into standard, through-hardened bearing steel can considerably affect ZDDP tribofilm formation. In particular, implantation of Ni greatly increases the rate of ZDDP tribofilm growth, while Mo and Cr reduce the rate of growth and thickness of film formed. These effects were observed at implanted element concentration levels similar to those present in many ferrous-based engineering alloys. Unfortunately, the effect of ion implantation on the hardness of the near-surface could not be measured. However, negligible wear occurred on any implanted disc after rubbing, as shown in Figure 6-7. Also, friction evolution shown in Figure 6-6 is mainly affected by ZDDP tribofilm formation. These suggest that any effect of hardness from implanted ions on tribological performance is unlikely to be significant and that the differences in tribofilm film formation are most likely to be due to the differences of surface chemical composition resulting from implantation; *i.e.* ZDDP tribofilm formation is dependent on surface chemical composition. It is therefore of interest to consider how ion implantation might influence each of the main chemical stages of ZDDP tribofilm formation. These

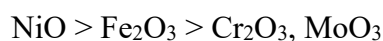


stages are (i) adsorption of ZDDP molecules; (ii) polymerization to polyphosphate; (iii) depolymerization to phosphate [67].

### 6.5.1 Surface Adsorption

Diffusion to and adsorption of ZDDP molecules or moieties derived from ZDDP onto the surface must be the first stage of tribofilm formation on a rubbing surface. While the presence of Fe is not needed for the growth of ZDDP tribofilm [287], Yamaguchi et al. [192] showed that ZDDP molecules adsorb on Al via the sulphur atom of the P=S bond, suggesting Al can play an important role in promoting tribofilm formation on steel by acting as an adsorption site for ZDDP molecules. As the ZDDP concentration was found to control tribofilm formation rate to a different extent between unimplanted steel and Ni-, Mo- and Cr-implanted steels in this study, it is probable that the implanted ions affected ZDDP adsorption behaviour. It is quite likely that some metals, but not all, can act as strong adsorption sites in a similar fashion to Fe in steel. Given the results in Figure 6-4, Ni ions may promote ZDDP adsorption more than Cr and Mo. Dacre et al. [196] studied ZDDP adsorption on steel surfaces containing different Cr concentrations and found that Cr deterred ZDDP adsorption. The authors suggested that the presence of Cr on a surface may decrease the reactivity of surfaces. It is possible that Mo ions may behave in a similar way to Cr ions in decreasing the adsorption of ZDDP.

One factor that may control ZDDP adsorption is the ionicity of the surface. Phillips [304], Gao et al. [305] and Lenglet [306] have discussed the order of the ionicity of chemical bonds in crystals. Ionicity ( $f_i$ ) is given by:  $f_i = 1 - E_h^2 / E_g^2$ , where  $E_g$  is the average energy gap and  $E_h$  is covalent or homopolar gap of crystal. Jones et al. [307] showed that ZDDP adsorbed well on iron oxide and cast iron, but relatively poorly on pure iron, suggesting that ZDDP may adsorb more easily on metal oxides. The order of estimated ionicity of metal oxides in this study may be listed as follows, based on a study by Lenglet [306]:



In the case of Mo,  $\text{MoO}_3$  was selected because the strongest XPS peak was  $\text{Mo}^{6+}$ . This follows the observed trend in the tribofilm growth rates in Figure 6-4. Therefore, it is likely that a surface with high ionicity may provide a polar surface with high surface energy, resulting in the increase of adsorption of polar ZDDP molecules.

### 6.5.2 Polymerization and Depolymerization

After adsorption, an intermolecular reaction between dialkyldithiophosphate (or dithioalkylphosphate) species is believed to lead to rapid polymerization to form long chain polyphosphates, followed by slower depolymerization of the long chain polyphosphates to short chain phosphates by loss of thioalkyl or alkoxy groups [34, 42]. This depolymerization increases anionic charge in phosphates which is balanced by cations such as Zn cations in ZDDP or Fe cations which may diffuse into the tribofilm from the steel substrate, resulting in the formation of iron phosphates [116]. In principle, the implanted metal ions of this study might also diffuse into the tribofilm and participate in depolymerization from polyphosphate to phosphate. However, although this mechanism may play a role in ZDDP film formation in this study, its relative significance is not entirely clear from the present results: STEM-EDX analysis only detected relatively low concentrations of Mo and Ni ions in the lower regions of the tribofilm, near the steel substrate, but not throughout the tribofilm despite the fact that almost full depolymerization of the films occurred.

It is of interest to compare the findings of this study with other work that looked at the effect of ion implantation of metals on tribofilm formation. Yang et al. [114,294,295] studied the effect of implantation of Ni, Mo and Al ions into pure Fe on friction and wear. In the absence of ZDDP they found that less wear occurred on the implanted specimens in base oil than on pure Fe and suggested that ion implantation might increase surface residual compressive stress and microhardness, resulting in less wear. They also found that all three implanted metals deterred the formation of an antiwear tribofilm by ZDDP, as measured by surface S and Zn content after rubbing. It should be noted that their study used pure sliding, reciprocating contact at room temperature at relatively low load and found very little P on the rubbed surfaces, suggesting that either the temperature or, because of the low hardness of pure iron, the contact pressure, was too low for polyphosphate tribofilm formation.

Pagkalis explored the influence of ion implantation of metals into AISI 52100 bearing steel on tribofilm formation with acid and ester based ashless S/P antiwear additives [288], and found that the influence of specific ions may be even greater on the formation of ashless tribofilms than on the ZDDP films shown here. He employed MTM-SLIM under very similar conditions to the current work, the main differences being the use of a PAO/ester base oil blend to ensure full solubility of the ashless additive studied, and much

longer test times. His results show both similarities to and differences from the current study. As in the current work, implantation of Cr reduced ashless tribofilm formation while Ni implantation resulted in very rapid film growth with ester based ashless additive. However, Pagkalis found that Mo-implantation resulted in an increase in film thickness with ashless additives, while in the current study it was detrimental to ZDDP tribofilm formation. Unlike for ZDDP that contains Zn, with ashless additives the formation of a thick tribofilm requires the generation of metal cations from the surface to form a phosphate, so differences between implantation metals may reflect, at least in part, differences in their release from the rubbing surfaces rather, as in the current study, differences in adsorption behaviour.

Overall, the observations discussed here suggest that ZDDP tribofilm thickness and growth rate vary with the chemical composition of the steel substrate and in particular, the metal ions present. This has practical implications in optimizing both lubricant formulation and the chemical compositions of rubbing materials to control antiwear behaviour of a given mechanical component.

## **6.6 Conclusions**

ZDDP tribofilm formation on Ni, Mo, Cr, V and W ion-implanted AISI 52100 bearing steel has been studied using an MTM ball on disc tribometer with post-test tribofilm analysis using STEM-EDX, XPS and TEM. Key conclusions are as follows:

- The implantation of different metal ions into steel surfaces results in variations in the rate of ZDDP tribofilm growth; Ni ions promote tribofilm growth whereas Mo and Cr ions deter tribofilm growth. The implantation of V and W ions does not significantly affect ZDDP tribofilm formation.
- The rate of tribofilm growth on steel, Ni-, Mo- and Cr-implanted steels varies with ZDDP concentration up to a critical concentration above which there is no further change. This critical, saturating concentration depends on the type of metal ion implanted and, for the ZDDP studied here, is no more than 800 ppm P for unimplanted AISI 52100 steel, 400 ppm P for Ni-implanted steel and more than 1600 ppm for Cr- and Mo-implanted steels. This suggests that the observed

variation in ZDDP tribofilm formation with different implanted ions may originate from differences in surface reactivity, and thus the ease of adsorption of ZDDP on the surfaces, resulting from different ion implantation.

- Fe was clearly detected in the ZDDP tribofilms using STEM-EDX analysis. Possible presence of Ni and Mo in relatively small concentrations was detected near the substrate-tribofilm interface but not higher up in the respective tribofilms. Therefore, their potential role in depolymerization stage of tribofilm formation is not entirely clear in the present results.
- XPS analysis showed that tribofilms near the outermost surface on steel, Ni-, Mo- and Cr-implanted steels mainly consisted of short chain phosphates and orthophosphates. TEM of FIB-extracted lamellae also showed that the tribofilms on Ni- and Mo-implanted steels were predominantly nanocrystalline throughout their thickness.
- The fact that alloying metals in steels affect tribofilm formation has practical implications for optimizing lubricants and the composition of substrate surfaces to protect components from wear.

## 7 ZDDP Tribofilm Formation on Non-metallic Surfaces

*This chapter describes a comparison of ZDDP tribofilm formation on ferrous and non-ferrous rubbing materials, namely steel,  $\text{Si}_3\text{N}_4$ , WC, SiC and a-C:H DLC coating. The chemical properties of tribofilms are discussed and a possible mechanism by which ZDDP forms tribofilm on non-metallic surfaces is suggested. The research described in this chapter has already been published in Tribology Online with an open access [308].*

### 7.1 Introduction

As described in 3.2.6, there is growing interest in the use of non-metallic materials as tribological components, both in the form of bulk materials and as coatings, and some research has studied the behaviour of ZDDP on such materials. However almost all studies on the behaviour of ZDDP with such surfaces have been conducted using a non-metallic-on-ferrous tribopair. These studies have reported the presence of tribofilms on various rubbed, non-metallic surfaces including Al-Si alloy,  $\text{Si}_3\text{N}_4$ , SiC,  $\text{ZrO}_2$  and DLC coatings [151,309–313] and researchers have generally suggested that these tribofilms have been transferred from the ferrous counterface during rubbing. This possible transfer of tribofilm or of ferrous or ferric ions from ferrous surfaces, although of practical relevance, makes it difficult to understand the reaction mechanism of tribofilm formation on non-metallic surfaces.

A few authors have investigated ZDDP tribofilm formation on non-metallic/non-metallic tribopairs including DLC/DLC [314–317], DLC/Si [216],  $\text{Si}_3\text{N}_4/\text{Si}_3\text{N}_4$  [318],  $\text{Al}_2\text{O}_3/\text{Al}_2\text{O}_3$  [73] and Al/ $\text{Al}_2\text{O}_3$  [287]. In most of these studies, although tribofilms formed on non-metallic surfaces, it was reported that some tribofilm properties and particularly adhesion to substrate surfaces, were different from those of ZDDP tribofilms present on ferrous surfaces. Tribofilms on non-metallic surfaces were generally easily removed by rubbing or washing in an ultrasonic bath because of their weak adhesion to the surface [314–316]. Equey et al. [316] showed that while ZDDP tribofilm on a steel/steel tribopair remained after a scratch test, tribofilm on a DLC/DLC tribopair was removed. This strength of adhesion might be affected by metallic elements in the DLC. Vengudusamy et al. [314] showed that ZDDP tribofilm on DLC/DLC tribopairs showed stronger adhesion to the

surface, and also increased thickness, as the concentration of doped tungsten in DLC was increased. This increase of W concentration in DLC promoted the formation of a pad-like structure of tribofilm, while tribofilm did not form a pad-like structure on metal-free DLC surfaces [216,314,315,317,318].

The research described in this Chapter aims to extend the above work to understand the extent to which ZDDP tribofilms form on non-metallic surfaces of tribological interest in rubbing contacts and, if they do form, the chemical properties of these films. To avoid complications due to a possible transfer of the film between different surfaces, contacts between tribopairs of the same material are studied. The influence of five materials, namely, AISI 52100 steel, Si<sub>3</sub>N<sub>4</sub>, WC, SiC and a-C:H DLC coating, is investigated in both boundary and full film elastohydrodynamic lubrication (EHL) conditions. Tribofilms formed are analysed using STEM-EDX and XPS and TEM.

## **7.2 Test Method**

For this research on the ZDDP tribofilm formation on non-metallic surfaces, experiments were carried out using MTM and ETM as detailed below.

### **7.2.1 Test lubricants and Materials**

Solutions of ZDDP2 in PAO4 were studied in low entrainment speed MTM tests. The low viscosity of PAO4 combined with low entrainment speed ensured thin film and thus boundary lubrication conditions. Solutions of ZDDP2 in PIB were studied in ETM tests at high entrainment speed. Here the relatively high viscosity of this base oil in combination with high entrainment speed ensured full-film elastohydrodynamic lubrication (EHL) conditions. PIB has a high EHL friction coefficient and thus, at high applied load, provides a sufficiently high shear stress to form ZDDP tribofilms on steel surfaces in full EHL conditions [218]. ZDDP2 was used at a concentration of 800 ppm of P in all tests except those shown in Figure 7-7 where additional results are presented for two other concentrations, corresponding to 400 and 1200 ppm of P blended in PIB.

AISI 52100 steel, WC, Si<sub>3</sub>N<sub>4</sub>, SiC and a-C:H DLC-coated specimens supplied by PCS Instruments were used to investigate the effect of surface material on tribofilm formation. For AISI 52100 steel, WC, Si<sub>3</sub>N<sub>4</sub> and SiC bulk material, MTM and ETM balls and discs were employed. For the DLC, the a-C:H DLC coating was deposited on AISI 52100 steel

balls and discs. This hydrogenated DLC consisted primarily of sp<sup>2</sup> with 30% of sp<sup>3</sup>, had a thickness of 2-4  $\mu\text{m}$  and did not contain any metal dopants. Its commercial name is Dymon-iC but it is denoted simply as DLC in this paper. The measured values of the surface roughness, hardness and elastic modulus of the balls and discs in each case are shown in Table 7-1. These are the average value of at least four measurements in different locations on each specimen, and tolerances show variation of measurements. These values of surface roughness, hardness and elastic modulus were measured using a Taylor Hobson Talysurf stylus profilometer, a Zwick Roell Z2.5 (ZHU 0.2) Vickers hardness tester and a Nanotest Platform 2 nanoindenter, respectively.

Table 7-1 Measured properties of MTM (a) discs and (b) balls

(a)

Material	Surface roughness Rq (nm)	Hardness (HV)	Elastic Modulus (GPa)
Steel	$8 \pm 2$	$800 \pm 20$	$210 \pm 10$
Si <sub>3</sub> N <sub>4</sub>	$10 \pm 2$	$1430 \pm 40$	$310 \pm 40$
WC	$11 \pm 3$	$1650 \pm 70$	$630 \pm 40$
SiC	$10 \pm 5$	$2460 \pm 170$	$430 \pm 60$
a-C:H DLC	$11 \pm 3$	$2450 \pm 130$	$170 \pm 20$

(b)

Material	Surface roughness Rq (nm)	Hardness (HV)	Elastic Modulus (GPa)
Steel	$7 \pm 2$	$830 \pm 30$	$210 \pm 10$
Si <sub>3</sub> N <sub>4</sub>	$9 \pm 2$	$1490 \pm 60$	$290 \pm 30$
WC	$8 \pm 3$	$1760 \pm 90$	$740 \pm 70$
SiC	$20 \pm 6$	$2110 \pm 150$	$350 \pm 50$
a-C:H DLC	$9 \pm 3$	$2320 \pm 120$	$170 \pm 20$

Table 7-2 shows the chemical compositions of the MTM balls and discs measured by SEM-EDX and XPS. Aside from the main metal constituents such as Fe in steel and W in WC, some metal-based sintering agents were detected, namely Al, Cr and Y in Si<sub>3</sub>N<sub>4</sub> and Co in WC, whereas no metal was detected in SiC. In the case of DLC, Cr and Fe were detected by EDX. These metals are present in the steel substrate beneath the DLC coating

itself and are detected because EDX is not a surface-sensitive method and analyses an approximate depth of penetration of about 1 – 1.5  $\mu\text{m}$ , so that the collected data were from both the surface and the bulk of the samples. To assess the surface composition of DLC more accurately, the DLC specimens were also analysed using XPS, which generally has a penetration depth of less than about 10 nm. No metals were detected on the DLC surfaces by XPS analyses. ETM ball and disc specimens were analysed their mechanical properties measured and these were the same as corresponding MTM specimens.

Table 7-2 Measured chemical composition of MTM (a) discs and (b) balls (atomic %)

(a)

Material	C	N	O	Al	Si	Cr	Mn	Fe	Co	W	Y
Steel	5.9		3.1		0.7	1.9	0.6	87.8			
Si <sub>3</sub> N <sub>4</sub>	8.2	33.5	18.9	1.6	34.9	1.4					1.5
WC	23.9		7.8						12.7	55.6	
SiC	41.8		0.6		57.6						
DLC	81.8					17.2	1.0				
DLC*	93.7	1.3	5.0								

(b)

Material	C	N	O	Al	Si	Cr	Mn	Fe	Co	W	Y
Steel	5.5		6.0		1.1	1.8	0.5	85.1			
Si <sub>3</sub> N <sub>4</sub>	10.2	40.9	5.8	2.9	38.5						1.7
WC	34.1		6.9						4.9	54.2	
SiC	44.3		1.2		54.5						
DLC	84.3					14.8	0.5	0.4			
DLC*	95.7	0.7	3.6								

\*measured using XPS

## 7.2.2 Test Procedure and Conditions

The MTM was used to investigate ZDDP tribofilm formation under boundary lubrication at the test conditions shown in Table 7-3. By using a very low entrainment speed (mean velocity of the two surfaces with respect to the contact), MTM tests were controlled to an initial theoretical lambda ratio (ratio of EHD film thickness to composite surface



roughness) of less than 0.2, corresponds to 3 nm of oil film thickness, thus providing boundary lubrication conditions. Load was set at values that gave a maximum Hertz pressure of 0.95 GPa for all material combinations. In addition, tribofilm strength/adhesion was investigated by measuring the evolution of tribofilm thickness after replacement of the ZDDP solution by pure PAO base oil once an initial ZDDP tribofilm had formed. In this case, tests consisted of two stages, one in which the ball and disc were rubbed in ZDDP solution to form a tribofilm and the second in which the ball and disc, having pre-formed ZDDP tribofilms, were rubbed in PAO for 30 minutes at the same rubbing conditions as the first stage. Before starting the second stage, the specimens and the MTM oil-bath were rinsed by toluene to remove all ZDDP solution and then rinsed by PAO4 to remove residual toluene.

Table 7-3 MTM test conditions (boundary lubrication conditions)

Entrainment speed; $U = (U_{\text{ball}} + U_{\text{disc}})/2$	50 mm/s
Slide-roll-ratio (SRR); $\text{SRR} = 100 \cdot (U_{\text{disc}} - U_{\text{ball}})/U$	50%
Applied load	Set to give maximum Hertz pressure of 0.95 GPa in all cases (loads; steel 31 N, Si <sub>3</sub> N <sub>4</sub> 15 N, WC 3 N, SiC 10 N, DLC 45 N)
Lubricant temperature	100 °C
Test duration	3 hours
Lubricant	PAO4 + ZDDP2 (P: 800 ppm)

The ETM was employed at the conditions shown in Table 7-4, set to achieve a full elastohydrodynamic lubricant film. These tests therefore evaluate the ability of ZDDP to adsorb and react to form tribofilms in full film, high shear stress EHL conditions without any asperity contact. Before the tests, a short running-in procedure was carried out to remove any surface contaminants and polish off any particularly high roughness asperities. The running-in was run for 1 minute using entrainment speed,  $U = 0.1$  m/s, slide-roll-ratio = 50% and maximum Hertz pressure of 3.0 GPa. Following this running-in period, the actual ETM tests were run at a much higher entrainment speed (750 mm/s) than the MTM tests in order to generate a sufficiently thick fluid film to ensure full film EHL

regime where surface asperities are fully separated. This entrainment speed provided lambda ratios of between 5 and 10 for all test materials. Load was set to achieve a maximum Hertz pressure of 3.0 GPa for all ETM tests, so that the mean shear stress was 200 MPa at a friction coefficient of 0.1. A low SRR of 2.0% was employed to limit flash temperature rise while rubbing.

Using the Archard equation [319,320], flash temperature rise under these speeds was estimated to be 5 °C for AISI 52100 steel specimens at 1000 N applied load when friction coefficient was 0.1. It should be noted that this flash temperature is the instantaneous surface temperature rise as the whole nominal contact area passes through the contact in full-film EHL conditions, rather than the flash temperature resulting from individual asperity contact [319]. All the different materials studied gave friction coefficients close to 0.1 under the test conditions used, so flash temperature effects can be neglected.

Table 7-4 ETM test conditions (full film EHL conditions)

Entrainment speed; $U = (U_{ball} + U_{disc})/2$	750 mm/s
Slide-roll-ratio (SRR); $SRR = 100 * (U_{disc} - U_{ball})/U$	2%
Applied load	Set to give maximum Hertz pressure of 3.0 GPa in all cases (loads; steel 1000 N, Si <sub>3</sub> N <sub>4</sub> 450 N, WC 102 N, SiC 320 N, DLC 1350 N)
Mean shear stress	200 MPa (from measured friction coefficient of 0.1)
Lubricant temperature	100 °C
Test duration	3 hours
Lubricant	PIB + ZDDP2 (P: 400, 800 and 1200 ppm)

Both MTM and ETM tests were interrupted after 0.5, 1 and 2 hours of rubbing to observe the morphology and thickness of tribofilms on the discs using an optical microscope and AFM. For these measurements, discs were removed from the MTM chamber and then gently rinsed by toluene to remove supernatant oil. This did not remove ZDDP tribofilm. After AFM measurement, the specimens were returned to the rig, and the rubbing tests restarted. The same lubricant sample remained in the test chamber for the whole 3 hours

test duration. After the tests, the morphology and thickness of formed tribofilms on the discs were measured using an AFM while the chemical properties of these tribofilms on steel, Si<sub>3</sub>N<sub>4</sub> and WC were analysed using XPS and STEM-EDX.

### **7.2.3 Tribofilm Analysis**

Tribofilms on discs were analysed using the procedures described below. Before measurements, discs were lightly rinsed in toluene without any wiping to remove supernatant liquid but avoid removing tribofilm from the surfaces.

#### **7.2.3.1 Tribofilm Thickness and Topography**

The thickness and topography of tribofilms after 0.5, 1, 2 hours and at the end of MTM and ETM tests after 3 hours rubbing were observed using both AFM and an optical microscope.

#### **7.2.3.2 Tribofilm Characterization**

In order to investigate the elemental distribution and crystallinity of tribofilms on steel, Si<sub>3</sub>N<sub>4</sub> and WC surfaces, lamellae of ZDDP tribofilm cross sections were extracted using FIB and studied using STEM-EDX and TEM. XPS was carried out to analyse surface composition of DLC specimens and the composition of ZDDP tribofilms on steel, Si<sub>3</sub>N<sub>4</sub> and WC.

### **7.2.4 ZDDP Adsorption Study using QCM-D**

QCM-D was used to monitor the adsorption of ZDDP from PAO solution on to Fe<sub>2</sub>O<sub>3</sub>, Si<sub>3</sub>N<sub>4</sub>, WC, SiC and carbon coated quartz sensors. Because of their availability, Fe<sub>2</sub>O<sub>3</sub> and carbon coated sensors were used instead of AISI 52100 steel and a-C:H DLC, respectively.

## 7.3 Results

### 7.3.1 Tribofilm Formation in Boundary Lubrication Conditions

The effect of surface material on ZDDP tribofilm formation in boundary lubrication conditions was investigated using MTM. Figure 7-1 shows optical micrographs and AFM profiles of tribofilms on the discs after 3 hours rubbing with all five tribo-pairs. On AISI 52100 steel discs, tribofilm formed on all parts of the wear track, with a pad-like topography and a maximum tribofilm thickness of 190 nm. In contrast, with  $\text{Si}_3\text{N}_4$  and WC specimens tribofilms formed only on some parts of the wear track and consisted of large, relatively smooth lumps, rather than the fine, pad structure seen on the steel specimens. Dashed circles in Figure 7-1. shows regions without tribofilm. The maximum thickness of tribofilm was 700 nm and 250 nm on  $\text{Si}_3\text{N}_4$  and WC, respectively. No measurable tribofilms were observed on SiC and DLC.

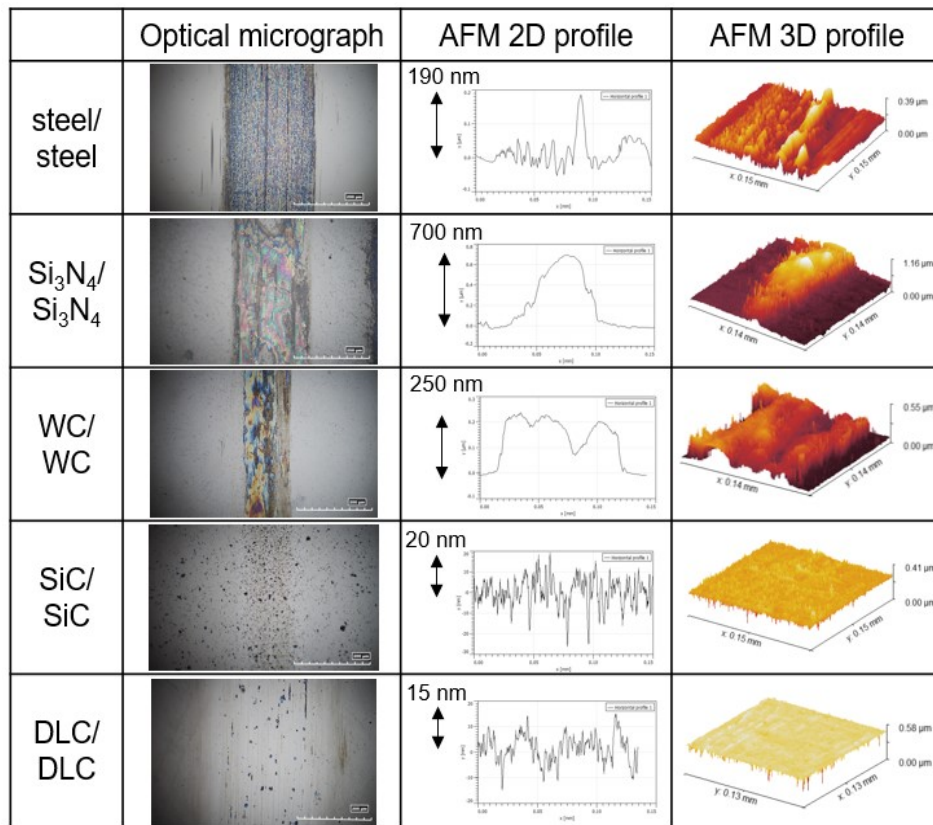


Figure 7-1 Optical micrographs and AFM profiles of ZDDP tribofilm on the disc of each material after 3 hours rubbing in thin film conditions

Figure 7-2 shows the evolution of maximum tribofilm thickness with rubbing time. Tribofilm on AISI 52100 steel grew steadily with rubbing time, to reach about 180 nm after 2 hours rubbing. A maximum thickness of about 190 nm was present at several locations after 3 hours rubbing. In comparison, tribofilms on  $\text{Si}_3\text{N}_4$  and WC formed more rapidly, and tribofilm thickness had a much greater variation, with local maximum thickness range of 470-700 nm on  $\text{Si}_3\text{N}_4$  and 140-250 nm on WC after 3 hours of rubbing. Note that there were regions without any tribofilms on the wear tracks of  $\text{Si}_3\text{N}_4$  and WC.

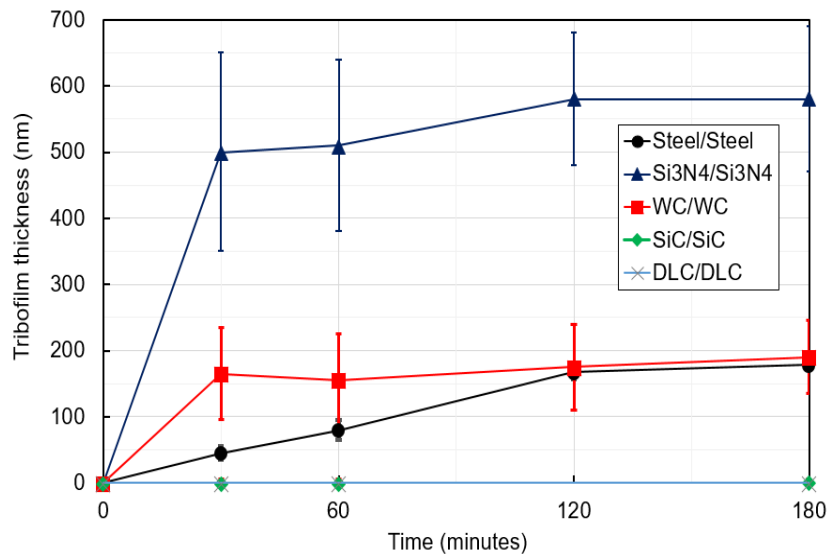


Figure 7-2 The evolution of ZDDP tribofilm thickness on each material during rubbing in thin film conditions

Figure 7-3 shows the evolution of tribofilm area coverage on the wear track. On steel, the tribofilm covered all regions of the wear track after rubbing, whereas the tribofilms on  $\text{Si}_3\text{N}_4$  and WC covered only some parts of the wear tracks and the locations of these fluctuated during rubbing. This suggests that tribofilms on  $\text{Si}_3\text{N}_4$  and WC were more easily removed from the surface during rubbing than those on steel.

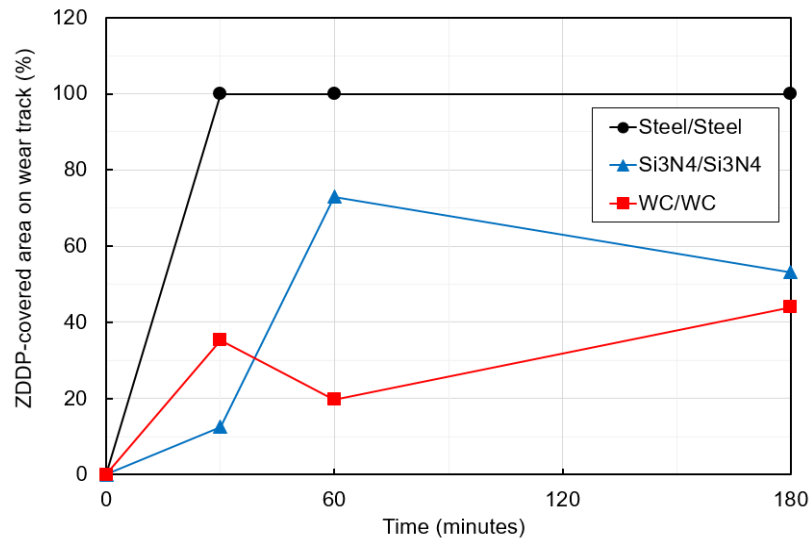


Figure 7-3 The evolution of ZDDP tribofilm area coverage on wear track of each material during rubbing in thin film conditions

To investigate tribofilm removal from each surface material, the effect of an additional 30 minutes of rubbing in pure PAO at the end of the film formation test was studied, as shown Figure 7-4. At the end of these 30 minutes, no tribofilm was removed from steel, whereas all the measurable tribofilm on Si<sub>3</sub>N<sub>4</sub> and WC was removed. This observation of relatively easy ZDDP tribofilm removal from non-metallic substrates is in line with some previous studies [314,316].

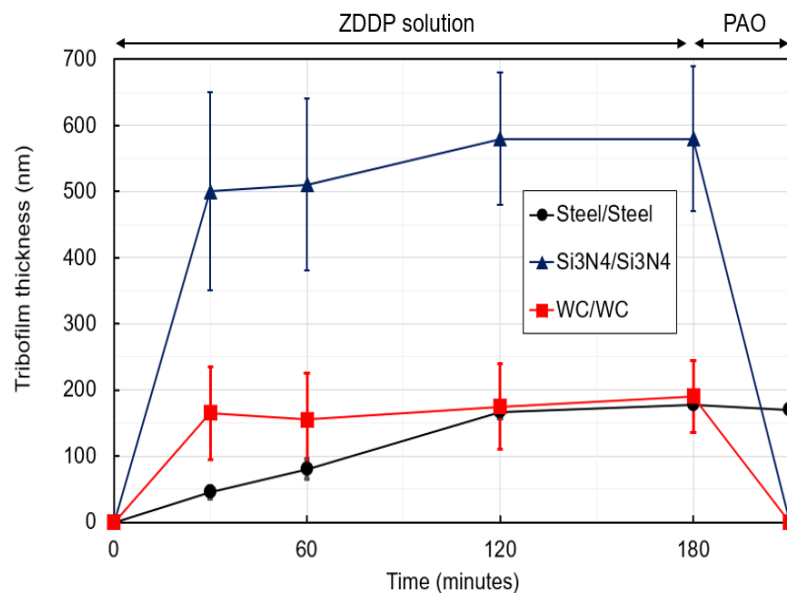


Figure 7-4 The effect of 30 min rubbing in pure PAO on ZDDP tribofilm removal for each material in thin film conditions (ZDDP solution was replaced with pure PAO after 180 minutes rubbing)

These results suggest that the mechanical and thus probably the chemical properties of tribofilms on  $\text{Si}_3\text{N}_4$  and WC are different from those on steel. The fact that with  $\text{Si}_3\text{N}_4$  and WC the tribofilm appears to be completely removed from selected regions of the surface during rubbing in ZDDP solution and completely removed by rubbing in pure PAO, suggests that adhesion of the tribofilm to the  $\text{Si}_3\text{N}_4$  and WC substrates is weaker than to steel substrate. Considering the behaviour of tribofilm formation on  $\text{Si}_3\text{N}_4$  and WC, it is difficult to ascertain whether tribofilm cannot form on SiC and DLC or whether tribofilm can form but is immediately removed. Equey et al. [314] showed *ca.* 100 nm of weakly adhered tribofilm to be formed on surfaces in a-C:H DLC tribopairs which was easily removed by cleaning in an ultrasonic bath. The same authors also showed that ZDDP tribofilm formed on a-C:H DLC tribopairs was easily removed by a nano-scratch test [316]. In these studies, maximum lambda ratio was 1.5, which is a much milder rubbing condition than the lambda ratio of 0.2 in the current study, and this may be the cause of the apparent discrepancy in the observed ZDDP tribofilms on a-C:H DLC substrates.

### 7.3.2 Tribofilm Formation in Full Film EHL Conditions

Since tribofilm appeared to be relatively easily removed from the non-metallic surfaces in thin film, boundary lubrication conditions, ZDDP's ability to form tribofilms on non-metallic surfaces could not be reliably quantified, making it difficult to understand the mechanism of tribofilm formation. To overcome this problem, tribofilm formation was studied in high shear stress EHL conditions which eliminate the possibility of tribofilm removal by asperity contacts. The ETM rig was used for these studies as it is capable of reaching very high pressures, and hence shear stresses, with all of the tribopairs employed here.

Figure 7-5 shows optical micrographs and AFM profiles of tribofilms formed after 3 hours rubbing on the disc of each material in EHL conditions. Tribofilms covering almost the whole wear track were formed on steel,  $\text{Si}_3\text{N}_4$  and WC, with maximum tribofilm thickness of 180 nm, 160 nm and 40 nm respectively. The tribofilms all had a similar topography and a smaller variation of thickness than the equivalent tribofilms formed in boundary lubrication conditions. As was the case in the MTM tests, no measurable tribofilms were found on SiC and DLC.

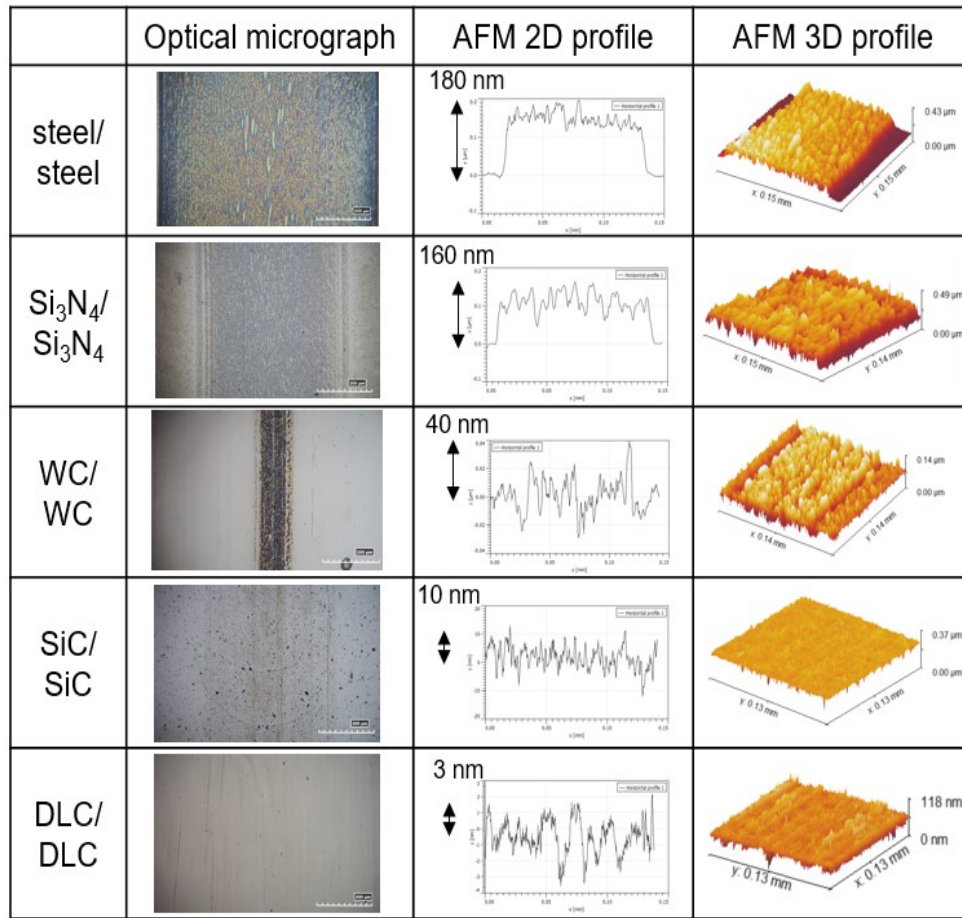


Figure 7-5 Optical micrographs and AFM profiles of ZDDP tribofilm on the discs of each material after 3 hours in full film EHL conditions

Figure 7-6 shows the evolution of maximum tribofilm thickness during full film EHL tests. Tribofilms on steel, Si<sub>3</sub>N<sub>4</sub> and WC grew steadily with rubbing time. These tribofilms formed over the whole wear track, with the local variation of thickness in each case being less than 40 nm.

These results suggest that, in contrast to what was observed in boundary lubrication, at least some of the tribofilm formed on Si<sub>3</sub>N<sub>4</sub> and WC in full EHL conditions is not being continuously removed. This allows quantitative comparison of the ZDDP's ability to adsorb and react to form tribofilms. The thickness of the ZDDP tribofilms formed on the five materials after 3 hours rubbing was in the following order; steel > Si<sub>3</sub>N<sub>4</sub> > WC > SiC and DLC.



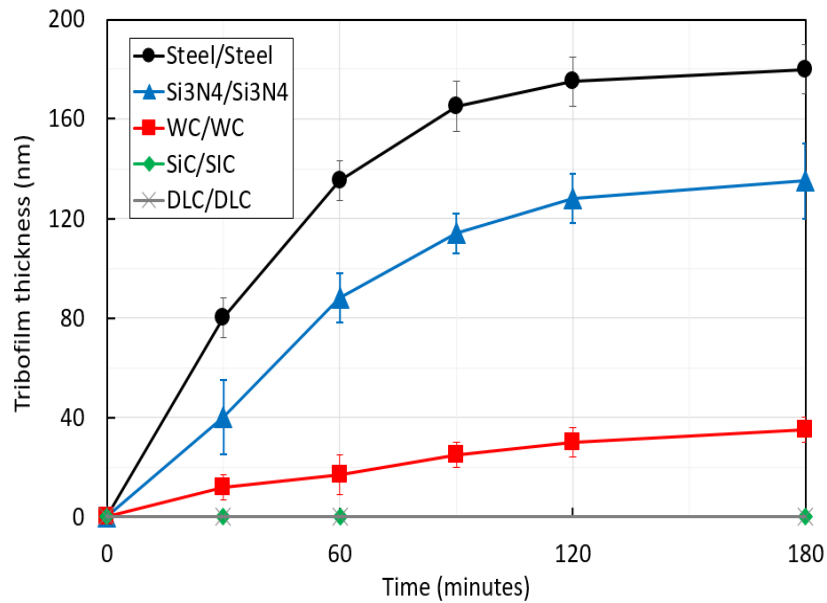


Figure 7-6 The evolution of ZDDP tribofilm thickness with rubbing time on each material in full film EHL conditions

These observations suggest that ZDDP adsorption and reaction to form tribofilm does occur on Si<sub>3</sub>N<sub>4</sub> and WC; however, in boundary lubrication these tribofilms are easily removed because of their weak adhesion to surface. By contrast, tribofilm did not form well on SiC and DLC either because ZDDP did not adsorb or because, although adsorbed, it did not react to form polyphosphate.

### 7.3.3 Effect of ZDDP Concentration on Tribofilm Formation in Full Film EHL Conditions

In order to investigate the ability of ZDDP to adsorb on non-metallic surfaces, the effect of ZDDP concentration on tribofilm formation on steel and Si<sub>3</sub>N<sub>4</sub> was studied in full film EHL conditions in ETM tests. Figure 7-7 shows the evolution of ZDDP tribofilm thickness at three ZDDP concentrations corresponding to 400, 800 and 1200 ppm of P. It is evident that with steel, the rate of tribofilm growth and its final thickness are almost independent of concentration of ZDDP over the range studied, with 180 nm of tribofilm after 3 hours rubbing. By contrast, with Si<sub>3</sub>N<sub>4</sub> the rate of tribofilm formation increases with ZDDP concentration, resulting in tribofilm thickness of 115 nm, 135 nm and 160 nm after 3 hours rubbing with 400, 800 and 1200 ppm P, respectively.

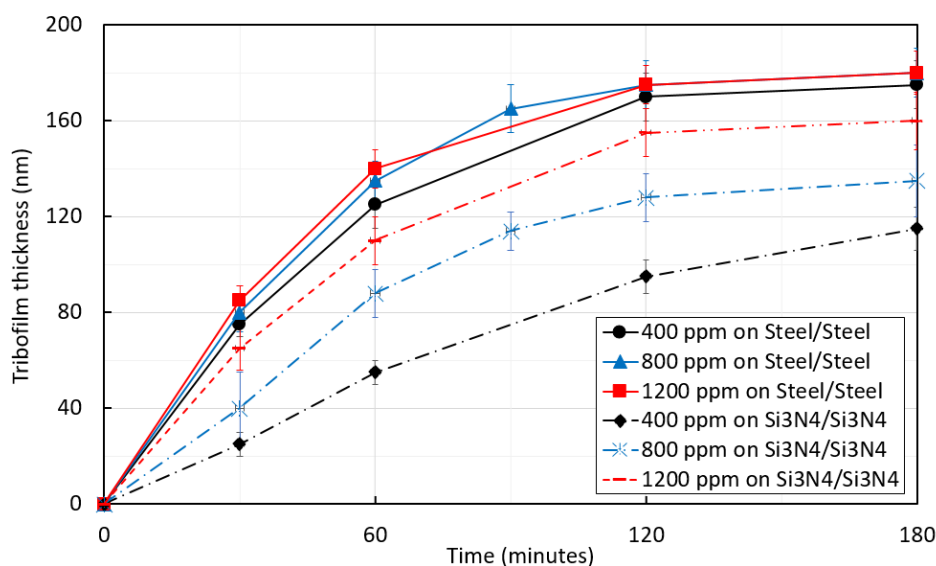


Figure 7-7 The evolution of ZDDP tribofilm thickness with different ZDDP concentrations on steel and Si<sub>3</sub>N<sub>4</sub> in full film EHL conditions

These results suggest that ZDDP may adsorb more easily on steel than on Si<sub>3</sub>N<sub>4</sub>. Active sites for ZDDP adsorption on steel might already be saturated at concentrations as low as 0.04 wt.% of P, whereas the adsorption sites on Si<sub>3</sub>N<sub>4</sub> are not fully covered with ZDDP up to 0.12 wt.% of P or higher, resulting in increase of tribofilm thickness with increasing ZDDP concentration. These results suggest that the ability of ZDDP to adsorb on a surface may considerably affect ZDDP tribofilm formation.

### 7.3.4 QCM-D Results on ZDDP Adsorption

To further understand the interaction of ZDDP with each surface material, the adsorption of ZDDP on Fe<sub>2</sub>O<sub>3</sub>, Si<sub>3</sub>N<sub>4</sub>, WC, SiC and carbon was studied using QCM-D. Figure 7-8 shows ZDDP mass adsorbed at 60 °C on sensors made of each of these materials. Little ZDDP is adsorbed on carbon and SiC coated sensors. By comparison, more ZDDP is adsorbed on Fe<sub>2</sub>O<sub>3</sub>, Si<sub>3</sub>N<sub>4</sub> and WC sensors, with constant mass increase in ZDDP solution. Overall, the amount of ZDDP adsorbed on the sensors was largest for Fe<sub>2</sub>O<sub>3</sub>, intermediate for Si<sub>3</sub>N<sub>4</sub> and WC and the smallest on SiC and carbon. This order follows exactly that shown earlier for the tribofilm thickness (Figure 7-6) and thus strongly suggests that higher amount of ZDDP adsorption may result in thicker tribofilm after 3 hours rubbing.

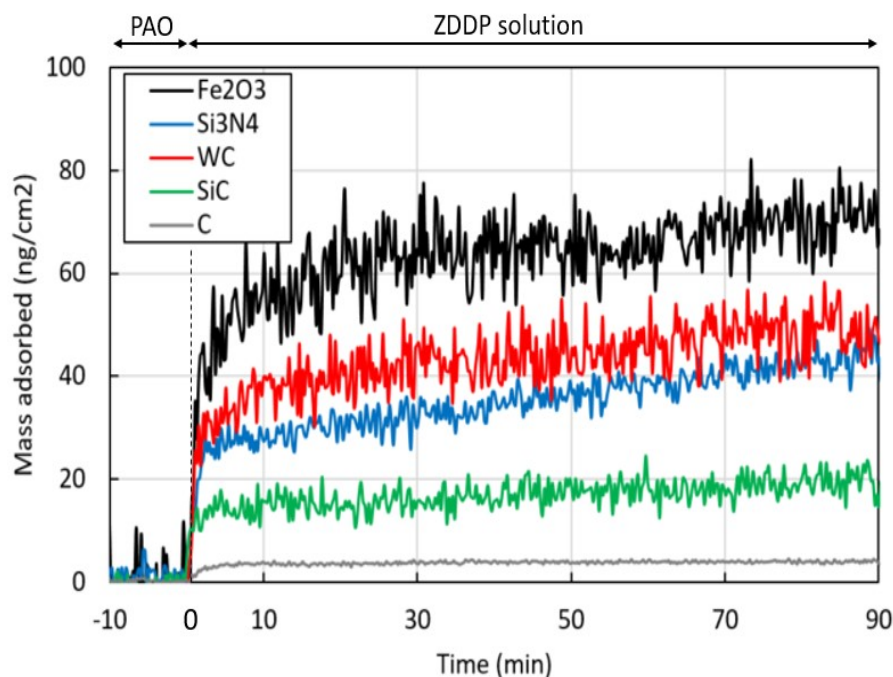


Figure 7-8 QCM-D results showing ZDDP mass adsorbed on sensors made of, or coated with, each of the 5 studied materials

### 7.3.5 Chemical Analysis of ZDDP Tribofilms Formed under Boundary Lubrication Conditions

As shown in Figure 7-1 and Figure 7-2, while ZDDP tribofilm thickness after 3 hours rubbing on WC was almost equivalent to that on steel at some regions, the tribofilms formed on Si<sub>3</sub>N<sub>4</sub> and WC non-metallic surfaces were generally both thicker and smoother than on those formed on steel in boundary lubrication. In addition, the adhesion of these ZDDP tribofilms on Si<sub>3</sub>N<sub>4</sub> and WC on non-metallic surfaces was weaker than on steel as shown in Figure 7-4. These results suggest that ZDDP tribofilm properties on non-metallic surfaces may be different from those on ferrous surface. To better understand these potential differences, the chemical properties of ZDDP tribofilms were investigated using STEM-EDX, XPS and TEM.

#### 7.3.5.1 STEM-EDX Results on the Elemental Distribution of Tribofilms

Cross sections of tribofilms formed on different materials were analysed using STEM-EDX to determine the elemental distribution within the tribofilms. Figure 7-9 shows the

EDX line spectra of tribofilms on steel, Si<sub>3</sub>N<sub>4</sub> and WC after 3 hours of rubbing in thin film, boundary lubrication conditions. The intensity of all peaks was adjusted by scaling to the same phosphorus peak intensity in order to easily compare the ratio of other elements to phosphorus. In terms of the distribution of metal from the substrate, Fe was present throughout the tribofilm formed on steel surface, but none of the metals present in the Si<sub>3</sub>N<sub>4</sub> and WC substrates were detected in the tribofilms formed on these two materials.

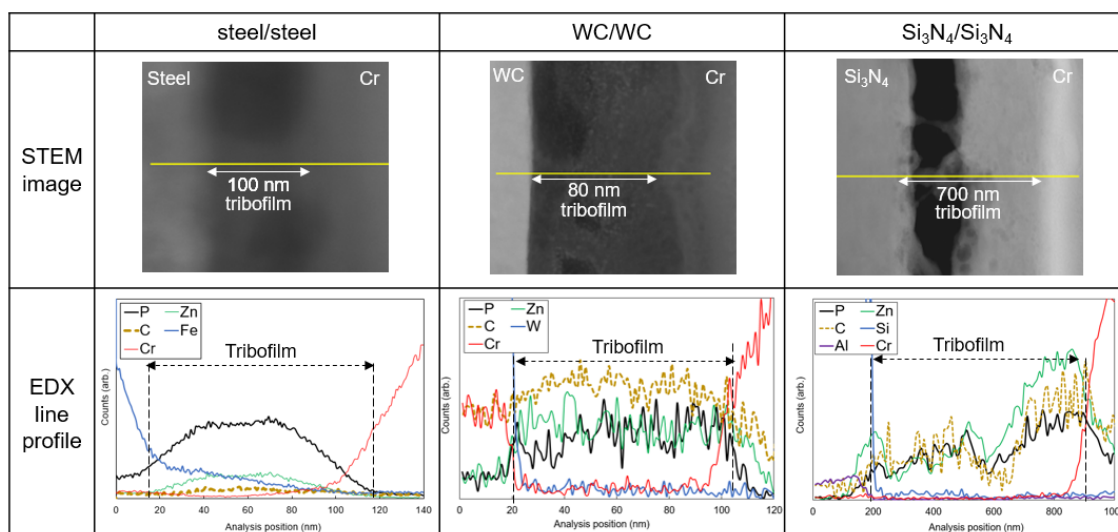


Figure 7-9 STEM images and EDX line profiles of sections of tribofilms formed on steel, WC and Si<sub>3</sub>N<sub>4</sub> surfaces after 3 hours of rubbing in boundary lubrication conditions

Interestingly, as well phosphate tribofilm, large amounts of carbon were detected in the tribofilms on Si<sub>3</sub>N<sub>4</sub> and WC; far more than on steel. This suggests that tribofilms on Si<sub>3</sub>N<sub>4</sub> and WC are mixtures of phosphate reaction film and carbon-rich material, or alternatively that not all the alkyl groups have been lost during polymerization to form polyphosphate.

### 7.3.5.2 XPS Results

XPS analysis was used to investigate the chemical state of carbon and oxygen within the near-surface of the tribofilms. Figure 7-10 shows the C 1s and O 1s XPS spectra of tribofilms on steel, Si<sub>3</sub>N<sub>4</sub> and WC after 3 hours rubbing in boundary lubrication conditions. In order to aid comparison, all peaks were normalized to their maximum peaks of each spectra; the peak at 284.8 eV of C 1s spectra and the peak at 531.5 eV of O 1s

spectra. Carbon related peaks are attributed to C-C and C-H at 284.8 eV, C-O at  $286.4 \pm 0.2$  eV, C=O at  $286.6 \pm 0.2$  eV and C-W at 282.2 eV [127,321,322]. Although W was not detected in the surface region of the tribofilm on WC using EDX analysis, the C 1s peak of tribofilm on WC shows a clear C-W bond. This is probably because even though a small spot size was employed in XPS analysis of tribofilm on WC, the wear track was quite narrow at 130  $\mu\text{m}$  in width, resulting in peak contamination from WC surface outside the track. The C-O peaks on  $\text{Si}_3\text{N}_4$  and WC were more intense than on steel, with the peak ratio of C-O/(C-C and C-H) being 0.15, 0.84 and 0.68 on steel,  $\text{Si}_3\text{N}_4$  and WC, respectively. The C-O peak can also be attributed to C-O-P [323]. These results suggest that tribofilms on  $\text{Si}_3\text{N}_4$  and WC contain either unreacted ZDDP or a considerable proportion of alkoxy groups attached to the polyphosphate.

The chain length of phosphates in ZDDP tribofilms can be estimated from the BO/NBO ratio [120,121,127], *i.e.* the ratio of the intensity of the bonding oxygen, BO (P–O–P), to that of the non-bonding oxygen, NBO (P=O and P–O–M). The BO peaks from tribofilms on  $\text{Si}_3\text{N}_4$  and WC were more intense than from tribofilms on steel, namely, the peak ratio of BO/NBO was 0.13, 0.55 and 0.57 on steel,  $\text{Si}_3\text{N}_4$  and WC, respectively. These results suggest that tribofilms on  $\text{Si}_3\text{N}_4$  and WC consisted of longer chain phosphates such as metaphosphates and polyphosphates than the tribofilms on steel. This is consistent with these tribofilms containing more residual alkoxy groups.

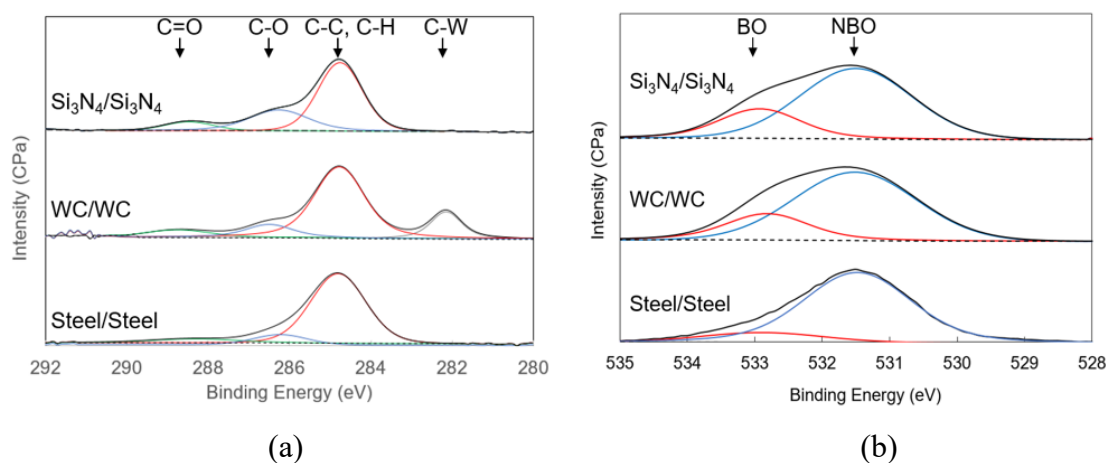


Figure 7-10 (a) C 1s and (b) O 1s XPS spectra of ZDDP tribofilms on steel,  $\text{Si}_3\text{N}_4$  and WC after 3 hours of rubbing in thin film conditions

Note that XPS signals originate almost entirely from within approximately 10 nm of the surface and consequently, it is difficult to discuss these peaks in terms of inner tribofilm composition. Within this near surface region, however, both the C-O peak in C 1s and BO peak in O 1s in tribofilms on WC and Si<sub>3</sub>N<sub>4</sub> were more intense than in tribofilms on steel.

#### **7.3.5.3 TEM Results on the Crystallinity of Tribofilms**

The nanocrystallisation of phosphate structure that might result from depolymerization of long chain phosphates (Chapter 6) was investigated using TEM. Figure 7-11 shows TEM images of cross sections of ZDDP tribofilms on steel, Si<sub>3</sub>N<sub>4</sub> and WC after 3 hours rubbing in boundary lubrication conditions, together with corresponding FFT images. A large hole can be observed in the tribofilm on steel and Si<sub>3</sub>N<sub>4</sub> and these result from damage caused during the FIB thinning of the TEM sample. Based on the lattice fringes and FFT images, the tribofilm on steel was crystalline both near the substrate and close to the surface. However, lattice fringes and specific FFT spots were not observed in the tribofilms on Si<sub>3</sub>N<sub>4</sub> and WC. These results suggest that the ZDDP tribofilms on Si<sub>3</sub>N<sub>4</sub> and WC are predominantly amorphous, unlike those on steel which are nanocrystalline throughout the film.

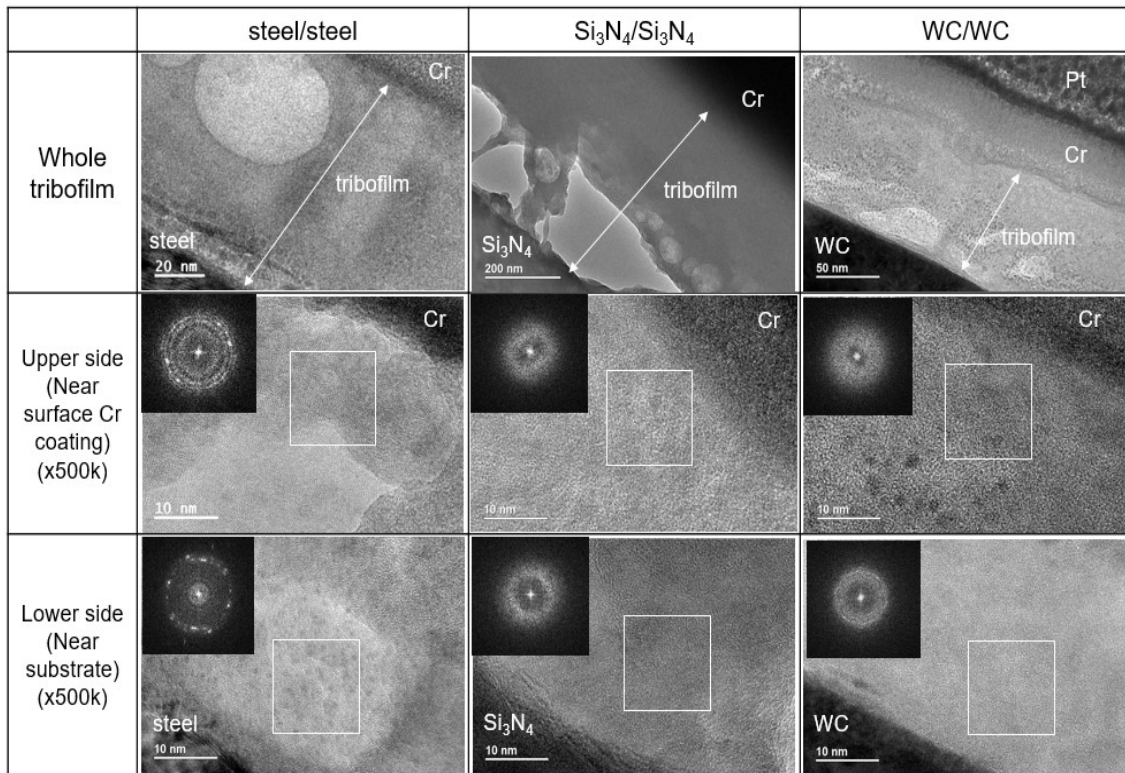


Figure 7-11 TEM images and FFTs of ZDDP tribofilms on steel, Si<sub>3</sub>N<sub>4</sub> and WC after 3 hours of rubbing in boundary lubrication conditions

## 7.4 Discussion

It is evident from the above results that ZDDP tribofilm formation is very dependent on the nature of the rubbing surfaces. It is of interest to consider these differences in terms of the mechanism of ZDDP tribofilm formation on steel and how this might be affected by the substitution of a predominantly ferrous surface by other materials.

### 7.4.1 Surface Adsorption

Yamaguchi et al. [140,192] showed that ZDDP molecules adsorb on Al via the sulphur atom of the P=S bond, while Bovington and Dacre [193] found that adsorption was accompanied by the release of Zn cations and the formation of dithiophosphate, as shown in Figure 7-12. Although the presence of Fe is not needed for the growth of ZDDP tribofilm [287], Fe can play an important role in promoting tribofilm formation on steel, particularly as a physical and /or chemical adsorption site for ZDDP molecules. It is quite



likely that other metals present in some non-metallic substrates may also act as adsorption sites in a similar fashion to Fe in steel.

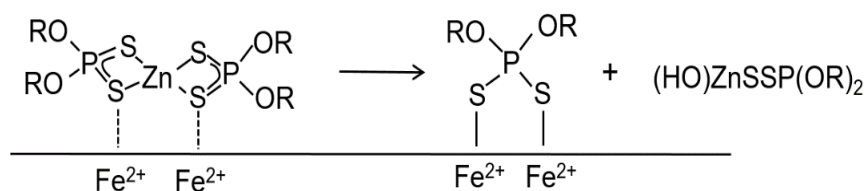


Figure 7-12 The adsorption of ZDDP molecule on ferrous surface and the formation of Fe dithiophosphate

The results of QCM measurements shown in Figure 7-8 indicate that ZDDP adsorption is dependent on material, with ZDDP adsorption being the highest on  $\text{Fe}_2\text{O}_3$  followed by  $\text{Si}_3\text{N}_4$  and WC and very low on SiC and carbon. The 55.6% of W present in WC discs may be covalently bound, but, as shown in Table 7-2, both  $\text{Si}_3\text{N}_4$  and WC discs include relatively large amounts of metallic sintering agents such as Al (1.6%), Cr (1.4%) and Y (1.5%) in  $\text{Si}_3\text{N}_4$  and Co (12.7%) in WC. These metals in  $\text{Si}_3\text{N}_4$  and WC may act as adsorption sites for ZDDP where ionic bonds are formed between these cations and sulphur of ZDDP molecules during adsorption. However, the proportions of these metals in  $\text{Si}_3\text{N}_4$  and WC are much smaller than that of Fe in steel, so that even if they act to promote ZDDP adsorption, it may be expected that there would be less ZDDP adsorption, and hence tribofilm formation on  $\text{Si}_3\text{N}_4$  and WC than on steel. For the same reasons, there may also be less metal sulphide formation on  $\text{Si}_3\text{N}_4$  and WC than on steel. These metal sulphides form ionic bonds between surface and tribofilms and may act as an interlayer that strengthens phosphate-based tribofilm adhesion. Therefore, the non-metallic substrates with their reduced metal content may be expected to form less of such interlayer between tribofilm and the substrate, hence resulting in weaker tribofilm adhesion as was observed in Figure 7-4. By contrast, SiC and DLC tested here do not contain any metals to promote ZDDP adsorption, resulting in no measurable tribofilms formed on these substrates. Previous studies with DLC/DLC tribopairs [314–317] have shown that the properties of the specific DLC coating type used heavily influence tribofilm formation. For example, Vengudusamy et al. [315] and Abdullah Tasdemir et al. [317] showed that W and Cr dopants promoted ZDDP tribofilm formation. These dopants



might behave as adsorption sites of ZDDP to promote film formation in the manner described above. In this study neither the carbon coated QCM sensor nor the DLC ball and disc MTM/ETM specimens contained dopant metals. However, DLC MTM/ETM specimens contain a higher amount of hydrogen than the carbon coated QCM sensor. The effect of hydrogen in DLC on ZDDP tribofilm formation is not well understood [315,317], and therefore, the ZDDP adsorption behaviour should ideally be studied with a hydrogenated DLC coated sensor instead of a non-hydrogenated carbon coated sensor as was the case here.

It is interesting to postulate on which factors are responsible for the observed ranking in the tribofilm growth rate for different substrates shown in Figure 7-6. The growth rate was largest for steel, followed by  $\text{Si}_3\text{N}_4$  and smallest for WC. Studt [73] studied the effect of rubbing surfaces on ZDDP tribofilm formation in boundary condition using steel/steel,  $\text{Al}_2\text{O}_3/\text{Al}_2\text{O}_3$  and  $\text{SiC}/\text{SiC}$  tribopairs and found that a thicker ZDDP tribofilm formed on steel than on  $\text{Al}_2\text{O}_3$ , with no tribofilm formation observed on  $\text{SiC}$ . Given that  $\text{Fe}_2\text{O}_3$  and  $\text{Al}_2\text{O}_3$  have ionic lattice and polar surfaces while  $\text{SiC}$  has covalently bonded crystal and non-polar surface, the author suggested that the polar surface of  $\text{Fe}_2\text{O}_3$  and  $\text{Al}_2\text{O}_3$  might support ZDDP adsorption to form tribofilms. As discussed in the previous chapter, one factor that might influence adsorption is the ionicity of the surface. The ionicity of materials used in this study is as follows;

$$\text{Fe}_2\text{O}_3 (0.68) [306] > \text{Si}_3\text{N}_4 (0.40) [304] > \text{WC} (0.14) [305]$$

This follows the observed trend in the tribofilm growth rates. It is therefore possible that high ionicity material may provide a polar reactive surface with high surface energy, which causes increased adsorption of polar ZDDP molecules, thus resulting in more tribofilm formation. However, it is important to note that the type and amount of sintering agents or dopants in non-metallic surfaces may change the reactivity of surfaces and may well exceed the effect of ionicity on ZDDP adsorption. The reason why QCM analyses did not show the expected trend  $\text{Si}_3\text{N}_4$  having higher adsorbed mass than WC is that some small amount of metal impurities may be present in  $\text{Si}_3\text{N}_4$  and WC coated sensors, resulting in changes to surface ionicity and hence changes in adsorption rates.

#### 7.4.2 Polymerisation

Although XPS analysis gives chemical information for the outermost tribofilm only, the P-O-P peak in O 1s XPS spectra shows that polymerization to form polyphosphates might occur on Si<sub>3</sub>N<sub>4</sub> and WC as it does on steel. On the other hand, the higher intensity of C-O peak in C 1s XPS spectra shows that the dealkylation of the polymer might only partially occur on Si<sub>3</sub>N<sub>4</sub> and WC compared to steel. Since a large amount of carbon was detected in tribofilms on Si<sub>3</sub>N<sub>4</sub> and WC at all depths, it is likely that some of the alkyl groups of ZDDP molecules may remain without dealkylation in these cases, resulting in a high intensity C-O peak in XPS spectra. This may be caused by the repetitive tribofilm removal from surface on Si<sub>3</sub>N<sub>4</sub> and WC, leading to increased proportion of unreacted ZDDP molecules, or simply lack of full dealkylation.

Sheasby et al. [318] showed that under boundary lubrication, ZDDP formed thicker tribofilms, consisting of larger pads, on Si<sub>3</sub>N<sub>4</sub>/ Si<sub>3</sub>N<sub>4</sub> than on steel/steel tribopairs. These observations agree with the present study (see Figure 7-2 and Figure 7-3). Considering that large amounts of carbon were detected here inside tribofilms on both Si<sub>3</sub>N<sub>4</sub> and WC, it may be that the presence of carbon compositions, probably attributed to unreacted ZDDP molecules or reactants before dealkylation, act to make tribofilms on Si<sub>3</sub>N<sub>4</sub> and WC thicker than those on steel.

#### 7.4.3 Depolymerisation

Depolymerisation of polyphosphate increases anionic charge in phosphates which must be balanced by cations. Aside from Zn cations, one possible way to balance charge is the transfer of Fe cations into tribofilm from the steel substrate, resulting in the formation of iron phosphates [116]. Since the BO/NBO ratio obtained from O 1s XPS spectra was much higher for tribofilms on Si<sub>3</sub>N<sub>4</sub> and WC than on steel, depolymerization of phosphates on Si<sub>3</sub>N<sub>4</sub> and WC may not be occurring to the same extent, which causes some long chain phosphates such as metaphosphates and polyphosphates to remain. This suggestion is further supported by the apparent lack of crystallization of tribofilms on Si<sub>3</sub>N<sub>4</sub> and WC as observed in the TEM images and FFT spots shown in Figure 7-11. The work described in Chapters 5 and 6 previous study suggest that tribofilms become crystallized only when long chain phosphates depolymerize into short-chain phosphates (Chapter 6). This lack of depolymerization and subsequent absence of crystallization of tribofilms on Si<sub>3</sub>N<sub>4</sub> and WC may result from fewer metal cations being available to transfer into tribofilms compared to steel.

The observations discussed here suggest that the ZDDP tribofilm thickness, coverage, growth rates and sequence of reactions leading to tribofilm formation vary with the composition of the substrate and, in particular, with its metal content. This has practical implications in optimizing lubricant formulation and tailoring the chemical compositions of rubbing materials to improve antiwear behavior of a given mechanical system. For example, the use of highly reactive ZDDPs, element doping and ion implantation on non-metallic surfaces can promote formation of stable antiwear tribofilms.

## 7.5 Conclusions

This study has used MTM and ETM ball on disc tribometers combined with AFM, STEM-EDX, XPS and TEM tribofilm analysis to show that ZDDP forms tribofilms in both ferrous/ferrous and non-metallic/non-metallic rubbing contacts. However, the composition and properties of tribofilms formed on non-metallic surfaces differ from those formed on steel substrates. The origins of these differences are suggested. Key conclusions are as follows.

- In the boundary lubrication conditions, ZDDP tribofilms formed on  $\text{Si}_3\text{N}_4$  and WC surfaces were thicker but less adhesive than those formed on steel, while no measurable tribofilms formed on SiC and a-C:H DLC coating. Tribofilms on  $\text{Si}_3\text{N}_4$  and WC were easily removed by rubbing in pure PAO base oil, indicating their weak adhesion to the substrate. Such easy tribofilm removal made quantification of ZDDP tribofilm formation rate and thickness on non-metallic surfaces difficult.
- In full-film EHL conditions under high pressures and shear stresses, thick tribofilms formed, in the order of decreasing thickness, on steel,  $\text{Si}_3\text{N}_4$  and WC and no apparent tribofilm removal was observed in this case. Once again, no measurable tribofilms formed on SiC and a-C:H DLC coating.
- Tribofilm formation on steel was unaffected by ZDDP concentration but thicker tribofilms formed on  $\text{Si}_3\text{N}_4$  as the ZDDP concentration was increased. This suggests that substrate composition affects the adsorption behaviour of ZDDP.

- The amount of ZDDP adsorption measured by QCM was greatest for steel, followed by  $\text{Si}_3\text{N}_4$  and WC, and smallest for SiC and carbon. This general trend correlates with the trends in thickness of tribofilms formed in EHD conditions.
- Results suggest that a potentially important factor in formation of ZDDP films on non-metallic surfaces is the presence and concentration of metal atoms or ions at the surface. The metals present in  $\text{Si}_3\text{N}_4$  and WC may act as adsorption sites for ZDDP in a similar manner to Fe in steel, forming ionic bonds between these cations and the sulphur atoms in ZDDP molecules. However, in the case of non-metallic substrates, such bonds appear to be less strong than with steel, resulting in weak adhesion of the tribofilm to the substrate, and hence its easier removal.
- Tribofilms on  $\text{Si}_3\text{N}_4$  and WC formed in the boundary lubrication regimes were composed of phosphate reaction films and a large amount of carbon-based material. This carbon might be attributed to unreacted ZDDP, resulting in the formation of relatively thick tribofilms.
- TEM images suggest that ZDDP tribofilms on  $\text{Si}_3\text{N}_4$  and WC may be predominantly amorphous unlike those on steel which are nanocrystalline throughout the film.
- The fact that metals, including iron but also other metals, affect tribofilm formation has practical implications for optimizing lubricants and the composition of non-metallic rubbing materials for improved antiwear performance of machines.

## 8 Wear of Hydrogenated DLC in MoDTC-containing Oils

*This chapter describes a study of the effect on MoDTC-promoted a-C:H DLC wear of adding various surface-active additives used in engine lubricants, including ZDDP, an ashless EP additive, Ca detergents, dispersants, an OFM and a PAMA, to an MoDTC solution. Tribofilms formed on wear tracks on steel were analysed using SLIM, TEM, STEM-EDX, Raman spectroscopy and XPS. Relevant mechanisms by which these additives reduce the impact of MoDTC on DLC wear are suggested. The research described in this chapter has already been published in Wear with an open access [324].*

### 8.1 Introduction

As described in 3.3.3.4, the use of MoDTC-containing oils with a-C:H DLC coatings can produce very high coating wear. It is important to note that this high wear is seen only when DLC is rubbed against a steel counterface and is not observed when DLC is rubbed against DLC and/or a ceramic [64,325].

Although the precise mechanism of a-C:H DLC wear in MoDTC oil has not been unambiguously determined, several studies have suggested that this wear is related to the formation of  $\text{MoO}_3$  from MoDTC in the DLC/steel tribocontact [62]. Masuko et al. [326] showed that DLC wear increased as surface  $\text{MoO}_3/(\text{MoO}_3+\text{MoS}_2)$  ratio increased, while Shinyoshi et al. [327] proposed that  $\text{MoO}_3$  on steel surfaces oxidized C-H and/or dangling bonds on DLC surfaces, resulting in a structural change of DLC from  $\text{sp}^3$  to  $\text{sp}^2$ , *i.e.* graphitization. This graphitized carbon was then worn more easily by rubbing. This proposed mechanism has been supported by several other studies [328–330]. After carbon is worn from DLC, such carbon may transfer to the steel counterface and some studies suggest that this transferred carbon then reacts with MoDTC to form molybdenum carbide (MoC) species on steel surfaces [59,61,328]. Okubo et al. [59] proposed that this MoC species on steel wear tracks is much harder than a-C:H DLC, resulting in severe abrasive DLC wear. All these studies suggest that DLC wear in an MoDTC-containing oil may be considerably affected, directly or indirectly, by the extent to which  $\text{MoO}_3$  is formed on the steel surface and interacts with the DLC counterface.

Some researchers have reported that the antiwear additive zinc dialkyldithiophosphate (ZDDP) can control the harmful effect of MoDTC on a-C:H DLC wear [59,64,331,332]. There are several possible origins of this response. ZDDP forms a thick phosphate tribofilm on rubbed surfaces and this should reduce asperity contact between DLC and steel, hence resulting in less DLC wear [59,332]. ZDDP also affects the MoDTC decomposition reaction which may alleviate oxidation of Mo compounds to maximize formation of MoS<sub>2</sub> [13]. The availability of additional sulphur in ZDDP may also promote MoS<sub>2</sub> formation. However, the precise mechanism by which both the chemical properties of MoDTC tribofilms affect DLC wear and the way that ZDDP partially alleviates this wear are not fully proven. It should also be noted that the impact of other surface-active additives used in engine lubricants on MoDTC/DLC wear has not been studied to any significant extent.

Based on the above, the research described in this Chapter aims to understand whether informed lubricant formulation can control the deleterious impact of MoDTC on a-C:H DLC wear and to determine the underlying mechanisms involved. To achieve this, the influence of various lubricant additives on wear of a DLC-coated component rubbed against a steel counterpart in MoDTC-containing oil has been investigated. Additives studied include a ZDDP, a phosphorus-based extreme pressure (EP) additive, Ca detergents, dispersants, an organic friction modifier (OFM) and a polymethacrylate (PAMA). The chemical properties of tribofilms generated were analysed by TEM, STEM-EDX, Raman spectroscopy and XPS.

## **8.2 Test Method**

### **8.2.1 Test Lubricants and Materials**

A single MoDTC was studied at a concentration of 300 ppm of Mo in a base oil (PAO). This is a slightly lower concentration than used in some modern engine oil formulations and represents the maximum solubility in the neat PAO [333]. To ensure thin film and thus boundary lubrication conditions, the relatively low viscosity PAO, PAO4 was chosen. A series of other additives commonly used in engine oils were blended individually into this MoDTC solution in PAO. These are all at their typically used concentrations except for the detergent that is often used at a somewhat higher concentration [51,333]. The oil formulations studied, together with their kinematic viscosities, are listed in Table 8-1.

Table 8-1 Test oil formulations (Mo denotes MoDTC)

Lubricant name	Additives concentration	Viscosity at 40 °C/100 °C, mm <sup>2</sup> /s
PAO	-	18.5/4.1
PAO+Mo	Mo: 300 ppm	17.4/4.0
PAO+Mo+ZDDP(25) (ZDDP: secondary C6)	Mo: 300 ppm, P: 25 ppm	17.8/4.0
PAO+Mo+ZDDP(50) (ZDDP: secondary C6)	Mo: 300 ppm, P: 50 ppm	17.9/4.1
PAO+Mo+ZDDP(800) (ZDDP: secondary C6)	Mo: 300 ppm, P: 800 ppm	18.0/4.1
PAO+Mo+EP (EP: Alkylated triphenyl phosphorothionate)	Mo: 300 ppm, P: 800 ppm	18.1/4.2
PAO+Mo+Ca(OB) (Ca(OB): Overbased calcium salicylate)	Mo: 300 ppm, Ca: 1000 ppm Base/Soap: 16.6/8.3 mmol/kg	18.3/4.1
PAO+Mo+Ca(Neu) (Ca(Neu): Neutral calcium salicylate)	Mo: 300 ppm, Ca: 1000 ppm Base/Soap: 7.1/17.7 mmol/kg	18.7/4.2
PAO+Mo+Disp (Disp: Succinimide dispersant)	Mo: 300 ppm, N: 400 ppm	21.0/4.6
PAO+Mo+Disp(B) (Disp(B): Borated succinimide dispersant)	Mo: 300 ppm, N: 400 ppm, B: 400 ppm	19.4/4.3
PAO+Mo+OFM (OFM: Glycerol monooleate)	Mo: 300 ppm, OFM: 0.5 wt. %	18.2/4.1

PAO+Mo+PAMA  (PAMA: Comb type poly- alkylmethacrylate, 40 wt.% solution in Gr. III base oil)	Mo: 300 ppm,  PAMA: 4.0 wt.%	18.4/4.4
--	------------------------------------	----------

AISI 52100 steel balls and a-C:H DLC-coated AISI 52100 discs supplied by PCS Instruments were used. This hydrogenated DLC consists primarily of  $sp^2$  with 30%  $sp^3$ , has a thickness of 2-4  $\mu m$  and does not contain any metal dopants and is the same DLC coating as described in Chapter 7; its mechanical properties and composition are listed in Table 7-1 and Table 7-2.

### 8.2.2 Test Procedure and Condition

The MTM was used to investigate DLC wear and tribofilm formation under boundary lubrication at the test conditions listed in Table 8-2. By using a very low entrainment speed (mean velocity of the two surfaces with respect to the contact), MTM tests were controlled to an initial theoretical lambda ratio (ratio of EHD film thickness to composite surface roughness) of less than 0.3, corresponds to 5 nm of minimum oil film thickness, thus providing boundary lubrication conditions. Load was set at a value that gave a maximum Hertz pressure of 0.95 GPa in the contact. After the tests, wear tracks on DLC discs were observed by an optical microscope, an optical white light interferometer and Raman spectroscopy. The wear tracks on steel balls were observed by the optical microscope, TEM, STEM-EDX, Raman spectroscopy, XPS and SEM-EDX. Most tribofilms formed on steel balls were quantified by SLIM, but tribofilms formed in PAO+Mo+OFM after 15, 30, 60 and 180 minutes were measured by a Talysurf profilometer since the tribofilm was too thick to be measured by SLIM. For Talysurf measurements, the steel ball was removed from the MTM, and then gently rinsed with toluene to remove supernatant oil. After stylus profilometer measurement, the ball was returned to the rig, and the rubbing test restarted. The same lubricant sample remained in the test chamber for the whole 3 hours test duration. All MTM tests were conducted twice to verify repeatability.

Table 8-2 MTM test conditions (boundary lubrication conditions)

Entrainment speed; $U = (U_{ball} + U_{disc})/2$	100 mm/s
--	----------



Slide-roll-ratio; $SRR = 100 \cdot (U_{disc} - U_{ball}) / U$	50%
Applied load (DLC on steel)	31 N; max. Hertz pressure = 0.95 GPa
Lubricant temperature	100 °C
Test duration	3 hours

### 8.2.3 Tribofilm Analysis

TEM, STEM-EDX, XPS and SEM-EDX were carried out using the same methodologies described in Chapters 5 and 6. Spot size for XPS analysis was 150  $\mu\text{m}$ . Before measurements, the specimens were gently rinsed by toluene to remove supernatant oil. This did not remove any measurable tribofilm. Raman spectroscopy was performed to examine the chemical composition of DLC discs and tribofilms on steels. This used a WiTec Confocal Raman spectrometer alpha 300 equipped with multiple objectives and a charge-coupled device detector. A laser with 532 nm wavelength was employed and Raman spectra was collected from a 20  $\mu\text{m} \times 20 \mu\text{m}$  area. The D band and G band peaks attributed to carbon were fitted with Lorentzians and the area ratio of D peak to G peak ( $I_D/I_G$ ) was estimated.

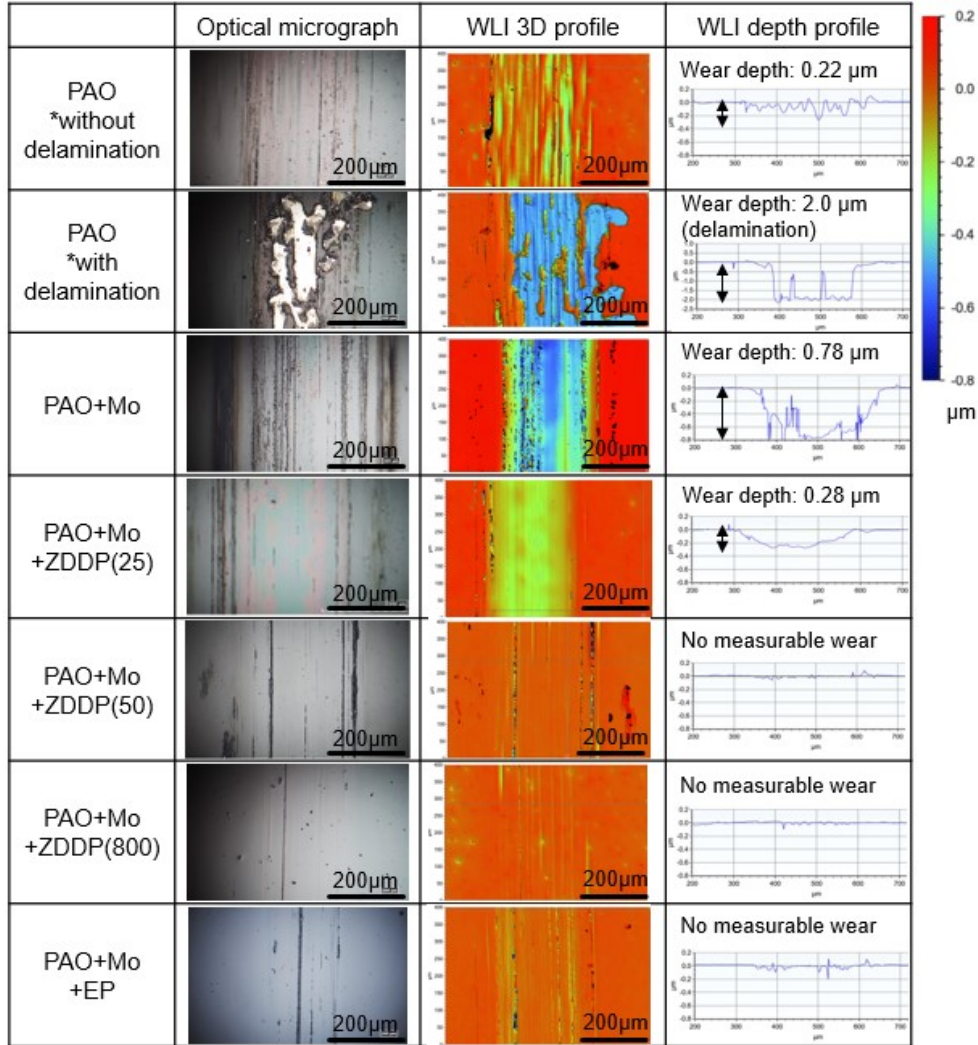
## 8.3 Results

### 8.3.1 DLC Disc Wear

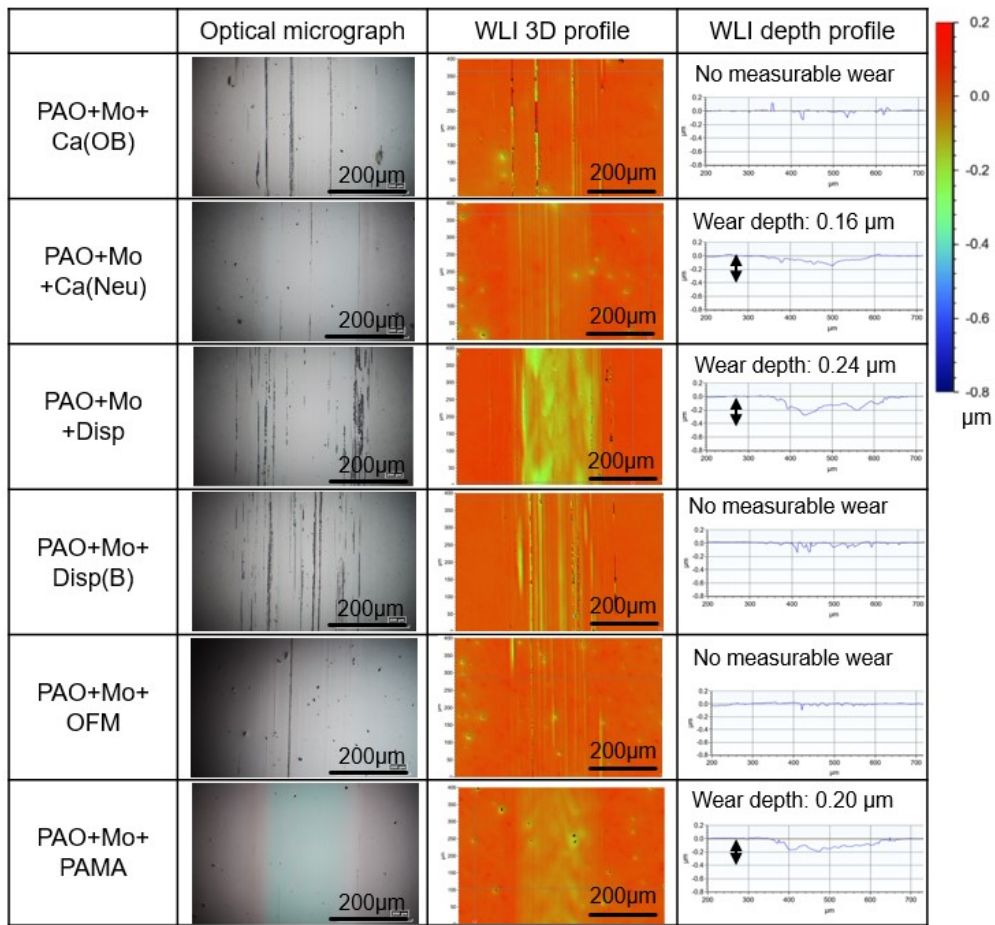
Worn DLC disc surfaces after MTM tests were observed by optical micrography and WLI as shown in Figure 8-1. It is important to note that the colour scale of WLI 3D profiles and the depth scale of WLI depth profiles correspond to -0.8  $\mu\text{m}$  to 0.2  $\mu\text{m}$  for most images, but that the scale in images obtained from PAO with delamination are -2.5  $\mu\text{m}$  to 1.0  $\mu\text{m}$ . The wear volumes of DLC discs over the areas shown in Figure 8-1 (400  $\mu\text{m} \times 600 \mu\text{m}$ ) are summarized in Figure 8-2. The wear volume from tests in PAO alone was obtained from a region without DLC delamination.

Rubbing the steel ball against DLC disc in PAO alone, without any additives, resulted in delamination of the DLC coating over approximately half of the track, with the remainder showing 0.22  $\mu\text{m}$  depth and  $0.9 \times 10^3 \mu\text{m}^3$  volume of predominantly abrasive wear. The worn surface was rougher than from other tests. By contrast, PAO+Mo oil generated a

high level of quite even wear of 0.78  $\mu\text{m}$  depth over the whole rubbed track, with  $3.7 \times 10^3 \mu\text{m}^3$  wear volume. The addition of all surface-active additives alleviated this DLC wear to varying extents. ZDDP(25), Ca(Neu), Disp and PAMA partially reduced wear, with maximum depths of 0.28  $\mu\text{m}$ , 0.16  $\mu\text{m}$ , 0.24  $\mu\text{m}$  and 0.20  $\mu\text{m}$ , respectively, corresponding to less than  $1.5 \times 10^3 \mu\text{m}^3$  of wear volume. ZDDP(50), ZDDP(800), EP, Ca(OB), Disp(B) and OFM gave less than  $0.2 \times 10^3 \mu\text{m}^3$  of wear volume.



(a)



(b)

Figure 8-1 Optical micrographs, WLI 3D profiles and depth profiles of wear tracks on DLC discs (Note that the colour scale is not applicable to the image with delamination obtained from PAO rubbing since its depth scale is much larger than others.)

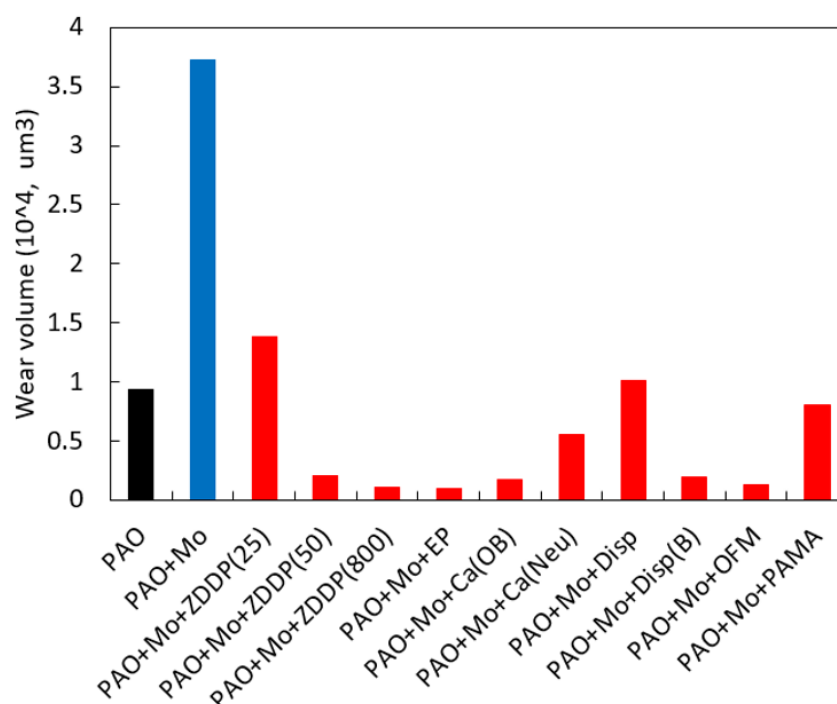


Figure 8-2 Wear volume of DLC wear tracks measured using WLI (area: 400  $\mu\text{m} \times$  600  $\mu\text{m}$  in Figure 8-1)

### 8.3.2 Tribofilm Formation on Steel Balls

The wear tracks on the steel balls were observed using an optical microscope and in SLIM images in order to relate any tribofilms present to DLC wear. The film rubbed in PAO+Mo+OFM was quantified by stylus profilometry since it was too thick to measure using SLIM. Figure 8-3 and Figure 8-4 shows the optical micrographs and the evolution of film thickness during the tests. PAO alone formed dark coloured films on the wear track of 26 nm thickness at the end of the 3 hours test. Given wear on the DLC disc and no additives in the lubricant, these dark coloured film may be attributed to carbon transferred from the DLC disc to the steel ball. PAO+Mo formed a lighter coloured film of 19 nm thickness. This film may consist of MoDTC tribofilm and/or transferred carbon from the DLC disc, since the latter experienced high wear in this oil. The addition of ZDDP(800), Ca(OB) and OFM resulted in thicker tribofilms than just PAO+Mo, respectively 39 nm, 40 nm and 410 nm. Interestingly, PAO+Mo+OFM formed a much thicker tribofilm than the other additives, covering the whole wear track. The addition of Ca(Neu) formed a tribofilm of *ca.* 20 nm, similar in thickness to that formed in PAO+Mo, whereas the oils with ZDDP(25), ZDDP(50), EP, Disp, Disp(B) and PAMA formed

thinner tribofilms, approximately 10 nm, than PAO+Mo. These results suggest that films on the steel balls are composed of one or both of transferred carbon and tribofilms produced by adsorption or reaction of the various lubricant additives.

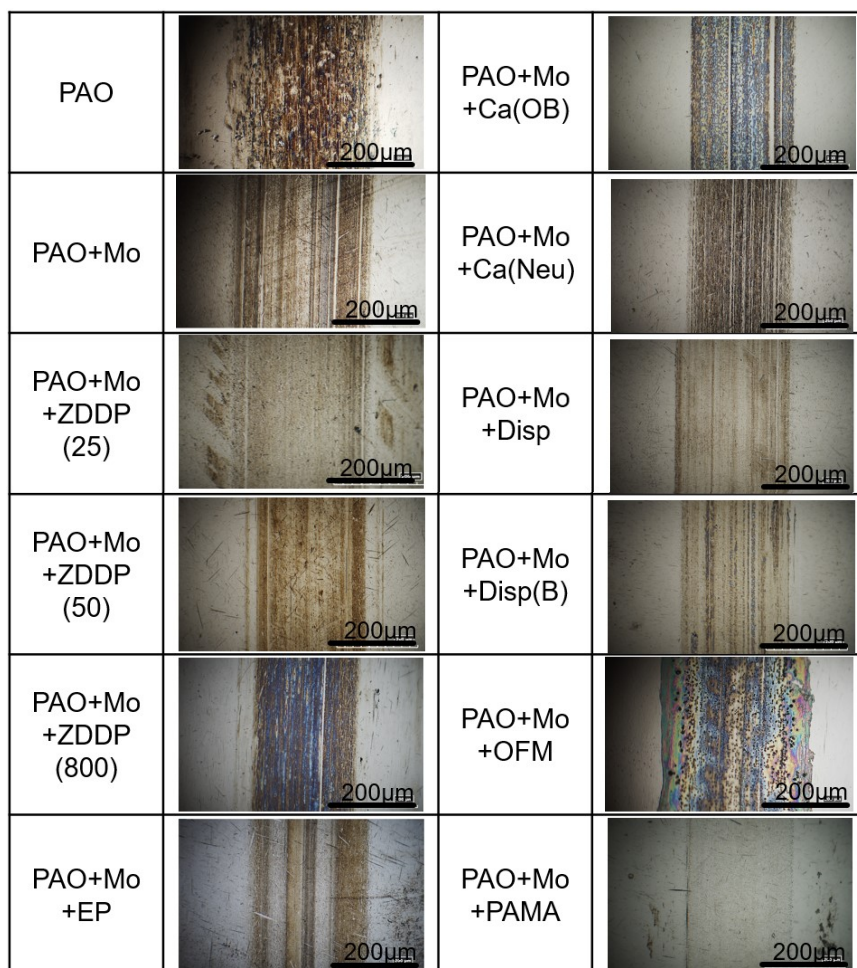
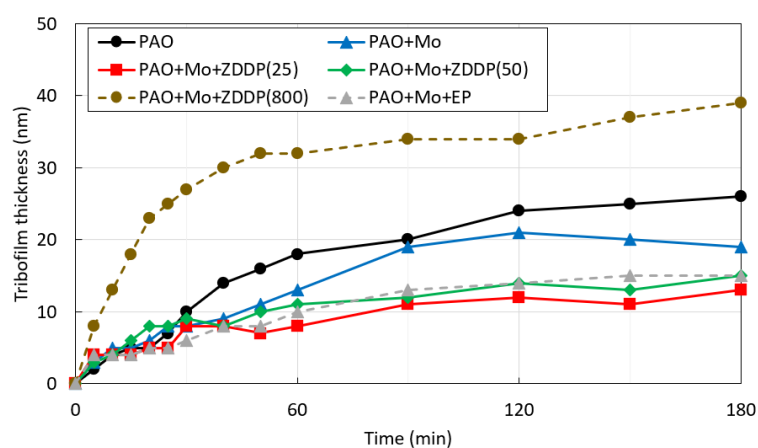
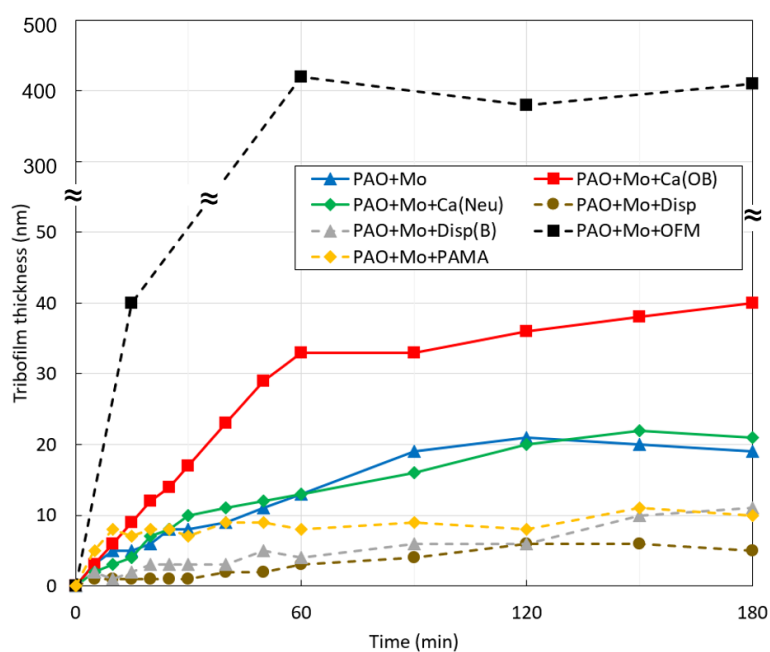


Figure 8-3 Optical micrographs of the wear tracks on the steel balls after three hours rubbing tests



(a)



(b)

Figure 8-4. The evolution of tribofilm thickness on the steel balls during the tests measured by using SLIM and, for PAO+Mo+OFM, using a stylus profilometer.

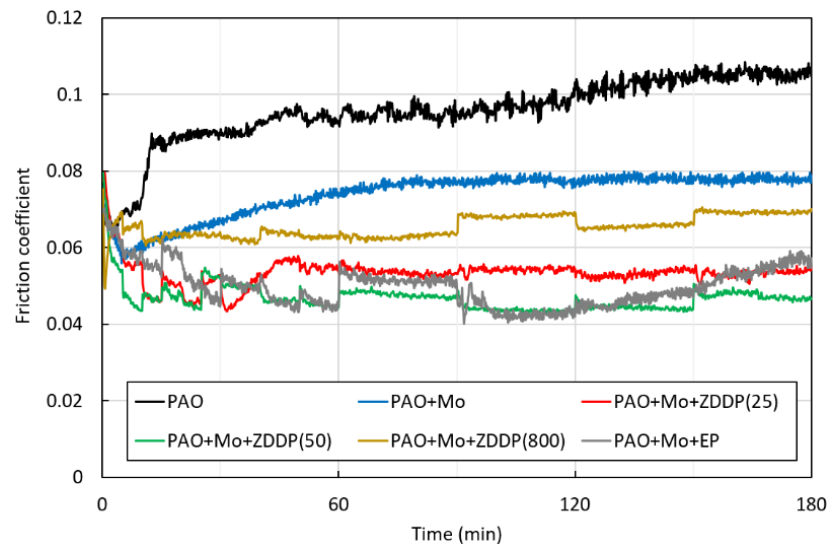
### 8.3.3 Friction Behaviour

To understand the effect of friction on DLC wear, the evolution of friction coefficient during the MTM tests was measured as shown in Figure 8-5. It should be noted that the sudden jumps obtained with all blends except PAO+Mo in the recorded friction coefficient traces in this figure are artefacts of the measurement method since they occur just after motion is paused for capture of a SLIM image.

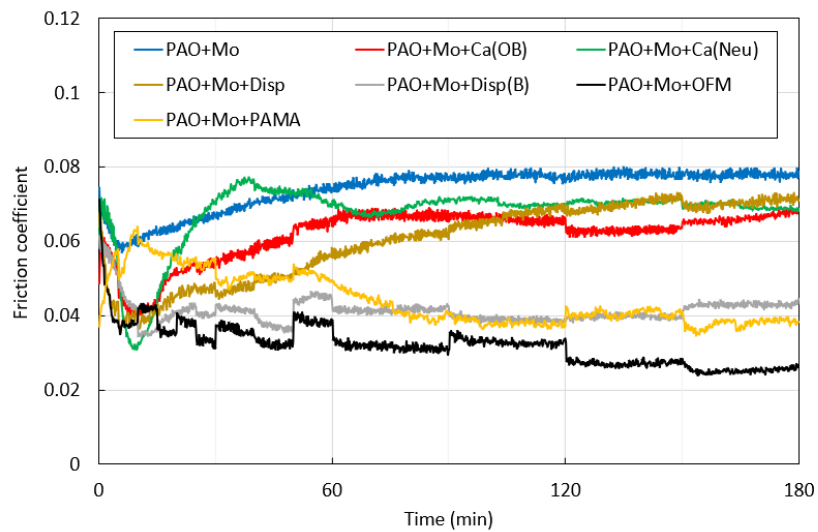
For PAO alone, friction coefficient decreased from 0.08 to 0.07 at the beginning of test, and then increased after 10 minutes rubbing to reach 0.09 - 0.11 at the end of the test. Friction also showed relatively high fluctuations. The reduction of friction coefficient during the tests with a-C:H DLC/steel tribopair has been reported in dry condition [334,335] and in PAO alone [336], and in the latter the authors suggested that lowered friction coefficient resulted from carbon films transferred from DLC to a steel wear track. Given the apparent carbon films on the steel ball in Figure 8-3 and Figure 8-4, the reduction of friction coefficient in the first 10 minutes may result from this transferred carbon films as reported. After this, the DLC coating probably started to be severely delaminated with an increase of surface roughness, resulting in high friction coefficient [337,338].

PAO+Mo showed lower friction coefficient during the test than PAO alone, reaching 0.06 after 5 minutes, and then increased to 0.08. Note that no sudden friction jumps were observed for this blend since the test was carried out without halting the rig for SLIM measurement. The addition of ZDDP(800), Ca(OB), Ca(Neu) and Disp to an MoDTC solution gave lower friction coefficients than PAO+Mo, that slightly increased towards the end of the tests to reach 0.07. By contrast, friction coefficient in the oils with ZDDP(25), ZDDP(50), EP, Disp(B), OFM and PAMA remained at a low level, 0.03 - 0.06 throughout the 3 hours tests.





(a)



(b)

Figure 8-5 The evolution of friction coefficient during the tests

### 8.3.4 Elemental Distribution of Tribofilm on Steel

The tribofilms formed on the steel balls rubbed against DLC in PAO+Mo at the end of 3-hour tests were analysed using TEM and STEM-EDX in order to determine the morphology and elemental distribution in the film. Figure 8-6 shows a TEM image, a



STEM image and a STEM-EDX line profile along the yellow line in the STEM image. The TEM image shows tribofilm thickness is approximately 20 nm, which agrees with the thickness value measured by SLIM in Figure 8-4. The EDX line profile shows that, while the tribofilm is mainly composed of Mo and S, smaller amount of C and O are present in all regions of the tribofilm. This result show that carbon is present within the MoDTC tribofilm rather than just being attached to the outermost surface.

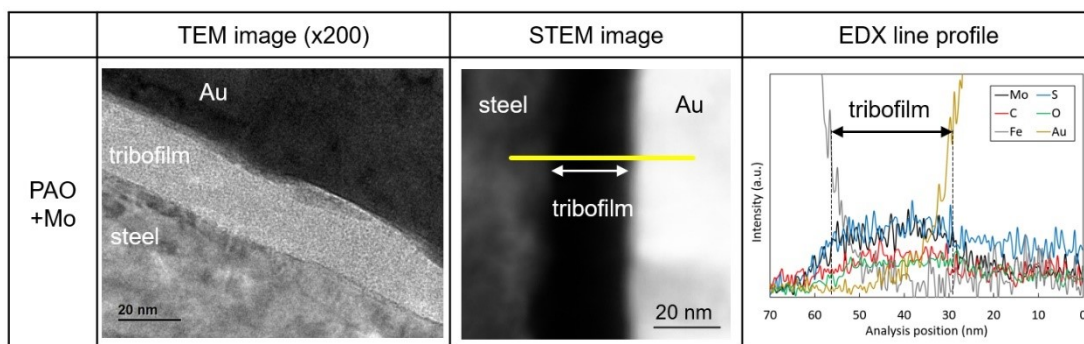


Figure 8-6 TEM image, STEM-EDX image and element distribution of tribofilm on the steel ball rubbed in PAO+Mo after a 3 hour test

### 8.3.5 Raman Spectra of Steel Wear Tracks

Worn surfaces on steel balls and the surface of a fresh DLC disc were analysed using Raman spectroscopy in order to examine the structure of transferred carbon on wear tracks on the steel ball. Abrasive type wear, high volume wear and mild volume wear were observed on DLC discs rubbed in PAO, PAO+Mo, and PAO+Mo+ZDDP(25) respectively. Also, no measurable wear was observed in the oils with ZDDP(50) and ZDDP(800). Therefore, the films formed on steel balls rubbed in these 5 oils were analysed. Figure 8-7 shows the resulting Raman spectra normalized to the maximum peak in spectral range 800 - 2200  $\text{cm}^{-1}$ . The D and G peaks that are characteristic of carbon at 1300 - 1380  $\text{cm}^{-1}$  and 1570 - 1600  $\text{cm}^{-1}$  respectively are evident in the PAO, PAO+Mo and PAO+Mo+ZDDP(25) spectra, without any significant peak shifts. The D peak corresponds to disordered carbon or defective graphitic structure whereas the G peak corresponds to the graphitic layer and tangential vibration of the carbon atom [29]. An increase of ratio of these peaks, the  $I_D/I_G$  ratio, represents an increase of  $\text{sp}^2$  structure of carbon, *i.e.* graphitization.

On the wear track rubbed in PAO alone, a similar  $I_D/I_G$  ratio of 1.10 compared to a fresh DLC disc ratio of 1.14, was observed. Given the optical image in Figure 8-3, this suggests

that carbon with a similar structure to fresh DLC disc was transferred to the steel ball rubbed in PAO. Understanding of  $I_D/I_G$  ratio of carbon film on steel transferred from a-C:H DLC is still controversial; Erdemir et al. [334] and Rabbani [335] found that carbon transferred from DLC to steel in dry contact had higher  $I_D/I_G$  than carbon in fresh DLC, suggesting that transferred carbon was graphitized. By contrast, Haque et al. [339] showed that an equivalent  $I_D/I_G$  ratio to DLC was observed in carbon film transferred onto a steel surface from DLC rubbed in PAO. In the current study, transferred carbon rubbed in PAO alone gave no significant change in  $I_D/I_G$ , as reported by Haque et al [339]. Possibly, rubbing conditions and initial a-C:H DLC properties affect the properties of transferred carbon films on steel surfaces.

The addition of Mo and Mo+ZDDP(25) to PAO show lower  $I_D/I_G$  ratios (0.97 and 1.01 respectively) than that of a fresh DLC disc (1.14). This trend was observed in a previous study of a steel/a-C:H DLC tribopair in an MoDTC oil by Okubo et al [59], and the authors suggested that a reduction of  $I_D/I_G$  ratio resulted from the formation of MoC species, which has a low  $I_D/I_G$  ratio, 0.45. Based on this suggestion, the low  $I_D/I_G$  ratio in this study may be tentatively attributed to MoC species on the steel balls rubbed in PAO+Mo and PAO+Mo+ZDDP(25). By comparison, the wear tracks rubbed in PAO+Mo+ZDDP(50) and PAO+Mo+ZDDP(800) do not give D and G peaks. This suggests that no carbon was transferred to the steel balls from the DLC discs and is consistent with the negligible DLC wear rubbed in this oil, as shown in Figure 8-1.

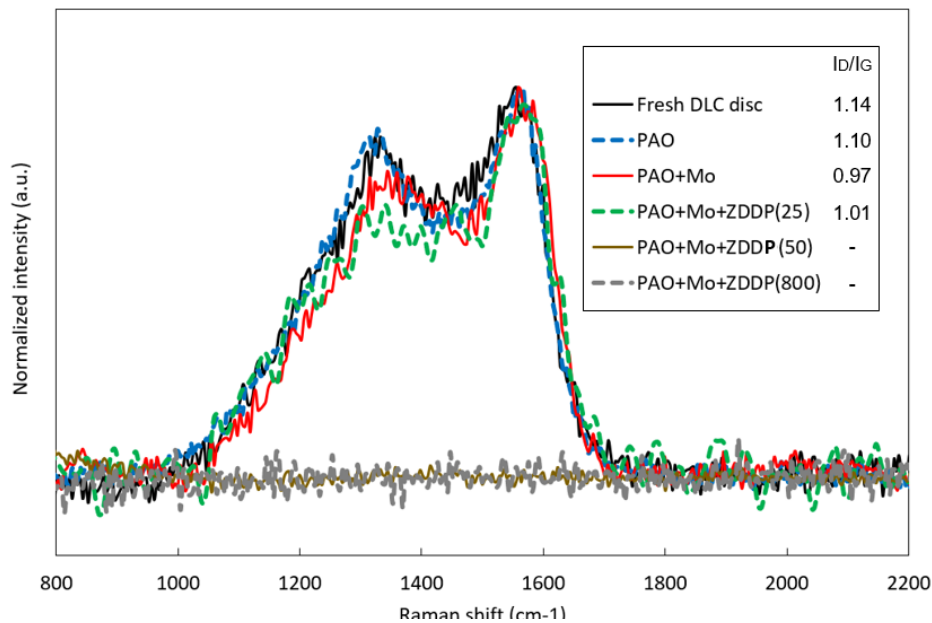


Figure 8-7 Raman spectra from the wear tracks on the steel balls after 3 hour tests and from the fresh DLC disc surface

### 8.3.6 XPS Analysis of Steel Wear Tracks

To understand the chemical environment of carbon and molybdenum in the tribofilms formed on the steel counterfaces, the wear tracks on the balls were analysed using XPS. C 1s and Mo 3d XPS spectra are shown in Figure 8-8 and Figure 8-9, respectively. All peaks were normalized by the highest peak. In Fig. 9, the C 1s spectra consist of the peaks of C-C at 284.8 eV, C-O at  $286.6 \pm 0.2$  eV, C=O at  $288.0 \pm 0.2$  eV and carbide at  $283.1 \pm 0.2$  eV [60]. The peak area ratio of carbide/C-C is included in the figure. The wear tracks rubbed in PAO+Mo and PAO+Mo+ZDDP(25) show relatively higher intensity carbide peaks than the others, with carbide/C-C ratio of 0.068 and 0.048 respectively. By comparison, a quite small carbide peak is observed on the wear track rubbed in PAO. Thus, given the results of Raman spectra in Figure 8-7, the carbide peaks obtained from PAO+Mo and PAO+Mo+ZDDP(25) may be attributed to mainly Mo-C species, not Fe-C species.

As reported in many previous XPS analyses of MoDTC-derived tribofilms on steel rubbed against DLC [59,60,326,328], the Mo 3d spectra contain mainly the peaks of  $\text{Mo}^{4+}$  at  $228.7 \pm 0.4$  eV and  $232.2 \pm 0.4$  eV,  $\text{Mo}^{5+}$  at  $230.0 \pm 0.3$  eV and  $233.9 \pm 0.3$  eV,  $\text{Mo}^{6+}$  at  $232.2 \pm 0.2$  eV and  $235.4 \pm 0.2$  eV, and S 2s at  $225.9 \pm 0.3$  eV.  $\text{Mo}^0$  and  $\text{Mo}^{2+}$ , attributed to Mo metal and Mo-C species, may exist in Mo 3d spectra, but unfortunately these peaks are difficult to distinguish from  $\text{Mo}^{4+}$ ,  $\text{Mo}^{5+}$  and  $\text{Mo}^{6+}$  because of peak overlap and low intensity. Thus, Mo 3d spectra in Figure 8-9 were fitted with,  $\text{Mo}^{4+}$ ,  $\text{Mo}^{5+}$  and  $\text{Mo}^{6+}$ , attributed to  $\text{MoS}_2$  and/or  $\text{MoO}_2$ , MoDTC, and  $\text{MoO}_3$ , respectively. Since  $\text{MoS}_2/\text{MoO}_3$  ratio is believed to be an important property of MoDTC tribofilms [326], the peak area ratios of  $\text{Mo}^{4+}/\text{Mo}^{6+}$  are shown in Figure 8-9. PAO+Mo gave a low  $\text{Mo}^{4+}/\text{Mo}^{6+}$  of 0.16, which is similar to the values obtained from PAO+Mo+Ca(OB), PAO+Mo+OFM and PAO+Mo+PAMA. The addition of ZDDP(25) and Disp slightly increased  $\text{Mo}^{4+}/\text{Mo}^{6+}$  to 0.43 and 0.48 respectively. By comparison, the addition of ZDDP(50), ZDDP(800), EP, Ca(Neu) and Disp(B) increased  $\text{Mo}^{4+}/\text{Mo}^{6+}$  to over 0.6. This suggests that the addition of some additives changes the chemical properties of MoDTC tribofilms and increases  $\text{Mo}^{4+}/\text{Mo}^{6+}$ , while others do not.

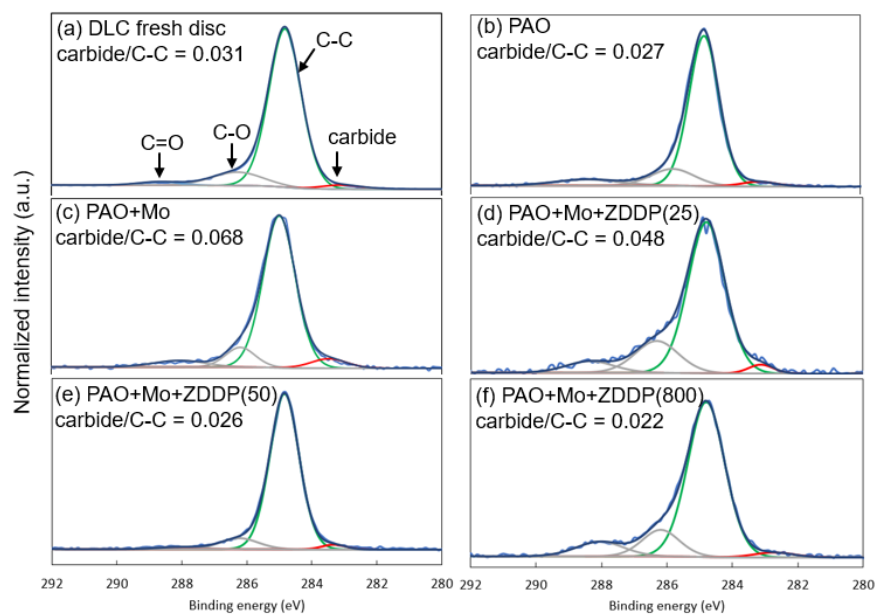


Figure 8-8 C 1s XPS spectra of tribofilms on the wear tracks on the steel balls  
(a) DLC fresh disc, (b) PAO, (c) PAO+Mo, (d) PAO+Mo+ZDDP(25), (e)  
PAO+Mo+ZDDP(50), (f) PAO+Mo+ZDDP(800)

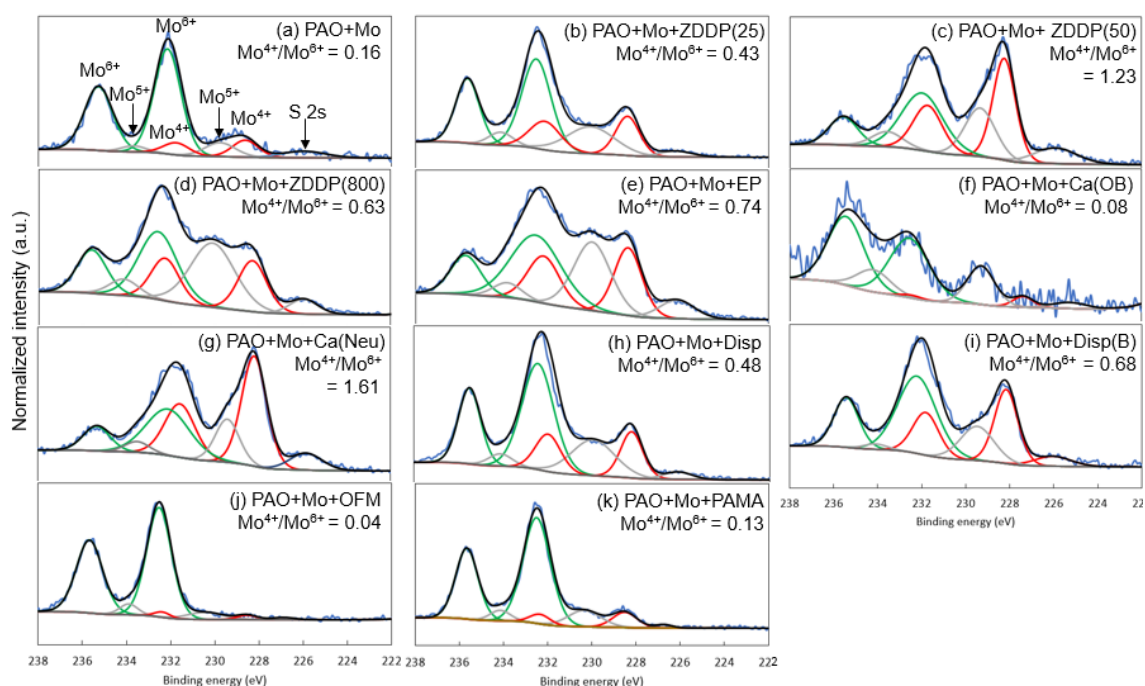


Figure 8-9 Mo 3d XPS spectra of tribofilms on the wear tracks on the steel balls (a) PAO, (b) PAO+Mo+ZDDP(25), (c) PAO+Mo+ZDDP(50), (d) PAO+Mo+ZDDP(800), (e) PAO+Mo+EP, (f) PAO+Mo+Ca(OB), (g) PAO+Mo+Ca(Neu), (h) PAO+Mo+Disp, (i) PAO+Mo+Disp(B), (j) PAO+Mo+OFM, (k) PAO+Mo+PAMA

#### 8.4 Discussion

It is evident from the above results that, while wear of a-C:H DLC against steel is promoted by MoDTC, such wear is mitigated to a greater or lesser extent by the addition of several commonly-used, surface-active engine oil additives to the MoDTC/base oil solution. Previous studies have suggested that addition of ZDDP to an MoDTC-containing oil forms a thick antiwear tribofilm, resulting in the prevention of asperity contact of DLC and steel surfaces and thus the reduction of DLC wear [59,64,331,332]. The results in this study provide some support for this suggestion as discussed below. However, based on the mechanism of DLC wear against steel, three possible reasons why DLC wear was reduced by the addition of surface-active additives to PAO+Mo can be suggested;

- (i) formation of thick antiwear tribofilm
- (ii) increase of MoS<sub>2</sub>/MoO<sub>3</sub> ratio in the MoDTC tribofilm
- (iii) reduction of MoDTC tribofilm formation

Each of these possibilities is discussed below with respect to the tribofilms observed with the various surface-active additives studied.

#### **8.4.1 Formation of Thick Antiwear Tribofilm**

As reported, one of the most effective ways to protect DLC surfaces from wear is to form thick antiwear tribofilms to alleviate asperity contact between DLC and steel. In this study, as shown in Figure 8-4, the addition of ZDDP(800), Ca(OB) and OFM formed thicker tribofilms than other additives. These also resulted in very little DLC wear. It is very well known that ZDDP forms surface-protective phosphate tribofilms on steel surfaces [67]. In this study, 800 ppm P concentration of ZDDP formed 39 nm tribofilm at the end of the test. This antiwear performance of ZDDP tribofilm on a-C:H DLC/steel tribopair agrees with previous studies [59,64,331,332].

Generally, overbased Ca detergents that contain colloidal  $\text{CaCO}_3$  form thick  $\text{CaCO}_3$  tribofilms on rubbed surfaces, and these provide antiwear performance [340]. In the current study, 40 nm of tribofilm was formed from PAO+Mo+Ca(OB) at the end of the test; a similar thickness to that formed by PAO+Mo+ZDDP(800). Because it contains far less colloidal  $\text{CaCO}_3$ , Ca(Neu) forms a thinner tribofilm and gives more wear in PAO with MoDTC. By contrast, OFMs form physically and/or chemically adsorbed films, and do not generally form thick tribofilm. In this study, however, very thick tribofilms, of approximately 410 nm thickness were observed on the steel ball surfaces at the end of the test. In order to understand the composition of the tribofilm formed in PAO+Mo+OFM, this was analysed using SEM-EDX as summarized in Figure 8-10, where it is compared with the tribofilm formed by PAO+Mo. Tribofilm formed in PAO+Mo+OFM was mainly composed of carbon with a higher carbon content than that formed in PAO+Mo, together with small amount of molybdenum. Given that there was no significant DLC wear in PAO+Mo+OFM in Figure 8-1, this carbon was not transferred from the DLC disc. Thus, this carbon was formed from a lubricant component, probably mainly from OFM. A previous study showed that carbon-based tribofilms formed from PAO gave surface protection performance [341], thus, this thick carbon-containing film may protect surface in a similar fashion to the protection afforded by the tribofilms formed from the oils with ZDDP(800) and Ca(OB).

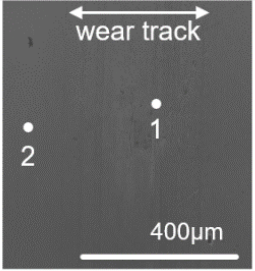
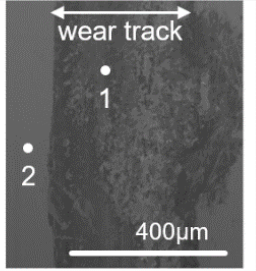
		PAO+Mo		PAO+Mo+OFM	
SEM image x150					
chemical composition (atomic%)		point 1	point 2	point 1	point 2
	Mo	2.1	None	1.0	None
	C	12.8	6.9	27.4	7.9
	O	10.4	8.9	16.5	9.4
	Fe	71.8	81.4	53.4	79.4
	Cr	1.7	1.3	1.1	1.9
	Mn	0.6	0.5	0.3	0.7
	Si	0.6	1.0	0.5	0.7

Figure 8-10 Chemical composition of tribofilms formed in PAO+Mo and PAO+Mo+OFM using SEM-EDX

Although the mechanism of a-C:H DLC wear has not been clearly understood, Okubo et al. [59] suggested that MoC compounds formed through tribochemical reaction on the steel counterface have significantly higher hardness, *ca.* 25 GPa, than a-C:H DLC, *ca.* 10 GPa, and that this hard MoC causes severe abrasive wear of DLC surface. This severe abrasive wear may be reduced by forming thick tribofilms even if hard MoC compounds are also formed on steel surfaces. The presence of carbon and Mo-C species in tribofilms rubbed in PAO+Mo and PAO+Mo+Zn(25) was based on analyses using STEM-EDX, Raman and XPS and little evidence of the presence of MoC species in tribofilms was observed. Alternatively, it has been proposed that the high wear of DLC promoted by MoDTC may originate from graphitization of the DLC that is easily abraded by the steel counterface [327–330]. In this case, the formation of a tribofilm on the steel counterface may limit this abrasion, or render the steel surface chemically inactive so that it does not, in combination with MoDTC, promote the graphitization.

#### 8.4.2 Increase of MoS<sub>2</sub>:MoO<sub>3</sub> Ratio

Many of the additives studied reduced the DLC wear promoted by MoDTC but did not form thick tribofilms. This suggests that as well as protection by thick tribofilms, there may be other mechanisms by which additives can mitigate the severe DLC wear that occurs with MoDTC. Since MoO<sub>3</sub> is believed to be a culprit for promoting DLC wear by oxidizing or abrading DLC surfaces [326–330], reduction of the MoO<sub>3</sub> in MoDTC tribofilms is a possible way to reduce DLC wear. Grossiord et al. [342] and De Barros' Bouchet et al. [343] proposed a tribochemical reaction mechanism of formation of MoO<sub>3</sub> from MoDTC. They suggested that after adsorption, MoDTC is tribochemically decomposed to form MoS<sub>2</sub>, MoS<sub>2-x</sub>O<sub>x</sub> and MoO<sub>x</sub>. While these compounds may be oxidized to form MoO<sub>3</sub>, the latter can react with sulphur to form MoS<sub>2</sub>. It is well studied that co-existent ZDDP provides sulphur to Mo compounds, promoting MoS<sub>2</sub> formation [239,241,343]. Thus, the prevention of oxidation and/or the promotion of sulphurisation are both ways to increase the ratio of MoS<sub>2</sub>:MoO<sub>3</sub> ratio in MoDTC tribofilms and thereby reduce DLC wear. In this study, while Mo<sup>4+</sup> can in principle be attributed to both MoS<sub>2</sub> and MoO<sub>2</sub>, MoS<sub>2</sub> is probably the main component as most studies discuss [326–328,343], since a higher intensity of S was observed than O in the MoDTC tribofilm in Figure 8-6. Thus, the ratio of Mo<sup>4+</sup> to Mo<sup>6+</sup> can be regarded as representing the ratio of MoS<sub>2</sub> to MoO<sub>3</sub>.

As shown in Figure 8-9, the addition of ZDDP(50), EP, Ca(Neu) and Disp(B) all gave much higher Mo<sup>4+</sup> to Mo<sup>6+</sup>, and thus higher MoS<sub>2</sub> to MoO<sub>3</sub> ratios, than PAO+Mo and this correlates with their giving low DLC wear. ZDDP(50) and EP both contain sulphur, so they may be increasing the MoS<sub>2</sub>:MoO<sub>3</sub> ratio by providing sulphur, but they are both also peroxide decomposers and so may also, or alternatively, be preventing oxidation of MoDTC breakdown products to MoO<sub>3</sub> [67]. From Figure 8-2 and Figure 8-9, it appears that the 25 ppm level of ZDDP in PAO+Mo+Zn(25) was too low to raise the MoS<sub>2</sub>:MoO<sub>3</sub> ratio to a high enough value to prevent high DLC wear. Ca(Neu) and Disp(B) also both reduce DLC wear and raise the MoS<sub>2</sub>:MoO<sub>3</sub> ratio but they do not contain any sulphur. In this case therefore, the likely mechanism by which they influence the MoS<sub>2</sub>:MoO<sub>3</sub> ratio is by inhibiting oxidation to MoO<sub>3</sub>. It has been reported that salicylates and borated additives can both prevent the oxidation of Mo compounds [85,246,333,344].

Although higher MoS<sub>2</sub>:MoO<sub>3</sub> usually corresponded to lower friction coefficient, a direct correlation between friction behaviour and MoS<sub>2</sub>:MoO<sub>3</sub>, as reported in a previous study [326,339] was not confirmed. This suggests that other factors that influence friction



behaviour may also be active, such as a low friction carbon film transferred from DLC to steel [339].

#### **8.4.3 Reduction of MoDTC Tribofilm Formation**

Although the influence of other additives on reducing DLC wear in the presence of MoDTC can be explained by the above two mechanisms, a third likely mechanism should also be considered. This is simply competitive adsorption of these other additives on surfaces to suppress the rate at which MoDTC reacts on steel, thereby reducing its harmful effect on DLC wear. In this study, all the additives tested are capable of adsorbing on steel surfaces and may act in this fashion to some extent. Clearly, this might be beneficial in terms of reducing wear, but would be undesirable if MoDTC tribofilm formation, and thus its ability to reduce boundary friction were completely suppressed. It is possible that the modest reduction in DLC wear provided by PAMA results from inhibition of MoDTC reaction via adsorption since thick film and increase MoS<sub>2</sub>:MoO<sub>3</sub> ratio were not observed. However, it is also possible that the PAMA adsorbs on the rolling/sliding ball on disc surfaces to form a thick separating film that prevents some asperity interaction and so limits wear via the mechanism outlined in Section 9.3.2 [92]. PAMA has been shown to form thick viscous surface films that increase separation in dynamic conditions but do not withstand static conditions, so boundary films generated from PAMA in rolling-sliding contacts might not be observed using SLIM.

This study shows that the addition of several types of surface-active additive can reduce DLC wear in an MoDTC-containing oil to a greater or lesser extent, and indicates three possible mechanisms by which this may occur. Figure 8-11 plots the wear volume against Mo<sup>4+</sup>/Mo<sup>6+</sup> ratio and, based on tribofilm thickness measurements and Raman analyses, maps the regions over which these mechanisms may be active. Thick tribofilms appear to suppress DLC wear very effectively without the need for increasing MoS<sub>2</sub>:MoO<sub>3</sub> ratio, while increasing MoS<sub>2</sub>:MoO<sub>3</sub> ratio without forming a thick tribofilm is also quite effective at suppressing wear. In practice, many surface-active additives exist together with MoDTC in engine lubricants and the extent to which these additives in combination suppress DLC wear in the presence of MoDTC remains to be determined. Also, modern requirements of high fuel economy and low emissions are resulting in considerable changes in the design of engine oils, as well, in some cases, increasing Mo-base friction modifier concentrations, so it is important to understand and take account of the impact of other additives on DLC wear in the presence of MoDTC.

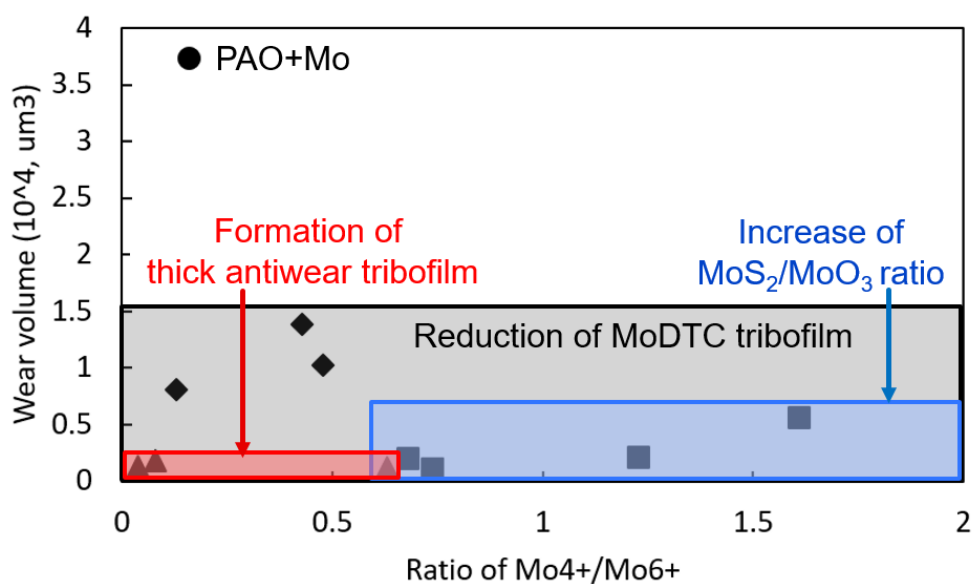


Figure 8-11 The relationship between Mo<sup>4+</sup>/Mo<sup>6+</sup> and wear volume of DLC disc

## 8.5 Conclusions

This study has used an MTM ball on disc tribometer, combined with SLIM and surface analysis based on TEM, STEM-EDX, Raman and XPS to understand the relevant mechanisms by which the addition of other surface-active additives improves a-C:H DLC wear of DLC against a steel contact rubbed in an MoDTC solution. The addition of all these additives reduces DLC wear to some extent, and in such a fashion that there appears to be more than one wear-reducing mechanisms. Key conclusions are as follows.

- While PAO+Mo resulted in severe wear of DLC surface, the addition of surface-active additives reduced this DLC wear. The addition of ZDDP(50), ZDDP(800), EP, Ca(OB), Ca(Neu), Disp(B) and OFM reduced DLC wear much more than Zn(25), Disp and PAMA.
- ZDDP(800), Ca(OB) and OFM, which gave negligible DLC wear, all formed thick tribofilms during rubbing. Despite not forming thick tribofilms, oils with ZDDP(50), EP, Ca(Neu) and Disp(B) also resulted in very little DLC wear.
- STEM-EDX analysis showed that the tribofilms formed on the steel ball in PAO+Mo consisted of Mo, S, O and C. This carbon was distributed throughout the tribofilm, and it is likely to attribute to carbon transferred from DLC disc.

- $I_D/I_G$  ratios of carbon transferred from DLC discs to on steel balls were analysed using Raman spectroscopy. PAO+Mo and PAO+Mo+ZDDP(25) gave smaller  $I_D/I_G$  than a fresh DLC disc, suggesting that transferred carbon existed as a different chemical structure which has low  $I_D/I_G$ . By comparison, measurable D peak and G peak were not observed on steel balls rubbed in PAO+Mo+ZDDP(50) and ZDDP(800), suggesting no transferred carbons on wear tracks.
- $Mo^{4+}/Mo^{6+}$  measured using XPS was increased by the addition of most of the surface-active additives to PAO+Mo, apart from OFM and PAMA. The prevention of oxidation of Mo compounds may reduce DLC wear even when thick antiwear tribofilms are not formed on steel surfaces, especially in the oils with ZDDP(50), EP, Ca(Neu) and Disp(B).
- DLC wear in PAO+Mo can be reduced by the presence of other surface-active additives in three ways. Firstly, asperity contact between DLC and steel can be mitigated by forming thick antiwear tribofilms. Secondly, other additives can increase the ratio of  $MoS_2:MoO_3$ , reducing the amount of wear-enhancing  $MoO_3$  in the tribofilm. Thirdly, the amount of MoDTC tribofilm including  $MoO_3$  can be reduced by the competitive adsorption of other surface-active additives.

## **9 In-situ Observations of the Effect of ZDDP Tribofilm Growth on Micropitting**

*As discussed in chapter 3, it has been suggested that the increase in micropitting produced by ZDDP originates from the fact that ZDDP forms tribofilms very rapidly and that this prevents adequate running-in. In this chapter, new research is described to test this mechanism, by developing and using a novel technique based on MTM-SLIM to obtain micropitting and observe ZDDP tribofilm growth in parallel throughout a test. The research described in this chapter has already been published in Tribology International with an open access [345].*

### **9.1 Introduction**

As described in 3.4.1, it is likely that a key factor in determining a ZDDP's effect on micropitting is the rate at which it forms a tribofilm to suppress further running in. However, although it has been established that ZDDP can affect micropitting, the correlation between ZDDP tribofilm growth rate and the evolution of micropitting has not been directly demonstrated. This is because current understanding is based on post-test analysis of the surfaces rather than in-situ observation of continuous surface evolution under the concurrent effects of mild wear and micropitting. Two recent studies have used an MPR to generate micropitting and MTM-SLIM to measure antiwear films with the tested oils [207,272] and these have shown a correlation between tribofilm growth and micropitting. However, film growth and micropitting were studied in different rigs under different conditions.

This chapter describes the development and use of a novel method based on the MTM-SLIM rig that is able to both monitor the growth of ZDDP tribofilm in-situ and observe any accompanying micropitting during the same test. The method is based on choice of optimal sliding-rolling conditions coupled with selection and control of specimen roughness and hardness so as to potentially enable micropitting on the ball specimen. This method is then applied to investigate the effect of ZDDP concentration and ZDDP alkyl structure on the parallel evolution of tribofilm and micropitting.

## 9.2 Test Procedure

### 9.2.1 Test Materials and Lubricants

MTM-SLIM was employed to generate micropitting on the ball specimen and to monitor ZDDP film formation within the same test in an MTM. Disc roughness and ball hardness were controlled to promote micropitting on the ball. For most MTM studies very smooth discs with centre-line average roughness,  $R_a$  of *ca.* 5 nm are employed. However, in this study (and also in Chapters 10 and 11), AISI 52100 steel discs with  $R_a = 0.4$  to  $0.5\ \mu\text{m}$  were used in order to subject the counterface ball to severe asperity contact stress cycles. This roughness is much more typical of that present in gears and bearing raceways than that of the smooth discs generally used. As is common in controlled contact fatigue tests [251,266,271,346], the ball on which micropitting damage is to be studied was made softer than the rough disc counterface, to ensure that disc roughness persists during a test, thereby promoting micropitting on the ball. This was achieved by softening the standard MTM steel balls (martensitic through-hardened AISI 52100 steel) from their normal value of 820 – 870 HV down to a measured range of 730 – 780 HV, by holding the balls at 250 °C for 1 hour in the base oil PAO100 in an air atmosphere. Mean speed, slide roll ratio (SRR), load and oil temperature were held the same in all tests. It is important to note that, in common with other controlled micropitting studies [248,249,271,347], the ball and disc rotational speeds are such that the surface speed of the ball specimen where the micropitting is being generated is slower than that of the disc. The chosen maximum contact pressure of 1.2 GPa and SRR of -0.05 (5%) are similar to rolling bearing and gear conditions.

Test oils and the initial lambda values are shown in Table 9-1. Test oils were formulated to isolate and study a single variable of interest. To investigate the effect of the lambda on micropitting, tests were conducted at three different lambda values (0.1, 0.3 and 0.7, correspond to 30 nm, 150 nm, 320 nm of minimum oil film thickness, respectively). This was achieved by blending different PAO base oil viscosities with the same ZDDP concentration (800 ppm P) of ZDDPM (Oils A, B, C in Table 9-1). In chemical terms, the different PAOs used can be considered identical since all are based on alkene oligomers, the only difference being the average number of monomers in each oligomer. To investigate the effect of ZDDP concentration on micropitting, five different concentrations of ZDDPM in the same PAO10 were studied (Oils B, D, E, F and G in Table 9-1). Finally, to test the effect of ZDDP type on micropitting, Oil H was formulated with ZDDP1 in PAO10 for comparison with Oil B that contained ZDDPM in PAO10. ZDDPM and ZDDP1 were described in Table 4-2.

Table 9-1 Test oil formulations and lambda value

Lubricant name	Base oil viscosity at 40/100 °C, mm <sup>2</sup> /s	P conc., ppm	Initial lambda
Oil A (PAO2+ZDDPM(800))	5.5/1.8	800	0.1
Oil B (PAO10+ZDDPM(800))	62.8/9.9	800	0.3
Oil C (PAO10/40+ZDDPM(800))	259.0/28.1	800	0.7
Oil D (PAO10)	62.8/9.9	0	0.3
Oil E (PAO10+ZDDPM(100))	62.8/9.9	100	0.3
Oil F (PAO10+ZDDPM(400))	62.8/9.9	400	0.3
Oil G (PAO10+ZDDPM(1200))	62.8/9.9	1200	0.3
Oil H (PAO10+ZDDP1(800))	62.8/9.9	800	0.3

### 9.2.2 Test Procedures and Conditions

Table 9-2 shows the materials and conditions of the rolling-sliding MTM tests. MTM-SLIM tests were conducted for a duration that subjected each position on the ball track to 8 million Hertzian contact cycles. At the entrainment speed used of 3 m/s this test time was 40 hours. Periodically, motion was halted and the ZDDP tribofilm thickness measured using SLIM. Tests were also interrupted after 0.1, 1, and 4 million cycles to observe and measure wear and micropitting on the ball and the roughness of the disc wear tracks. Before these surface measurements, ball and disc were rinsed in toluene in an ultrasonic bath for 10 minutes to remove supernatant oil. Rinsing the ball and disc with toluene did not influence the thickness of the ZDDP tribofilm which can only be removed by chemically-active solutions such as EDTA [147]. The wear depth on the ball and the roughness of the disc were then measured at four different locations using a Talysurf stylus profilometer and micrographs of surface cracks and micropitting on the ball obtained using an optical microscope. After these measurements, the specimens were returned to MTM and the rolling-sliding test continued without changing the lubricant. All tests were repeated one time. The values plotted on the relevant graphs are the average values obtained from the two results, while the extremes of the error bars indicate the actual values from each test. The benefit of using the MTM-SLIM for micropitting tests lies in its ability to continuously follow the development of ZDDP tribofilms while

micropitting is evolving, which may shed new light at mechanisms at play. This ability comes at the expense of a longer test time compared to other, more established test methods for micropitting such as the triple-disc MPR rig [248,251,271], which can impose more stress cycles on a test specimen in a given time.

Table 9-2 MTM specimen materials and test conditions

Ball specimen	Material: AISI 52100 steel; Measured hardness: $760 \pm 30$ HV; Measured roughness $R_a \sim 0.02 \mu\text{m}$
Disc specimen	Material: AISI 52100 steel; Measured hardness: $800 \pm 20$ HV; Measured roughness $R_a \sim 0.45 \mu\text{m}$
Test temperature ( $^{\circ}\text{C}$ )	65
Test Load (N)	75 (Maximum Hertzian pressure: 1.2 GPa)
Entrainment speed (m/s)	3
Slide-roll-ratio (SRR) $2*(U_{\text{ball}}-U_{\text{disc}})/(U_{\text{ball}}+U_{\text{disc}})$	-0.05
Test cycles	8 million cycles (40 hours): Test paused for specimen inspection after 0.1 million cycles, 1 million cycles, 4 million cycles, 8 million cycles

### 9.3 Results

#### 9.3.1 Effect of Lambda on Micropitting and ZDDP Tribofilm Formation

This section presents results of the tests designed to investigate the influence of lambda value on tribofilm formation and micropitting. The lubricants used are Oils A, B and C, which had different viscosities in order to achieve different lambda values at the specified test conditions.

##### 9.3.1.1 Evolution of Surface Damage on Balls

Figure 9-1 shows representative optical micrographs of the rubbed track on the ball after 0.1, 1, 4 and 8 million cycles at three different lambda values, 0.1, 0.3 and 0.7. Figure 9-2 shows the corresponding depth of the ball rubbed track measured using a stylus profilometer. The reported values are averages of the maximum wear depth measured at four different locations.

At a  $\lambda$  value of 0.1, a small amount of localized damage is visible on the ball surface after 4 and 8 million cycles (Figure 9-1). However, a relatively large amount of material was lost from the ball, with the depth of rubbing track reaching  $1.1\text{ }\mu\text{m}$  as early as 0.1 million cycles and increasing to  $3.1\text{ }\mu\text{m}$  by the end of the test (Figure 9-2).

At a  $\lambda$  value of 0.3, a significant number of surface cracks are observed as early as 0.1 million cycles (Figure 9-1). These cracks are tens of microns in length and appear to grow across the rolling track in a fanned, shallow 'V' shape, typical of surface-initiated fatigue cracks (see image for  $\lambda = 0.3$  at 1 million cycles in Figure 9-1). Appearance of these cracks is the first visible sign of micropitting processes taking place. As the test progresses, the number of cracks increases considerably. Small pits (tens of microns in size) associated with these cracks become apparent at 4 million cycles. By the end of the test, these micro-pits cover most of the rubbing track (Figure 9-1). The loss of material from the ball was measured to be much less than at  $\lambda = 0.1$ , with the depth of the running track being  $0.2\text{ }\mu\text{m}$  at 0.1 million cycles and staying relatively constant at this low level for the remainder of the test (Figure 9-2).

At a  $\lambda$  value of 0.7, far fewer cracks are observed after 1 million cycles and these appear isolated (Figure 9-1). After 4 and 8 million cycles, a few micropits associated with such cracks become apparent. These are larger than micropits seen at  $\lambda = 0.3$  and they appear in isolation, probably because the associated cracks are also discrete, with minimal interaction between them, unlike at  $\lambda = 0.3$ . The amount of material lost from the ball rubbing track was lower than in the case of  $\lambda = 0.1$ , but greater than for  $\lambda = 0.3$ , with the depth of the ball wear track being  $1.0\text{ }\mu\text{m}$  after 8 million cycles (Figure 9-2).

Figure 9-3 shows an optical micrograph of a polished cross-section of the ball rubbing track along the rolling direction obtained from a test with  $\lambda$  value 0.3 after 8 million cycles. Multiple, surface-breaking cracks, growing at an angle of approximately  $30^\circ$  to the surface and against the direction of the applied friction force, are evident. Small micro-pits, approximately  $30\text{ }\mu\text{m}$  across and about  $10\text{ }\mu\text{m}$  deep, can be seen to be formed by detachment of surface material due to interaction of these cracks. These observations all confirm that the generated damage is indeed micropitting.



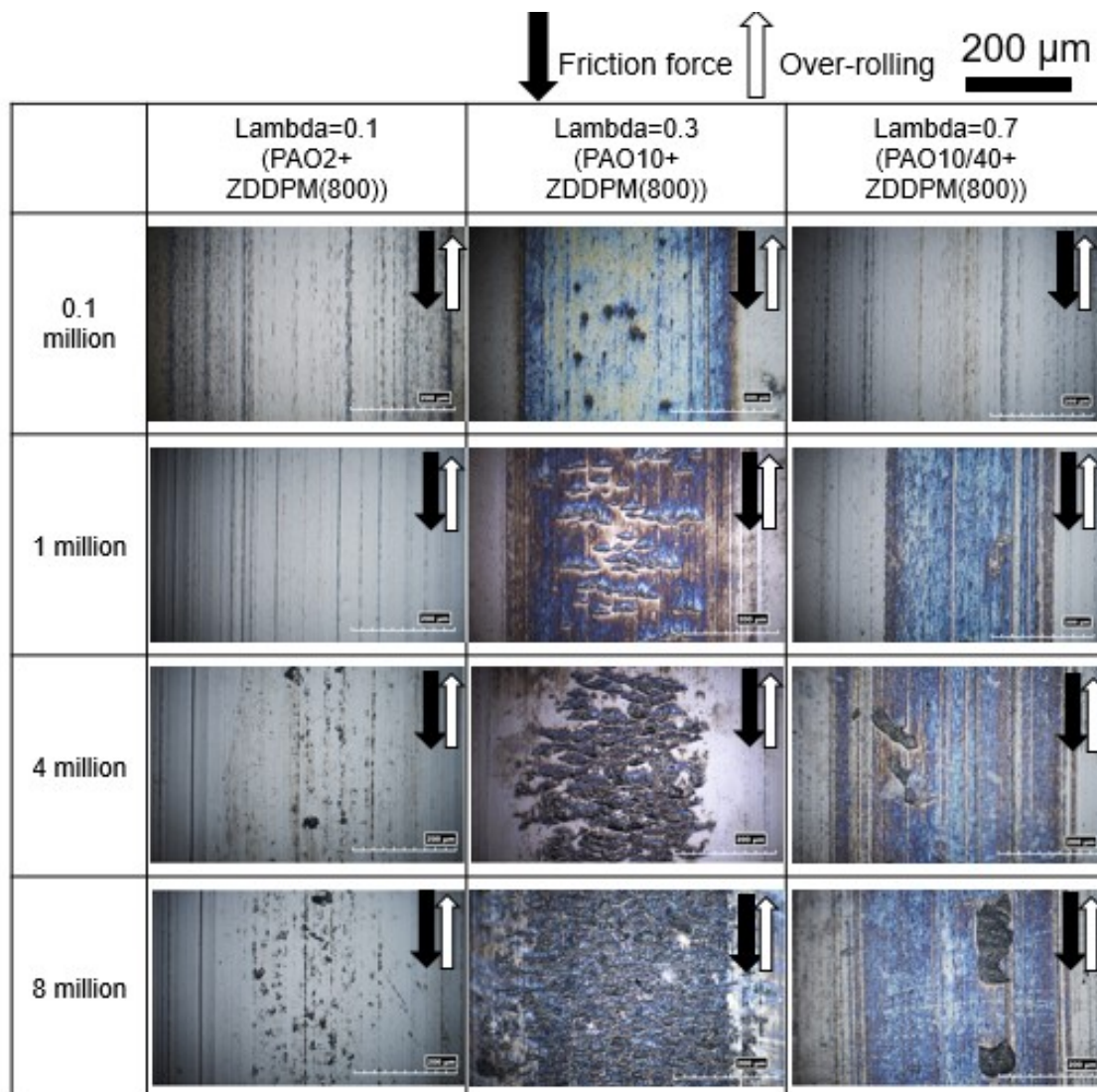


Figure 9-1 Optical micrographs of rubbing tracks on balls at different lambda values (Note: the scale bar included in the top right corner of the figure applies to all images shown)

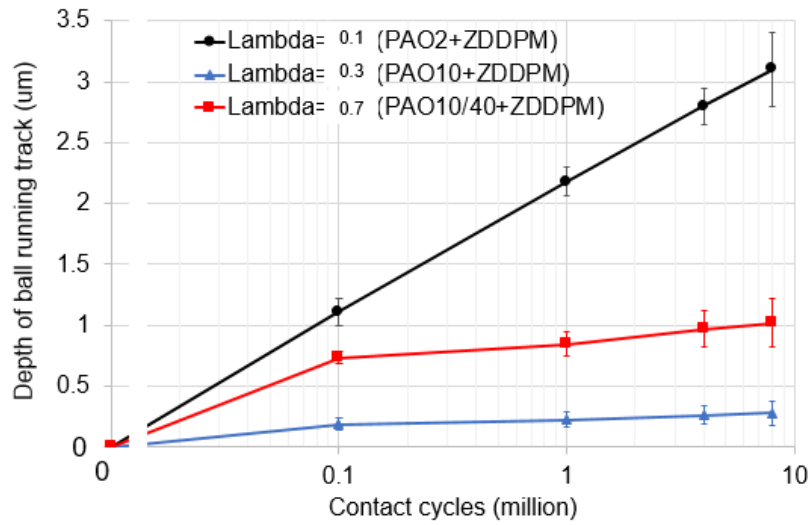


Figure 9-2 Measured depth of ball wear track at different lambda values

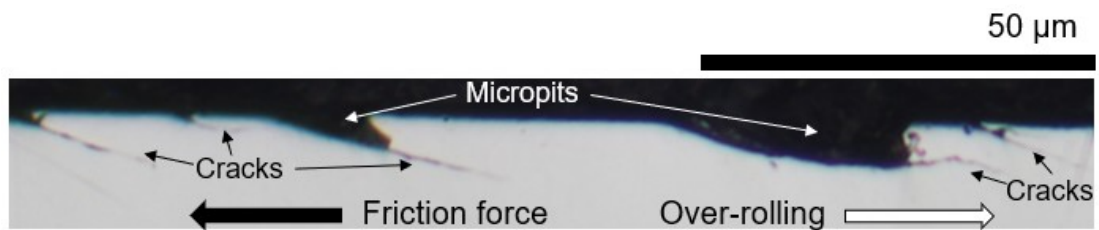


Figure 9-3 Optical micrograph of the cross section of the ball rubbing track in the rolling direction at the end of the test with the lambda = 0.3 showing typical surface-initiated cracks and resulting micropits.

### 9.3.1.2 Evolution of Surface Roughness of Counterface Discs

Micropitting is observed on the balls which were deliberately made softer and smoother than the counterface discs. However, some changes in disc roughness were also observed. Figure 9-4 shows the evolution of the disc roughness in the same tests. In all cases the disc roughness reduced in the initial stages of the test and then remained relatively stable, a behaviour indicative of running-in. However, considerable differences are evident in the level of roughness reduction at different the lambda values. In the test with lambda = 0.3 the disc roughness reduced considerably less than at other two lambda values, falling from the initial Ra value of 0.45 μm to 0.30 μm after 0.1 million cycles and staying constant at this level for the rest of the test. In the tests at the lambda = 0.1 the disc roughness reduction was the greatest, with Ra falling from 0.45 μm to 0.11 μm after 1 million cycles and then remaining stable for the remainder of the test. At lambda = 0.7,

the roughness reduction was intermediate, with Ra decreasing from 0.45  $\mu\text{m}$  to 0.21  $\mu\text{m}$  during the first 1 million cycles and then remaining stable for the rest of the test duration.

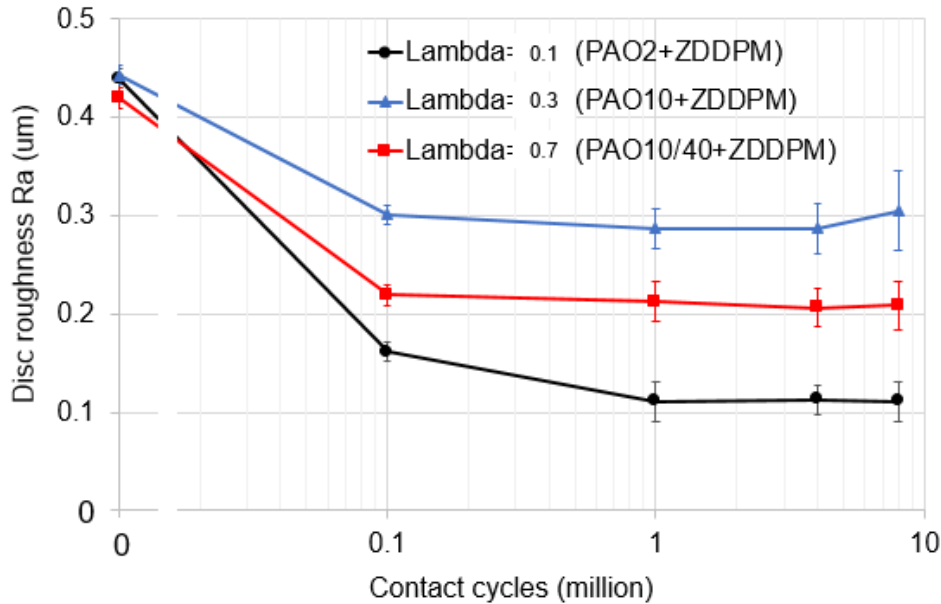


Figure 9-4 Disc roughness evolution at different lambda values

### 9.3.1.3 ZDDP Tribofilm Evolution

Figure 9-5 shows ZDDP tribofilm thickness in the ball rubbed track obtained from SLIM images. No measurable ZDDP tribofilm formed on balls at  $\lambda = 0.1$ . At  $\lambda = 0.3$ , a tribofilm grew rapidly in the first 0.15 million cycles, to reach 170 nm after 0.2 million cycles; after this tribofilm thickness decreased, to stabilize at *ca.* 30 nm. In the case of  $\lambda = 0.7$ , tribofilm grew relatively slowly at the beginning of the test to reach *ca.* 40 nm after 1 million cycles and then remained stable for the rest of the test. Average friction coefficients for  $\lambda = 0.1$  and 0.3 were very similar at  $\sim 0.1$ , while that at  $\lambda = 0.7$  was  $\sim 0.07$ . It should be noted that the logarithmic x axis used in Figure 9-5 to illustrate the variation in film thickness throughout the test distorts the appearance of the film growth rate from that observed in more normal, linear axis plots. In a linear plot, the film thickness grows at an approximately constant rate for the first 2 h (0.4 million cycles) and then reduces slowly over the remaining 38 h of the test.

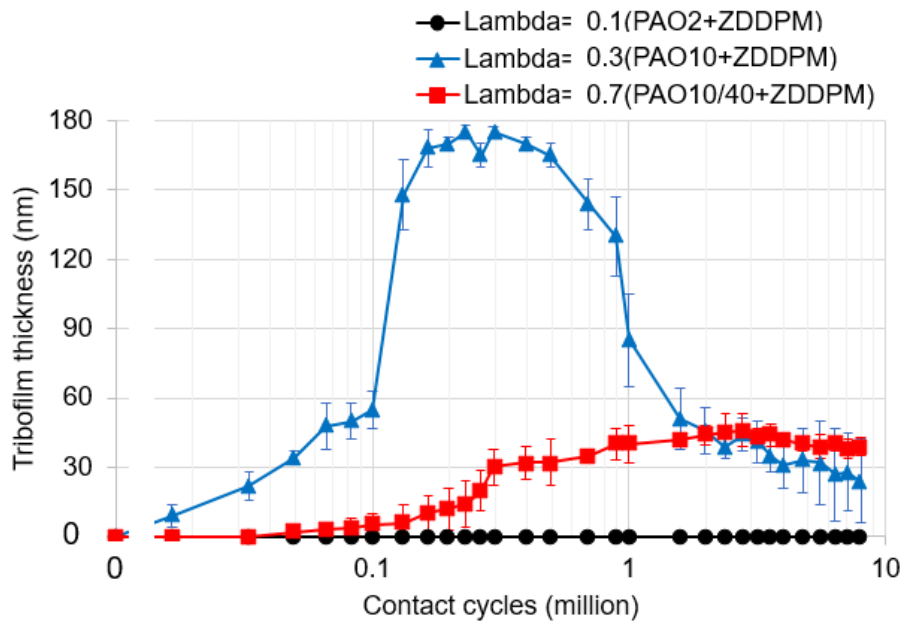


Figure 9-5 ZDDP tribofilm thickness development at different lambda values

### 9.3.2 Effect of ZDDP Concentration on Micropitting and Tribofilm

This section presents results of the tests designed to isolate the influence of ZDDP concentration on the evolution of micropitting damage and its relation to the development of ZDDP anti-wear tribofilms. The oils used in these tests are all PAO10 base oil with the same ZDDP additive (mixed ZDDP denoted as ‘ZDDPM’ in Table 9-1) blended in at different concentrations of P, namely 0, 100, 400, 800 and 1200 ppm (oils D, E, F, B, G respectively in Table 9-1).

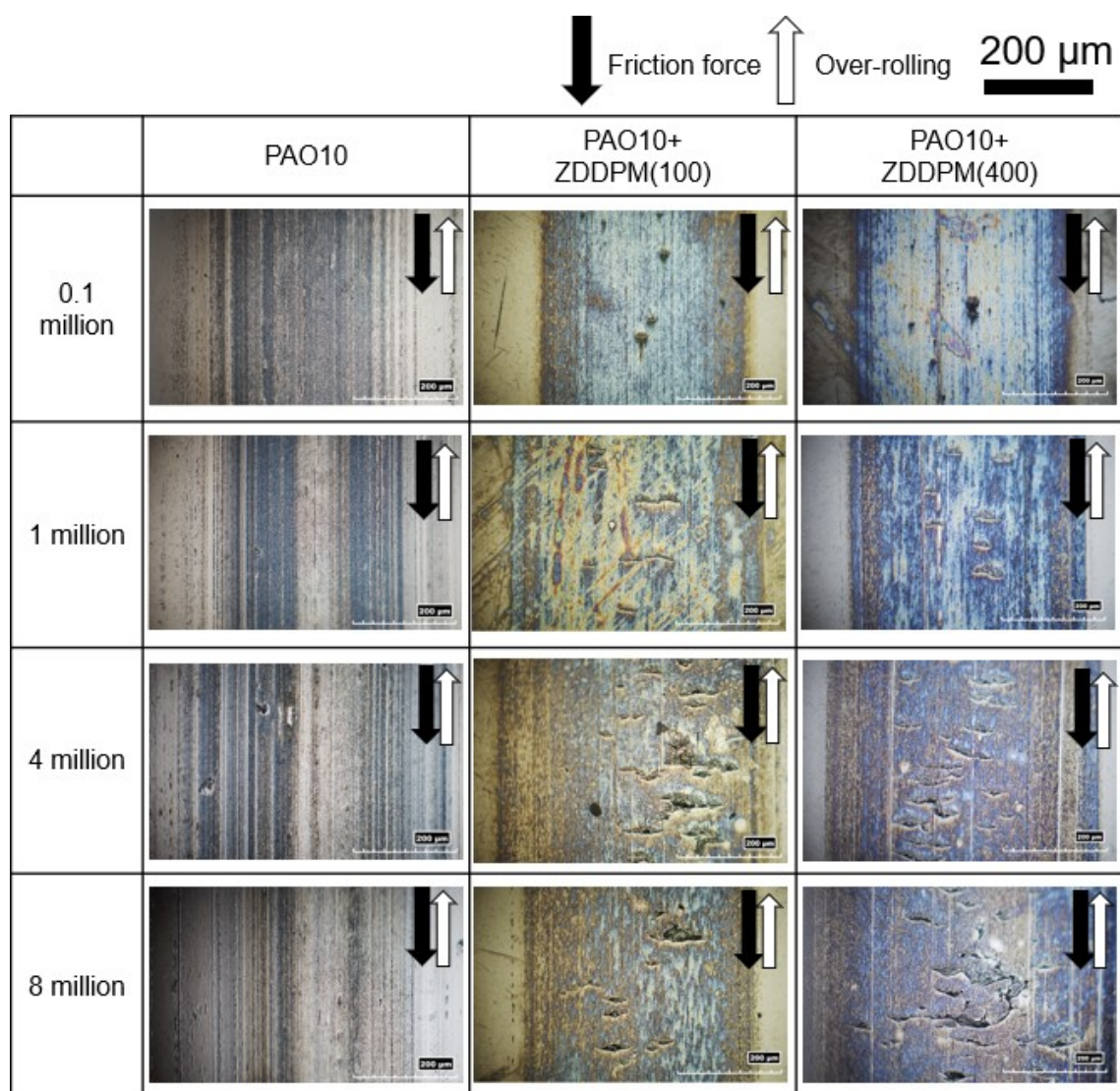
#### 9.3.2.1 Evolution of Surface Damage on Balls

Figure 9-6 shows representative optical micrographs of ball rubbing tracks from tests lubricated with the 5 different oils, while Figure 9-7 shows the evolution of the maximum wear track depth. In the case of pure PAO10 base oil (P: 0 ppm), some minor surface damage is apparent at 4 and 8 million cycles (Figure 9-6), but no obvious fatigue cracks or pits are evident at any stage. However, Figure 9-7 shows that a significant amount of material was lost from the rubbed track, with the depth of the track being 0.7  $\mu\text{m}$  as early as 0.1 million cycles and progressing to reach 1.2  $\mu\text{m}$  after 8 million cycles.

In the case of balls lubricated with 100 and 400 ppm P oils, a few isolated, short cracks (tens of microns in length) are observed after 0.1 million cycles, with their size and

number increasing as the test progressed and a few, isolated small pits becoming apparent at 8 million cycles (Figure 9-6). The observed cracks exhibit typical characteristics of surface-initiated fatigue. The loss of material from the ball track for these oils was smaller than that with the pure PAO base oil, with the measured depth of the track being 0.25  $\mu\text{m}$  at 1 million cycles, reaching only 0.35  $\mu\text{m}$  at 8 million cycles (Figure 9-7).

By contrast, in the tests with 800 and 1200 ppm P oils, surface cracks are observed as early as 1 million cycles (Figure 9-6). Comparison of relevant surface images at 1, 4 and 8 million cycles in Figure 9-6 shows that cracks grow in length and become more numerous as the test progresses, so that they cover most of the rubbing track width after 8 million cycles. The cracks are tens of microns in length and exhibit typical characteristics of surface-initiated fatigue cracks, with a fanned, shallow 'V' shape, and growth against the direction of friction (see images in Figure 9-6 at 4 and 8 million cycles for ZDDPM 100 and ZDDPM 400 for example). Small pits associated with these cracks become apparent as early as 4 million cycles and their number increases by the end of the test at 8 million cycles, indicating a significant amount of fatigue damage on the surface. The material loss from the ball running track in this case was slightly smaller than for balls lubricated with 100 and 400 ppm P oils, with the depth of the track reaching only 0.28  $\mu\text{m}$  at 8 million cycles (Figure 9-7).





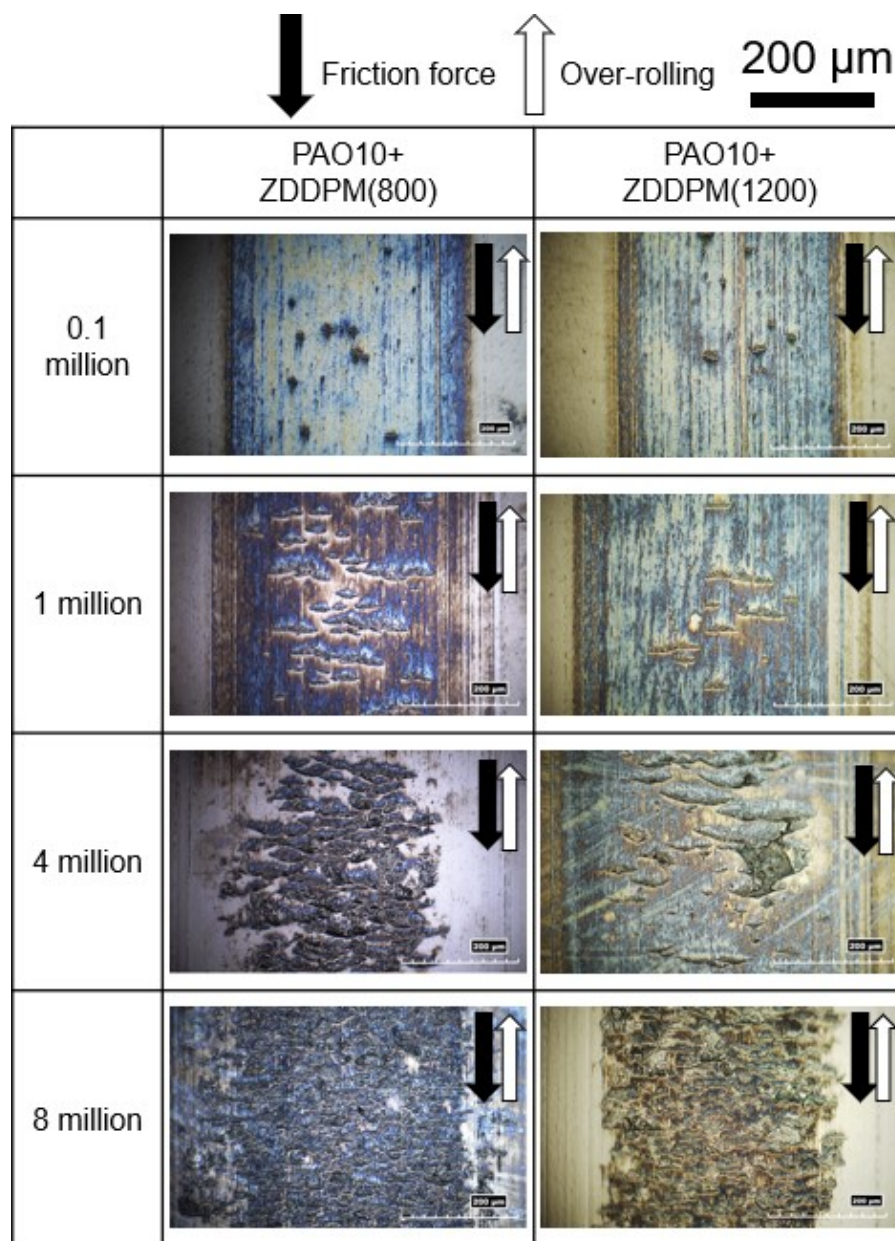


Figure 9-6 Optical micrographs of ball rubbing tracks from tests conducted with oils with different ZDDPM concentrations

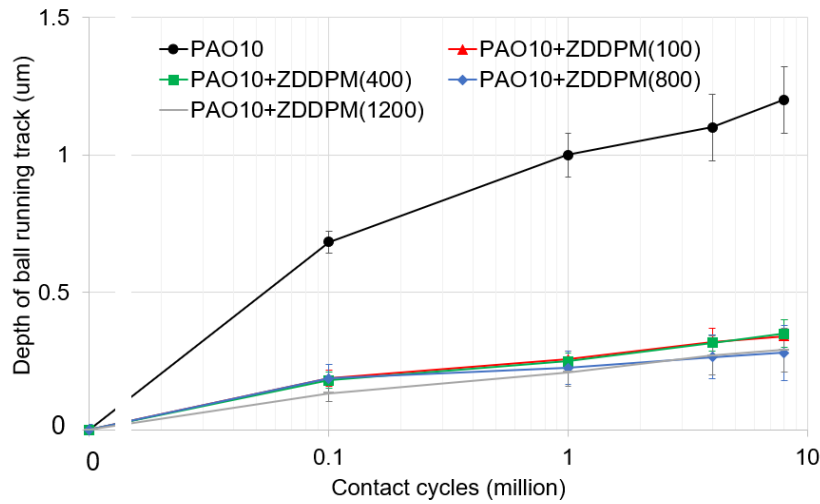


Figure 9-7 Depth of the wear track on balls in tests.

### 9.3.2.2 Evolution of Surface Roughness of Counterface Discs

Figure 9-8 shows how disc roughness changed during tests with different ZDDP concentrations. The roughness of the disc in the test with pure PAO oil decreased drastically over the first 0.1 million cycles, with Ra falling from initial 0.45  $\mu\text{m}$  to 0.25  $\mu\text{m}$ , and then decreased further to reach 0.15  $\mu\text{m}$  after 8 million cycles. In contrast, in the tests with the 800 and 1200 ppm P oils, the disc roughness reduced much less, falling only to about 0.3  $\mu\text{m}$  during the initial 0.1 million cycles and then remaining at this level for the rest of the test. In the tests with oils containing 100 and 400 ppm P, the decrease in disc roughness lay somewhere between these extremes, falling to 0.28 in the first 0.1 million cycles, and then stabilizing at 0.23  $\mu\text{m}$  from 1 million cycles onwards.

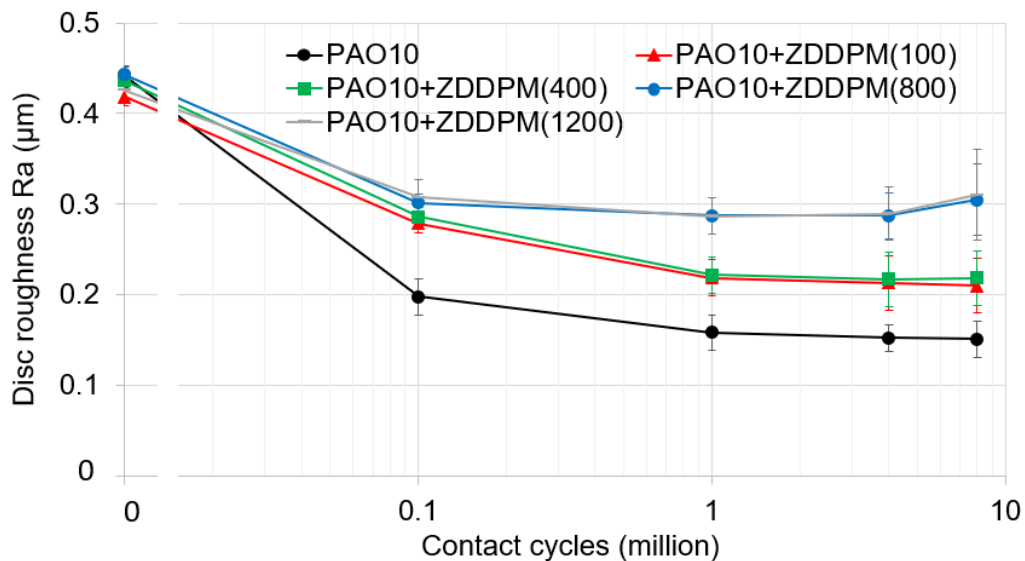


Figure 9-8 Evolution of counterface disc roughness



### 9.3.2.3 Friction Behaviour

Figure 9-9 shows the evolution of friction coefficient in tests conducted with oils with different P concentrations. It is evident that friction behaviour is very similar for all P concentrations, with initial friction coefficient being about 0.1 and gradually decreasing to reach 0.08 at the end of the test. For pure PAO oil, friction coefficient was 0.08 initially but very quickly decreased to about 0.06 and remained constant at this level for the rest of the test. The reduced friction with PAO probably resulted from rapid running-in, which produced an increase in  $\lambda$ . The first disc roughness measurement was at 0.1 million cycles and  $R_a$  was drastically reduced by then when PAO oil was used. However running-in is believed to have occurred much faster than this, and hence the friction with PAO is reduced from very early in the test. It should also be noted that the momentary blips in the recorded friction trace apparent in the figure are artefacts of the measurement method and occur just after motion is paused for capture of a SLIM image.

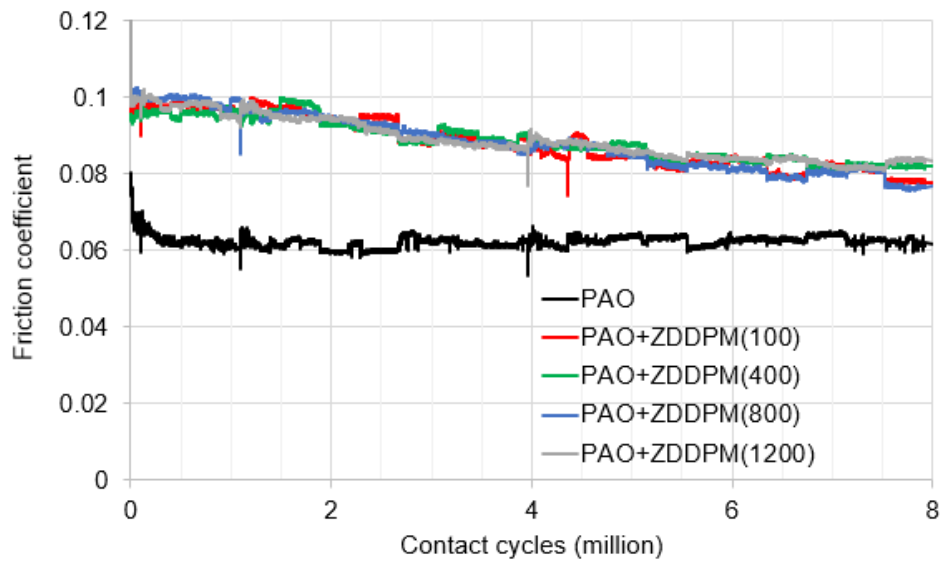


Figure 9-9 Friction behaviour in tests conducted with oils with different ZDDPM concentrations

### 9.3.2.4 Evolution of the ZDDP Tribofilm on the Ball

Figure 9-10 shows representative SLIM images of the ball track from tests with different P concentrations, while Figure 9-11 plots the evolution of ZDDP tribofilm thickness obtained from these images. The development of cracks and micropits on the ball surface are apparent in the SLIM images from tests with 800 and 1200 ppm P oils, indicating significant micropitting in these tests. No such micropits are evident in the images from the pure PAO base oil test. The SLIM images with pure PAO oil clearly show excessive wear of the ball, in that the contact shape stops being circular shortly after the start of the test. Tribofilms were seen to develop at different rates at different concentrations of P, particularly in the first 0.3 million cycle phase of the tests. In the case of 100 and 400 ppm P oils, tribofilm thickness reached a maximum of *ca.* 115 nm in this phase, and then decreased, to stabilize at *ca.* 40 nm from 4 million cycles onwards. In the case of 800 and 1200 ppm P oils, the initial film growth rate was much faster, and the film reached *ca.* 180 nm in the initial 0.2 million cycles before reducing to stabilize at *ca.* 30 nm from 5 million cycles onwards.

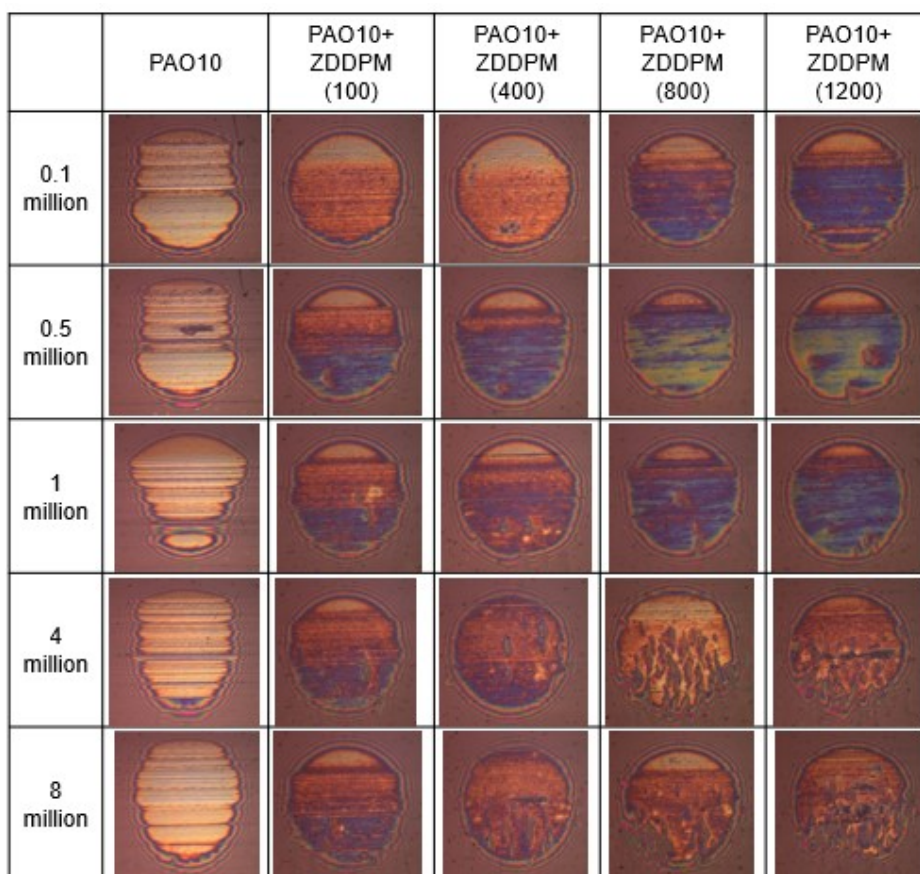


Figure 9-10 SLIM images of ball running track recorded in tests conducted with oils with different ZDDPM concentrations

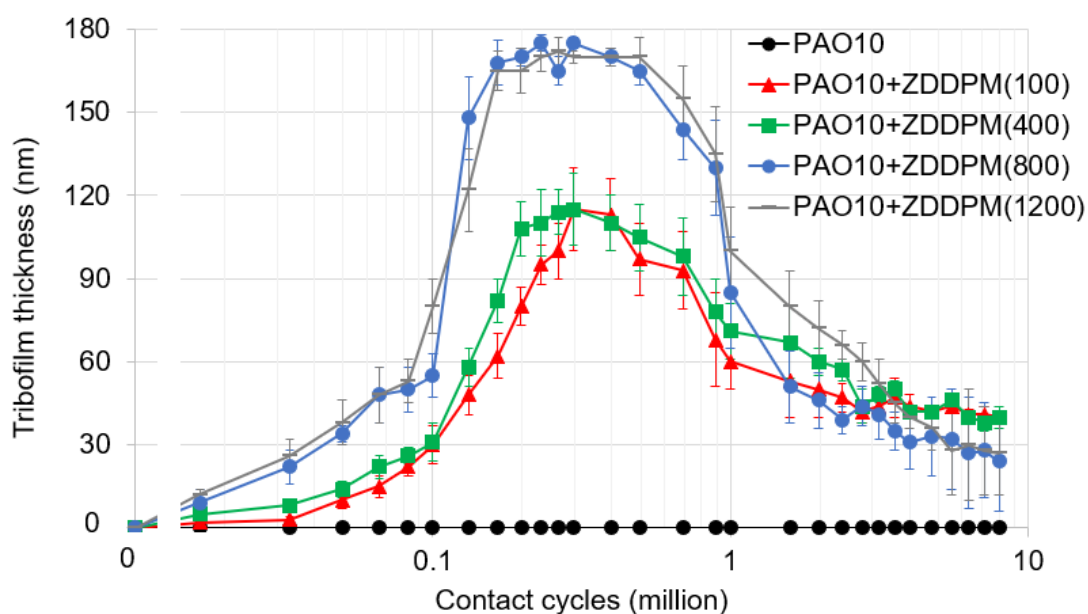


Figure 9-11 Tribofilm thickness development measured in tests conducted with oils with different ZDDPM concentrations

### 9.3.3 Effect of ZDDP Alkyl Structure on Micropitting and ZDDP Tribofilm

This section presents results of the experiments designed to investigate the influence of the ZDDP alkyl structure on the observed surface damage and its correlation with tribofilm formation. Oils with two different ZDDP structures were tested: a mix of primary and secondary ZDDP denoted ZDDPM (oil B in Table 9-1) and a pure primary ZDDP denoted ZDDP1 (oil H). Both ZDDPs were dissolved in PAO10, at a P concentration of 800 ppm.

#### 9.3.3.1 Evolution of surface damage on balls

Figure 9-12 shows representative optical micrographs of ball rubbing tracks from tests using the two ZDDPs. Both oils produced a significant number of cracks on the surface after 1 million cycles. These cracks are tens in microns in length and exhibit characteristics of typical surface-initiated fatigue cracks. However, after 4 and 8 million cycles it is evident that these cracks result in micropits only for ZDDPM; with ZDDP1 the cracks have grown in length to over hundred microns but do not appear to have caused any micropits by this stage. Figure 9-13 shows the corresponding evolution of the ball wear track depth as measured using a stylus profilometer. The loss of material was small

and very similar for the two blends; by the end of the test the primary ZDDP1 and mixed ZDDPM showed around 0.30  $\mu\text{m}$  and 0.28  $\mu\text{m}$  material removal respectively.

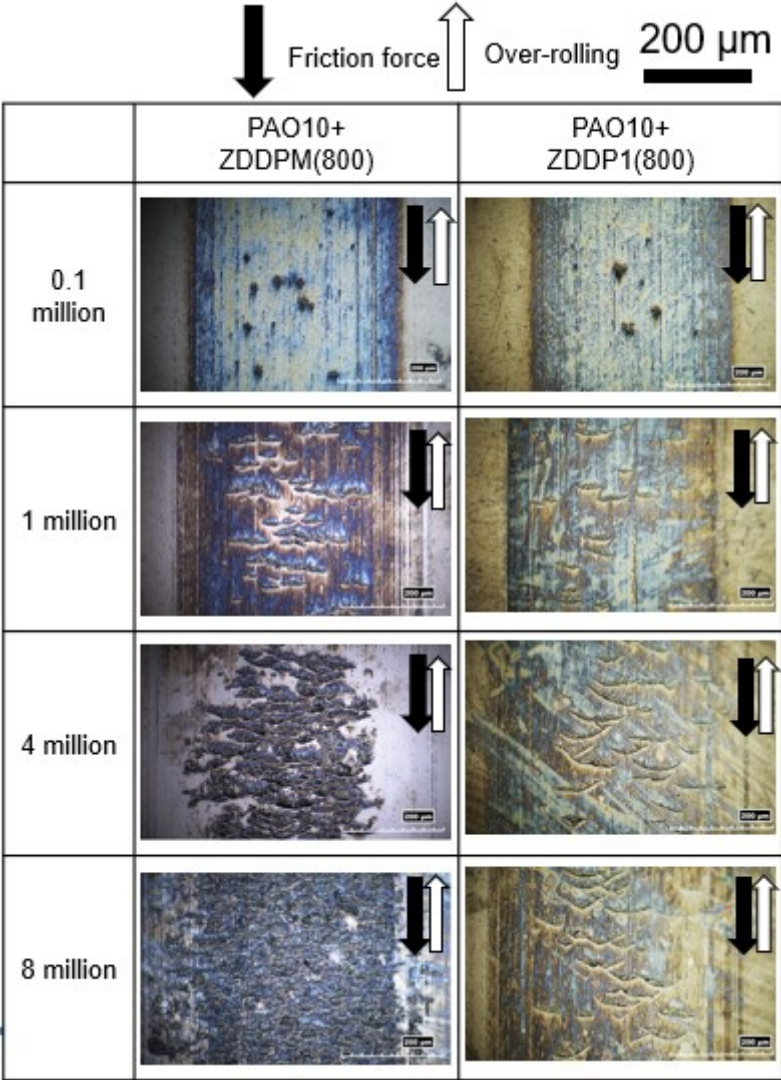


Figure 9-12 Optical micrographs of ball rubbing tracks from tests conducted with oils containing different ZDDP alkyl structures, mixed (ZDDPM) and primary (ZDDP1)

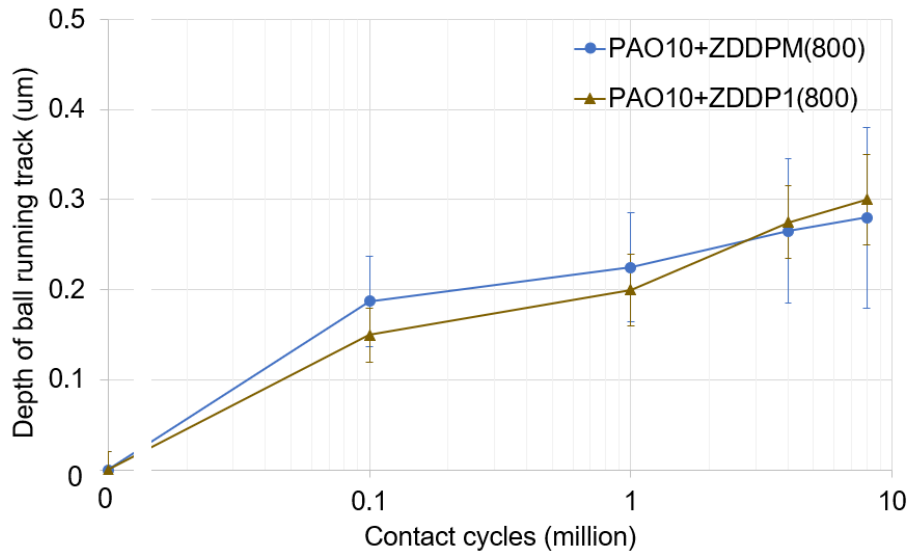


Figure 9-13 Depth of the wear track on balls in tests conducted with oils containing different ZDDP alkyl structures

### 9.3.3.2 Evolution of Surface Roughness of Counterface Discs

Figure 9-14 shows how the counterface disc roughness evolved over the duration of these micropitting tests. Disc roughness decreased more with the ZDDP1-containing oil than with the one containing ZDDPM. After 0.1million cycles the Ra roughness in the ZDDP1 test fell from the initial  $0.45\ \mu\text{m} - 0.27\ \mu\text{m}$ , with a slight further reduction to  $0.22\ \mu\text{m}$  by 1 million cycles. By contrast, in the test with ZDDPM, Ra roughness fell to  $0.3\ \mu\text{m}$  in the first 0.1 million cycles and then remained stable at this relatively high value for the rest of the test.

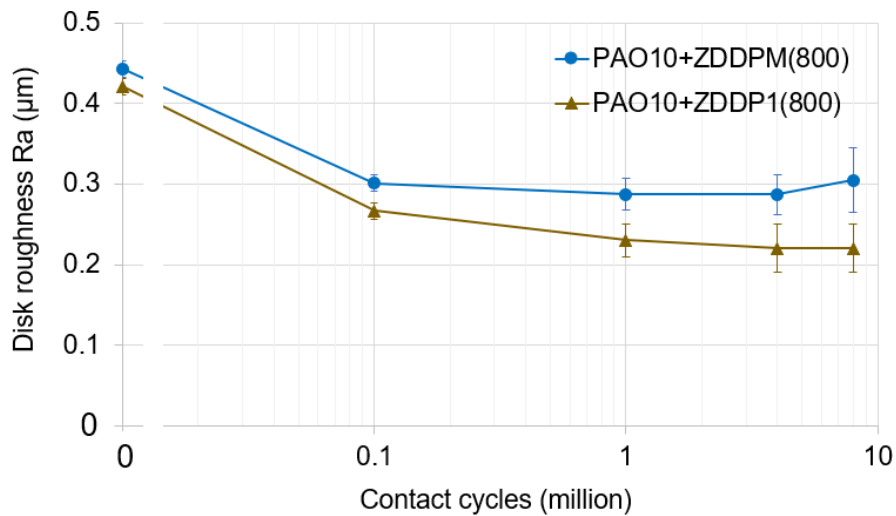


Figure 9-14 Evolution of counterface disc roughness in tests conducted with oils containing different ZDDP alkyl structures

### 9.3.3.3 Friction Behaviour

Figure 9-15 compares the evolution of friction in tests conducted with ZDDP1 and ZDDPM-containing oils. It is evident that both ZDDPs produce almost identical behaviour, with friction gradually decreasing from 0.1 at the start to 0.08 at the end of the test.

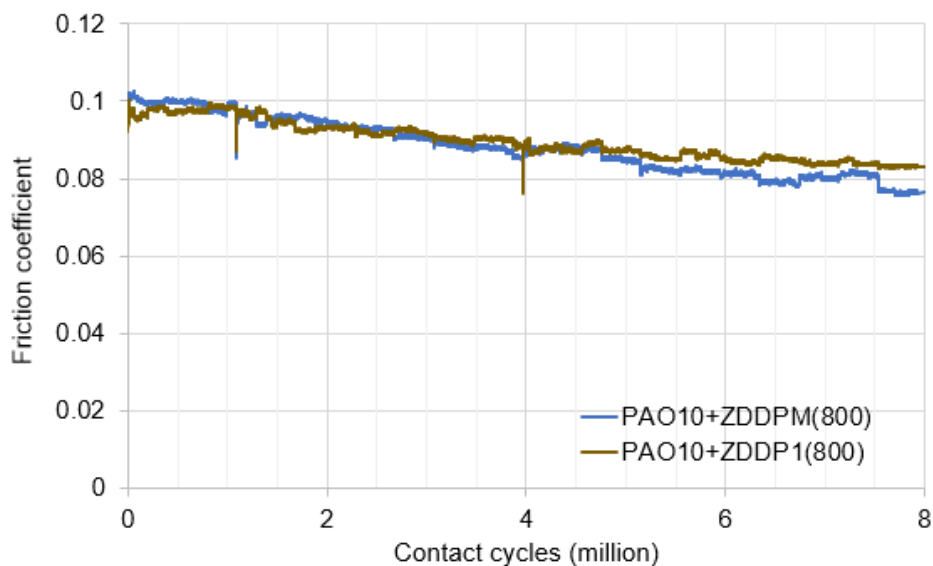


Figure 9-15 Friction behaviour in tests conducted with oils containing different ZDDP alkyl structures

### 9.3.3.4 Evolution of the ZDDP Tribofilm on The Ball

Figure 9-16 shows representative SLIM images for the tests with ZDDP1 and ZDDPM, while Figure 9-17 shows tribofilm thickness obtained from these images. It is apparent that in the initial stages of rubbing the ZDDP1 forms a tribofilm at a much slower rate than ZDDPM. Figure 9-17 shows that over the first 0.2 million cycles (1 h test time) the tribofilm thickness of ZDDPM reached its maximum at *ca.* 170 nm, while the ZDDP1 tribofilm was only about 50 nm by this time. The ZDDP1 tribofilm continued to grow to reach a maximum of *ca.* 100 nm after 0.7 million cycles. Subsequent to these maxima, both tribofilms decreased steadily in thickness to reach a similar value of *ca.* 30 – 35 nm after 4 million cycles.

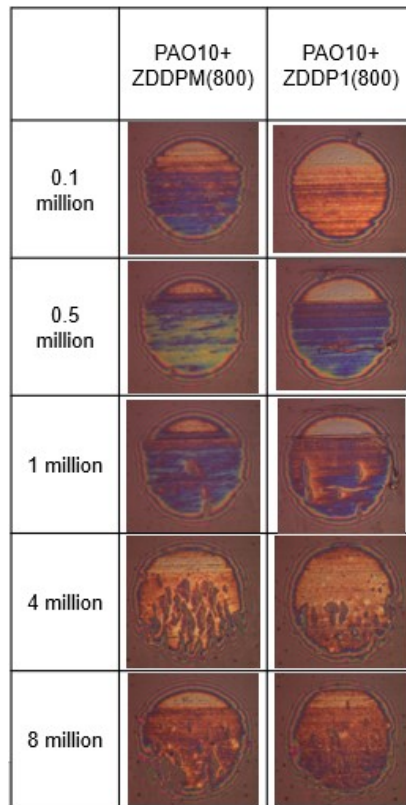


Figure 9-16 SLIM images recorded in tests conducted with oils containing different ZDDP alkyl structures

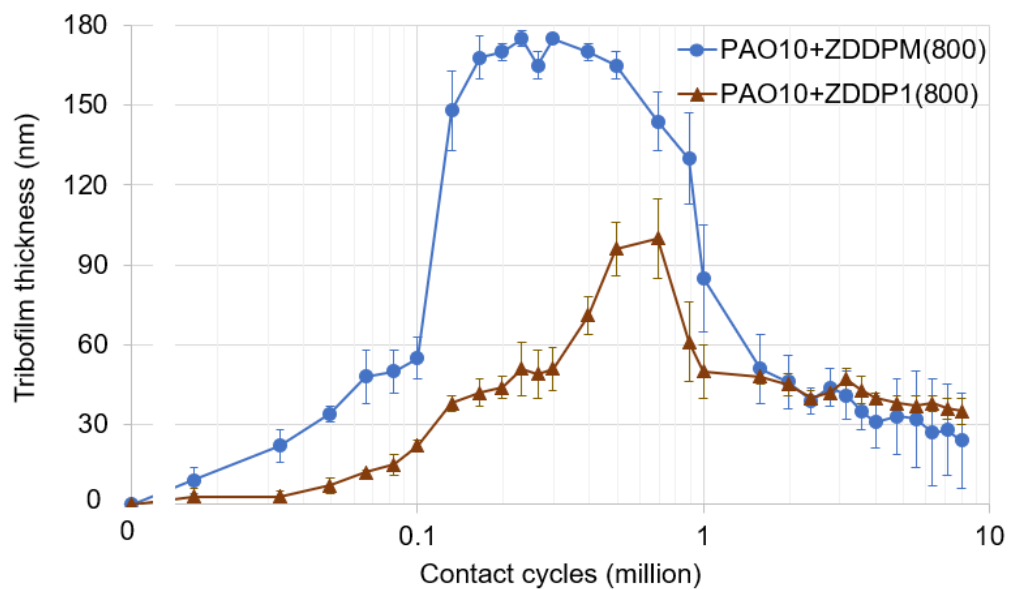


Figure 9-17 Tribofilm thickness evolution measured in tests conducted with oils with different ZDDP alkyl structures



## **9.4 Discussion**

### **9.4.1 Pros and Cons of the MTM-SLIM to Study Micropitting**

The results presented show for the first time that MTM-SLIM can be used to generate and study micropitting provided that non-standard specimens are used, namely a rough hard disc and a relatively low hardness ball. The benefit of this approach over the more commonly used twin and triple-disc rigs is that it enables the in-situ monitoring of the tribofilm development during a micropitting test using SLIM. The SLIM images obtained also provide a means of visually monitoring the development of cracks and pits on the ball surface. These characteristics provide valuable information into the mechanisms by which lubricant formulation influences the generation of micropitting. The obvious drawback of the method is that a considerably longer time is necessary to obtain micropitting than the MPR rig, which is specifically designed to increase the rate of stress cycle accumulation in the roller test specimen by employing three contacts per roller revolution. Both rigs are therefore useful and ultimately the choice of the rig for a particular study will depend on the insights sought and the test equipment available.

There are two additional benefits of using MTM-SLIM for surface fatigue. One is that the disc is completely immersed in the oil-bath, which minimises the bulk temperature increase of the specimens during a test. This ensures that the effective  $\lambda$  value is well-defined. In the MPR a thermal analysis is needed at high loads and sliding speeds. Another advantage is that it is straightforward to investigate the effect of small cross-slip in the contact on crack growth direction. This can be achieved by slightly skewing the direction of ball rotation during calibration, so that the direction of friction force on the ball is at an angle to the rolling direction. The direction of surface crack propagation in rolling contact is highly dependent on the direction of friction [266,271,348] and the introduction of skew allows this to be directly observed. As an example, Figure 9-18 compares the morphology of surface cracks on the MTM ball generated with and without skew of the ball shaft. The differences in the crack orientation are immediately apparent, with crack growth direction being determined by the direction of friction force rather than the over-rolling direction in both cases.



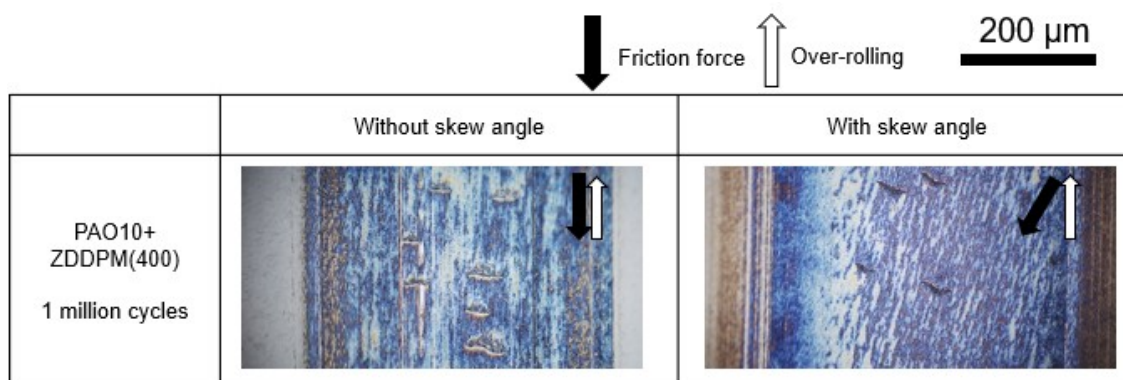


Figure 9-18 Example optical micrographs of ball rubbing track showing surface cracks generated with and without ball shaft skew on the MTM rig

#### 9.4.2 Mechanism by which ZDDP Influences Micropitting

Examination of ZDDP tribofilm evolution during micropitting tests provides further insight into the mechanism by which ZDDP influences the development of micropitting. The results presented here reveal a clear trend. In all cases where the ZDDP tribofilm builds up very quickly, the ball surface suffers subsequent micropitting in the form of surface fatigue cracks and associated micropits. In these cases, the counterface disc roughness also reduces relatively little from its initial value. By contrast, in tests where ZDDP tribofilm builds up very slowly or no ZDDP film forms at all (e.g. in pure PAO tests), no obvious cracks or micropits are subsequently observed. In these cases, the counterface disc roughness reduces considerably from its initial value and most of this reduction occurs very soon after the start of the test. These trends suggest that the fast formation of effective ZDDP tribofilms promotes micropitting by preventing running-in of the rough, hard counterface through suppression of mild wear. This in turn means that the contact is subjected to both higher asperity stresses and more asperity stress cycles throughout the test, which cause surface fatigue damage [248,347,349,350] and hence micropitting on the softer ball. This mechanism is in agreement with that described by Olver and co-workers [249,251].

The influence of ZDDP on micropitting is therefore primarily through mechanical rather than chemical means, via its influence on running-in and thus subsequent asperity contact stress history. As such, the proposed mechanism should be applicable to other, non-ZDDP types of antiwear chemistry that are fast-acting and hence build effective antiwear tribofilms rapidly at the start of the test to prevent adequate running-in. A totally non-effective anti-wear additive would reduce micropitting but is clearly not a solution to the

problem since it would lead to failure through excessive surface wear, as is exemplified here by the pure PAO tests. An appropriate oil formulation needs to prevent both micropitting and excessive wear through controlled build-up of antiwear films as discussed below.

Perhaps just as importantly, the increased amount of micropitting is not caused by increases in surface roughness or friction that are sometimes associated with formation of ZDDP tribofilms. In all cases shown here, the counterface roughness decreases from its initial value and friction is very similar in all tests. ZDDP tribofilms are reported to increase surface roughness [167] of rubbing surfaces, which may intuitively be expected to lead higher asperity stresses. However, this is only relevant if the initial roughness is extremely low, as is the case with standard MTM specimens,  $R_a \sim 20$  nm. It has no influence at realistic roughness levels, as is the case here and in real engineering components, since any ZDDP films formed do not result in significant further increase in surface roughness.

#### **9.4.3 Effect of Lambda on Micropitting and Tribofilm Formation**

As shown in Figure 9-1 and Figure 9-5, the amount of micropitting and ZDDP tribofilm formation were both strongly dependent on lambda value. The amount of micropitting was seen to be the largest for the intermediate lambda value of 0.15. This observation is in agreement with the theoretical predictions of Morales-Espejel et al. [248] who proposed that micropitting may be reduced at very low lambda due to an increased amount of mild wear, as well as at relatively high lambda values because of the reduced severity of asperity stress cycles. Also, Fujita et al. [167] showed that ZDDP tribofilms form more slowly when lambda is increased because of lower asperity contact pressures. The observations of the evolution of micropitting damage (Figure 9-1) and ZDDP tribofilm growth (Figure 9-5) presented here are in line with these reported trends. At  $\lambda = 0.1$  no appreciable ZDDP tribofilm was observed, most likely due to very severe contact conditions, leading to excessive ball wear and a large reduction in the counterface disc roughness. This, in turn, reduced both the subsequent level of asperity stresses and number of asperity stress cycles, limiting the formation of cracks and pits on the ball counterface. At  $\lambda = 0.7$ , ZDDP tribofilm formed relatively slowly at the start of the test, allowing for mild wear and running-in of disc roughness to occur in the first 0.1 million cycles. This subsequently reduced the severity of asperity stresses, minimising

surface fatigue and micropitting. However, in contrast to  $\lambda = 0.1$ , after 0.1 million cycles significant ZDDP tribofilm formed, preventing excessive surface wear.

In the intermediate case of  $\lambda = 0.3$ , a ZDDP tribofilm formed very quickly at the start of the test (tribofilm thickness of 55 nm after 0.1 million cycles) which prevented wearing-in and hence promoted micropitting by increasing subsequent asperity contact stresses. In this case, the observed reduction of ZDDP tribofilm thickness between 4 and 8 million cycles is likely to be due to local conditions becoming very severe once micropits are formed, which then acts to gradually remove the ZDDP tribofilm. The logarithmic x-axes used in Figure 9-5, Figure 9-11 and Figure 9-17 make this loss of ZDDP tribofilm thickness appear very abrupt, but in fact it is quite slow.

#### **9.4.4 Effect of ZDDP Concentration and Alkyl Structure on Micropitting**

As shown in Figure 9-6 and Figure 9-17, both ZDDP concentration and ZDDP alkyl structure influence ZDDP tribofilm growth and micropitting. The observed relationship between the formulation of the ZDDP additive and micropitting can be summarized as follows:

- Pure PAO base oil: When no ZDDP anti-wear additive is present, practically no micropitting damage is observed on the ball surface; instead the ball experiences severe wear. Such a wear rate would quickly lead to a failure of a real engineering components.
- The two lower concentrations of mixed ZDDP (ZDDPM) tested, 100 and 400 ppm P, form tribofilms relatively slowly in the initial 1 million cycles (Figure 9-11). The slow growth rate allows running-in of the rough counterface discs (Figure 9-8) which in turn minimises micropitting on the ball. The anti-wear tribofilm then develops from 1 million cycles onwards and the steady state tribofilm thickness is similar to that of the two higher concentrations for the remainder of the test time (Figure 9-11). This minimises further wear of both discs and balls.
- Mixed ZDDP (ZDDPM) blends with 800 ppm P form tribofilms faster than those with primary ZDDP (ZDDP1) at the same P concentration (Figure 9-17). This provides better wear protection in the early stages but prevents running-in of the disc (Figure 9-14), subsequently leading to micropitting (Figure 9-12). By contrast, the slow initial film formation of ZDDP1 permits running-in to occur and thus limits subsequent micropitting.

These observations indicate that an oil formulation that forms a thick and effective anti-wear film very quickly at the start of operation can lead to inadequate running-in and consequent increased levels of surface fatigue and micropitting due to high asperity stresses, while one with inadequate anti-wear tribofilm formation can lead to excessive wear. Both of these situations are likely to cause component failure. Therefore, an oil formulation that allows for adequate running-in of the surfaces through controlled and relatively slow tribofilm growth in the initial stages of operation appears to be the best compromise. Such an oil will allow for adequate running-in of the components to minimize subsequent micropitting but also form an adequate antiwear tribofilm to minimize excessive long-term wear.

## 9.5 Conclusions

This study has used the MTM-SLIM test rig to investigate systematically the mechanisms by which ZDDP anti-wear tribofilms influence micropitting. Key conclusions are as follows.

- The MTM-SLIM can be used to generate and study micropitting. The main advantage of this method compared to other, more established micropitting tests is that it provides the means to simultaneously observe the development of tribofilm and micropitting, thus providing insight into the mechanisms by which lubricant formulation affects surface fatigue.
- The mechanism by which ZDDP and probably anti-wear additives in general affect micropitting is through their influence on asperity stresses in rough rubbing contact and the subsequent competition between surface wear and asperity contact fatigue. Too rapid formation of antiwear tribofilms early in operation acts to prevent adequate running-in of the initially rough surfaces, which in turn means that both the level of asperity stresses and the number of asperity stress cycles remains high throughout subsequent operation, causing increased surface fatigue damage accumulation and eventually micropitting.
- At the other extreme, a lack of effective antiwear tribofilm enables running in, and thus reduces micropitting damage, but eventually leads to component failure due to excessive wear. The intermediate case of a controlled rate of tribofilm build-up

at the start of operation, which allows for some mild wear and hence adequate running-in, followed by an effective antiwear tribofilm for the rest of component life, is thus the ideal situation to minimize both micropitting and surface wear.

- The effect of tribofilms on the competition between surface wear and micropitting means that with ZDDP-containing oils, the extent of micropitting is critically dependent on  $\lambda$ , ZDDP concentration and ZDDP alkyl structure.

## 10 Influence of Black Oxide Coating on Micropitting and ZDDP Tribofilm Formation

*The research described in this chapter uses the MTM-SLIM-based approach developed in the previous chapter to investigate the effect of black oxide coatings on micropitting and the influence of tribofilm formation by the antiwear additive ZDDP on this micropitting. It is found that in a steel ball on disc rolling/sliding contact, micropitting of the ball is completely prevented by applying a black oxide (BO) coating to rough counterface steel discs in both steel ball on BO-coated disc and BO-coated ball on BO-coated disc tribopairs. The key to this mechanism of prevention of micropitting is the low hardness of BO coating, which is only one quarter that of the steel substrate, so that it is easily worn during rubbing to reduce surface roughness; in effect accelerating running-in even in the presence of ZDDP. ZDDP is still able to form a protective film on the rubbing surfaces, however, so controlling other forms of wear. The research described in this chapter has already been published in Tribology Transactions with an open access [351].*

*It should be noted that the numerical simulation of the distribution of contact pressure described in section 10.3.2 was conducted by Dr. Amir Kadiric.*

### 10.1 Introduction

As described in 3.4.2, the application of surface coatings, particularly black oxide (BO) coating, is currently believed to be one of the most practical approaches to alleviating micropitting. The consequences of the low hardness of the BO coatings in relation to running-in are now relatively well-established [254,255,257–260], but the potential enhancement of the running-in process, and hence reduced micropitting, via chemical effects of the BO coating in suppressing the antiwear film build-up has not been directly observed. This is important since it is now recognised that micropitting and adhesive wear are competing modes of surface failure and that antiwear tribofilm growth plays an important role in both mitigating adhesive wear and promoting micropitting [248,251]. In addition, it is unclear whether any potential reduction in the boundary friction coefficient that may be afforded by the BO coating plays a role in the latter's apparent ability to reduce micropitting.

To help resolve these issues, this Chapter describes new research that aims to clarify the effect of BO coating on ZDDP tribofilm growth and its effect on micropitting. The evolution of tribofilm growth and the micropitting of a ball against a rough disc counterface in a ZDDP solution are observed simultaneously using MTM-SLIM and this is augmented by a comparison of tribofilm growth on the surfaces of steel and BO coating using smooth counterface surfaces. Also, the adsorption behaviour of ZDDP on  $\text{Fe}_2\text{O}_3$  and  $\text{Fe}_3\text{O}_4$  is investigated using a quartz crystal microbalance. From this study, relevant mechanisms by which BO coatings mitigate micropitting are suggested.

## 10.2 Test Methodology

### 10.2.1 Test Conditions

Two types of rolling-sliding MTM tests were carried out; (i) using rough disc counterfaces to generate micropitting and measure ZDDP tribofilm at the same time, and (ii) using smooth disc counterface in slower speed rubbing condition to quantify and compare ZDDP tribofilm formation on steel and BO-coated steel.

### 10.2.2 Micropitting Tests with Rough Disc Counterface

All micropitting tests were conducted using the same method as described in the previous chapter. Table 10-1 shows the measured properties of MTM specimens and conditions of the rough counterface MTM tests to generate micropitting. As in the previous chapter, rough AISI 52100 steel discs with  $R_a = 440$  nm were used in order to subject the smooth counterface ball to severe asperity contact stress cycles and promote micropitting. BO coating was applied to both the ball and the disc, and four tribopair combinations of a steel ball/steel disc, a steel ball/BO-coated steel disc, a BO-coated steel ball/steel disc, and a BO-coated steel ball/BO-coated steel disc were studied. In this study the abbreviation steel/BO denotes an uncoated steel ball rubbed against a BO-coated disc while BO/steel denotes a BO-coated ball against a steel disc.

Table 10-1 Measured properties of MTM specimens and micropitting test conditions

Ball specimen	AISI 52100 steel; hardness $755 \pm 25$ HV, roughness $R_a 8 \pm 3$ nm
	BO-coated AISI 52100 steel; roughness $R_a 8 \pm 3$ nm

Disc specimen	AISI 52100 steel; hardness $825 \pm 25$ HV, roughness $Ra\ 440 \pm 20$ nm
	BO-coated AISI 52100 steel; hardness $2.6 \pm 0.1$ GPa (see Fig. 2), roughness $Ra\ 420 \pm 20$ nm
Test temperature (°C)	65
Test load (N)	75 (Maximum Hertzian pressure: 1.2 GPa)
Entrainment speed (m/s)	3
Slide-roll-ratio (SRR) $2*(U_{ball}-U_{disc})/(U_{ball}+U_{disc})$	-0.05
Test cycles	8 million cycles (40 hours): Test paused for specimen inspection after 1000 cycles, 0.1 million cycles, 1 million cycles, 4 million cycles, 8 million cycles

### 10.2.3 Tribofilm Formation Tests with Smooth Disc Counterface

In order to study the influence of a BO coating on tribofilm formation, some tests were also carried out using smooth MTM discs in slow speed rubbing conditions, more typical of those generally used in tribofilm formation studies [352] including the research described in Chapter 5. Table 10-2 lists the measured properties of materials and conditions of the MTM tests. Two tribopairs, steel ball/steel disc and BO-coated steel ball/BO-coated steel disc, were studied. To help suppress wear of BO, smooth discs with  $Ra$  less than 10 nm, were used and a low load of 15 N, corresponding to a maximum Hertzian pressure of 0.75 GPa was employed. The tests lasted 180 minutes, and were paused for the inspection of specimens after 60 minutes and 120 minutes.

Table 10-2 Measured properties of MTM specimens and film forming test conditions

Ball specimen	AISI 52100 steel; hardness $755 \pm 25$ HV, roughness $Ra\ 8 \pm 3$ nm
	BO-coated AISI 52100 steel; roughness $Ra\ 8 \pm 3$ nm
Disc specimen	AISI 52100 steel; hardness $825 \pm 25$ HV, roughness $Ra\ 7 \pm 3$ nm



	BO-coated AISI 52100 steel; hardness $2.6 \pm 0.1$ GPa (see Fig.2), roughness $Ra\ 7 \pm 3$ nm
Test temperature (°C)	65
Test load (N)	15 (Maximum Hertzian pressure: 0.75 GPa)
Entrainment speed (mm/s)	50
Slide-roll-ratio (SRR) $2*(U_{ball}-U_{disc})/(U_{ball}+U_{disc})$	-0.5
Test duration	180 minutes Test paused for specimen inspection after 60 mins and 120 mins

#### 10.2.4 Test Lubricants

The test lubricant used throughout was a solution of ZDDPM at a concentration of 800 ppm P in PAO10 base oil. For all MTM tests, at conditions listed in both Table 10-1 and Table 10-2, 50 ml of lubricant was used to provide the same aging condition of lubricants during the tests. In all experiments, the initial lambda was *ca.* 0.3 (corresponds to *ca.* 150 nm minimum oil film thickness) to ensure boundary and mixed lubrication regimes, where lambda is defined as the ratio of the calculated EHD film thickness to the initial composite root mean square roughness of the two surfaces. Although alternative antiwear chemistries are often used in gear oils, ZDDP is employed here as its antiwear behaviour and its influence on micropitting in steel-steel contacts is relatively well understood, thus enabling any effects of BO coating to be more readily discerned. This also allows the observations made here to be related to previous relevant studies which also used ZDDP.

#### 10.2.5 BO Coating Properties

The general properties of BO coatings used in this work are described in [353]. Figure 10-1 shows an SEM image of the taper-section of a BO-coated steel disc ( $Ra\ 8$  nm) and EDX analysis at three points; (1) in the protective resin film; (2) in the BO coating; (3) in the steel substrate. An approximately  $1\ \mu m$  thick, uniform BO layer is present on the steel substrate. This layer is mainly composed of iron and high proportion of oxygen, which roughly corresponds to the chemical composition of  $Fe_3O_4$ .

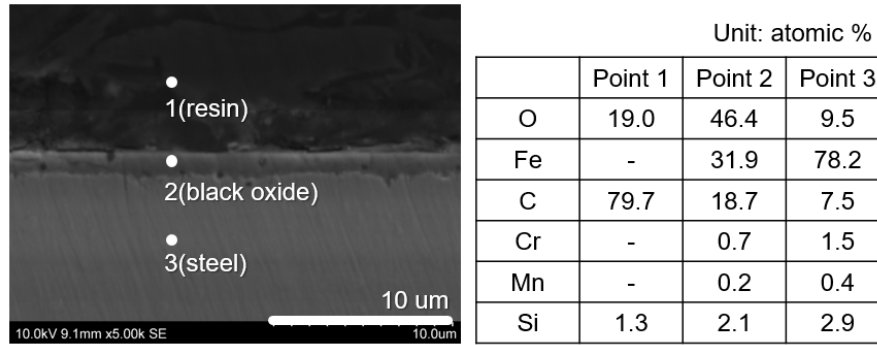


Figure 10-1 SEM image of BO-coated steel disc (Ra 8 nm) and EDX analyses

To enable the effect of BO coating on asperity contact pressure to be determined, nano-scale depth profiles of hardness and elastic modulus of the smooth BO-coated steel discs (Ra = 8 nm) were measured using a Nano Indenter G 200 with a Berkovich tip as described in Section 4.4.5. Measured nanoindentation hardness were obtained over the range between 0.05 μm and 0.1 μm since the BO coating was approximately 1.0 μm thick. Measured values were obtained by averaging the values of 25 indentations. Figure 10-2 shows that BO coating has *ca.* a quarter of the hardness,  $2.6 \pm 0.1$  GPa, and elastic modulus,  $52.9 \pm 3.1$  GPa, compared to steel. These values agree with a previous study [354]. Although the BO coating is much less stiff than steel, because it is very thin compared to the overall dimensions of the contact it will not significantly affect the Hertzian contact pressure. This was confirmed by the simulation of contact pressure using the established model [350,355,356]. Therefore, regardless the presence of BO coating, rolling-sliding tests were conducted in the same load.

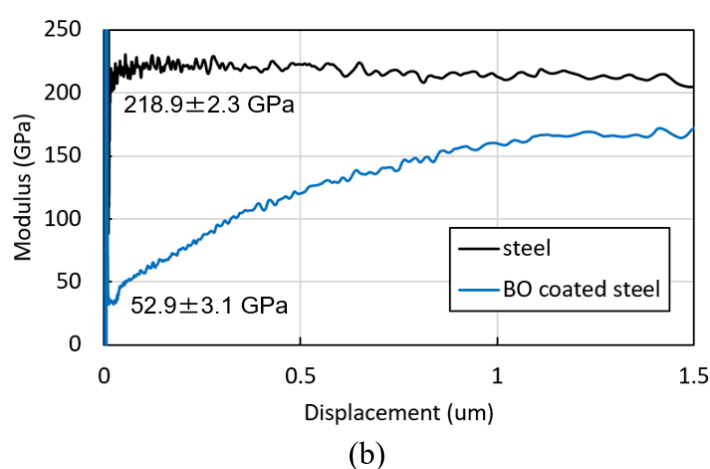
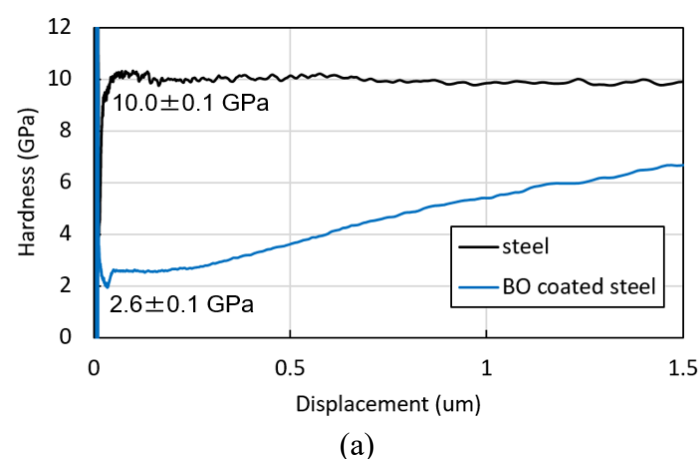


Figure 10-2 Depth profile of (a) hardness and (b) elastic modulus of steel disc and BO-coated steel disc measured using nano-indentation in CSM mode. Note that values are taken from the range between 0.05  $\mu\text{m}$  and 0.1  $\mu\text{m}$  from the surfaces.

### 10.2.6 Test Procedures

All micropitting tests were conducted using the same procedure as described in Chapter 9. The MTM micropitting tests with the conditions in Table 10-1 were interrupted after 1000 cycles, 0.1, 1, and 4 million cycles to observe and measure wear and micropitting on the ball and the roughness of the disc wear tracks. The tests with the conditions of Table 10-2 were stopped after 60 minutes and 120 minutes to observe the wear tracks on the balls and the discs. Before these surface measurements, the balls and the discs were rinsed in toluene in an ultrasonic bath for 10 minutes to remove supernatant oil. Rinsing the ball and disc with toluene did not influence the thickness of the ZDDP tribofilm. After measurements of the balls and the discs, the specimens were returned to the MTM and the rolling-sliding tests continued. During tests, motion was periodically halted and the

ZDDP tribofilm thickness was measured using SLIM. All tests shown in this study were repeated one time.

#### **10.2.7 ZDDP Adsorption using QCM-D**

A QCM-D monitoring was used to monitor the adsorption of ZDDP from PAO solution on  $\text{Fe}_3\text{O}_4$  and also on  $\text{Fe}_2\text{O}_3$ . These oxides are believed to represent the outermost surface composition of steel. The tests were carried out as described in Section 4.5.

#### **10.2.8 Calculation of Distribution of Contact Pressure**

In order to determine the influence on contact pressure of BO coatings on rough counterfaces, the distribution of contact pressure was predicted using an existing numerical contact mechanics model in purely elastic analysis [350,355,356]. Significant assumptions of the model are as follows; strains are relatively small allowing linear elastic theory, and surface slopes are assumed to be relatively small so that forces act normal to the surface. The values of AISI 52100 steel of Poisson's ratio = 0.3 and elastic modulus = 207 GPa were used. For the case of a fresh steel/BO tribopair, 1  $\mu\text{m}$  of BO-coated steel disc was employed (BO Poisson's ratio = 0.3, elastic modulus = 53 GPa). The surface profiles used were obtained using a Talysurf profilometer.

### **10.3 Results**

#### **10.3.1 Effect of BO Coating on Micropitting**

This section presents the results of the influence of BO coating on micropitting. MTM tests were conducted according to the conditions listed in Table 10-1. Note that the same result in Chapter 9 is used for the result obtained from a steel/steel tribopair in this section.

##### **10.3.1.1 Evolution of Surface Damage on Balls**

Figure 10-3 shows representative optical micrographs of the wear tracks on the balls from the steel-steel, steel/BO, BO/steel and BO/BO tribopair tests after 0.1, 1, 4 and 8 million. The blue colour in these images indicates the presence of a ZDDP tribofilm. The extent of micropitting damage in terms of density of cracks and pits varies somewhat over the ball rubbing track. The images shown here illustrate typical damage extent for each material combination. In steel/steel and BO/steel tests, cracks are formed on the balls after

0.1 million cycles. At 1 million cycles these cracks are seen to have grown to a length of tens of microns across the rolling track in a fanned, shallow 'V' shape, typical of surface-initiated contact fatigue. As the test progresses, the number of cracks significantly increases and they start to interact and join up. After 4 million cycles, small pits (tens of microns in size) associated with these cracks become apparent. After 8 million cycles, these micropits cover large areas of the wear tracks in these two cases. By contrast, cracks and micropits are not observed on the balls in the tests with steel/BO and BO/BO tribopairs at any time throughout the 8 million cycle tests. The actual percentage of micropitted area on the entire ball wear track after 8 million cycles was also estimated. This was obtained by taking a series of optical images to cover the entire ball wear track and then manually identifying the size of the area covered by cracks and micropits in each of these images as a percentage of the wear track. The reported value is the average of all values obtained in the individual image and therefore represents an estimate of the total extent of micropitting over the entire wear track rather than just the example image shown in Figure 10-3 to account for any variability in the damage along ball circumference. For steel/steel and BO/steel tribopairs this was 27% and 25% respectively while for BO/BO and steel/BO it was zero as no micropitting was observed anywhere in the wear track. These results show that micropitting can be successfully prevented when the rougher, harder disc is coated with BO regardless of whether the ball is coated or not. In contrast, micropitting always occurs when the rough disc is not coated, regardless of whether the ball is coated or not.

An attempt was also made to measure the evolution of loss of material on balls due to conventional mild wear, as opposed to micropitting. This was done to capture any loss of the BO coating through wear, but it also helps to understand the mechanisms at play since mild wear is known to compete with micropitting [248,345]. Average wear depth of ball rubbing track was obtained from stylus profilometer measurements taken at four locations around the ball circumference. In the case of micropitted balls from steel/steel and BO/steel tests, care was taken to avoid micropits so that the obtained maximum depth is not distorted by any deep, discrete micropits and hence represents loss of material due to general mild wear. Any ZDDP tribofilm that may have been present in the tracks was not removed prior to making these measurements. This is so that rubbing tests can be resumed after each inspection without introducing unwanted disturbances. The presence of any ZDDP tribofilm would therefore potentially act to make the measured wear depths in this plot smaller than reality. However, since the maximum ZDDP tribofilm thicknesses observed in this work are of the order of 100 nm (see Figure 10-9) the effect of this in

practice is inconsequential to the presented trends given that the measured wear depths are up to 1.1  $\mu\text{m}$ .

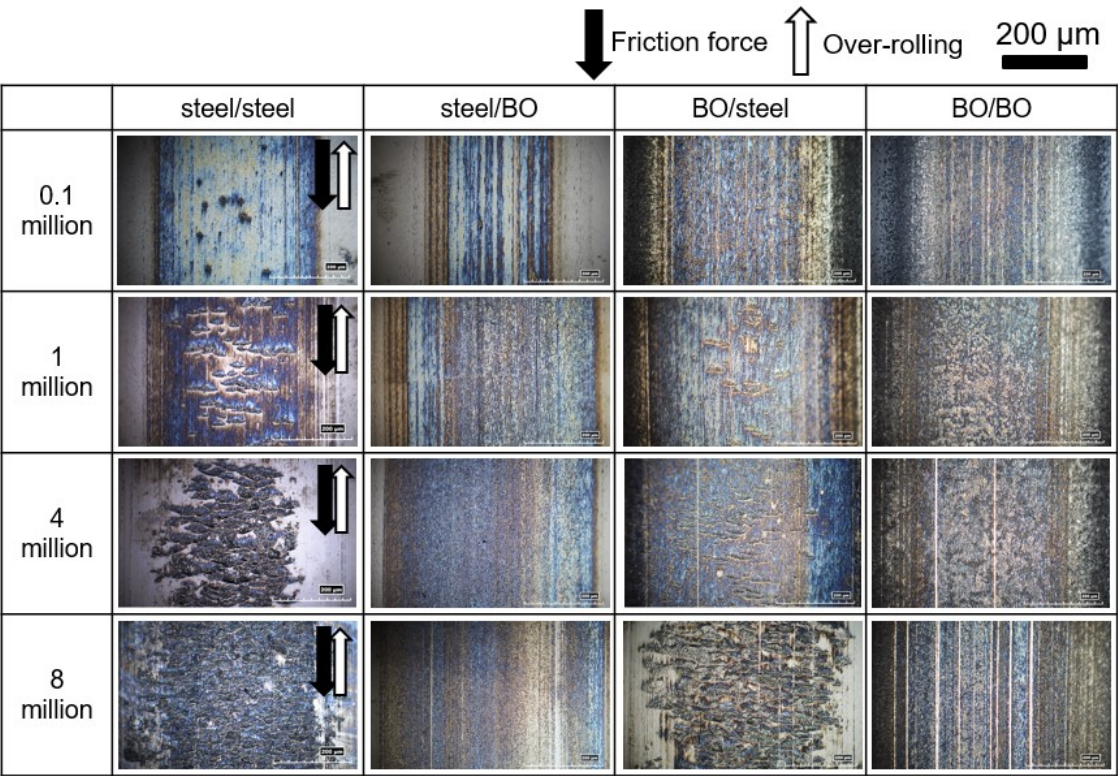


Figure 10-3 Optical micrographs of wear tracks on balls of the tribopairs with BO coating. (steel/BO denotes steel ball on BO-coated disc and vice versa). It is important to note that the scale bar included in the top right corner of the figure applies to all image

Figure 10-4 shows the maximum depth of the wear tracks on the balls obtained in this way. It is evident that the tribopair of steel/BO produces almost no material loss on the ball. The tribopair steel/steel produces only a relatively small amount of mild wear, with maximum wear track depth (outside micropitted areas) being less than 0.3  $\mu\text{m}$  after 8 million cycles. In contrast, the tribopairs of BO/steel and BO/BO result in a high amount of material loss due to wear on the BO-coated balls very early in the tests, with 0.83  $\mu\text{m}$  and 1.1  $\mu\text{m}$  wear depths respectively after 1000 cycles. However, after the initial 1000 cycles there is no further loss of material from the ball in case of BO/BO disc. The reasons for this are discussed in more detail later but are likely due to the fact that once the harder steel substrate is exposed on the ball it resists further damage when rubbed against the counterface disc which has been significantly smoothed by this time due to BO coating wear. The material loss from the ball due to wear in the BO/steel test (outside micropitted

areas) continues after 1000 cycles but the rate of loss drops drastically to become similar to that seen on the balls from steel/steel tests. In this case, the continued loss of material is likely due to continued mild wear induced on the ball by the steel disc which remains rough throughout the test just as in the case of steel/steel pair. Considering that BO coating has approximately 1  $\mu\text{m}$  thickness, these results suggests that most of the BO coating on the balls is removed by wear in the first 1000 cycles, well before microptting damage itself is initiated on the balls. Finally, given that ZDDP tribofilms were observed in all four tribopairs (indicated by blue colour in Figure 10-3) at and after 1000 cycles, this implies that these ZDDP tribofilms continue to grow on the steel substrate after the early removal of the BO coating.

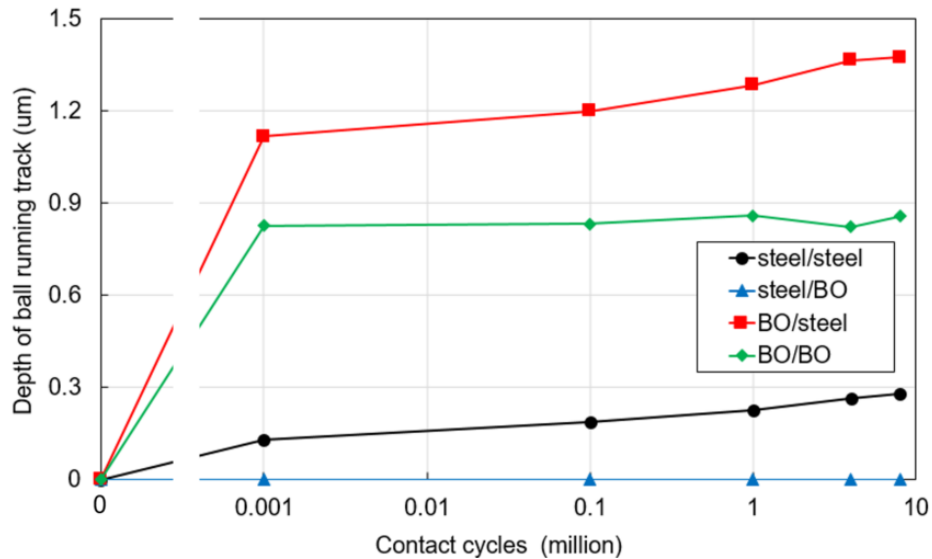


Figure 10-4 Measured depth of ball wear track of the tribopairs with BO coating (steel/BO denotes steel ball on BO-coated disc and vice versa).

#### 10.3.1.2 Evolution of Surface Roughness of Counterface Discs

Figure 10-5 shows the evolution of the disc roughness during the tests. In all cases, the disc roughness reduces significantly in the initial stages of the test and then remains relatively stable thereafter - behaviour indicative of running-in. However, considerable differences are evident between non-coated and BO-coated discs. The tribopairs of steel/steel and BO/steel (*i.e.* cases where the disc was not coated) show a disc roughness reduction from the initial Ra value of 0.44  $\mu\text{m}$  to approximately 0.3  $\mu\text{m}$  after 1000 cycles and this then stays constant at this level for the rest of the test. In contrast, in the tests where the disc is coated, namely steel/BO and BO/BO, disc roughness is reduced much more quickly in the initial period of the test, from 0.42  $\mu\text{m}$  to approximately 0.18  $\mu\text{m}$

after the first 1000 cycles; it then remains relatively constant, reaching approximately  $0.13\ \mu\text{m}$  after 8 million cycles at the end of the tests. These results show that steel discs coated with BO experience a very considerable roughness reduction very quickly after the start of the test, within the first 1000 cycles, which corresponds to 30 seconds of rubbing.

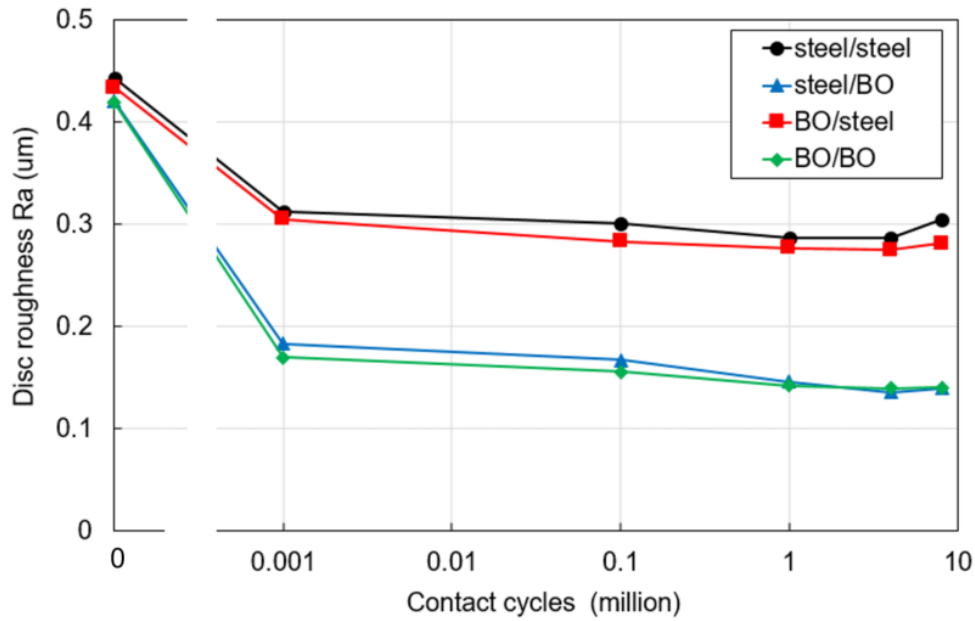
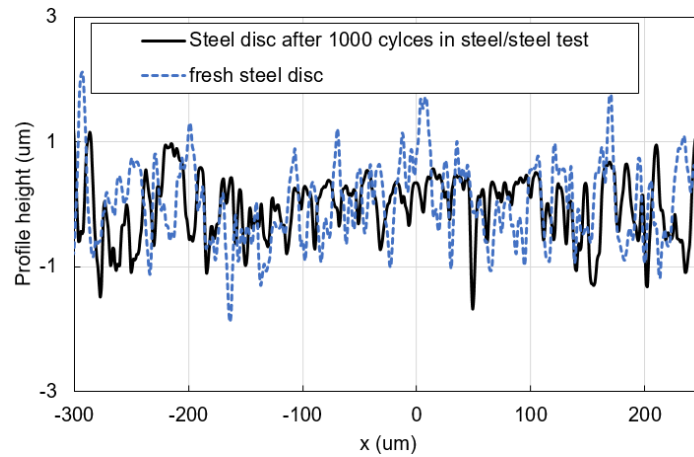


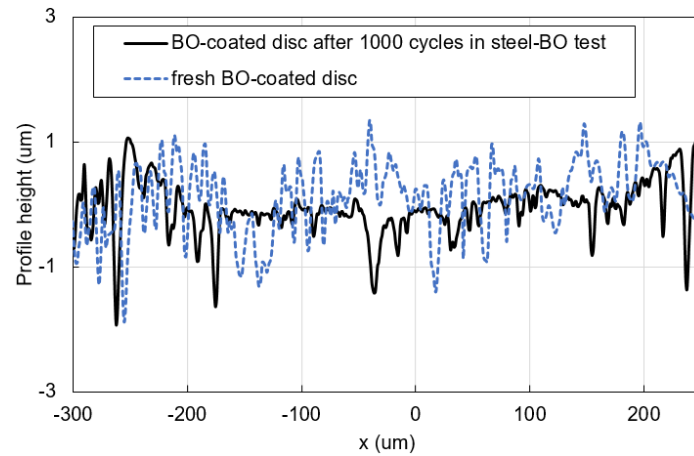
Figure 10-5 Disc roughness evolution of the tribopairs with BO coating (steel/BO denotes steel ball on BO-coated disc and vice versa).

Figure 10-6 shows the corresponding surface profiles of the steel and BO-coated discs when fresh and after 1000 cycles in tests against a steel ball. These profiles clearly indicate that after 1000 cycles, the roughness peaks of the BO-coated disc have been polished considerably more than those of the steel disc under the same test conditions. This is in agreement with the results of Figure 10-5.





(a)



(b)

Figure 10-6 Disc surface profiles recorded before the test and at 1000 cycles for (a) steel disc tested against a steel ball and (b) BO-coated disc tested against a steel ball

### 10.3.1.3 Friction Behaviour

Figure 10-7 shows the evolution of friction coefficient in tests conducted with the four tribopair combinations. The friction coefficient obtained in the test with steel/steel and BO/steel is initially ca. 0.1, and gradually decreases to reach 0.08 at the end of the test. By contrast, the friction coefficient just after the start of steel/BO and BO/BO tests is 0.05 and it remains relatively constant for the rest of the test. It should be noted that the first friction measurement in the MTM rig is recorded at 550 cycles. This result is in line with the rapid running-in of the BO-coated disc shown in Figure 10-4 and Figure 10-5 above:

The high surface roughness of the steel discs generates high friction as the contact operates in mixed lubrication conditions, but when BO coating is applied to rough steel discs, their roughness decreases almost immediately after the tests start, resulting in an increase in lambda ratio and thus a significant drop in friction coefficient. It should be noted that the momentary blips in the recorded friction traces apparent in Figure 10-7 are artifacts of the measurement method and occur just after motion was paused for capture of a SLIM image.

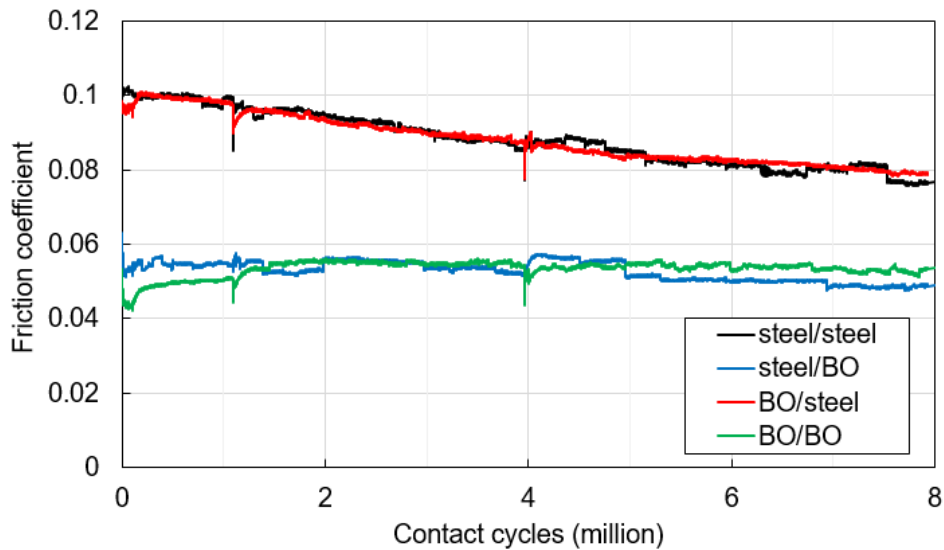


Figure 10-7 Friction behaviour in tests of the tribopairs with BO coating (steel/BO denotes steel ball on BO-coated disc and vice versa).

#### 10.3.1.4 Evolution of ZDDP Tribofilm in Micropitting Tests

Figure 10-8 shows representative SLIM images of the ball tracks at different times during four micropitting tests. Since the BO-coated balls were less reflective than the uncoated balls, light intensity was adjusted to obtain clear SLIM images from BO-coated balls during the tests; this is the reason for different colour of the first images of the BO coated balls in Figure 10-8. While the development of cracks and micropits on the ball surface are apparent in the SLIM images from the tests of steel/steel and BO/steel tribopairs, this damage is not observed on the ball wear tracks of steel/BO and BO/BO tribopairs. This corresponds with the observations made in Figure 10-3. SLIM images indicate that similar ZDDP tribofilms are formed on balls from all four tribopair combinations.

Figure 10-9 shows tribofilm thickness in the middle region of the ball rubbed tracks obtained from SLIM images for steel/steel and steel/BO tests. Unfortunately, the low reflectivity of the BO-coated balls, combined with the fact that the BO coating was rapidly worn off meant that thicknesses could not be reliably quantified from SLIM images of the BO-coated balls. The initial rate of tribofilm growth for steel/BO appears to be very slightly smaller than that for steel/steel but the two are very similar for all practical purposes. After 0.1 million cycles, the tribofilm in the steel/steel test continues to grow rapidly to reach approximately 180 nm after 0.3 million cycles, whereas that in the steel/BO test grows more slowly, reaching 140 nm after 0.3 million cycles. This difference in the tribofilms on steel balls rubbed against a steel disc and BO disc is also evident in the SLIM images of Figure 10-8 at 0.5 million cycles, where relatively thicker tribofilms, indicated by the green colour in the figure, appear to exist on the coated and uncoated balls rubbed against steel discs than those rubbed against BO coated disc. It may be that the lower friction resulting from fewer or milder asperity contacts generated by the worn BO-coated discs may result in thinner tribofilms on the balls [217,218] at this stage of the test. The tribofilms then continually reduce in thickness and become very similar for all tribopairs after about 1 million cycles where they are ~85 nm, and drop to ca. 30 to 40 nm at 8 million cycles.

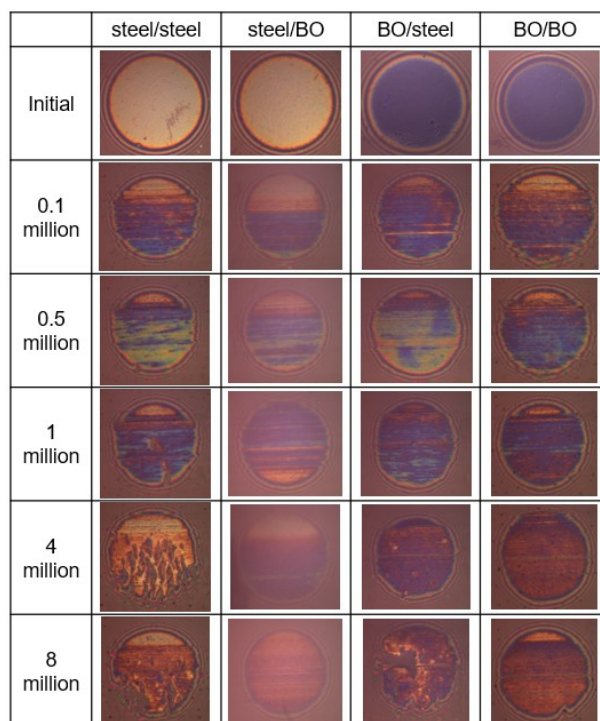


Figure 10-8 SLIM images of ball running track recorded in tests conducted in the tribopairs with BO coating (steel/BO means steel ball on BO-coated disc and vice versa).

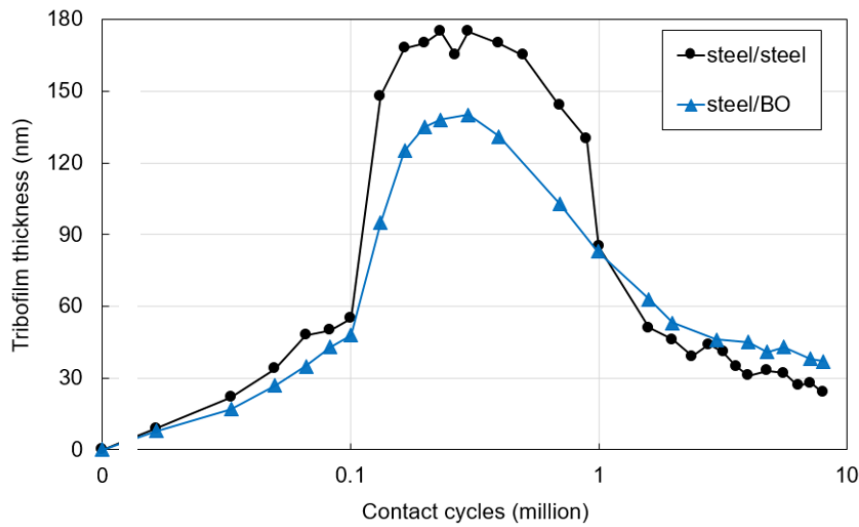


Figure 10-9 Tribofilm evolution on the ball wear tracks for steel/steel and steel/BO tribopairs

While the results above describe tribofilm formation on the balls, it was also of interest to assess tribofilm formation on the discs. Figure 10-10 shows surface profiles of the balls (a and c) and the discs (b and d) from tests with steel/steel and steel/BO tribopairs after 0.1 million cycles, obtained using a Talysurf stylus profilometer. In all cases, profiles are shown before and after EDTA treatment, where EDTA treatment was used to remove ZDDP tribofilms from surfaces [159]. The results show that while tribofilms of 50 - 100 nm thickness were formed on both of the balls, no measurable tribofilms were observed on either steel or BO-coated discs from the steel/steel and steel/BO tribopair tests respectively. As shown in Figure 10-6, most of the decrease in the surface roughness of the discs occurs between 0 to 1000 cycles. This continuous asperity removal may inhibit the growth of tribofilm on the discs up to this point in the tests and hence no tribofilms are observed here at 1000 cycles. However, it is difficult to accurately measure tribofilm thickness on such rough surfaces using a stylus profilometer so the existence of some tribofilm cannot be excluded.

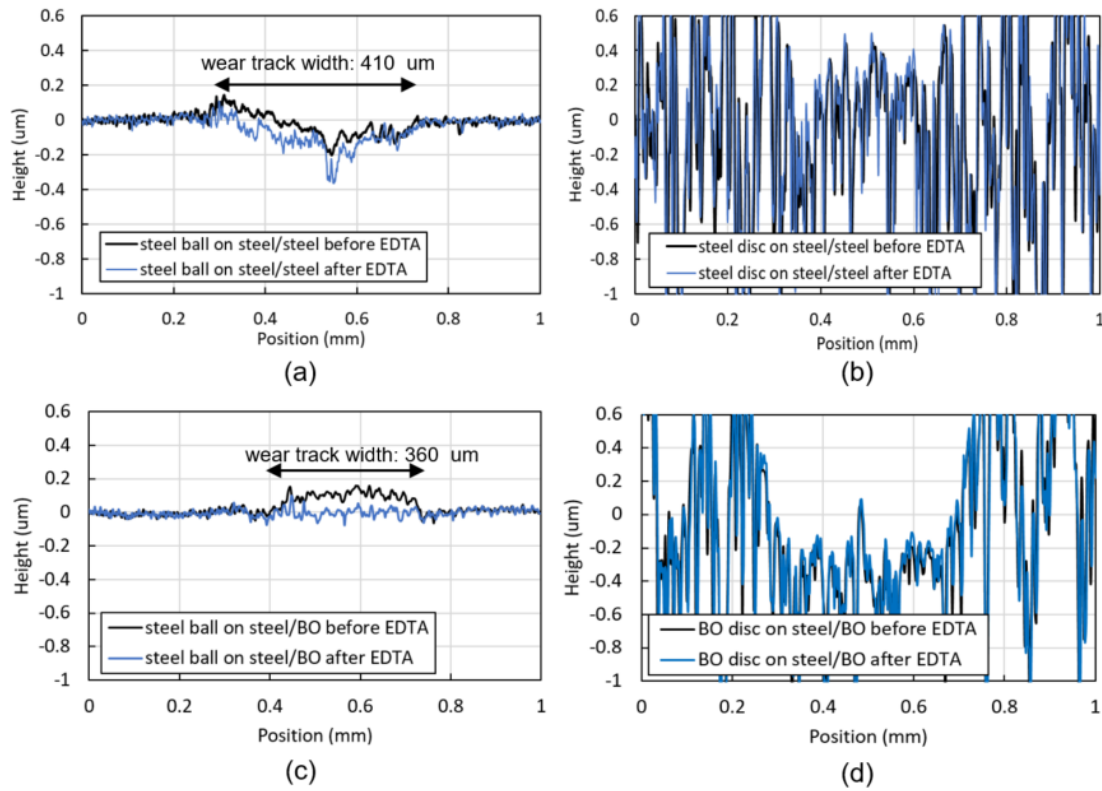


Figure 10-10 Surface profiles before and after EDTA treatment of (a) the ball and (b) the disc of steel/steel contact and (c) the ball and (d) the disc of steel/BO contact after 0.1 million cycles.

### 10.3.2 Influence of BO Coating on Tribofilm Formation using Smooth Discs

In this section, ZDDP tribofilm growth on BO coating was assessed in the test conditions shown in Table 10-2, *i.e.* with smooth balls and discs at low entrainment speed and relatively low load conditions during 180-minute tests. The combinations of steel ball on steel disc and BO-coated ball on BO-coated disc were compared.

### 10.3.2.1 Wear of Balls and Discs

Figure 10-11 shows the evolution of wear depth of the balls and the discs in tests with steel/steel and BO/BO tribopairs. While no measurable wear is observed on the ball or the disc from the steel/steel test, some wear of both surfaces is seen in the tests with the BO/BO tribopair. The wear is continuous throughout the test and the maximum wear depth at the end of the 180-min test is  $0.50\ \mu\text{m}$  and  $0.42\ \mu\text{m}$  for the BO-coated ball and the BO-coated disc respectively. Given that thickness of BO coating was approximately  $1.0\ \mu\text{m}$ , this indicates that some BO coating remains at the end of these tests.

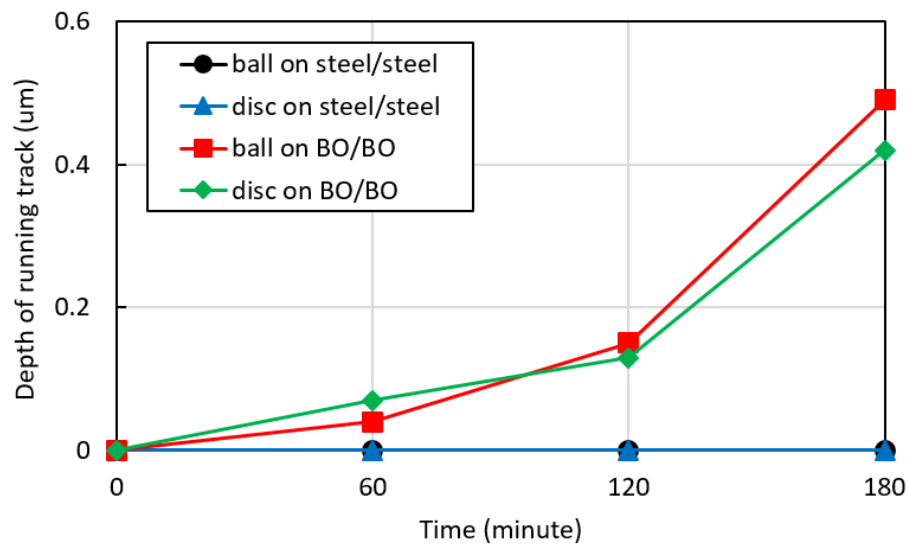


Figure 10-11 Wear evolution of the balls and the discs of steel/steel and BO/BO tribopairs (Note that BO coating thickness is approximately  $1\ \mu\text{m}$ ).

### 10.3.2.2 Friction Behaviour

Figure 10-12 shows the friction coefficient evolution of steel/steel and BO/BO tribopairs. For steel/steel tribopair, friction coefficient was around 0.04 at the beginning of the test, and this gradually increases to stabilize at approximately 0.11 after 120 minutes. By contrast, the BO/BO tribopair initially gives a higher friction coefficient, around 0.06, which then increases at a similar rate to a steel/steel contact, to reach 0.11 after 60 minutes. BO/BO friction shows greater fluctuations during the 180-minute test than that of the steel/steel contact. It is well known that the growth of ZDDP tribofilm can increase friction coefficient in mixed lubrication conditions since its pad-like structure can increase the roughness of the rubbing surfaces, particularly if the latter are very smooth to start with, resulting in a reduction of the effective lambda ratio and consequent transition from mixed to boundary lubrication [236]. Since both steel/steel and BO/BO tribopairs show an increase in friction from an initially lower value to 0.11 - 0.12, which

corresponds to friction of ZDDP tribofilms in boundary lubrication, this behaviour suggests that ZDDP tribofilms are built up in both cases during the initial phases of rubbing. Unlike in the steel/steel contact, some wear occurred on the BO/BO tribopair, which presumably also removed ZDDP tribofilm from the rubbing surface. This continuous tribofilm removal and formation may result in the relatively unstable friction coefficient of BO/BO contact during the test.

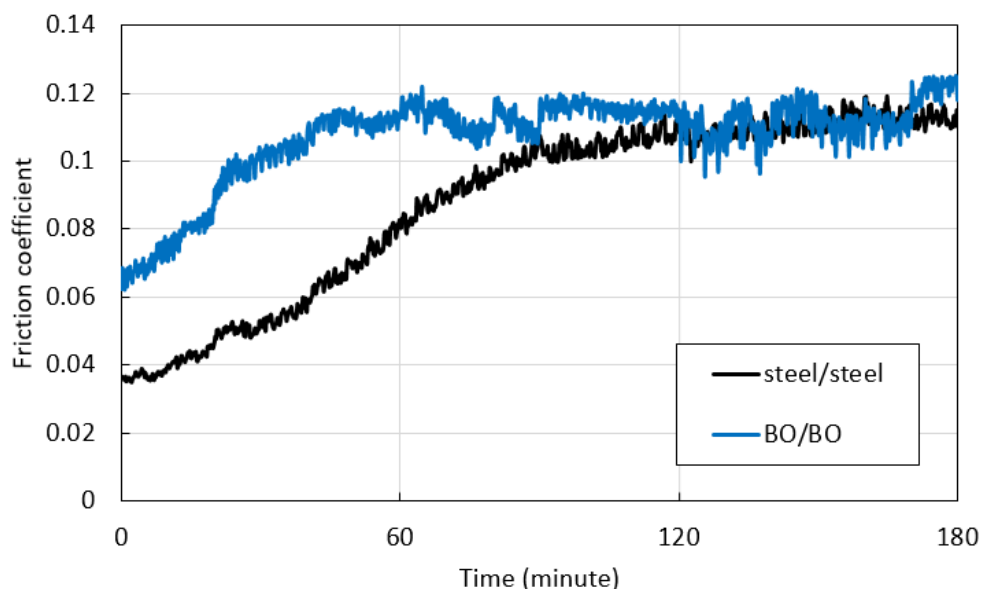


Figure 10-12 Friction coefficient of steel/steel and BO/BO tribopairs.

### 10.3.3 Observation of ZDDP Tribofilm Formation

Figure 10-13 shows optical micrographs of the wear tracks of the balls and discs from steel/steel and BO/BO tests under conditions listed in Table 10-2 after 60, 120 and 180 minutes. After 60 minutes, the surfaces of steel and BO specimens appear relatively similar. After 120 minutes and 180 minutes of rubbing, while ZDDP tribofilm, indicated by blue-colour, is present on the steel ball and disc, no such tribofilm is observed on the BO-coated ball and disc.

Figure 10-14 shows the SLIM images obtained from the balls at various times during the steel/steel and BO/BO tests. To help observe the tribofilm formation more clearly, magnified SLIM images after 10 minutes and 30 minutes rubbing are also included. Note that SLIM images obtained from the BO-coated ball are darker than from the steel ball because of BO's low reflectivity. Quantitative tribofilm thickness values for steel/steel



tests obtained from these SLIM images are included in the respective images of Figure 10-14. Tribofilm grows steadily on steel/steel contact during the test to reach ca. 40 nm after 180 minutes rubbing. Although tribofilm thickness could not be quantified on the BO-coated ball due to its low reflectivity, some tribofilm formation on BO is clearly visible in the SLIM images, with a colour change on the wear track of BO-coated ball observed after 10 minutes rubbing. Unlike in the case of steel/steel contact, the edges of the nominally circular ball-flat contact area in the SLIM images from the BO/BO tests are distorted, indicating some wear of the BO-coated ball.

Based on the increase of friction coefficient (Figure 10-12) and the optical micrographs (Figure 10-13), ZDDP tribofilm initially formed and grew on the BO-coated ball and disc in a similar fashion to the surface of steel/steel contact. However, the ZDDP tribofilm on BO balls after this initial period appears to be thinner than that on steel balls as evident in the images of Figure 10-13, probably due to continuous wear of the very soft BO-coating that effectively prevents further build-up of the ZDDP tribofilm on the BO surface.

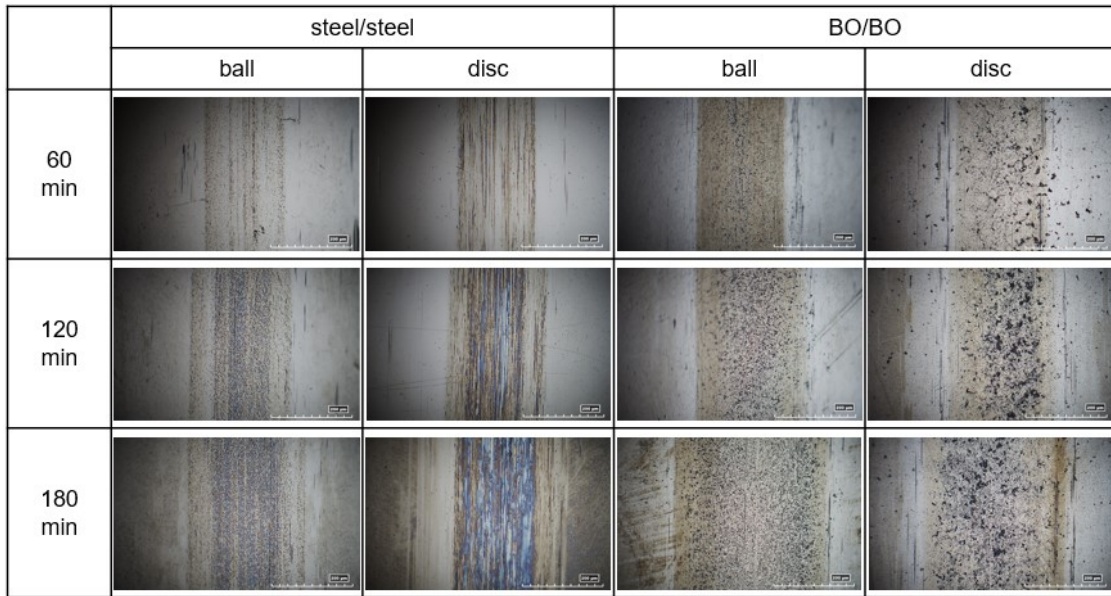


Figure 10-13 Optical micrographs of the ball and the disc wear tracks of steel/steel and BO/BO tribopairs



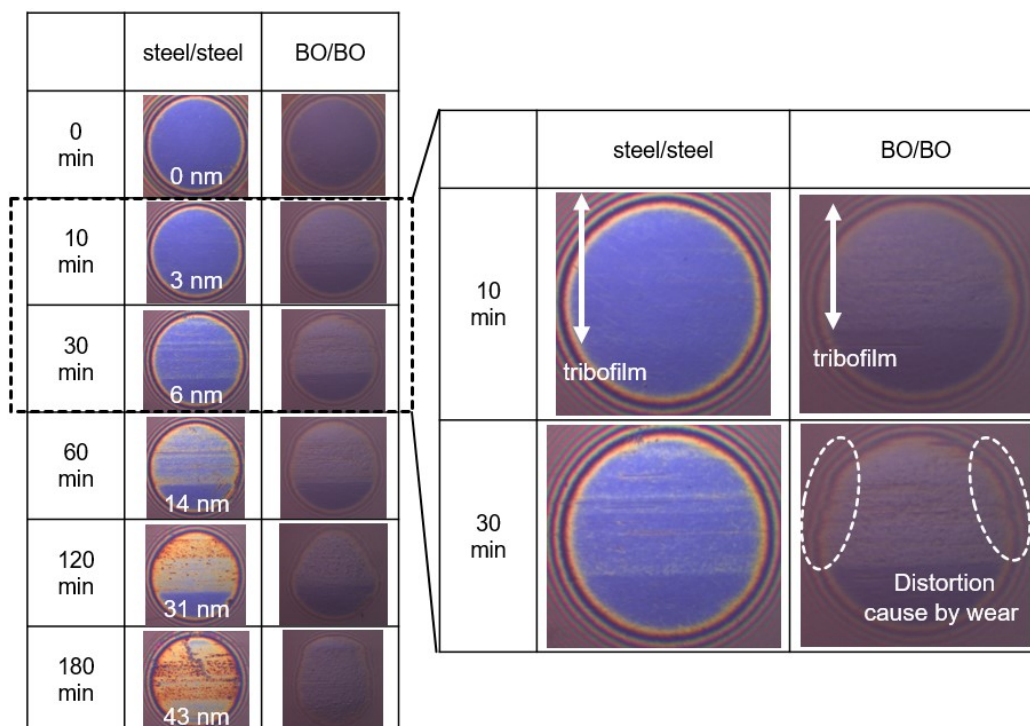


Figure 10-14 SLIM images obtained from the ball wear tracks of steel/steel and BO/BO tribopairs

#### 10.3.4 ZDDP Adsorption on Black Oxide Coating

Since the ability of ZDDP to adsorb on surfaces has a significant influence on tribofilm formation and growth [308], to further understand the interaction of ZDDP with BO surfaces, the adsorption of ZDDP on  $\text{Fe}_3\text{O}_4$ , present in BO, and  $\text{Fe}_2\text{O}_3$ , believed to be the composition of the outermost surface of steel were studied using QCM-D. Figure 10-15 shows ZDDP mass adsorbed at 60°C on sensors made of each of these materials. After the replacement of PAO with a ZDDP solution, ZDDP adsorbed on both surface at the equivalent rate for 90 minutes to reach approximately 70  $\text{ng}/\text{cm}^2$  mass adsorbed. This result shows that ZDDP should adsorb on BO coatings to a similar extent to its adsorption on steel surfaces.

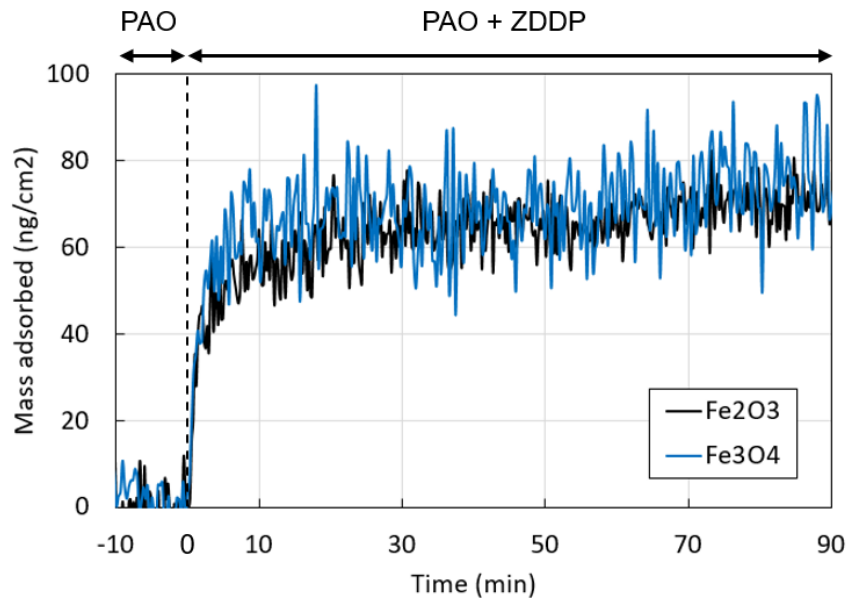


Figure 10-15 ZDDP adsorption on Fe<sub>2</sub>O<sub>3</sub> and Fe<sub>3</sub>O<sub>4</sub> using QCM-D

#### 10.4 Discussion

The results presented in this paper clearly show that the BO coating can effectively reduce, or even prevent, micropitting, but only when it is applied to the rougher, harder of the two rubbing surfaces; in this case the MTM disc specimens. The BO coating is largely ineffective in terms of micropitting prevention when applied solely to the softer, smoother body, in this case the MTM ball specimens. This basic observation is of obvious practical importance and is in line with the results reported by other authors [260]. The present results also offer some important insights into the actual mechanism by which BO mitigates micropitting. Previous studies have suggested that the low hardness of BO coatings provides fast running-in of initially rough surfaces, which means that the contact operates under relatively low asperity stresses throughout its life [254,255,257,259,260,357] which mitigates microcrack growth and thus micropitting. However, it has also been suggested that it is the suppression of the ZDDP antiwear tribofilm build-up on the rough counterface by the BO coating that is essentially responsible for the rapid running-in and hence the reduction in micropitting [260].

It is relatively well accepted that the chemical composition of rubbing surfaces can affect their reactivity with lubricant additives, including ZDDP, and hence their ability to form tribofilms [152,208,308]. Additionally, it has also been suggested that the ZDDP reaction

mechanisms on an  $\text{Fe}_3\text{O}_4$  surface containing  $\text{Fe}^{2+}$  and  $\text{Fe}^{3+}$  ions, as may be expected to be present on the BO coating, and the resulting tribofilm properties, might be different from those on the predominantly  $\text{Fe}_2\text{O}_3$  surface normally be present on steel [143,261]. Therefore, it is quite plausible that BO coating might affect ZDDP tribofilm formation. Given that the rate of ZDDP tribofilm build-up is known to strongly influence micropitting propensity [345], this potential interference of the BO coating with the development of ZDDP tribofilm through chemical means warrants a further consideration as a potential mechanism by which BO mitigates micropitting. In this section the potential mechanisms by which BO coating mitigates micropitting are discussed considering both chemical and mechanical effects.

#### **10.4.1 Chemical Effects of Black Oxide on Micropitting**

Under the relatively harsh conditions employed for the micropitting tests (Table 10-1) it was not possible to reliably observe ZDDP tribofilms on the BO coating itself because the coating was worn off almost immediately at the beginning of the tests. In this case, any tribofilms apparent in the SLIM images of the BO-coated balls in Figure 10-8 are likely exist on the steel substrates which are exposed after the removal of the original BO coating. However, ZDDP tribofilm growth on BO coated balls was successfully observed in the tests conducted at the more benign contact conditions listed in Table 10-2. The results of these tests show that in the initial stages of rubbing ZDDP forms tribofilms on the BO coating in a similar fashion to that on steel. This is further supported by the results of the QCM-D absorption tests performed here which showed that ZDDP adsorbed similarly on  $\text{Fe}_3\text{O}_4$ , as present in BO, and  $\text{Fe}_2\text{O}_3$ , as may be present on uncoated steel surfaces. As the test progresses under these mild conditions the ZDDP tribofilm on the BO coating grows but it does not reach as high a thickness as it does on steel under the same conditions as evident in the images of Figure 10-13. This is probably because the continuous wear of the BO coating, which was observed in these tests, results in a continuous tribofilm removal. The presence of wear despite the evident tribofilms suggests that any ZDDP tribofilms formed on the BO-coating are not sufficient to protect the BO coating from wear even under the mild rubbing condition used in these tests (as listed in Table 10-2). Given that bearings and gears normally operate at more severe conditions than those in Table 10-2, rapid wear of BO coating is very likely to occur in practical situations.

Overall, the fact that ZDDP forms tribofilms on BO coatings that are, at least initially, similar to those formed on steel under the equivalent conditions, suggests that the mechanism by which BO coating mitigates micropitting is not related to its chemical properties or to interference with ZDDP tribofilm build up, but most probably originates predominantly from its mechanical properties such as its low hardness.

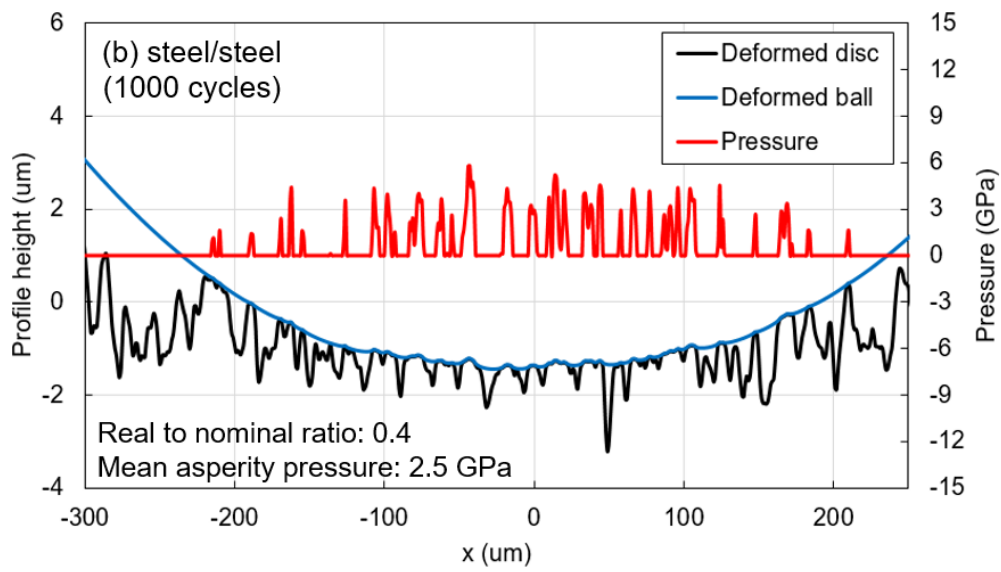
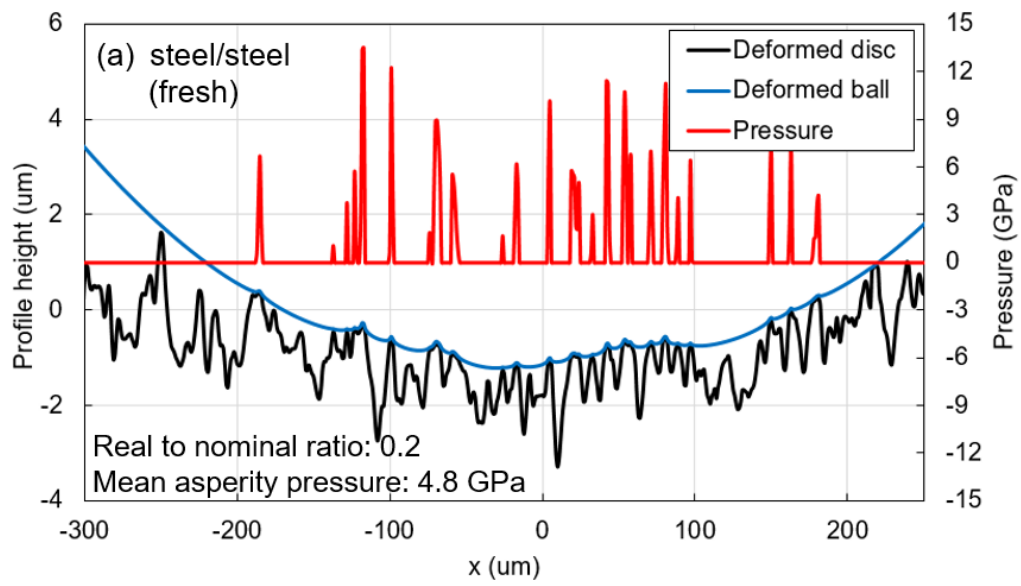
#### **10.4.2 Mechanical Effects of Black Oxide on Micropitting**

The hardness and elastic modulus of the BO coating were found to be only about one-quarter those of steel. In principle, this might help to reduce micropitting in three ways, all of which are related to the impact of BO on reducing asperity stresses and thus microcrack formation and growth: (i) The relatively low hardness of BO might enable faster running-in of the rough surface so that the flatter asperities reduce local asperity stresses; (ii) the lower elastic modulus of the BO might directly reduce asperity pressures by increasing areas of asperity microcontacts (the same does not hold for the macro contact area since the coating thickness is much smaller than the size of the contact so has negligible influence on macro scale) (iii) the BO might act to directly reduce asperity friction and hence local tensile stresses which can be particularly detrimental in terms of crack initiation and propagation.

Figure 10-5 and Figure 10-6 clearly show a strong effect of BO on the running-in of the rough disc counterface where the asperity peaks present on the virgin surface have been significantly reduced, much more than in the case of equivalent steel-steel contact. In order to quantify how beneficial this running-in might be in terms of reduction of asperity pressures, an existing numerical contact mechanics model was used to predict asperity pressure distributions before and after running-in. The reader is referred to references [355,356,358] for full details of this model but in brief, the model is based on the influence coefficient approach and uses real, measured roughnesses as input and can deal with single or multi-layered surface coatings. The model is capable of 3D simulations but in the examples shown here, it is run in 2D by setting the applied load to match the maximum Hertz pressure used in the experiments i.e. 1.2 GPa. In the present simulations, the BO coating is modelled as a layer of thickness 1  $\mu\text{m}$  with elastic modulus of 53 GPa (as measured here, see Figure 10-2) on a steel substrate with elastic modulus of 207 GPa. Poisson's ratio is set to 0.3 for both the coating and the substrate. Although all cases presented here were run with the full model, accounting for the presence of the 1  $\mu\text{m}$  BO coating, the coating is in fact predicted to have negligible influence on the asperity

pressure distribution because of its very small thickness. This suggests that the second of the three potential mechanisms listed above by which the BO can mitigate micropitting, namely that it directly reduces asperity contact pressures due to its elastic modulus being much lower than that of steel, is not of great significance. Given the significant wear of the BO coating with both rough and smooth specimens, any small effects of the coating on asperity elastic pressures would be overwhelmed by the much more significant changes in roughness.

Figure 10-16 shows the predicted pressure distributions for steel/steel and steel/BO tribopairs with both the fresh specimen roughnesses and the roughnesses measured after 1000 cycles. The estimated ratio of real to nominal contact area and the mean asperity pressure are also shown in each of the four cases. In order to clearly illustrate the effects of running-in, a purely elastic solution is shown in all cases; note that the elastic assumption does produce asperity pressures at a few discrete points in the case of fresh surfaces (Figure 10-16 a and c) that are perhaps unrealistically high (being just over the plastic limit) but the plasticity was deliberately not modelled in order not to obscure the differences in contact pressure distributions between the fresh and run-in samples. Indeed, it is evident that for both tribopairs after 1000 cycles asperity pressures at all points are below the plastic limit for the steel used (through hardened AISI 52100) confirming that any plastic deformation has already taken place by this time and that the contact is now purely elastic. In the case of fresh specimens, the real/nominal contact area ratio is  $\sim 0.2$  and the mean asperity pressure is over 4 GPa for both steel/steel (Figure 10-16 a) and steel/BO (Figure 10-16 c) contacts. These values are typical for a contact of rough surfaces made of hard steels. After 1000 cycles, the real to nominal area ratio for steel/BO tribopair is now 0.6, considerably larger than that for steel/steel contact which is 0.4. The corresponding mean asperity pressures are approximately 1.7 GPa for steel/BO contact and 2.5 GPa for steel/steel contact. The larger contact area and the generally lower asperity pressures for steel/BO contact compared to steel/steel are evident in the corresponding pressure distributions shown in Figure 10-16 b and Figure 10-16 d. These quantitative results confirm the first of the three potential mechanisms listed above by which BO coating can reduce micropitting damage: it provides for enhanced running-in which reduces asperity pressures and hence reduces surface fatigue damage accumulation and micropitting. Given that bearing life theories suggest that contact fatigue life is inversely proportional to the applied contact stress to the power of around 9 [359] the effect of mean asperity pressure reduction from 2.5 GPa to 1.7 GPa on micropitting damage is likely to be considerable.



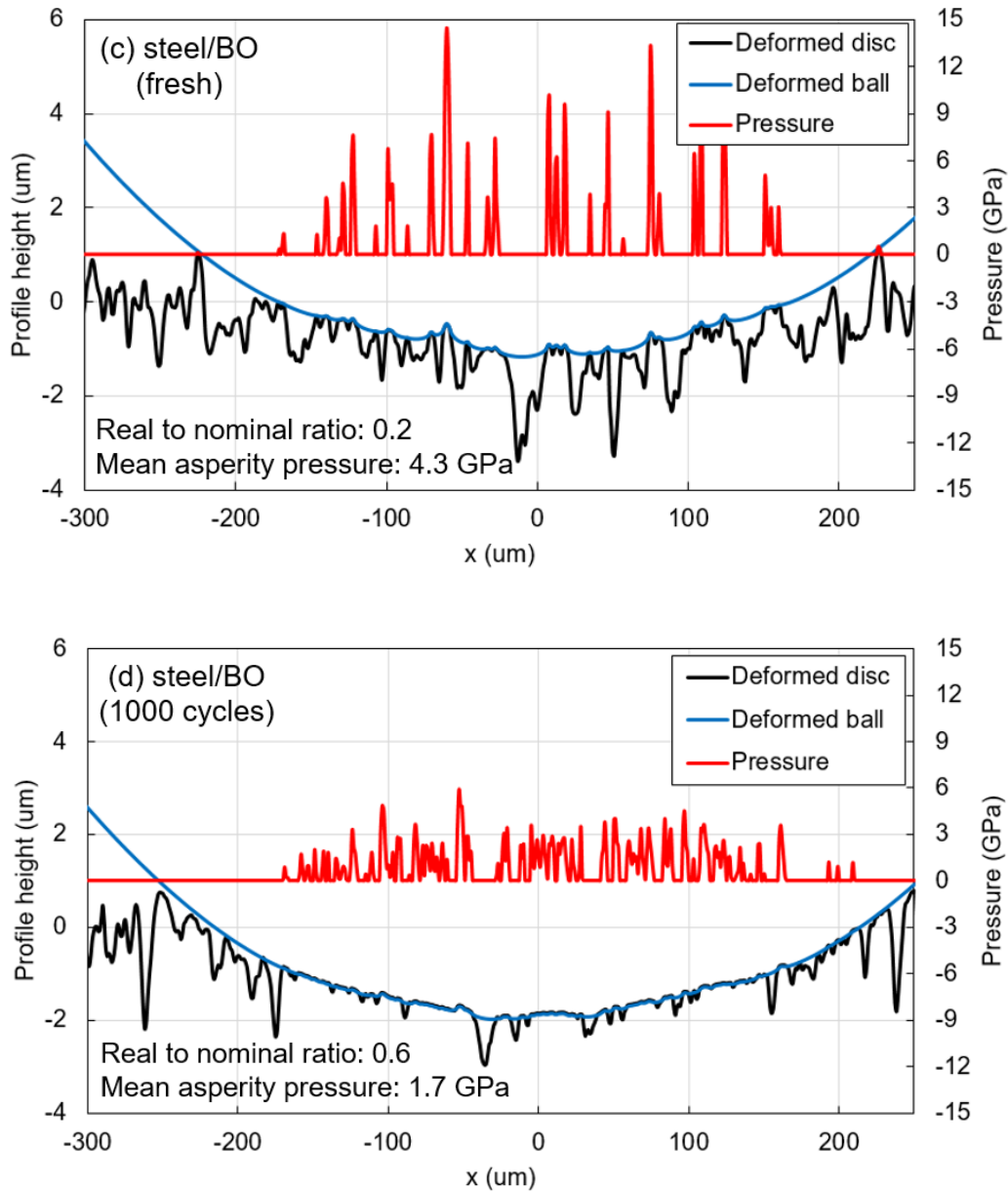


Figure 10-16 Predicted surface pressure distribution and deformation for (a) steel/steel contact with original (fresh) roughness, (b) steel/steel tribopair with roughness measured after 1000 cycles under conditions in Table 1 (c) steel/BO tribopair with fresh roughness and (d) steel/BO tribopair with roughness after 1000 cycles. All roughnesses measured using a stylus profilometer. (Note: purely elastic solution are shown in all cases to clearly illustrate the effects of running-in; this may result in some asperity pressures with fresh roughnesses appearing unrealistically high)

To further investigate the manner in which the BO coating enhances the running-in process, cross sections of the steel disc from the steel/steel and the BO-coated disc from the steel/BO micropitting tests were inspected at different number of cycles using SEM. The resulting images are shown in Figure 10-17. The cross section of the fresh discs show that BO was evenly coated on a rough steel substrate. The images of the discs after 1000 cycles, show that the BO coating has been removed from the asperity peaks and that tops of these peaks have been flattened in many places, producing flat plateaus. At the flattened regions of the BO-coated disc, no BO coating remains and steel substrate is exposed. In contrast, the BO coating is still intact in the valleys, with its thickness in these regions being, at 1  $\mu\text{m}$ , more or less the same as in fresh specimen. This combination of the coating being worn off the peaks and surviving in the valleys results in the worn BO-coated surface having much lower surface roughness than that of the equivalent worn uncoated disc. In addition to the effect this has on reducing asperity stresses as discussed above, it is possible that the additional beneficial effect of flatter peaks and shallower valleys is one of improved micro-EHD lubrication in the asperity microcontacts [360,361]. It is of course very difficult to provide direct observations of micro-EHL conditions and this is outside the scope of the present study, but if this effect were indeed present, it would serve to further alleviate asperity normal stresses and reduce asperity friction, both of which would mitigate micropitting.

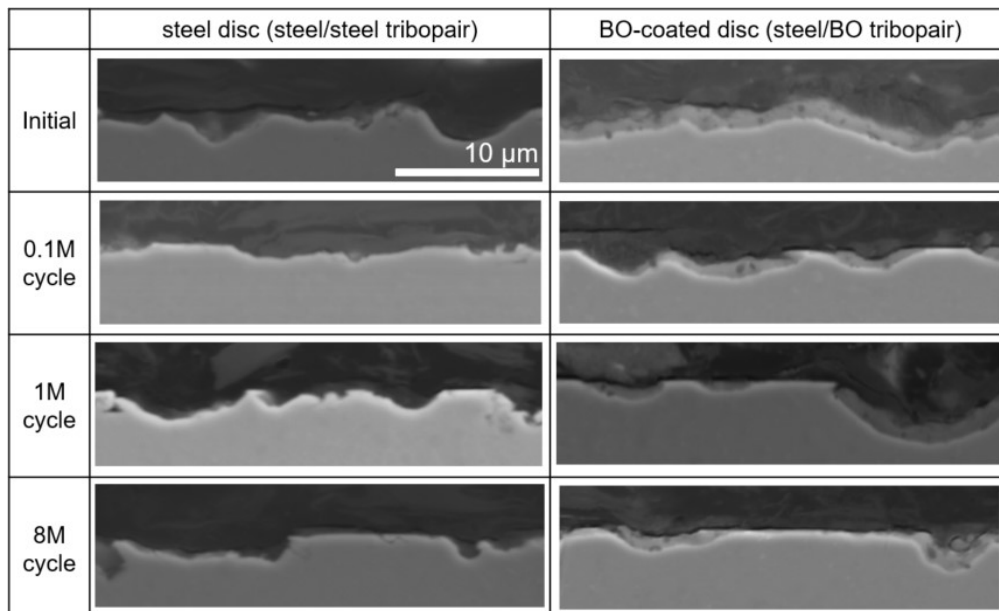


Figure 10-17 SEM images cross sections of steel disc from steel/steel test and BO-coated disc from steel/BO test at different number of. The scale bar shown in the top right image is applicable to all images.



The third potential mechanism mentioned above is that BO coating provides a lower friction coefficient than uncoated steel, and thereby reduces asperity tensile stresses and hence micropitting. Figure 10-7 shows that with rough counterface discs in micropitting tests, friction is much lower in tests where the disc has a BO coating than when it is uncoated. When only the smooth ball is coated, friction is practically the same as that for steel-steel contacts. However, in tests with smooth counterface discs, friction is initially higher with BO-coated discs than with uncoated ones as shown in Figure 10-12. This difference is believed to occur due to tests with rough and smooth counterface discs operating in different lubrication regimes. In rough counterface tests, because of the high roughness of the discs, the contact starts in mixed/boundary lubrication ( $\lambda \sim 0.3$ ) for both uncoated and BO-coated counterface discs. With steel discs, as running-in progresses, there is a slow transition further away from the boundary regime and more into mixed lubrication ( $\lambda \sim 0.5$ ), with a corresponding friction reduction. However, for BO-coated rough discs, very rapid smoothening of rough discs occurs and this results in an almost immediate transition to conditions further towards EHD lubrication ( $\lambda \sim 1.0$ ) at these test conditions, in particular because of the relatively high entrainment speed of 3 m/s. This occurs before the first MTM friction measurement is recorded at 550 ball loading cycles (10 seconds after the start of the test). Thus, the low friction shown in Figure 10-7 for the tests with BO-coated discs does not represent an inherently low boundary friction coefficient of the BO coating itself, but rather it is a result of partial fluid film lubrication existing at this time. This conclusion is also supported by the fact that when only the ball (much smoother than the discs and hence not affected by running in) is coated with BO, the friction is the same as that in steel/steel contacts. Further evidence for this is provided by the SEM images in Figure 10-17. These show that negligible BO coating is left on tops of asperity peaks after 1000 cycles so that if the contact were still operating in boundary/mixed regime, friction after this time would have been expected to be the same as for steel/steel contacts which was not the case. Friction recorded in the smooth surface tests, where BO was not completely removed from the asperity peaks and less running-in occurred, indicate that BO coating actually has a higher initial friction against itself than for steel on steel (Figure 10-12). As the test progresses, a rough ZDDP tribofilm develops on both BO and steel which pushes the contact further towards the boundary regime and this causes the friction coefficient in both cases to increase to about 0.11 which is typical for the boundary friction of ZDDP tribofilm. This same friction is reached for both steel/steel and BO/BO tribopairs. It thus seems unlikely

that BO reduces micropitting by directly reducing the asperity friction coefficient. Of course, the presence of BO can still reduce the magnitude of asperity shear stresses indirectly, via the enhancement of the running-in process and the subsequent reduction in the magnitude of the asperity pressures (as shown in Figure 10-16) which also lowers asperity shear stresses. In addition, any potential improvements in the micro-EHL lubrication conditions afforded by the running-in of the asperity peaks when coated by BO, as briefly discussed above, would also help to reduce shear stresses in the asperity contacts.

While mitigation of micropitting using a BO-coated counterface has been observed in multiple studies using lubricants containing either ZDDP or ashless antiwear additives, a study by Mahmoudi et al. [362] stands out as it showed that in tests with pure base oil and with BO coating on both rubbing steel components, *i.e.* a BO/BO tribopair, no reduction of micropitting was observed compared to a steel/steel tribopair under the same conditions. It was shown in Chapter 9 that the very limited wear protection provided by an additive-free base oil results in extremely rapid reduction of roughness and substantial amounts of adhesive wear of the components, both of which act to prevent formation and propagation of surface cracks and hence suppress micropitting regardless of other conditions imposed. Mahmoudi et al. [362], did not present measurements on the evolution of surface roughness in their tests, but it is probable that due to their use of pure base oil, the surface roughness of the rough counterface in their steel/steel tribopair was rapidly decreased to mitigate micropitting to a similar extent to that with BO/BO tribopair. This excessive wear would have masked any relative improvement in micropitting otherwise afforded by the BO coating, leading to their observation of no difference in micropitting between steel/steel and BO/BO tribopairs in the tests with pure base oil.

#### **10.4.3 Mechanisms of Influence of BO Coating on Micropitting**

Based on the results and discussion presented in this paper, the primary mechanism by which BO coating is able to mitigate micropitting when applied to a rough counterface is summarized schematically in Figure 10-18. The relevant steps in this mechanism are as follows:

##### **(1) Before test**

Black oxide is applied as a uniform thickness conversion coating on the rough counterface (AISI 52100 steel disc in the present tests). This very slightly reduces the surface

roughness compared to fresh uncoated surface, but this roughness reduction is insufficient to significantly affect micropitting.

## (2) Very early stages of rubbing

Due to the low hardness of the BO conversion coating, the BO coating as well as some steel substrate immediately underneath are rapidly removed from the very tops of the asperities that participate in the initial contact. This occurs in the first few hundreds of cycles and before any significant ZDDP tribofilm forms on the surface. This results in a very considerable reduction in surface roughness of the (initially) rough counterface. The large reduction in roughness means that the contact then operates further into the mixed lubrication regime, away from the boundary regime and closer to full film lubrication, with a consequent overall friction coefficient reduction. The polishing of asperity tips means that contact pressures, and hence shear stresses, in asperity micro-contacts are reduced. The BO coating is not removed from the valley regions and this further contributes to roughness reduction. It may also improve the micro-EHL lubrication at asperity conjunctions and hence further reduce asperity level stresses.

Some running-in also occurs in equivalent steel/steel contacts but owing to much higher hardness of steel, the roughness reduction in this case is vastly smaller than that for a BO-coated surface so that asperity stresses continue to be relatively high.

## (3) Remainder of test

A ZDDP tribofilm is seen to be formed on the rubbing surfaces in tests with both steel/BO and steel/steel tribopair although it is somewhat thinner in the case of steel/BO. This ZDDP tribofilm, which is formed mainly on the balls, is sufficient to effectively protect the rubbing surfaces from further excessive wear for both steel/steel and steel/BO tribopairs. Note that at this stage, BO has been removed from the contacting asperities, so the tribofilm forms mainly on the underlying steel. This tribofilm suppresses any further running-in of surface roughness. With steel/steel tribopairs, the contact operates under higher friction and the asperities continue to experience high pressures and shear stresses and a large number of stress cycles, all of which promotes initiation and propagation of surface cracks through to the rest of the test, and thus cause micropitting. With steel/BO tribopairs, effective polishing of the asperity tops and the persistence of BO coating in the valley regions means that the contact operates under higher effective lambda ratio and consequently lower friction, even if still in mixed lubrication. The lower slopes of asperity peaks mean that magnitude of asperity pressures is also reduced. All of

this leads to a substantial reduction in the normal and shear (and hence tensile) stresses acting on asperities and hence successfully mitigates micropitting throughout the test.

Our observations and discussion show that a BO coating when applied to a rough steel counterface can effectively reduce micropitting and give low wear of steel substrates by facilitating the running-in and hence reduction of roughness in the very early stages of rubbing even in the presence of ZDDP tribofilm formation. As well as with ZDDP-containing oils, this reduction in micropitting is also likely to occur with oils containing the ashless phosphorus-based antiwear additives that are commonly used in gear oils. This has practical implications in tailoring surface materials and optimising lubricant formulations to improve surface fatigue resistance and antiwear behaviour of rolling-sliding contacts in a given mechanical system.

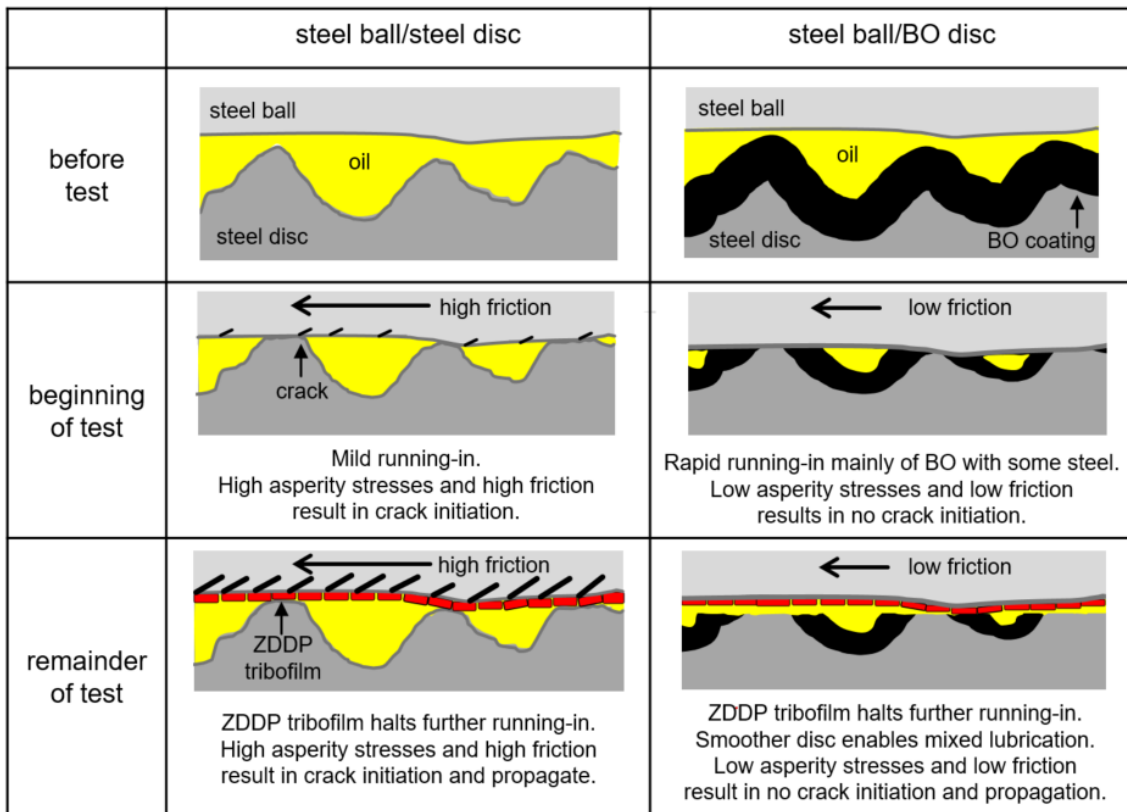


Figure 10-18 Schematic illustration of the primary mechanism by which BO coating mitigates micropitting

## 10.5 Conclusions

This chapter describes the use of the MTM-SLIM ball-on-disk tribometer to investigate the effect of black oxide (BO) conversion coating on the occurrence of micropitting damage in lubricated contacts of bearing steel specimens. This is complemented by various material analysis techniques and a numerical model for rough surface contacts. The results show how the BO coating can effectively mitigate against micropitting and suggest the relevant mechanisms at play. The key conclusions are as follows:

- Application of a BO coating to the rougher, harder counterface (steel discs in the present MTM tests) prevents the occurrence of micropitting damage on the mating surface (MTM ball in the present study) regardless of whether this mating surface is also coated or not. This reduction in micropitting afforded by BO exists even in the presence of ZDDP containing oils which usually promote micropitting. In contrast, application of BO to the smoother, softer counterface only has no effect on micropitting and in this case the damage is the same as that observed in uncoated steel-steel contacts.
- The mechanism by which BO coating reduces micropitting is essentially through optimisation of the running-in process and consists of the following steps:
  - (i) BO coating is rapidly removed from the tops of the surface asperities shortly after the onset of rubbing. BO coating survives in the roughness valleys. This results in an almost immediate and very significant reduction in overall disc surface roughness as well as reduction in asperity slopes.
  - (ii) These changes in roughness lead to a rapid reduction in asperity pressures, and hence shear stresses, and an increase in the effective lambda ratio to give a reduction in the overall contact friction. This reduction in asperity normal and tangential stresses leads to reduction in initiation and propagation of surface fatigue cracks and thus less micropitting than is the case in an equivalent steel-steel contact where the running-in process is not as effective
  - (iii) With further rubbing, an effective antiwear boundary film forms, mainly on the exposed steel substrate, and prevents further wear of the surface.
- The key to this behaviour is the low hardness of the BO coating, which was measured here to be only one quarter that of the steel substrate. This means that BO coating can be easily worn from the asperity peaks to reduce surface roughness and asperity slopes within the first few hundred rubbing cycles.

- In mild rolling-sliding test conditions with relatively smooth surfaces in which BO is not immediately worn off, ZDDP forms a similar antiwear tribofilm on BO coating to that formed on steel. This shows that the enhanced running-in provided by the BO coating, and the subsequent reduction in micropitting, does not stem from BO suppressing antiwear film growth. However, this has little practical relevance since on rough surfaces, such as present on gears and bearing raceways, BO coating is not likely to survive on the rubbing surfaces during operation.
- In the same mild rolling-sliding test conditions, BO-BO contact is shown to initially have higher friction than the equivalent steel-steel contact. This shows that the ability of the BO coating to reduce micropitting does not stem from it having a lower boundary friction coefficient than steel.

## 11 Effect of Friction on Micropitting

*This aim of the work described in this chapter is to clarify the impact of friction on micropitting and explore the relevant mechanisms involved. The contribution of friction to micropitting was isolated from the effect of counterface roughness by adding a ZDDP and MoDTC blend after a running-in period lubricated by ZDDP solution alone, resulting in the same counterface roughness throughout micropitting tests in each lubricant. To monitor the evolution of tribofilm during the micropitting tests, MTM-SLIM was used to provide understanding of the influence of tribofilm on micropitting and wear. The research described in this chapter has been published in Wear with open access [363].*

*It should be noted that the numerical simulation of the distribution of contact pressure and stresses described in section 11.3.2 was conducted by a fellow PhD student, Mr. Benjamin Wainright.*

### 11.1 Introduction

Given its effects on initiation and growth of surface cracks as described in 3.4.3, reduction of friction is clearly one potential measure that may help to reduce micropitting. However, there appear to be very few studies that directly investigate the effect of friction on micropitting. Morales-Espejel and Brizmer [364] used a numerical model to show that increasing the boundary friction coefficient from 0.12 to 0.15 almost doubled the extent of micropitted area for a given set of contact conditions. Perhaps the most notable study on the effects of friction on micropitting is that of Lainé et al. [252] who used a triple-disc machine (MPR) and lubricant blends containing ZDDP with and without molybdenum dialkyldithiocarbamate (MoDTC) friction modifier to produce different friction coefficients in their micropitting tests. They showed that a reduction of friction from 0.08 to 0.04, achieved via addition of MoDTC (0.12 wt.% of Mo) to their test oil, significantly reduced micropitting damage compared to the original oil which contained zinc dialkyldithiophosphate (ZDDP, 0.10 wt% of P) only. The authors suggested that friction was decreased by the formation of an MoS<sub>2</sub> tribofilm from MoDTC on the rubbing surface of the counterface MPR disc. More recently, Soltanahmadi et al [272] showed that addition of ashless amine friction modifier could also reduce micropitting through reduction of friction in a similar general manner to that of MoDTC. They suggested that

this reduction in micropitting originated both from a reduction in boundary friction and from partial suppression of the growth of a ZDDP tribofilm.

These previous studies varied the friction coefficient by using oils with different amounts of friction modifier additive added to the reference test oil containing ZDDP. However, it is known the addition of friction modifiers such as MoDTC and ashless amine compounds in this manner slows the growth of antiwear tribofilms because of competitive adsorption with antiwear additives [52,272]. As indicated in Chapter 9, such slower growth of antiwear tribofilm with a friction modifier and ZDDP blend is most likely to result in a greater reduction of counterface roughness during the running-in phase than is the case with a ZDDP solution alone. This reduction in roughness will in itself reduce micropitting, thus making it impossible to isolate and quantify the effects of friction on micropitting.

To address this problem, the research described in this Chapter aims to clarify the effect of friction on micropitting by adopting a test methodology which makes it possible to disentangle the effect of friction from other influential factors and in particular from the evolution of counterface roughness. The approach involves conducting micropitting tests in which an oil containing ZDDP antiwear additive only is used during the early stages of all tests until the running-in of the counterface roughness is complete, and any further changes in counterface roughness are negligible. Only then is the chosen concentration of MoDTC introduced into the test oil. Thus, by varying the concentration of MoDTC in the test oil, it is possible to conduct micropitting tests with different friction coefficients, but negligible differences in counterface roughness evolution between the tests.

## **11.2 Test Methodology**

### **11.2.1 Experimental Equipment**

All micropitting tests were conducted using the same method as described in Chapter 9. MTM-SLIM was employed to generate micropitting on the ball specimen and to monitor ZDDP film formation within the same test.

### **11.2.2 Test Conditions**

All micropitting tests were conducted using the conditions described in Table 9-2 in Chapter 9.



### 11.2.3 Test Lubricants

For each test, 50 ml of lubricant was used. Test oils were formulated as shown in Table 11-1. Varying concentrations of MoDTC (Adeka Sakura Lube 165 at 0, 25, 50, 100, 200 and 500 ppm Mo) and ZDDP (secondary-primary) at a fixed concentration of 800 ppm P were mixed with PAO 10 (62.8 mm<sup>2</sup>/s and 9.9 mm<sup>2</sup>/s kinematic viscosity at 40 °C and 100 °C, respectively). In all experiments the initial lambda ratio was *ca.* 0.3 (corresponds to *ca.* 150 nm minimum oil film thickness). Following the running-in, lambda ratio was 0.5 in all tests.

Table 11-1 Test oil formulations

Lubricant name	Base oil	ZDDP (secondary-primary mixed), P concentration, ppm	MoDTC, Mo concentration, ppm
ZDDP	PAO10	800	0
ZDDP+Mo(25)	PAO10	800	25
ZDDP+Mo(50)	PAO10	800	50
ZDDP+Mo(100)	PAO10	800	100
ZDDP+Mo(200)	PAO10	800	200
ZDDP+Mo(500)	PAO10	800	500

### 11.2.4 Test Procedures

The test procedures were the same as described in Chapter 9. To isolate friction from the effect of counterface roughness, tests were run using two methods as shown schematically in Figure 11-1. In Method 1, the entire test was conducted with a single test oil (ZDDP and ZDDP+Mo at Mo concentration of 25, 50 or 500 ppm). In Method 2, the test was first run for 0.1 million cycles, corresponding to the running-in phase, with the ZDDP only oil. The oil was then replaced with one containing the chosen concentration of MoDTC, *i.e.* a ZDDP+Mo solution with 50, 100, 200 or 500 ppm Mo as listed in Table 11-1. This is because the study described in Chapter 9 showed the reduction of disc roughness due to running-in ceased after 0.1 million cycles, after which the disc roughness remained more or less the same to the end of the 8 million cycle test. Before oil replacement at 0.1 million

cycles, the specimens were removed for inspection (see below) and the MTM test chamber was cleaned with toluene.

During tests, the rubbing was periodically paused to measure the ZDDP tribofilm thickness using SLIM, while at 0.1, 1 and 4 million cycles the specimens were removed from the rig to observe and measure wear and micropitting on the ball and the roughness of the disc wear tracks as described in Chapter 9. At the end of the micropitting tests, in addition to inspecting the surfaces of the specimens as described above, a polished cross-section of the ball rubbing track in the rolling-direction was prepared and inspected with an optical microscope. This was to investigate the morphology of the generated surface cracks and micropits, and establish any correlation of these with friction. All tests shown in this paper were repeated one time.

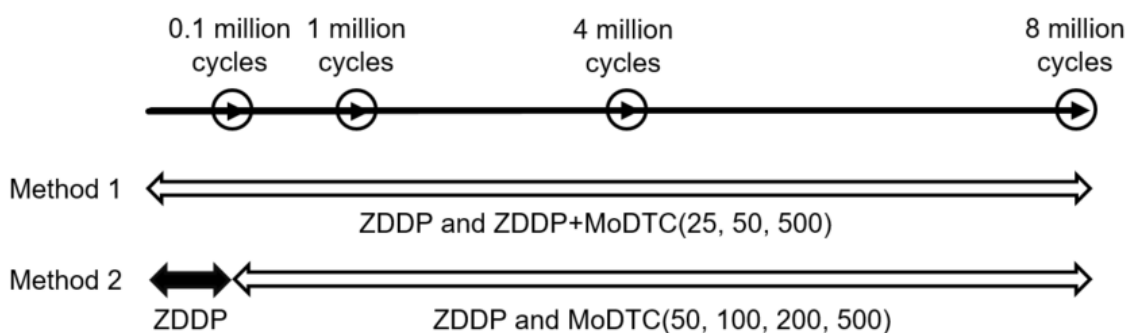


Figure 11-1 Micropitting test procedures

### 11.2.5 Calculation of Contact Pressure and Stress

To calculate the distribution of contact pressure and stress, the model described in Chapter 10 was employed.

### 11.2.6 Tribofilm Elastic Modulus

To calculate the contact pressure distribution in the presence of tribofilm, the elastic modulus of ZDDP tribofilm formed on MTM balls was measured using the nanoindentation method described in Section 4.4.5. The elastic modulus was estimated using 0.26 for the Poisson's ratio of ZDDP tribofilm [365].

## 11.3 Results

### 11.3.1 Effect of MoDTC Addition at the Beginning of the Test (Method 1)

This section presents results of friction, surface damage and tribofilm formation when MoDTC was present from the beginning of the tests. The lubricants used are a ZDDP-only solution and three solutions consisting of ZDDP and MoDTC at concentrations of 25, 50 and 500 ppm. The same lubricants were used from the beginning to the end of the tests with no replacement. Note that the same test result in Chapter 9 is used for the result shown from a ZDDP alone oil in this Chapter.

#### 11.3.1.1 Friction Behaviour

Figure 11-2 shows the evolution of friction coefficient in tests conducted with oils having different Mo concentrations. The friction coefficient of the Mo-free ZDDP oil is initially *ca.* 0.1 and gradually decreases to reach 0.08 at the end of the test (8 million contact cycles). The addition of 25 ppm of Mo does not reduce friction, resulting in the same friction coefficient as the ZDDP-only oil. 50 ppm and 500 ppm of MoDTC reduce friction coefficient from 0.1 to about 0.04 - 0.05 almost immediately after starting the tests. While the friction coefficient of ZDDP+Mo(500) remains at 0.04 throughout the test, the friction coefficient of ZDDP+Mo(50) gradually increases again to reach 0.07 at 4 million cycles, and then remains stable at this value to the end of the test. It should be noted that the reduction in friction with increasing MoDTC is not due to any extra smoothing of the specimen surface roughness – this was specifically controlled by only adding the MoDTC once the running-in was over and the anti-wear tribofilm had formed with the ZDDP only oil. Instead friction reduction is due to the well-established mechanism of MoDTC action originating from the formation of nanocrystals of low shear strength MoS<sub>2</sub> on rubbing asperities [75,342]. Since MoS<sub>2</sub> forms on contacting asperities that support load, it has a strong effect on reducing friction in the mixed lubrication regime conditions present in this study. MoS<sub>2</sub> formed in this way is not durable, but is continually being formed and rubbed off [238,247]. It is likely that 50 ppm of Mo is not sufficient to reduce friction throughout the test because of the oil aging. It should also be noted that the momentary blips in the recorded friction traces apparent in the figure are artefacts of the measurement method on the MTM-SLIM rig and occur just after motion was paused to capture a SLIM image.

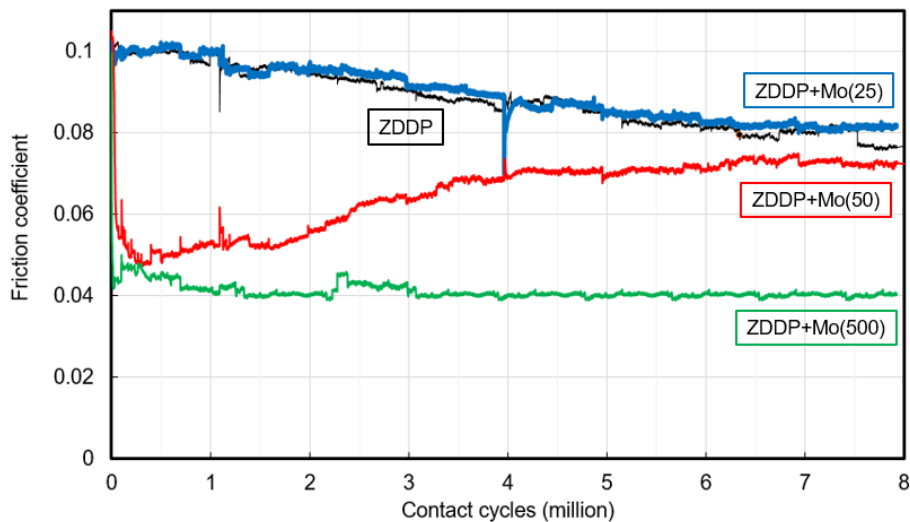


Figure 11-2 Friction behaviour in tests conducted with oils having different concentrations of MoDTC from the outset

### 11.3.1.2 Evolution of Surface Damage on Balls

Figure 11-3 shows representative optical micrographs of the rubbed track on the balls after 0.1, 1, 4 and 8 million cycles with different MoDTC concentrations, as well as measured percentage of micropitted area on the ball wear track after 8 million cycles. The severity of micropitting on the wear tracks varies with MoDTC concentration (Figure 11-3). ZDDP and ZDDP+Mo(25) show similar densities of surface cracks and after 0.1 million cycles these cracks are tens of microns in length. The appearance of these cracks is the first visible sign of micropitting taking place. As the test progresses, the number of cracks increases considerably. Small pits (tens of microns in size) associated with these cracks become apparent at 4 million cycles. By the end of the test, these micropits cover 25-27% of areas of the rubbing track. By contrast, with ZDDP+Mo(50 and 500), far fewer cracks and micropits are observed. With ZDDP+Mo(50) a few isolated cracks are present after 1 million cycles. The density of these cracks increases after 4 and 8 million cycles to cover 8.9% of area of the rubbing track after 8 million cycles, but is clearly significantly less than in the case of ZDDP only and ZDDP+Mo(25) oils. In the case of ZDDP+Mo at 500 ppm, the highest concentration used here, only a very few very isolated micropits are apparent and the surface damage is minimal, covering 1.3% of areas of the rubbing track even after 8 million cycles.

The bluish colour evident in the wear tracks in Figure 11-3 is caused by ZDDP tribofilms, and hence allows a qualitative comparison of the effect of Mo concentration on ZDDP tribofilm growth, which is an important factor to consider in isolating the influence of

friction on micropitting. In the tests with ZDDP and ZDDP+Mo(25 and 50) a tribofilm is formed over most of the wear track width after 0.1 million cycles. In contrast, in the tests with ZDDP+Mo(500), tribofilm is only apparent in the regions towards both edges of the wear track, but not in the central region where the contact pressure is highest (Figure 11-3). Similar results have not been previously reported and may be a consequence of the unusual MTM test conditions used here to produce micropitting. However, considering that friction was low from the start of the test it is likely that a large amount of MoS<sub>2</sub> tribofilm formed in the central, high pressure region of the wear track relatively quickly after the start of the test and this may compete with ZDDP adsorption to reduce ZDDP tribofilm formation during the test [252]. Indeed, the low friction resulting from MoS<sub>2</sub> formation may lower the shear stress at asperities to the extent that the mechanochemically-driven reaction of ZDDP is no longer possible or is very slow [217,218]. Any MoS<sub>2</sub> tribofilm formed would be much thinner than ZDDP tribofilm [221] so that it would not necessarily be apparent in the optical micrographs.

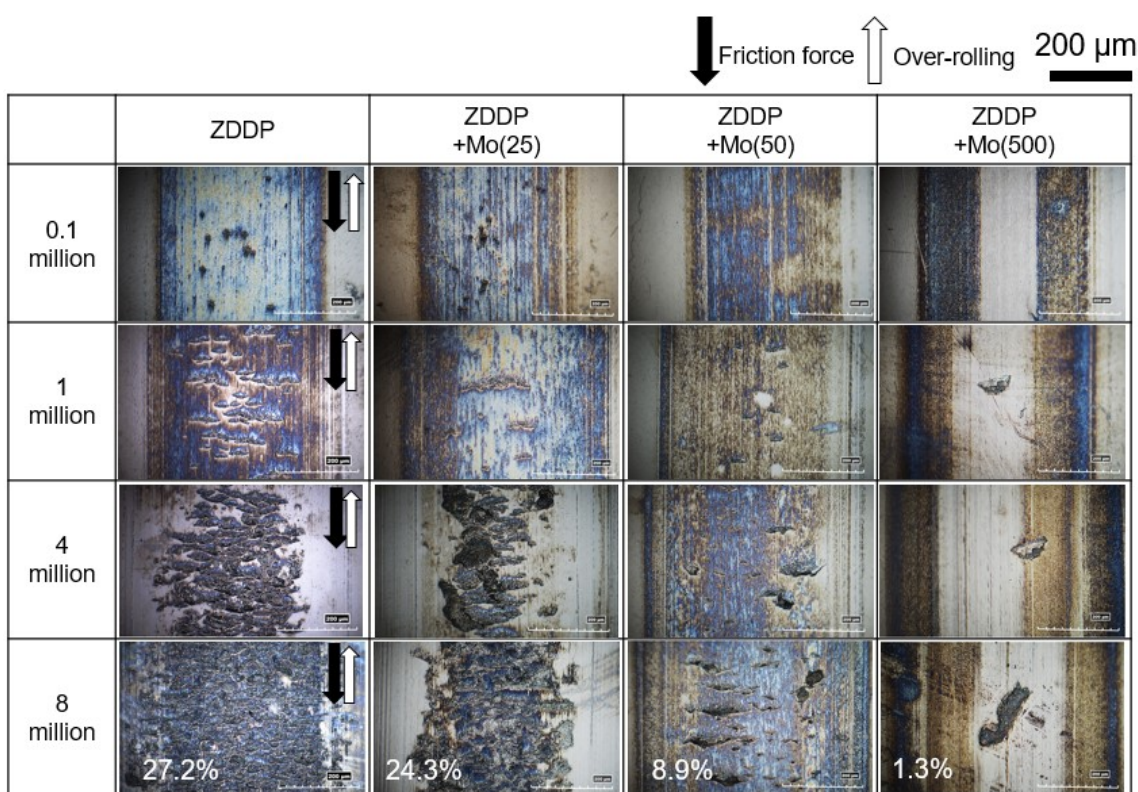


Figure 11-3 Typical examples of optical micrographs of wear tracks on balls from tests conducted with different MoDTC concentrations from the outset as well as measured percentage of micropitted area on ball wear track after 8 million cycles (Note: the scale bar included in the top right corner of the figure applies to all images shown)

### 11.3.1.3 Evolution of Surface Roughness of Counterface Discs

Figure 11-4 shows the evolution of the disc roughness during tests. In all cases the disc roughness reduces in the initial stages of the test and then remains relatively stable, a behaviour indicative of running-in. However, considerable differences are evident in the level of roughness reduction with different MoDTC concentrations. ZDDP and ZDDP+Mo(25) oils reduces disc roughness less than the higher MoDTC concentrations ZDDP+Mo(50 and 500). In the former cases, the roughness is reduced from the initial Ra value of  $\sim 0.45 \mu\text{m}$  to  $0.30 \mu\text{m}$  after 0.1 million cycles and stays constant at this level for the rest of the test. By contrast, oils with 50 and 500 ppm of MoDTC reduce disc roughness from the initial  $\sim 0.45 \mu\text{m}$  Ra to *ca.*  $0.25 \mu\text{m}$  Ra after the first 0.1 million cycles and to  $\sim 0.22 \mu\text{m}$  Ra after 1 million cycles, after which roughness remains at this value for the rest of the tests.

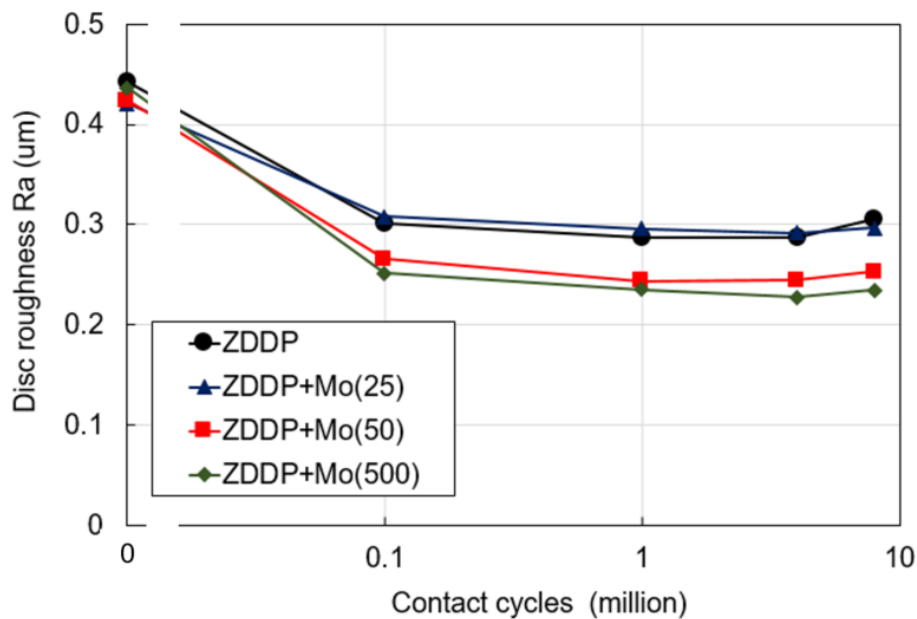


Figure 11-4 Disc roughness evolution with oils containing different MoDTC concentrations when MoDTC is present from the start of the test

### 11.3.1.4 Evolution of Tribofilm

Figure 11-5 shows tribofilm thickness in the middle region of the ball rubbed tracks obtained from SLIM images. ZDDP and ZDDP+Mo(25) form tribofilms rapidly during the first 0.1 million cycles, to reach 175 nm after 0.2 million cycles. After this, tribofilms

thickness decreases slowly to stabilize at *ca.* 30 nm and 60 nm, respectively. ZDDP+Mo(50) form tribofilm at a much slower rate in the first 0.1 million cycles, to reach *ca.* 90 nm after 0.3 million cycles before decreasing to 60 nm by 1 million cycles. By contrast, with ZDDP+Mo(500) oil negligible film thickness is observed using SLIM in the central area of the rubbed wear track. This result suggests that the addition of over 50 ppm of MoDTC hinders ZDDP tribofilm formation. Interestingly, after about 1 million cycles, the presence of low concentrations of MoDTC in the ZDDP solution results in thicker tribofilm thicknesses than ZDDP alone. Possibly, MoDTC functions as an antioxidant, resulting in the increase of active ZDDP to form tribofilm [79].

The results in this section show that although addition of more than 50 ppm of MoDTC to the ZDDP oil from the beginning of the test reduces friction coefficient and visibly reduces micropitting damage, the counterface roughness is also reduced because MoDTC slows ZDDP tribofilm growth during running-in. This makes it impossible to establish the effect of friction on micropitting from these results alone since the observed reduction of counterface roughness itself is known to strongly reduce micropitting.

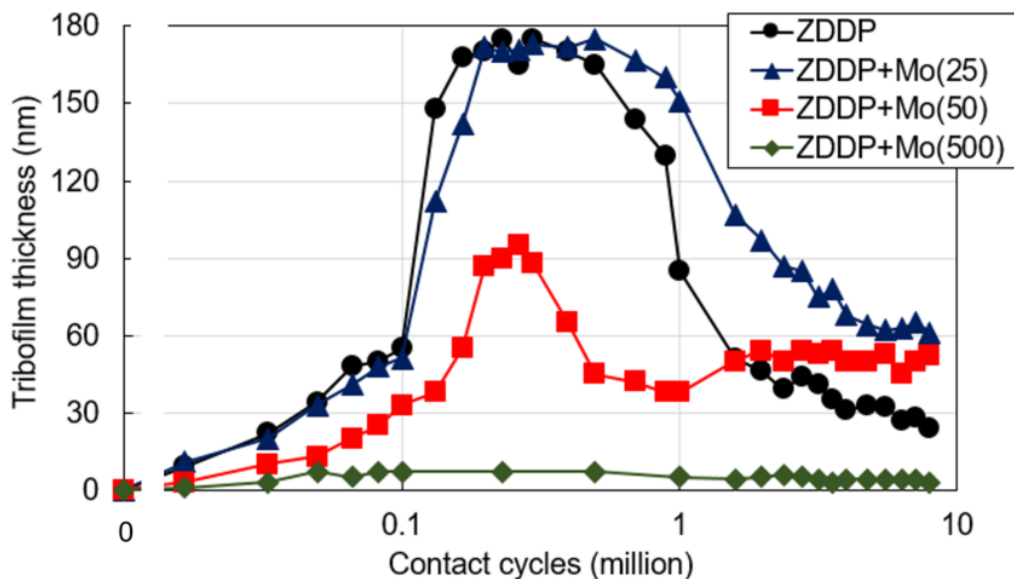


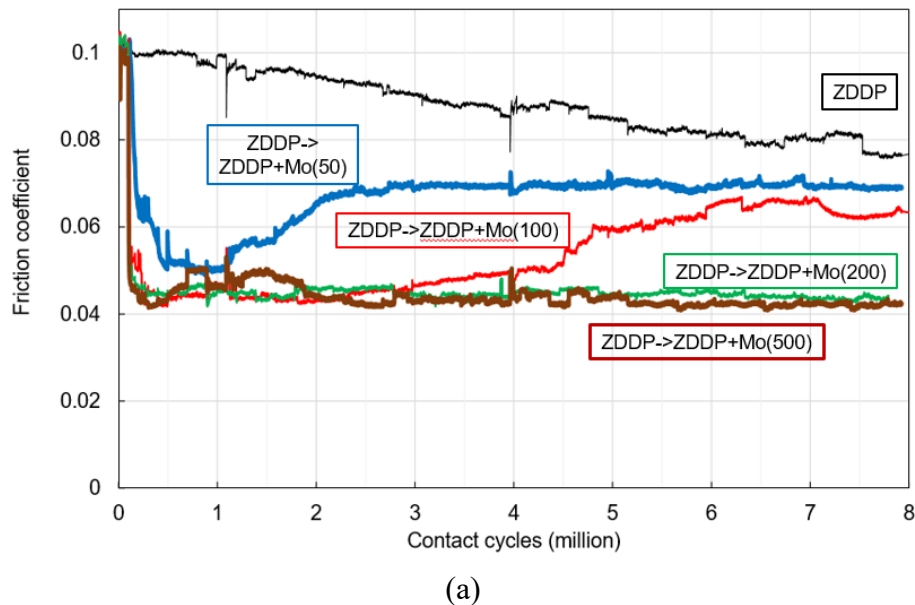
Figure 11-5 Tribofilm evolution in tests with oils containing different MoDTC concentrations present from the start of the test

### 11.3.2 Effect of MoDTC Addition after Running-in (Method 2)

This section presents the results of tests designed to investigate the influence of concentration of MoDTC when the latter is introduced after running-in for an initial 0.1 million cycles with an oil containing ZDDP only. Four different concentrations of Mo were tested, *i.e.* 50, 100, 200 and 500 ppm, blended with a ZDDP containing oil. ZDDP+Mo(25) was not tested here because no friction reduction was seen with this blend using method 1 as described above.

#### 11.3.2.1 Friction Behaviour

Figure 11-6a shows the evolution of friction coefficient in tests with different MoDTC concentrations over the 8 million cycles. Figure 11-6b shows the same data, but zoomed in to 0-0.5 million cycles range. It is evident that for all four Mo concentrations, friction coefficient decreases from the initial value of 0.1 obtained with ZDDP oil to 0.04 - 0.05 after the addition of MoDTC at 0.1 million cycles. The friction coefficient at Mo concentrations of 50 and 100 ppm then increases slowly after 1 and 3 million cycles and stabilised at 0.06 and 0.07, respectively. This slow increase in friction coefficient is probably caused by oil aging. By contrast, for ZDDP+Mo(200 and 500) the friction coefficient remains low, at between 0.04 - 0.05, throughout the test duration.





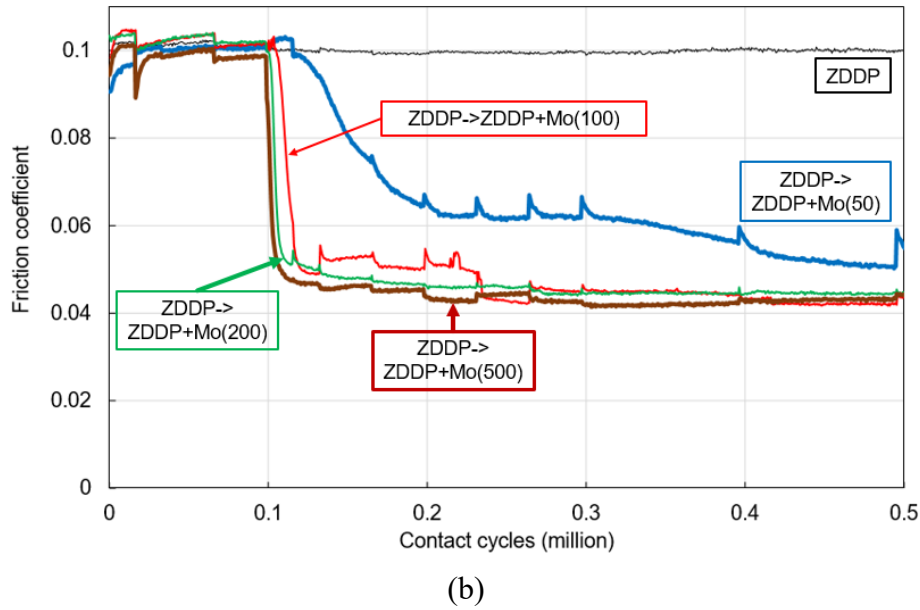


Figure 11-6 Friction behaviour in tests conducted where oils with different MoDTC concentrations were added after 0.1 million cycles. (a) 0 - 8 million cycles and (b) the same data by zoomed in to highlight the 0 - 0.5 million cycles range.

### 11.3.2.2 Evolution of Surface Damage on Balls

Figure 11-7 shows representative optical micrographs of rubbed tracks on balls from tests lubricated with ZDDP for the first 0.1 million cycles and then ZDDP+MoDTC(50, 100, 200 and 500) for the rest of each test. Figure 11-8 shows optical micrograph and SEM images of polished sections of the ball rubbed track along the rolling-direction after 8 million cycles. Figure 11-9 shows the evolution of the micropitting damage on the balls expressed as a percentage micropitted area over total area of the ball rubbing track. This was quantified from optical micrographs of entire wear tracks.

Figure 11-8 clearly shows multiple surface-breaking cracks, growing at a shallow angle of approximately  $20^\circ$  to  $30^\circ$  to the surface and against the direction of the applied friction force. Small micropits, approximately  $30\ \mu\text{m}$  across and about  $10\ \mu\text{m}$  deep, can be seen to be formed by detachment of surface material due to interaction of these cracks. These observations confirm that the generated damage is micropitting. As is evident in the images of Figure 11-7 and the quantitative data in Figure 11-9, the amount of micropitting varies significantly with MoDTC concentration. ZDDP without any MoDTC produced considerable micropitting after 4 and 8 million cycles as shown in Figure 11-7. By

contrast, all the MoDTC-containing blends produced very little micropitting damage with only isolated cracks and pits present.

Figure 11-9 shows that the percentage of micropitted area on the rubbed track decreases with increasing concentration of Mo. For the blend containing ZDDP only, the percentage of micropitted area increases slowly between 0.1 million (where very little damage was seen) and 1 million cycles (4.2% micropitted area), and then rises sharply to reach 14.7% at 4 million cycles and 27.2% after 8 million cycles. This micropitted area is markedly reduced by the addition of MoDTC after 0.1 million cycles, producing 11.5%, 6.4% 3.8% and 1.7% micropitted area after 8 million cycles with 50, 100, 200, and 500 ppm MoDTC respectively.

Figure 11-7 shows that the ZDDP+Mo(500) blend appears to retard the formation of tribofilm in the central region of the rubbing track in a manner similar to that observed in Figure 11-3, as discussed above.

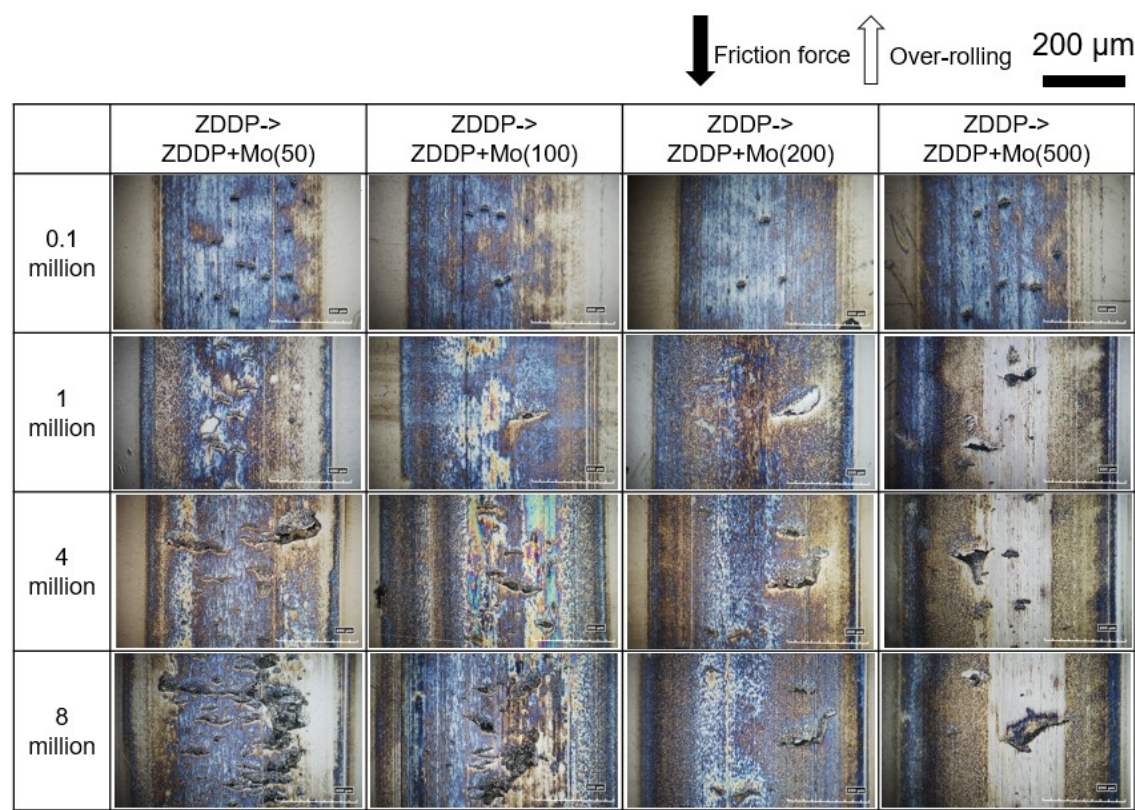


Figure 11-7 Typical optical micrographs of wear tracks on balls in tests conducted where oils with different MoDTC concentrations were added after 0.1 million cycles of running-in with ZDDP solution.

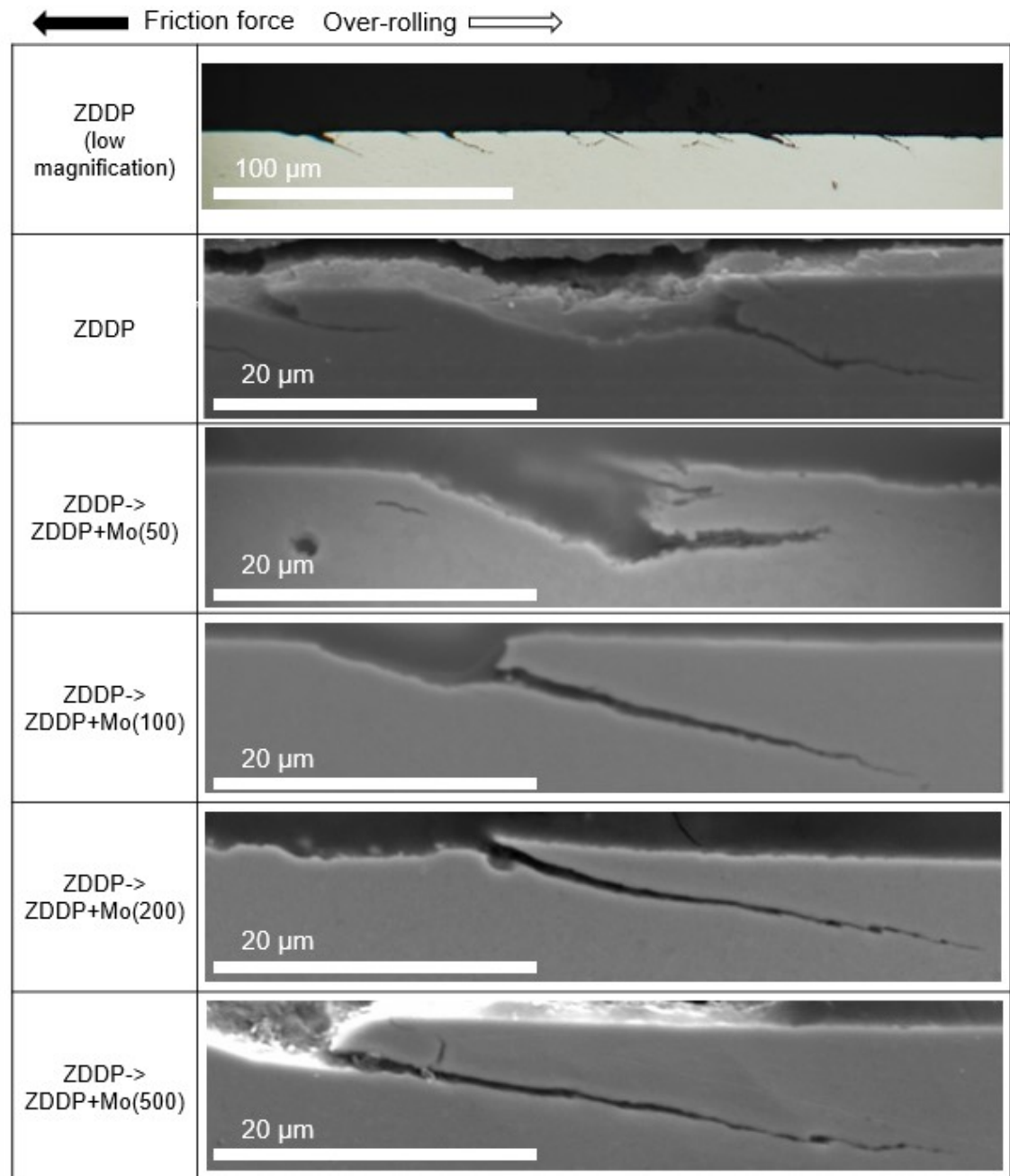


Figure 11-8 Typical SEM images of polished cross-sections of the ball rubbing track along the rolling-direction in tests conducted where oils with different MoDTC concentrations were added after 0.1 million cycles. These show the appearance of typical micropits formed by crack propagation (Note: the cross-section obtained in ZDDP with low magnification shown in the upper-most image was captured using an optical microscope.)

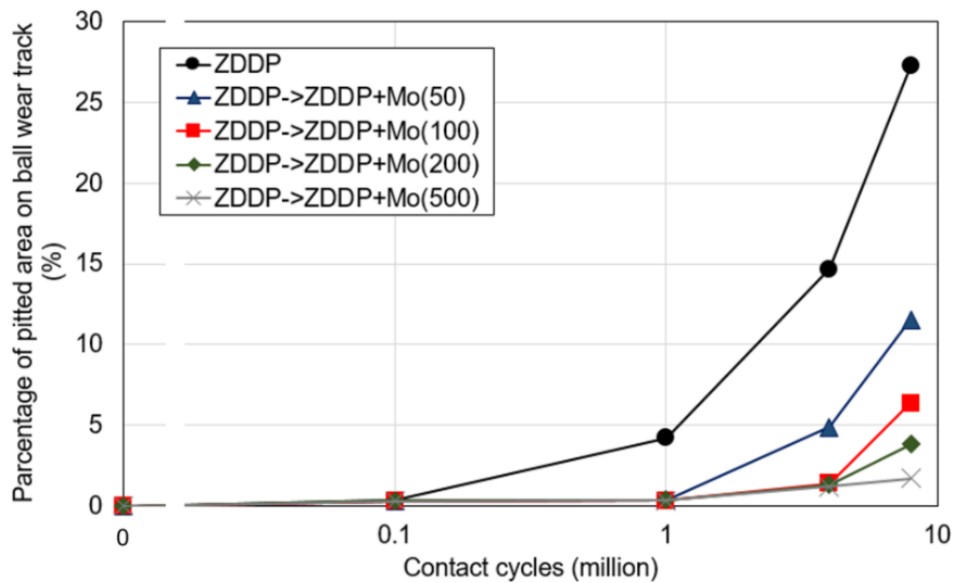


Figure 11-9 Measured percentage of micropitted area on ball wear track in tests in which different MoDTC concentrations were added after 0.1 million cycles of running in with ZDDP solution

### 11.3.2.3 Evolution of Surface Roughness of Counterface Discs

Figure 11-10 shows how the disc roughness changes during the tests with different MoDTC concentrations added after 0.1 million cycles. It is evident that in all tests, the disc roughness reduces from the initial  $0.45 \mu\text{m Ra}$  to  $0.3 \mu\text{m Ra}$  during the initial 0.1 million cycles of running in with lubricant containing only ZDDP. There is then no further change in roughness once the initial ZDDP blend is replaced with the MoDTC-containing blends at Mo concentrations of 50, 100 and 200 ppm. This shows that the running-in of the counterface discs was complete when MoDTC oil was added, and that therefore the addition of MoDTC at 0.1 million cycles did not interfere with this running-in process. The addition of MoDTC at Mo concentration of 500 ppm at 0.1 million cycles did decrease disc roughness further, to  $\sim 0.23 \mu\text{m Ra}$  after 4 million cycles, after which the roughness remained relatively unchanged to the end of the test.

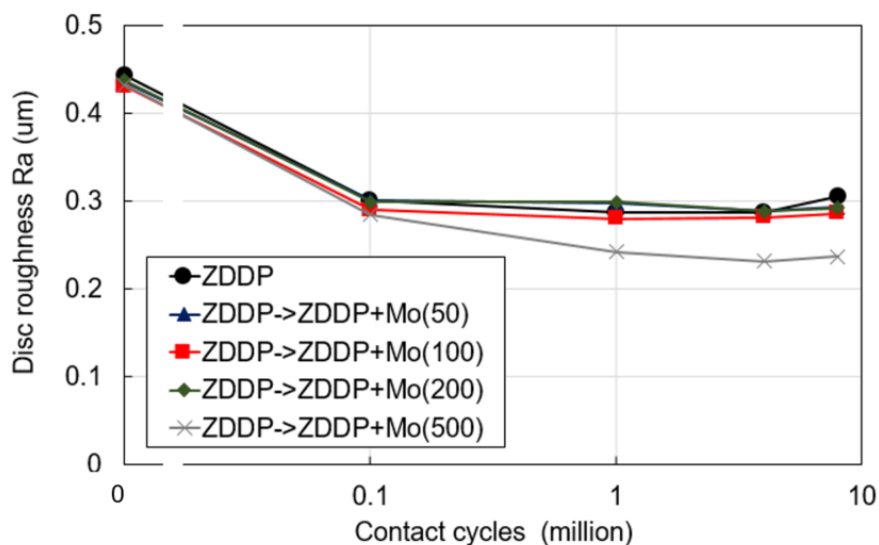


Figure 11-10 Disc roughness evolution in tests conducted where oils with different MoDTC concentrations are added after 0.1 million cycles

#### 11.3.2.4 Evolution of the Tribofilm on the Ball

Figure 11-11 shows the evolution of tribofilm thickness measured in the central region of the rubbed tracks using SLIM. As expected, tribofilms developed at the same rate (reaching *ca.* 50 nm at 0.1 million cycles) in all tests during the first 0.1 million cycles conducted with a blend containing ZDDP only. After replacement with MoDTC-containing lubricants at 0.1 million cycles, the evolution of tribofilm thickness varies with MoDTC concentration. Lubricants containing ZDDP and MoDTC grew tribofilms more slowly than the ZDDP-only oil. ZDPP + Mo at 50, 100 and 200 ppm blends reached a maximum tribofilm thickness after about 0.2 - 0.3 million cycles with thickness values being 160 nm, 125 nm, 110 nm, respectively. The tribofilm thicknesses then decreased to stabilise at *ca.* 70 nm after *ca.* 0.5 million cycles. These stabilised tribofilms were thicker than those from the Mo-free ZDDP solution from about 2 million cycles onwards. By contrast, as is evident in Figure 11-11 (as well as Figure 11-7) the addition of ZDDP+Mo at 500 ppm at 0.1 million cycles leads to rapid removal of the tribofilm formed during the initial 0.1 million cycles of rubbing in the ZDDP only oil. The tribofilm thickness then remains negligible to the end of the test.

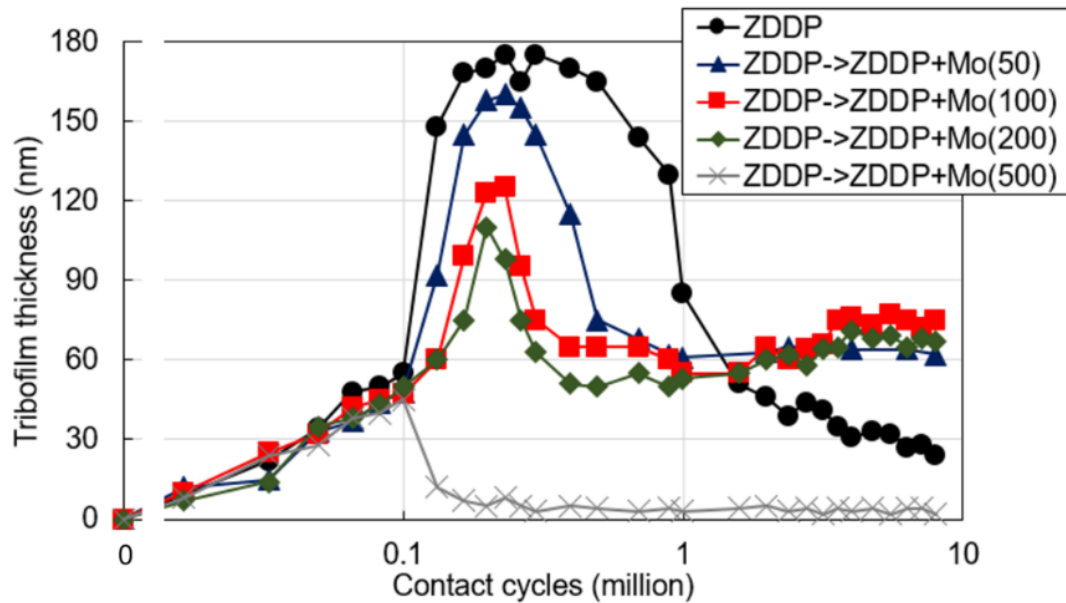


Figure 11-11 Evolution of tribofilm thickness in tests conducted where oils with different MoDTC concentrations were added after 0.1 million cycles of running-in with ZDDP solution

#### 11.4 Discussion

The results described above show that decreasing friction by addition of MoDTC to the lubricating oil decreases micropitting damage. Crucially, the methodology employed in the present paper allows for the effect of friction on micropitting to be isolated from other factors that may influence micropitting. In particular, the potential effect of increased running-in of the counterface, which can occur due to reduction in antiwear tribofilm effectiveness when MoDTC is added to the oil blend, is eliminated by only adding the MoDTC at 0.1 million cycles, at which point the running-in process is already complete.

##### 11.4.1 Other Factors that may Influence Micropitting

As well as the effect of running-in, which was controlled in the present tests, two other factors that might potentially change when friction is changed, and in turn affect the observed micropitting trends, are the specimen bulk temperature and the magnitude of asperity contact pressures due to the growth of a tribofilm on a steel substrate whose thickness might vary with concentration of MoDTC.

Higher friction produces more frictional heating in the contact. In some conditions this heating can result in an increase in the bulk temperature of the specimens, which will in



turn reduce the viscosity of the oil in the contact inlet region and hence reduce the film thickness. This effect might be expected to increase micropitting damage. However, this effect is not present in the current experiments because the specimens were immersed in an oil bath at the temperature which is actively controlled by the MTM rig to remain at 65°C throughout all the tests. The specimen bulk temperature and film thickness are therefore the same in all tests regardless of the level of friction.

It is also possible that the presence of a relatively compliant tribofilm on the steel substrate might reduce the magnitude of the asperity contact pressures and hence affect micropitting. The magnitude of pressure change induced by a surface layer is determined by the elastic properties of the layer and the ratio of its thickness to the contact dimensions [350,366]. Given that tribofilm thicknesses produced by the ZDDP antiwear additive are of the order of 100 nm and the Hertz contact radius is 170  $\mu\text{m}$ , the effect of this tribofilm on macro contact level is negligible. However, at the asperity contact level, where the micro-contact dimensions are of the order of a few microns even this small tribolayer thickness might have some effect on asperity contact pressure. If these pressure changes were significant then any differences in tribofilm thickness with different MoDTC concentrations might potentially affect the observed trends. To investigate this, the elastic properties of the tribofilm formed in the present experiments were measured using nano-indentation, and then used in an existing numerical model for layered, rough surface contacts [356,358,366] to predict the asperity pressure distribution with and without the tribofilm. The model uses real measured surface roughness profiles and accounts for different elastic properties of the layer and the substrate and the layer thickness to predict the asperity pressure distribution in non-conformal, layered, rough contacts.

The analysis presented here is for the thickest tribofilm measured in the present tests, namely 175 nm (see Figure 11-5 and Figure 11-11), and therefore presents the worst-case scenario in terms of the magnitude of potential changes in asperity pressures due to the presence of the tribofilm. In this analysis, ZDDP tribofilm was assumed to have a Poisson's ratio of 0.26 based on Matori et al. [365], who cite this value for zinc phosphate glasses. Figure 11-12 shows representative nanoindentation results for a ZDDP tribofilm, as measured within the rubbed track, and for steel substrate, as measured outside of the wear track. In all tests, elastic modulus shows a high value at an indentation depth of less than 10 nm. This is an artefact due to imperfections in the tip geometry and does not represent the surface properties of tribofilm or steel [367,368]. For steel substrate, elastic modulus is measured to be around 220 GPa as expected. For ZDDP tribofilm the elastic

modulus was in the range of 30 - 40 GPa up to 30 nm of tip displacement. As tip displacement increases further, elastic modulus increases steadily and at a tip displacement of about 400 - 500 nm it reached a similar value to that of steel. This increase of elastic modulus is caused by the well-known substrate effect [297], so that, generally, the true mechanical properties of nanofilms on substrates can only be determined from indentation data originating from the outermost 10% of the film thickness. Considering this, the elastic modulus of ZDDP tribofilm was determined to be an average of 37.7 GPa with 5.0 % standard deviation based on 25 indentations in different positions on the specimen all within tip displacement range of 15 - 25 nm. It should be noted that although this modulus was measured at room temperature while the micropitting tests were carried out at 65°C, Pereira et al. [172] have shown that the elastic modulus of ZDDP tribofilm does not vary significantly between 25 °C and 100 °C.

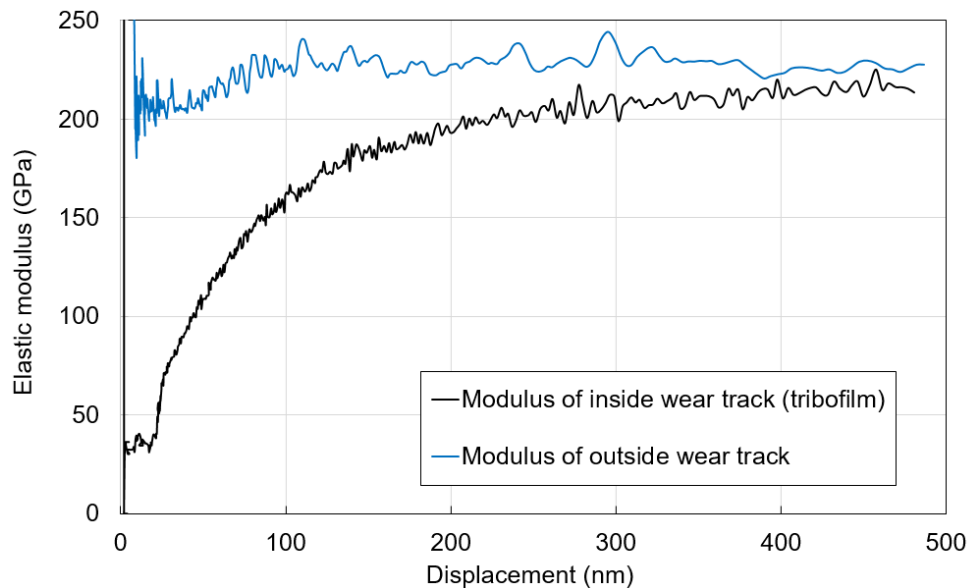


Figure 11-12 Elastic modulus of ZDDP tribofilm formed on AISI 52100 steel substrate after 0.3 million cycles of rubbing in ZDDP only solution as measured by nano indentation in CSM mode. The measured ZDDP tribofilm thickness was 175 nm.

Figure 11-13 shows the predicted pressure distributions for a steel on steel contact and for a steel on 175 nm thick ZDDP tribofilm (elastic modulus 37.7 GPa) on steel substrate. Both cases use the same measured roughness profile of a fresh MTM disc as employed in the present experiments. It should be noted that to illustrate the maximum possible influence of the tribofilm on contact pressures, the example results shown here are from a pure elastic analysis since limiting the pressure to some plastic limit would result in a



similar pressure distribution in both cases, given that roughness is high enough to push the pressures to this plastic limit in both cases. The use of elastic analysis does cause some discrete pressure spikes to be artificially high in this hypothetical example; in practice these pressures would quickly be reduced to the plastic limit on first contact. The results show that 175 nm thick ZDDP tribofilm can reduce the contact pressures on individual asperities by up to about 10% compared to the equivalent steel-on steel contact, with the reduction being the largest for higher asperity pressures. Given that this elastic analysis is an extreme case and in practice (i) the tribofilm thickness of 175 nm used here is much larger than any differences in tribofilm thickness between different tests, and (ii) the virgin disc roughness used here would quickly be modified during the running-in process, it is reasonable to conclude that any differences in asperity pressures caused by small differences in tribofilm thickness are very small and inconsequential in practice. In addition, the tribofilm thicknesses from oils including MoDTC were lower than that from the oil containing just ZDDP, and this could only increase the asperity pressures; this would, in turn act, to increase micropitting, but the opposite trend of lower damage with MoDTC blends was observed here. This confirms the conclusion that reducing friction reduces micropitting damage and this remains true even if there are small increases in asperity pressures due to reduced thickness of the relatively compliant ZDDP tribofilm when MoDTC is added.

#### **11.4.2 Mechanism by which Friction Influences Micropitting**

This study shows that friction has a direct effect on micropitting, with low friction reducing the tendency to micropit and vice-versa. Because MoDTC reduces asperity-asperity friction by forming  $\text{MoS}_2$  on asperities, It is likely that the primary mechanism by which reduction in friction alleviates micropitting is by reducing mechanical stresses experienced by asperities during rubbing. For an ideally smooth contact it is well known that frictional force moves the location of the maximum subsurface shear stress nearer to the surface, as well as generating tensile stress at the rear of the contact region [262,369–373]. In real, rough surface contacts such as those used here, the presence of roughness and friction combines to generate high shear stresses at or very near the surface [350,370]. These stresses are associated with micro-asperity contacts and are ultimately responsible for the formation of surface fatigue cracks which can lead to micropitting.

Using a pure elastic analysis of rough contacts as a worst case scenario, Bailey and Sayles [370] showed that the magnitude of the near surface shear stresses associated with local

asperity contacts for a virgin ground surface with friction coefficient of 0.1 can be twice as high as the maximum subsurface shear stress for an equivalent 'smooth' contact. The magnitude of these local shear stresses due to asperity contacts may be expected to increase with increasing friction. The higher shear stresses would result in higher accumulation of the plastic strain on the local level which is ultimately thought to be responsible for the formation of fatigue cracks [265,372].

In addition to these near surface shear stress effects, since friction is known to generate tensile stresses at the trailing edge of macro-scale contacts it is reasonable to assume that the same effect will occur at the trailing edge of asperity micro-contacts. These tensile stresses enhance crack propagation rates by increasing mode I stress intensity factors. Although, under rolling contact, mode II stress intensity factors are commonly dominant, mode I stress intensity is significant and increases the most with increasing friction. Furthermore, higher friction also increases mode I intensity due to pressurisation of any fluid that may have entered the crack [268,269] as it acts to open up the crack mouth ahead of the approaching contact thus allowing the fluid to enter it. In the case of micropitting, multiple cracks are generated due to asperity stress fields, but, unlike in macro-pitting, they only propagate to a relatively short length, in the region of tens of microns, before creating a micropit. The reasons for this are likely to be twofold. Firstly, the closely-spaced, multiple surface cracks are very likely to interact with each other, and this leads to a formation of a micropit before cracks are able to propagate to longer lengths. Secondly, for a crack to grow longer, it needs to cross the low-stress 'quiescent' zone that exists between the highly-stressed near-surface regions and the subsurface stress region associated with macro-level Hertzian stresses [374,375]. The size of this 'quiescent' zone is determined by the surface roughness properties and the macro stresses resulting from the applied loading and macro geometry so that the exact combination of these will favour micropitting or macropitting.

To test these arguments further, (i) the effect of friction on near surface stresses in the present experiments was investigated and (ii) the morphology of surface cracks obtained at different friction levels was analysed.

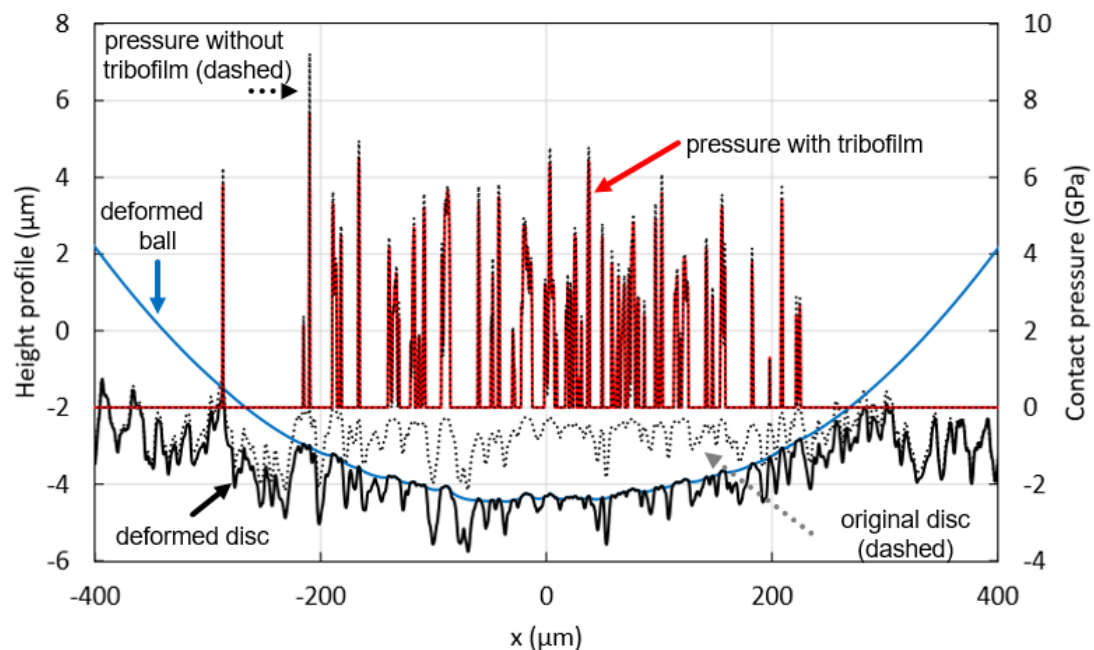


Figure 11-13 Predicted contact pressure distributions for a steel-on-steel contact and an equivalent steel on 175 nm thick ZDDP tribofilm on steel substrate contact. Analysis uses measured roughness profile from a fresh MTM disc with  $R_a \sim 0.43 \mu\text{m}$  and measured elastic modulus of ZDDP film ( $E = 37.7 \text{ GPa}$ ). Note that the results shown are from a pure elastic analysis to illustrate the extreme case.

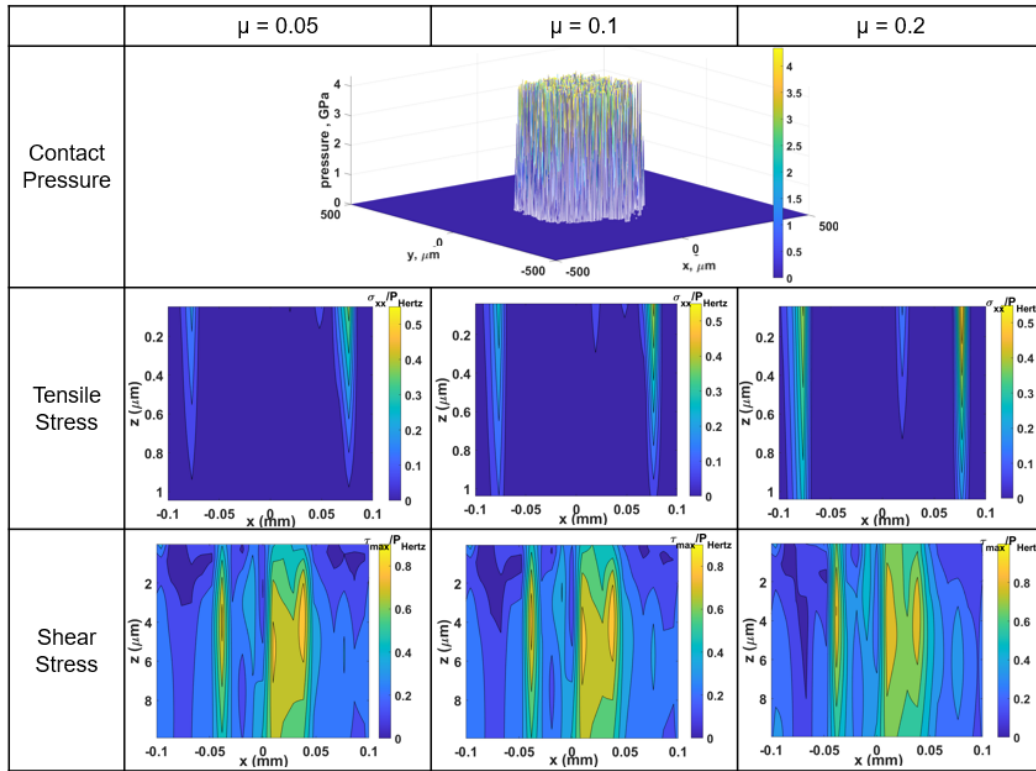
#### 11.4.2.1 Influence of Friction on Near-surface Stresses

A well-established numerical model for contact of rough surfaces [356,358,366,370] was employed to analyse the subsurface stress fields under the conditions of the present experiments. The numerical results presented in this section use an existing model and are not novel in themselves but serve to illustrate the mechanisms at play. The simulations make a number of simplifying assumptions including ignoring any effect of lubricant on contact stresses and assuming elastic-perfectly plastic material behaviour with an imposed plastic limit for asperity pressures of 4 GPa. The former is justified on the grounds of very low lambda ratios employed in the tests. The latter is a very common way to deal with elastic-plastic rough contacts although it ignores important phenomena such as work hardening and asperity persistence [376,377]. ZDDP tribofilm is not modelled here given that its effects were earlier shown to be small. The simulation considers the conditions used in the tests *i.e.* a 19.05 mm diameter steel ball pressed against a steel disc with a load of 75 N, and utilises the real measured roughness profile of the MTM disc. The ball is treated as ideally smooth given that its  $R_a$  is less than 20

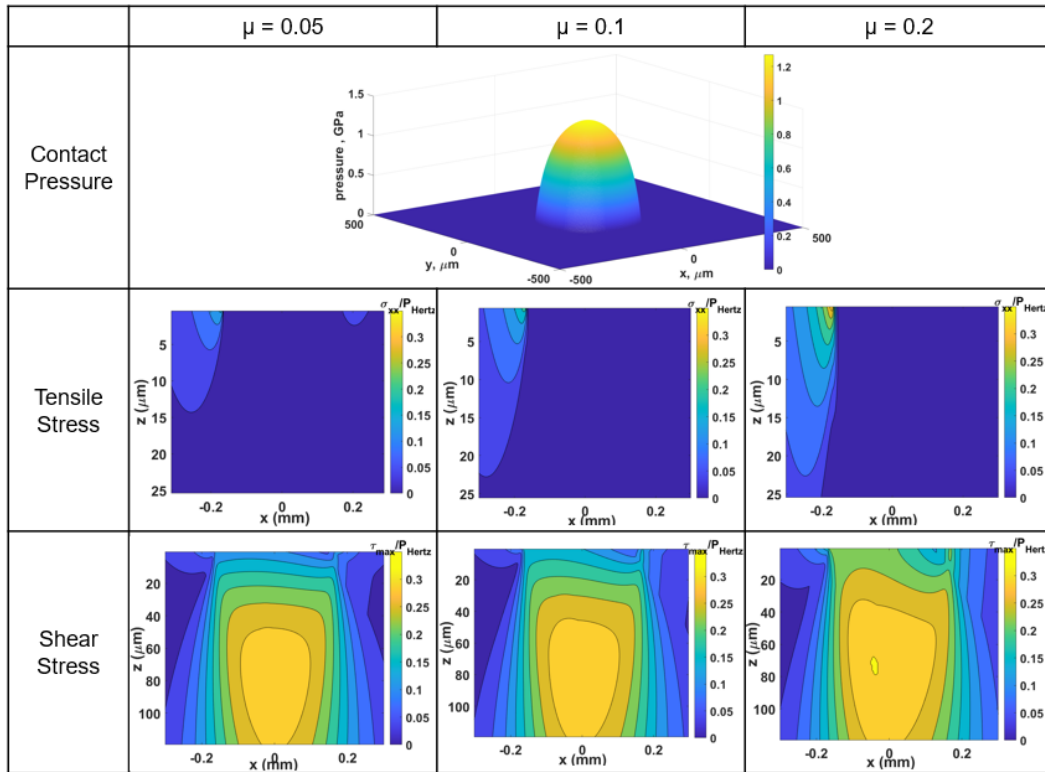
nm. Results for an equivalent smooth contact are shown for comparison and to illustrate the validity of the model predictions. Simulations are performed at friction coefficients of 0.05 and 0.1 *i.e.* similar to those measured in the present tests with and without MoDTC. Further results are also obtained at a friction coefficient of 0.2 to highlight the trends in contact stresses with increasing friction.

Figure 11-13a shows the predicted contact pressure distribution and the contour plots of maximum shear stress and positive (tensile)  $\sigma_{xx}$  stress in the central plane section in rolling direction ( $y = 0$ ), obtained in the manner described above for a smooth ball on rough disc contact. For comparison, Figure 11-13b shows the equivalent results for a smooth disc contact. Tensile and shear stresses,  $P_{hertz}$ , are shown relative to the maximum Hertzian pressure for a smooth contact. It should be noted that only the tensile  $\sigma_{xx}$  stresses are shown, with compressive stresses set to zero so that tensile stress contours are clearly visible. The sliding direction (direction of friction) is from left to right in all cases. The results for the smooth surface show that friction produces tensile stress at the trailing edge of the contact at all three friction coefficients studied. For the rough contact, there are local regions of tensile  $\sigma_{xx}$  stress near the surface associated with asperity contacts. These tensile stresses are very shallow, reaching only to about 1  $\mu\text{m}$  below the surface. It is evident that for both smooth and rough contacts, higher friction increases the size of the tensile  $\sigma_{xx}$  regions and increases their maximum magnitude. For a smooth surface, these magnitudes are 0.20 GPa, 0.28 GPa and 0.44 GPa for friction coefficients of 0.05, 0.1 and 0.2 respectively. The equivalent magnitudes for the rough disc are about twice as high at 0.50 GPa, 0.56 GPa and 0.70 GPa, respectively.

For the smooth contact, the maximum shear stress is located in the subsurface at a depth that is about half the contact radius, but moves closer to the surface as friction increases from 0.05 to 0.2, as is in line with contact mechanics theory [378]. For the rough disc case, there are several local regions of high shear stresses all occurring very near the surface, generally within 5  $\mu\text{m}$  of the surface. These local shear stress maxima are caused by asperity contacts and the general trends shown here are in line with previous studies [268,350,370–373]. The magnitudes of the local high shear stress regions increase with increasing friction (See Figure 11-13b). In addition, the existence multiple regions of high shear stress mean that the number of fluctuations in shear stress experienced by a point in material within this near surface zone during the passage of one surface over another in rolling-sliding contact is increased.



(a)



(b)

Figure 11-14 Surface pressure distribution, contours of positive (tensile)  $\sigma_{xx}$  stress (compressive  $\sigma_{xx}$  stresses set to zero for clarity) and contours of maximum shear stress in the central plane ( $y = 0$ ) in the rolling direction in the contact of an MTM ball and disc under normal load of 75 N and friction as stated: (a) smooth MTM ball on the rough disc (disc roughness as used in present tests and measured using a stylus profilometer); (b) smooth ball on smooth disc under same loading conditions. All stresses have been normalised by the maximum Hertz pressure. Note that the top of the figures of stress distribution ( $z = 0$ ) are the contact surfaces.

#### 11.4.2.2 Effect of Friction on Observed Crack Morphology

To investigate the effect of friction on surface crack morphology, all cracks in each prepared ball cross section in the rolling direction after 8 million cycles (parts of each cross section are illustrated in Figure 11-8) were analysed to measure (i) crack lengths in the subsurface and (ii) the angle at which the cracks grow in relation to the surface. The analysed cross sections are from tests run using Method 2 (*i.e.* MoDTC added after the initial running-in was complete) at different concentrations of the MoDTC, and hence different friction. Figure 11-15 shows the relationship between the measured crack subsurface length and crack angle. The results of ZDDP+Mo(500) were excluded because of its lower counterface roughness after 1 million cycles compared to other blends, which in itself obscures the influence of friction on micropitting as explained above. It should be noted that the number of cracks observed increased with increasing friction coefficient, so that the tests with ZDDP alone (black circles) generated the most cracks. Two features are immediately apparent in Figure 11-15, (i) higher friction resulted in shorter cracks on average after 8 million cycles, and (ii) at higher friction cracks grew at a steeper angle to the surface. For example, in the test with ZDDP only (friction coefficient of *ca.* 0.1) cracks were. However, for tests where 200 ppm Mo was added after 0.1 million cycles (friction coefficient *ca.* 0.04), the crack lengths were between 15  $\mu\text{m}$  and 40  $\mu\text{m}$  and the crack angle to the surface was between 10° and 20°.

The exact reason for the apparent change of crack angle with friction is difficult to establish with certainty as both friction and crack length are changing as one moves from left to right along the  $x$  axis in Fig. 16. However, this must be related to the changes in

the stress fields experienced by the crack for different friction coefficients and observed crack lengths (longer at lower friction).

The trend for shorter cracks at higher friction may seem counterintuitive given that high friction gives higher shear and tensile stresses as shown above. However, there are plausible reasons for these observations. Firstly, the fact that the number of cracks is higher for higher friction coefficients is in accord with the higher magnitude of the near surface stresses discussed above. However, if there is a higher density of cracks, these are more likely to interact to form a micropit, thus truncating any further growth of the affected cracks. Consequently, any remaining cracks that may be observed in the cross-sections from high friction tests are likely to be shorter than in the case of low friction, which must grow longer before interacting.

The entrainment of oil into the surface-breaking crack may also play a part in determining the relevant lengths of cracks at high and low friction. Several authors [268–270,379] have shown numerically that once entrained into the crack, the lubricant can be pressurised during over-rolling, which increases mode I stress intensity factor and hence promotes crack propagation. Olver et al. [380] have provided remarkable direct observations of such lubricant interaction with a micropit passing through the contact. However, another consequence of lubricant entering the crack is a likely reduction in crack face friction. This is a less-studied effect, but it has been shown to be important in relation to crack propagation under rolling contact [269,345,381]. If high friction exists between crack faces during the passage of the crack through the contact, the crack faces will lock and be less able to slide past each other. This will reduce the mode II stress intensity factor, and hence reduce crack propagation rate [269,381]. Bower [269] predicts that mode II crack propagation is unlikely if crack face friction exceeds 0.2. If the lubricant enters the crack, it is likely to significantly reduce the crack face friction and hence allow the crack faces to slide past each other more easily, thus promoting crack propagation under shear mode II. It is reasonable to expect that if a lubricant has low friction properties, such as the MoDTC blends used in the present tests, it will decrease crack face friction more than a lubricant that has higher friction (such as that containing ZDDP only in the present tests). Consequently, the propagation of surface-breaking cracks under mode II may well be enhanced by the presence of low friction oil. This may be the reason why the cracks observed here in the tests with MoDTC blends were longer than those observed with the oil containing ZDDP only. This assumes that mode II propagation is dominant, which is likely under a rolling contact where tensile stresses are generally low, even if friction increases them somewhat. This does not imply that more

micropitting would be caused by a lower friction oil, indeed the opposite is true as shown here, because fewer cracks are initiated.

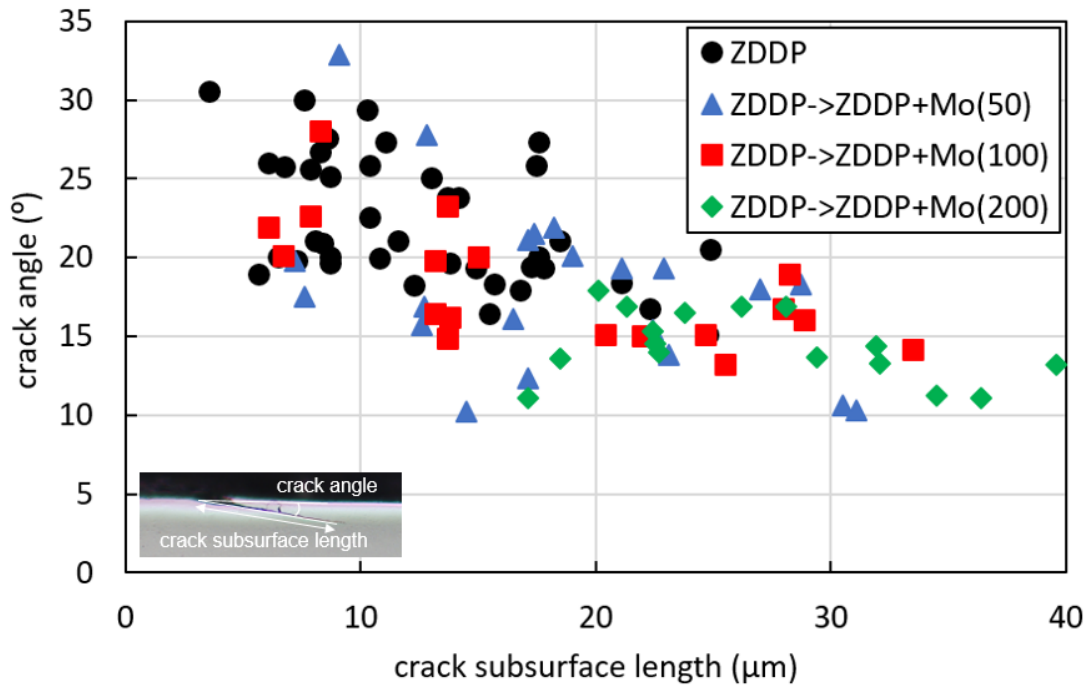


Figure 11-15 Relationship between crack subsurface length and crack angle relative to the surface as measured for all cracks observed in the prepared cross sections of the balls in the rolling direction at 8 million cycles for the lubricant blends containing different amounts of MoDTC as stated. Parts of the relevant cross sections are shown in Figure 11-8.

### 11.5 Conclusions

This Chapter has described MTM-SLIM ball-on-disc tests with custom oil blends containing ZDDP and different concentrations of MoDTC friction modifier to investigate the effect of friction on micropitting. In order to generate micropitting on the balls, non-standard MTM discs with roughness of  $0.42 \pm 0.02 \mu\text{m Ra}$  and softer balls were used. The main findings can be summarised as follows:

- The addition of MoDTC at Mo concentrations of 50, 100, 200 and 500 ppm to the ZDDP oil blend reduces friction and also reduces micropitting. This general reduction in micropitting with addition of MoDTC has been shown by previous



studies, and attributed to the reduced friction. However, it was shown here that presence of MoDTC at common treat rates also slows ZDDP tribofilm growth during the crucial running-in phase, which in turn leads to a greater reduction in counterface roughness than with the oils containing ZDDP alone. It is known that a reduction in counterface roughness during running-in is, in itself, a key parameter influencing micropitting. This means that tests where the MoDTC and ZDDP are both present in the oil blend from the outset cannot isolate the effect of friction on micropitting. This issue was confirmed in the present study.

- To isolate the effect of friction on micropitting, micropitting tests have been carried out in which the initial 0.1 million cycles were conducted with a lubricant blend containing ZDDP alone, after which the solution was replaced by one containing ZDDP and MoDTC at the chosen concentration until the end of the test at 8 million cycles. Results confirm that this method produces the same reduction in the counterface roughness regardless of whether MoDTC was present or not in the second stage of the test. This makes it possible to isolate the effect of friction on micropitting from that of running-in.
- Reduction of friction coefficient from *ca.* 0.10 (ZDDP alone) to *ca.* 0.04 (ZDDP + MoDTC at Mo concentration of 200 ppm) resulted in an order of magnitude reduction in the extent of micropitted area within the ball wear track. This shows that friction has a very significant impact on micropitting.
- Lower friction resulted in fewer surface cracks that were longer and grew at a shallower angle to the surface compared to those produced at higher friction.
- An existing rough surface contact model was used to analyse the contact stresses in the present MTM ball-on-disc contact at different friction coefficients. The analysis suggests that the primary mechanism by which friction affects micropitting is through its effects on the near-surface shear stresses and direct tensile stresses associated with asperity contacts. These stresses affect surface crack initiation and propagation.

## 12 Conclusions and Future Work

In this thesis, a wide range of work has been carried out to further understand important aspects of tribochemical behaviour of the lubricant additive ZDDP, as described in Chapters 5 to 11. Detailed conclusions in each research area were listed at the end of each of these chapters. In this chapter, the main overall findings of the research and some suggestions for future work are described.

### 12.1 Main Conclusions

The most important findings from this research are summarized below. These findings have practical implications for the design of lubricants, lubricant additives and machine components.

#### 12.1.1 ZDDP Tribofilm Properties

- As shown in Chapter 5, ZDDP tribofilms undergo a structural transformation during rubbing from a predominantly amorphous structure to one that is nanocrystalline. This occurs due to the depolymerization of initially-formed polyphosphate chains to much shorter phosphates, possibly predominantly to the orthophosphate, driven by temperature, applied stress and diffusion into the tribofilm of depolymerizing agents including iron cations. Importantly, this amorphous-to-nanocrystalline structural transformation results in the tribofilm becoming much stronger and more durable after extended rubbing. The results also show that primary ZDDP tribofilms convert from amorphous to nanocrystalline structure more slowly than those of secondary ZDDP.

#### 12.1.2 Reaction Mechanism of ZDDP Tribofilm on Non-ferrous Surfaces

- Chapter 6 shows that ion implantation of metallic alloying elements provides a valuable way to explore the influence of alloy steel composition on ZDDP tribofilm formation. This shows that Ni implantation promotes ZDDP tribofilm formation, while Mo and Cr implantations deter tribofilm growth. V and W implantation do not significantly change tribofilm formation. Study of the influence of ZDDP concentration on tribofilm formation rate with different

implanted metals suggests that an important way that steel composition influences tribofilm formation may be by controlling the extent of ZDDP adsorption.

- Chapter 7 studies the formation of ZDDP tribofilms on non-metallic surfaces and finds that the ZDDP tribofilms formed on  $\text{Si}_3\text{N}_4$  and WC surfaces were thicker, but less adhesive, than those formed on steel, while no measurable tribofilms formed on SiC and a-C:H DLC coating. The amount of ZDDP adsorption measured by QCM was greatest for steel, followed by  $\text{Si}_3\text{N}_4$  and WC, and smallest for SiC and carbon. Results suggest that a potentially important factor in formation of ZDDP films on non-metallic surfaces is the presence and concentration of dopant metal atoms or ions at the surface. The metals present in  $\text{Si}_3\text{N}_4$  and WC may act as adsorption sites for ZDDP in a similar manner to Fe in steel, forming ionic bonds between these cations and the sulphur atoms in ZDDP molecules. However, in the case of non-metallic substrates such bonds appear to be less strong than with steel, resulting in weak adhesion of the tribofilm to the substrate, and hence its easier removal.

### 12.1.3 ZDDP Tribofilm Performance

- The research described in Chapter 8 shows that DLC wear in an MoDTC solution can be reduced by the presence of several other surface-active additives commonly present in formulated lubricants, including ZDDP, and that this wear reduction can originate from three factors. Firstly, asperity contact between DLC and steel can be mitigated by the formation of thick antiwear tribofilms. Secondly, some S-containing additives can increase the ratio of  $\text{MoS}_2$ : $\text{MoO}_3$  in the tribofilm formed by MoDTC, reducing the amount of wear-enhancing  $\text{MoO}_3$ . Thirdly, the amount of MoDTC tribofilm including  $\text{MoO}_3$  can be reduced by the competitive adsorption of other surface-active additives.
- Chapter 9 describes the development of a novel method of observing micropitting and tribofilm formation simultaneously in an MTM-SLIM set-up. Using this method, it is confirmed that the mechanism by which ZDDP affects micropitting is through its influence on asperity stress evolution in rough rubbing contacts and the subsequent competition between surface wear and asperity contact fatigue. Too rapid formation of antiwear tribofilms early in operation acts to prevent adequate running-in of the initially rough surfaces, which in turn means that both

the magnitude of asperity stresses and the number of asperity stress cycles remains high throughout subsequent operation, causing increased surface fatigue damage accumulation and eventually micropitting. At the other extreme, a lack of effective antiwear tribofilm enables running-in, and thus reduces micropitting damage, but eventually leads to component failure due to excessive wear. The optimum formulation results in adequate running-in, and hence reduced micropitting, while limiting further wear.

- In Chapter 10, MTM-SLIM is used to explore how black oxide (BO) coatings help alleviate micropitting. It is found that micropitting is completely prevented by applying BO coating on the rough disc counterface in steel ball/BO coated disc and BO coated ball/BO coated disc tribopairs. It is shown that the presence of the BO coating, whose hardness is approximately only one quarter that of the bearing steel substrate, enables very rapid reduction in roughness of the rough disc surface and this provides low asperity stresses and low shear stresses throughout the tests, mitigating crack initiation and propagation and thus micropitting. This rapid reduction of disc roughness occurs despite the presence of ZDDP, while the ZDDP is still able to subsequently form tribofilms on the two surfaces and limit further undesired adhesive wear.
- Chapter 11 describes research to decouple the effects of running-in and friction reduction on micropitting in the presence of MoDTC friction modifier so as to understand the separate roles played by ZDDP and friction modifier in micropitting performance. It is shown that reduction in friction coefficient from 0.08 - 0.10 to 0.04 - 0.05 results in an order of magnitude reduction of micropitted area. This is believed to originate from the reduction in tensile and shear stresses in the near surface region affected by asperity contacts. This reduction in stress mitigates crack initiation and propagation.

## **12.2 Suggestions for Future Work**

Further investigations are suggested for deeper understanding of the tribochemical phenomena of ZDDPs as follows.

- It has been shown that the structure of ZDDP tribofilms is transformed during rubbing from a predominantly amorphous structure to one that is nanocrystalline. This transformation occurs due to the depolymerization of initially formed polyphosphate chains to much shorter phosphates, possibly predominantly the orthophosphate. Although this research has used nanoindentation to measure the hardness and elastic modulus of ZDDP tribofilms this has not yet been correlated directly with the tribofilm structure evolution. It would be of interest to study the development of hardness and elastic modulus of tribofilm using nanoindentation in CSM mode measurements as ZDDP tribofilms transform from amorphous to crystalline structure.
- It was found that thick tribofilms were formed on non-metallic substrates as the amount of ZDDP adsorption increased. As discussed, ionicity of surfaces may be one of the influential factors governing ZDDP adsorption. However, the research carried out studied a quite limited range of non-metallic surfaces;  $\text{Si}_3\text{N}_4$ , WC, SiC, a-C:H DLC. To confirm this ionicity hypothesis, it may be worth studying a wider range of non-metallic surfaces, for example  $\text{Al}_2\text{O}_3$  which has higher ionicity than steel.
- In this study QCM has proved to be useful in observing ZDDP adsorption behaviour on surfaces. In practice, when lubricants are formulated, FMs and VMs are added into the solution of base oil and also additive packages including ZDDP, detergent and dispersant. The addition of FMs and VMs including polar groups often inhibit ZDDP adsorption on surfaces, resulting in less ZDDP tribofilms and more wear. However, the effect of FMs and VMs on ZDDP adsorption has not been systematically investigated. Therefore, it would be of great practical interest to study adsorption of different additives and their combinations using QCM, ideally over a range of temperature.
- It was found that the growth rate of ZDDP tribofilms significantly affects micropitting wear. Micropitting commonly occurs on gears and rolling bearings that are lubricated predominantly by oils containing ash-less antiwear additives, primarily phosphorus-type additives, and not ZDDPs. Considering practical applications, a study of the effect of phosphorus-type additives on micropitting with the simultaneous observation of tribofilm growth may be useful. Generally,

tribofilms generated from phosphorus-type additives are thinner than ZDDPs; thus it may be a challenge to quantify and analyse such thin tribofilms precisely.

- Although it has been widely reported that black oxide coating on the rough counterface component can mitigate micropitting, the evolution of asperity slopes caused by the wear of black oxide may also have an effect on macro-scale pitting and this has not been studied. Thus, it is of interest to investigate such effects further.
- Micropitting and wear can be balanced by controlling friction coefficient through the formation of ZDDP and MoDTC tribofilms. Considering the importance of predicting rolling contact fatigue failures, it should be useful to estimate stress intensity factors in a rolling contact for a given friction coefficient using a numerical crack model. This may improve our ability to predict contact fatigue lives for different friction coefficients.

## References

- [1] D. Dowson, History of tribology, 146 (1979).
- [2] F.P. Bowden, D. Tabor, Mechanism of metallic friction, *Nature*. 150 (1942) 197–199.
- [3] J.A. Martin, A.D. Eberhardt., Identification of potential failure nuclei in rolling contact fatigue, *Trans. ASME*. (1967) 932–942.
- [4] F.J. Wren, C.A. Moyer, Paper 9: Modes of Fatigue Failures in Rolling Element Bearings, *Proc. Inst. Mech. Eng. Conf. Proc.* 179 (1964) 236–247.
- [5] D. Dowson, T.L. Whomes, Second Paper: Effect of Surface Quality upon the Traction Characteristics of Lubricated Cylindrical Contacts, *Proc. Inst. Mech. Eng.* 182 (1967) 292–299.
- [6] T.E. Tallian, J.I. McCool, L.B. Sibley, Partial elastohydrodynamic lubrication in rolling contact, *Proc. Inst. Mech. Eng. Conf. Proc.* 180 (1965) 169–186.
- [7] H. Spikes, The borderline of elastohydrodynamic and boundary lubrication, *J. Mech. Eng. Sci.* 214 (2000) 23–37.
- [8] R.L. Errichello, Morphology of Micropitting, *GEAR Technol.* 4 (2012) 74–81.
- [9] D. Nélías, M.L. Dumont, F. Champiot, A. Vincent, D. Girodin, R. Fougères, L. Flamand, Role of Inclusions, Surface Roughness and Operating Conditions on Rolling Contact Fatigue, *J. Tribol.* 121 (1999) 240–251.
- [10] Imperial College London, Tribology lecture 1. Introduction, *Imp. Coll. London Lect. Note*. (2018).
- [11] S.C. Tung, M.L. McMillan, Automotive tribology overview of current advances and challenges for the future, *Tribol. Int.* 37 (2004) 517–536.
- [12] R. Cléménçon, The two sides of the Paris climate agreement: Dismal failure or historic breakthrough?, *J. Environ. Dev.* 25 (2016) 3–24.
- [13] International Energy Agency, Data & Statistics, (2017) <https://www.iea.org/data-and-statistics?country=WO>.
- [14] International Council on Clean Transportation, CO2 emission standards for passenger cars and light-commercial vehicles in the European Union, (2014) <https://theicct.org/sites/default/files/publicatio>.
- [15] International Council on Clean Transportation, 2017 Global update: Light-duty vehicle greenhouse gas and fuel economy standards, (2017) <https://theicct.org/publications/2017-global-updat>.
- [16] U. Kugler, J. Brokate, C. Schimeczek, S. Schmid, Powertrain Scenarios for Cars in European Markets to the Year 2040, (2017)

- [https://elib.dlr.de/114744/1/20170331\\_Powertrain\\_S](https://elib.dlr.de/114744/1/20170331_Powertrain_S).
- [17] ROBEKO, Electric vehicles coming of age, (2017) <https://www.robeco.com/en/insights/2018/11/electri>.
  - [18] M. Ehsani, Y. Gao, S. Longo, K. Ebrahimi, Modern electric, hybrid electric, and fuel cell vehicles, CRC Press. (2018).
  - [19] Accenture, The Electric Vehicle Challenge, (2014) [https://www.accenture.com/mz-en/~/\\_media/Accenture/](https://www.accenture.com/mz-en/~/_media/Accenture/).
  - [20] V.W. Wong, S.C. Tung, Overview of automotive engine friction and reduction trends—Effects of surface, material, and lubricant-additive technologies, *Friction*. 4 (2016) 1–28.
  - [21] D.E. Richardson, Review of power cylinder friction for diesel engines, *J. Eng. Gas Turbines Power*. 122 (2000) 506–519.
  - [22] R. Nozawa, Y. Morita, M. Shimizu, Effects of engine downsizing on friction losses and fuel economy, *Tribol. Int.* 27 (1994) 31–37.
  - [23] Automotive World, Powertrain in focus: what’s hot on the road to 2020?, (2016) <https://www.automotiveworld.com/articles/powertrai>.
  - [24] J. Vetter, G. Barbezat, J. Crummenauer, J. Avissar, Surface treatment selections for automotive applications, *Surf. Coatings Technol.* 200 (2005) 1962–1968.
  - [25] G. Dumitru, V. Romano, H.P. Weber, S. Pimenov, T. Kononenko, J. Hermann, S. Bruneau, Y. Gerbig, M. Shupegin, Laser treatment of tribological DLC films, *Diam. Relat. Mater.* 12 (2003) 1034–1040.
  - [26] A. Ronen, I. Etsion, Y. Kligerman, Friction-reducing surface-texturing in reciprocating automotive components, *Tribol. Trans.* 44 (2001) 359–366.
  - [27] G. Ryk, Y. Kligerman, I. Etsion, Experimental investigation of laser surface texturing for reciprocating automotive components, *Tribol. Trans.* 45 (2002) 444–449.
  - [28] Y. Mabuchi, T. Hamada, H. Izumi, Y. Yasuda, M. Kano, The Development of Hydrogen-free DLC-coated Valve-lifter, *SAE Tech. Pap.* (2007).
  - [29] A.C. Ferrari, J. Robertson, Interpretation of Raman spectra of disordered and amorphous carbon, *Phys. Rev. B*. 61 (2000) 14095.
  - [30] C. Öner, H. Hazar, M. Nursoy, Surface properties of CrN coated engine cylinders, *Mater. Des.* 30 (2009) 914–920.
  - [31] T. Haque, A. Morina, A. Neville, R. Kapadia, S. Arrowsmith, Non-ferrous coating/lubricant interactions in tribological contacts: Assessment of tribofilms, *Tribol. Int.* 40 (2007) 1603–1612.
  - [32] I. Etsion, G. Halperin, E. Becker, The effect of various surface treatments on piston



- pin scuffing resistance, *Wear*. 261 (2006) 785–791.
- [33] M. Kennedy, S. Hoppe, J. Esser, Lower friction losses with new piston ring coating, *MTZ Worldw.* 75 (2014) 24–29.
  - [34] P. Hupperich, M. Dürnholz, Exhaust emissions of diesel, gasoline and natural gas fuelled vehicles, *SAE Tech. Pap.* (1996).
  - [35] N. Takahashi, H. Shinjoh, T. Iijima, T. Suzuki, K. Yamazaki, K. Yokota, H. Suzuki, N. Miyoshi, S. Matsumoto, T. Tanizawa, T. Tanaka, S. Tateishi, K. Kasahara, The new concept 3-way catalyst for automotive lean-burn engine: NO<sub>x</sub> storage and reduction catalyst, *Catal. Today*. 27 (1996) 63–69.
  - [36] Y. Iwamoto, K. Noma, O. Nakayama, T. Yamauchi, H. Ando, Development of gasoline direct injection engine, *SAE Trans.* (1997) 777–793.
  - [37] L. Liu, Z. Li, S. Liu, B. Shen, Effect of exhaust gases of Exhaust Gas Recirculation (EGR) coupling lean-burn gasoline engine on NO<sub>x</sub> purification of Lean NO<sub>x</sub> trap (LNT), *Mech. Syst. Signal Process.* 87 (2017) 195–213.
  - [38] T. Johnson, Vehicular Emissions in Review, *SAE Int. J. Engines*. 9 (2016) 1258–1275.
  - [39] O. Kröcher, M. Elsener, Chemical deactivation of V<sub>2</sub>O<sub>5</sub>/WO<sub>3</sub>–TiO<sub>2</sub> SCR catalysts by additives and impurities from fuels, lubrication oils, and urea solution: I. Catalytic studies, *Appl. Catal. B Environ.* 77 (2008) 215–227.
  - [40] A. Sappok, V. Wong, Ash effects on diesel particulate filter pressure drop sensitivity to soot and implications for regeneration frequency and DPF control, *SAE Int. J. Fuels Lubr.* 3 (2010) 380–396.
  - [41] M.J. Rokosz, A.E. Chen, C.K. Lowe-Ma, A. V. Kuchеров, D. Benson, M.C. Paputa Peck, R.W. McCabe, Characterization of phosphorus-poisoned automotive exhaust catalysts, *Appl. Catal. B Environ.* 33 (2001) 205–215.
  - [42] Infineum, ACEA 2016 Oil Sequences, (2016) <https://www.infineuminsight.com/media/1976/acea-20>.
  - [43] Infineum, API Engine Oil Classifications, (2020) <https://www.infineuminsight.com/media/2841/api-eng>.
  - [44] Japan Lubricating Oil Society, AUTOMOTIVE DIESEL ENGINE OIL STANDARD (JASO M 355: 2017) APPLICATION MANUAL, (2018) [http://www.jalos.or.jp/onfile/pdf/DH\\_E2002.pdf](http://www.jalos.or.jp/onfile/pdf/DH_E2002.pdf).
  - [45] ACEA, ACEA EUROPEAN OIL SEQUENCES, (2016) [https://www.acea.be/uploads/news\\_documents/ACEA\\_Eu](https://www.acea.be/uploads/news_documents/ACEA_Eu).
  - [46] Southwest Research Institute, Sequence VID Engine Test, (2009) <https://www.swri.org/sites/default/files/sequence->.

- [47] Infineum, Moving to even lower viscosities, Infineum Insight. (2020) <https://www.infineuminsight.com/en-gb/articles/lub>.
- [48] N. Ushioda, T.W. Miller, C.B. Sims, G. Parsons, M. Sztenderowicz, Effect of low viscosity passenger car motor oils on fuel economy engine tests, SAE Tech. Pap. (2013).
- [49] M.J. Souza De Carvalho, P. Rudolf Seidl, C.R. Pereira Belchior, J. Ricardo Sodr, Lubricant viscosity and viscosity improver additive effects on diesel fuel economy, Tribol. Int. 43 (2010) 2298–2302.
- [50] Y. Nakamura, K. Tomizawa, T. Onishi, T. Hashimoto, M. Sato, T. Tatani, A. Akamatsu, H. Inaba, R. Aoki, Development of Fuel Economy Engine Oil for Heavy Duty Diesel Engine, SAE Tech. Pap. (2015).
- [51] T. Sagawa, S. Nakano, Y. Bito, Y. Koike, S. Okuda, R. Suzuki, Development of Low Viscosity API SN 0W-16 Fuel-Saving Engine Oil Considering Chain Wear Performance, SAE Int. J. Fuels Lubr. 10 (2017) 469–477.
- [52] K.T. Miklozic, T.R. Forbus, H.A. Spikes, Performance of friction modifiers on zddp-generated surfaces, Tribol. Trans. 50 (2007) 328–335.
- [53] K. Hoshino, H. Kawai, K. Akiyama, Fuel Efficiency of SAE 5W-20 Friction Modified Gasoline Engine Oil, SAE Tech. Pap. (1998).
- [54] D. Kenbeek, T. Buenemann, H. Rieffe, Review of organic friction modifiers-contribution to fuel efficiency?, SAE Tech. Pap. (2000).
- [55] M. Kano, Y. Yasuda, Y. Okamoto, Y. Mabuchi, T. Hamada, T. Ueno, J. Ye, S. Konishi, S. Takeshima, J.M. Martin, M.I. De Barros Bouchet, T. Le Mogne, Ultralow friction of DLC in presence of glycerol mono-oleate (GMO), Tribol. Lett. 18 (2005) 245–251.
- [56] R. Zahid, M.B.H. Hassan, M. Varman, R.A. Mufti, M.A. Kalam, N.W.B.M. Zulkifli, M. Gulzar, A Review on Effects of Lubricant Formulations on Tribological Performance and Boundary Lubrication Mechanisms of Non-Doped DLC/DLC Contacts, Crit. Rev. Solid State Mater. Sci. 42 (2017) 267–294.
- [57] M. Kano, Super low friction of DLC applied to engine cam follower lubricated with ester-containing oil, Tribol. Int. 39 (2006) 1682–1685.
- [58] B. Vengudusamy, R.A. Mufti, G.D. Lamb, J.H. Green, H.A. Spikes, Friction properties of DLC/DLC contacts in base oil, Tribol. Int. 44 (2011) 922–932.
- [59] H. Okubo, C. Tadokoro, T. Sumi, N. Tanaka, S. Sasaki, Wear acceleration mechanism of diamond-like carbon (DLC) films lubricated with MoDTC solution: Roles of tribofilm formation and structural transformation in wear acceleration of DLC films lubricated with MoDTC solution, Tribol. Int. 133 (2019) 271–287.

- [60] M. De Feo, M.I. De Barros Bouchet, C. Minfray, T. Le Mogne, F. Meunier, L. Yang, B. Thiebaut, J.M. Martin, MoDTC lubrication of DLC-involving contacts. Impact of MoDTC degradation, *Wear*. 348–349 (2016) 116–125.
- [61] M. De Feo, M.I. De Barros Bouchet, C. Minfray, C. Esnouf, T. Le Mogne, F. Meunier, L. Yang, B. Thiebaut, S. Pavan, J.M. Martin, Formation of interfacial molybdenum carbide for DLC lubricated by MoDTC: Origin of wear mechanism, *Wear*. 370 (2017) 17–28.
- [62] B. Vengudusamy, J.H. Green, G.D. Lamb, H.A. Spikes, Behaviour of MoDTC in DLC / DLC and DLC / steel contacts, *Tribology Int.* 54 (2012) 68–76.
- [63] Y. Al-jeboori, S. Kosarieh, A. Morina, A. Neville, Investigation of pure sliding and sliding/rolling contacts in a DLC/Cast iron system when lubricated in oils containing MoDTC-Type friction modifier, *Tribol. Int.* 122 (2018) 23–37.
- [64] S. Kosarieh, A. Morina, J. Flemming, E. Lainé, A. Neville, Wear Mechanisms of Hydrogenated DLC in Oils Containing MoDTC, *Tribol. Lett.* 64 (2016).
- [65] Y. Shimizu, H. Fujita, M. Kasai, Study of Non-Phosphorus and Non-Ash Engine oil, *SAE Tech. Pap.* (2011).
- [66] M. Kasai, N. Yoshimura, Y. Takashima, I. Terada, The Effect of Ashless Additives for Non-Phosphorus and Non-Ash Engine Oil on Piston Detergency, *SAE Tech. Pap.* (2015).
- [67] H. Spikes, The history and mechanisms of ZDDP, *Tribol. Lett.* 17 (2004) 469–489.
- [68] H.A. Spikes, A. Cameron, Additive interference in dibenzyl disulfide extreme pressure lubrication, *ASLE Trans.* 17 (1974) 283–289.
- [69] J. Lara, K.K. Surerus, P. V. Kotvis, M.E. Contreras, J.L. Rico, W.T. Tysoe, The surface and tribological chemistry of carbon disulfide as an extreme-pressure additive, *Wear*. 239 (2000) 77–82.
- [70] E.S. Forbes, A.J.D. Reid, Liquid phase adsorption/reaction studies of organo-sulfur compounds and their load-carrying mechanism, *ASLE Trans.* 16 (1973) 50–60.
- [71] H. Spikes, Friction modifier additives, *Tribol. Lett.* 60 (2015) 5.
- [72] S. Jahanmir, M. Beltzer, An adsorption model for friction in boundary lubrication, *ASLE Trans.* 29 (1986) 423–430.
- [73] P. Studt, Boundary lubrication: adsorption of oil additives on steel and ceramic surfaces and its influence on friction and wear, *Tribol. Int.* 22 (1989) 111–119.
- [74] W.B. Hardy, I. Doubleday, Boundary lubrication. - The paraffin series., *Proc. R. Soc. London. Ser. A, Contain. Pap. a Math. Phys. Character.* 100 (1922) 550–574.
- [75] I.M. Feng, W.L. Perilstein, M.R. Adams, Solid film deposition and non-sacrificial boundary lubrication, *ASLE Trans.* 6 (1963) 60–66.

- [76] G. Scott, Antioxidants, *Bull. Chem. Soc. Jpn.* 61 (1988) 165–170.
- [77] P.A. Willermet, L.R. Mahoney, C.M. Bishop, Lubricant Degradation and Wear III. Antioxidant Reactions and Wear Behavior of a Zinc Dialkyldithiophosphate in a Fully Formulated Lubricant, *ASLE Trans.* 23 (1980) 225–231.
- [78] E.S. Yamaguchi, A. Onopchenko, M.M. Francisco, C.Y. Chan, The relative oxidation inhibition performance of some neutral and basic zinc dithiophosphate salts, *Tribol. Trans.* 42 (1999) 895–901.
- [79] V.J. Gatto, Y.L. Bezjak, The antioxidant properties of organomolybdenum compounds in engine oils, *Tribol. Lubr. Technol.* 62 (2006) 32–39.
- [80] L. Cizaire, J.M. Martin, T. Le Mogne, E. Gresser, Chemical analysis of overbased calcium sulfonate detergents by coupling XPS, ToF-SIMS, XANES, and EFTEM, *Colloids Surfaces A Physicochem. Eng. Asp.* 238 (2004) 151–158.
- [81] L.K. Hudson, J. Eastoe, P.J. Dowding, Nanotechnology in action: Overbased nanodetergents as lubricant oil additives, *Adv. Colloid Interface Sci.* 123–126 (2006) 425–431.
- [82] K. Komvopoulos, G. Pennecot, E.S. Yamaguchi, S.W. Yeh, Antiwear properties of blends containing mixtures of zinc dialkyl dithiophosphate and different detergents, *Tribol. Trans.* 52 (2009) 73–85.
- [83] A. Greenall, A. Neville, A. Morina, M. Sutton, Investigation of the interactions between an overbased, organic anti-wear additive, ZDDP and overbased calcium sulphonate, *Tribol. Int.* 46 (2012) 52–61.
- [84] A.M. Barnes, K.D. Bartle, V.R.A. Thibon, A review of zinc dialkyldithiophosphates (ZDDPS): Characterisation and role in the lubricating oil, *Tribol. Int.* 34 (2001) 389–395.
- [85] C. Grossiord, J.M. Martin, K. Varlot, B. Vacher, T. Le Mogne, Y. Yamada, Tribochemical interactions between ZnDTP, ModTC and calcium borate, *Tribol. Lett.* 8 (2000) 203–212.
- [86] E.S. Forbes, E.L. Neustadter, The mechanism of action of polyisobutenyl succinimide lubricating oil additives, *Tribology.* 5 (1972) 72–77.
- [87] A. Tomlinson, B. Scherer, E. Karakosta, M. Oakey, T.N. Danks, D.M. Heyes, S.E. Taylor, Adsorption properties of succinimide dispersants on carbonaceous substrates, *Carbon N. Y.* 38 (2000) 13–28.
- [88] J. Zhang, E. Yamaguchi, H. Spikes, The Antagonism between succinimide dispersants and a secondary zinc dialkyl dithiophosphate, *Tribol. Trans.* 57 (2013) 57–65.
- [89] K. Inoue, H. Watanabe, Interactions of engine oil additives, *ASLE Trans.* 26 (1983)

- 189–199.
- [90] S. Plaza, The Effect of Other Lubricating Oil Additives on the Adsorption of Zinc Di-isobutyldithiophosphate on Fe and  $\gamma$  - Fe<sub>2</sub>O<sub>3</sub> Powders, ASLE Trans. 30 (1987) 241–247.
  - [91] M. Müller, J. Fan, H. Spikes, Influence of polymethacrylate viscosity index improvers on friction and wear of lubricant formulations, SAE Trans. (2007) 580–588.
  - [92] M. Smeeth, H. Spikes, S. Gunsel, Boundary film formation by viscosity index improvers, Tribol. Trans. 39 (1996) 726–734.
  - [93] Y. Matsui, S. Aoki, M. Masuko, Influence of coexisting functionalized polyalkylmethacrylates on the formation of ZnDTP-derived tribofilm, Tribol. Int. 100 (2016) 152–161.
  - [94] G. Gavlin, E.A. Swire, S.P. Jones, Pour Point Depression of Lubricating Oils, Ind. Eng. Chem. . 45 (1953) 2327–2335.
  - [95] C. O’Neal Jr, N. Borger Richard, Corrosion Inhibiting Synergism By Triazoles in Aqueous Multimetal Systems, Mater. Perform. 15 (1976) 9–13.
  - [96] H. Gisser, J. Messina, J. Snead, Hydroxyarylstearic Acids as Oxidation and Rust Inhibitors in Lubricants, Ind. Eng. Chem. 48 (1956) 2001–2004.
  - [97] H.R. Baker, C.R. Singleterry, E.T. Solomon, Neutral and Basic Sulfonates Corrosion-Inhibiting and Acid-Deactivating Properties, Ind. Eng. Chem. 46 (1954) 1035–1042.
  - [98] M. Andriot, S.H. Chao, A.R. Colas, S.E. Cray, F. DeBuyl, J.V. DeGroot, A. Dupont, T. Easton, J.L. Garaud, E. Gerlach, F. Gubbels, Silicones in Industrial Applications, Inorg. Polym. (2007) 61–161.
  - [99] P.W. Centers, Behavior of silicone antifoam additives in synthetic ester lubricants, Tribol. Trans. 36 (1993) 381–386.
  - [100] Infineum, A question of base stocks, Infineum Insight. (2020) <https://www.infineuminsight.com/en-gb/articles/bas>.
  - [101] A. Pettersson, High-performance base fluids for environmentally adapted lubricants, Tribol. Int. 40 (2007) 638–645.
  - [102] Infineum, Lubricant base stocks, Infineum Insight. (2018) <https://www.infineuminsight.com/media/1814/3-lubri>.
  - [103] T. Mang, W. Dresel, Lubricants and Lubrication, Lubr. Lubr. Second Ed. (2007).
  - [104] S.A. Francis, A.H. Ellison, Reflection Infrared Studies of Zinc Dialkyl Dithiophosphate Films Adsorbed on Metal Surfaces, J. Chem. Eng. Data. 6 (1961) 83–86.

- [105] G. Harrison, P. Brown, External reflection FTIR,  $^{31}\text{P}$  MAS NMR and SEM study of the thermal decomposition of zinc (II) bis (O, O'-dialkyldithiophosphates) on 316 stainless steel, *Wear*. 148 (1991) 123–134.
- [106] P.A. Willermet, R.O. Carter, P.J. Schmitz, M. Everson, D.J. Scholl, W.H. Weber, Formation, structure and properties of lubricant-derived antiwear films, *Lubr. Sci.* 9 (1997) 325–348.
- [107] S. Aoki, A. Suzuki, M. Masuko, Comparison of sliding speed dependency of friction between steel surfaces lubricated with several ZnDTPs with different hydrocarbon moieties, *Proc. Inst. Mech. Eng. Part J J. Eng. Tribol.* 220 (2006) 343–351.
- [108] F.M. Piras, A. Rossi, N.D. Spencer, Combined in situ (ATR FT-IR) and ex situ (XPS) study of the ZnDTP-iron surface interaction, *Tribol. Lett.* 15 (2003) 181–191.
- [109] F.M. Piras, A. Rossi, N.D. Spencer, Growth of Tribological Films: In Situ Characterization Based on Attenuated Total Reflection Infrared Spectroscopy, *Langmuir*. 18 (2002) 6606–6613.
- [110] S. Berkani, F. Dassenoy, C. Minfray, J.M. Martin, H. Cardon, G. Montagnac, B. Reynard, Structural changes in tribo-stressed zinc polyphosphates, *Tribol. Lett.* 51 (2013) 489–498.
- [111] S. Berkani, F. Dassenoy, C. Minfray, M. Belin, B. Vacher, J.M. Martin, H. Cardon, G. Montagnac, B. Reynard, Model formation of ZDDP tribofilm from a mixture of zinc metaphosphate and goethite, *Tribol. Int.* 79 (2014) 197–203.
- [112] J.L. Paddy, N.C.J. Lee, D.N. Waters, W. Trott, Zinc dialkyldithiophosphate oxidation by cumene hydroperoxide: kinetic studies by Raman and  $^{31}\text{P}$  NMR spectroscopy, *Tribol. Trans.* 33 (1990) 15–20.
- [113] I.N.A. Sieber, K. Meyer, H. Kloss, A. Schöpke, Characterization of boundary layers formed by different metal dithiophosphates in a four-ball machine, *Wear*. 85 (1983) 43–56.
- [114] D. Yang, J. Zhou, Q. Xue, Tribochemical behavior of Ni ion implanted pure iron lubricated with ZDDP as an additive, *Wear*. 199 (1996) 60–65.
- [115] A. Dorgham, A. Azam, A. Morina, A. Neville, On the Transient Decomposition and Reaction Kinetics of Zinc Dialkyldithiophosphate, *ACS Appl. Mater. Interfaces*. 10 (2018) 44803–44814.
- [116] R. Mourhatch, P.B. Aswath, Tribological behavior and nature of tribofilms generated from fluorinated ZDDP in comparison to ZDDP under extreme pressure conditions Part 1: Structure and chemistry of tribofilms, *Tribol. Int.* 44 (2011) 187–

200.

- [117] S. Hashimoto, K. Hirokawa, Y. Fukuda, K. Suzuki, T. Suzuki, N. Usuki, N. Gennai, S. Yoshida, M. Koda, H. Sezaki, H. Horie, A. Tanaka, T. Ohtsubo, Correction of Peak Shift and Classification of Change of X-ray Photoelectron Spectra of Oxides as a Result of Ion Sputtering, *Surf. Interface Anal.* 18 (1992) 799–806.
- [118] H.M. Naguib, R. Kelly, Criteria for bombardment induced structural changes in non metallic solids, *Radiat. Eff.* 25 (1975) 1–12.
- [119] P. Parsaeian, A. Ghanbarzadeh, M.C.P. Van Eijk, I. Nedelcu, A. Neville, A. Morina, A new insight into the interfacial mechanisms of the tribofilm formed by zinc dialkyl dithiophosphate, *Appl. Surf. Sci.* 403 (2017) 472–486.
- [120] M. Crobu, A. Rossi, F. Mangolini, N.D. Spencer, Chain-length-identification strategy in zinc polyphosphate glasses by means of XPS and ToF-SIMS, *Anal. Bioanal. Chem.* 403 (2012) 1415–1432.
- [121] M. Crobu, A. Rossi, F. Mangolini, N.D. Spencer, Tribochemistry of bulk zinc metaphosphate glasses, *Tribol. Lett.* 39 (2010) 121–134.
- [122] R.J. Bird, G.D. Galvin, The application of photoelectron spectroscopy to the study of EP films on lubricated surfaces, *Wear.* 37 (1976) 143–167.
- [123] G.C. Smith, J.C. Bell, Multi-technique surface analytical studies of automotive anti-wear films, *Appl. Surf. Sci.* 144 (1999) 222–227.
- [124] L.L. Cao, Y.M. Sun, L.Q. Zheng, Chemical structure characterization of the boundary lubrication film using X-ray photoelectron spectroscopy scanning Auger microprobe techniques, *Wear.* 140 (1990) 345–357.
- [125] J.M. Martin, C. Grossiord, T. Le Mogne, S. Bec, A. Tonck, The two-layer structure of ZnDTP tribofilms Part I : AES , XPS and XANES analyses, *Tribol. Int.* 34 (2001) 523–530.
- [126] J.C. Bell, K.M. Delargy, A.M. Seeney, Paper IX (ii) the removal of substrate material through thick zinc dithiophosphate anti-wear films, *Tribol. Ser.* 21 (1992) 387–396.
- [127] R. Heuberger, A. Rossi, N.D. Spencer, XPS study of the influence of temperature on ZnDTP tribofilm composition, *Tribol. Lett.* 25 (2007) 185–196.
- [128] A. Rossi, M. Eglin, F.M. Piras, K. Matsumoto, N.D. Spencer, Surface analytical studies of surface-additive interactions, by means of in situ and combinatorial approaches, *Wear.* 256 (2004) 578–584.
- [129] J.M. Georges, J.M. Martin, T. Mathia, P. Kapsa, G. Meille, H. Montes, Mechanism of boundary lubrication with zinc dithiophosphate, *Wear.* 53 (1979) 9–34.
- [130] M.L.S. Fuller, M. Kasrai, G.M. Bancroft, K. Fyfe, K.H. Tan, Solution

- decomposition of zinc dialkyl dithiophosphate and its effect on antiwear and thermal film formation studied by X-ray absorption spectroscopy, *Tribol. Int.* 31 (1998) 627–644.
- [131] Y.-R. Li, G. Pereira, A. Lachenwitzer, M. Kasrai, P.R. Norton, Studies on ZDDP Thermal Film Formation by XANES Spectroscopy, Atomic Force Microscopy, FIB / SEM and <sup>31</sup>P NMR, *Tribol. Lett.* 19 (2008) 11–22.
- [132] R.W.M. Kwok, L.J. Huang, W.M. Lau, M. Kasrai, X. Feng, K. Tan, S. Ingre, D. Landheer, X-ray absorption near edge structures of sulfur on gas-phase polysulfide treated InP surfaces and at SiN<sub>x</sub>/InP interfaces, *J. Vac. Sci. Technol. A.* 12 (1994).
- [133] Z. Yin, M. Kasrai, G.M. Bancroft, K.F. Laycock, K.H. Tan, Chemical characterization of antiwear films generated on steel by zinc dialkyl dithiophosphate using X-ray absorption spectroscopy, *Tribol. Int.* 26 (1993) 383–388.
- [134] G.M. Bancroft, M. Kasrai, M. Fuller, Z. Yin, K. Fyfe, K.H. Tan, Mechanisms of tribochemical film formation: stability of tribo- and thermally-generated ZDDP films, *Tribol. Lett.* 3 (1997) 47–51.
- [135] E.S. Ferrari, K.J. Roberts, M. Sansone, D. Adams, A multi-edge X-ray absorption spectroscopy study of the reactivity of zinc di-alkyl-di-thiophosphates anti-wear additives 2. In situ studies of steel/roil interfaces, *Wear.* 236 (1999) 259–275.
- [136] G.W. Canning, M.L.S. Fuller, G.M. Bancroft, M. Kasrai, J.N. Cutler, G. De Stasio, B. Gilbert, Spectromicroscopy of tribological films from engine oil additives. Part I. Films from ZDDP's, *Tribol. Lett.* 6 (1999) 159–169.
- [137] M.L.S. Fuller, L.R. Fernandez, G.R. Massoumi, W.N. Lennard, M. Kasrai, G.M. Bancroft, The use of X-ray absorption spectroscopy for monitoring the thickness of antiwear films from ZDDP, *Tribol. Lett.* 8 (2000) 187–192.
- [138] Z. Yin, M. Kasrai, G.M. Bancroft, K. Fyfe, M.L. Colaianni, K.H. Tan, Application of soft X-ray absorption spectroscopy in chemical characterization of antiwear films generated by ZDDP Part II: The effect of detergents and dispersants, *Wear.* 202 (1997) 192–201.
- [139] Z. Zhang, M. Kasrai, G.M. Bancroft, E.S. Yamaguchi, Study of the Interaction of ZDDP and Dispersants Using X-ray Absorption Near Edge Structure Spectroscopy—Part 1: Thermal Chemical Reactions, *Tribol. Lett.* 15 (2003) 377–384.
- [140] M. Fuller, Z. Yin, M. Kasrai, G.M. Bancroft, E.S. Yamaguchi, P.R. Ryason, P.A. Willermet, K.H. Tan, Chemical characterization of ochemical and thermal films erated from neutral and basic ZDDPs using X-ray absorption spectroscopy, *Tribol.*



- Int. 30 (1997) 305–315.
- [141] K. Varlot, M. Kasrai, J.M. Martin, B. Vacher, G.M. Bancroft, E.S. Yamaguchi, P.R. Ryason, Antiwear film formation of neutral and basic ZDDP : influence of the reaction temperature and of the concentration, *Tribol. Lett.* 8 (2000) 9–16.
  - [142] P.A. Willermet, D.P. Dailey, R.O. Carter, P.J. Schmitz, W. Zhu, J.C. Bell, D. Park, The composition of lubricant-derived surface layers formed in a lubricated cam/tappet contact II. Effects of adding overbased detergent and dispersant to a simple ZDTP solution, *Tribol. Int.* 28 (1995) 163–175.
  - [143] K. Ito, J.M. Martin, C. Minfray, K. Kato, Low-friction tribofilm formed by the reaction of ZDDP on iron oxide, *Tribol. Int.* 39 (2006) 1538–1544.
  - [144] D. Philippon, M.I. De Barros-Bouchet, T. Le Mogne, B. Vacher, O. Lerasle, J.M. Martin, A multi-technique approach to the characterization of iron phosphide tribofilm, *Thin Solid Films.* 524 (2012) 191–196.
  - [145] C.J. Hsu, J. Barrirero, R. Merz, A. Stratmann, H. Aboulfadl, G. Jacobs, M. Kopnarski, F. Mücklich, C. Gachot, Revealing the interface nature of ZDDP tribofilm by X-ray photoelectron spectroscopy and atom probe tomography, *Ind. Lubr. Tribol.* (2020).
  - [146] J.M. Martin, T. Le Mogne, C. Grossiord, T. Palermo, Adsorption and friction in the UHV tribometer, *Tribol. Lett.* 3 (1997) 87–94.
  - [147] K. Topolovec-Miklozic, T.R. Forbus, H.A. Spikes, Film thickness and roughness of ZDDP antiwear films, *Tribol. Lett.* 26 (2007) 161–171.
  - [148] M.A. Nicholls, P.R. Norton, G.M. Bancroft, M. Kasrai, T. Do, B.H. Frazer, G. De Stasio, Nanometer scale chemomechanical characterization of antiwear films, *Tribol. Lett.* 17 (2004) 205–216.
  - [149] J. Dawczyk, N. Morgan, J. Russo, H. Spikes, Film Thickness and Friction of ZDDP Tribofilms, *Tribol. Lett.* 67 (2019) 34.
  - [150] Z. Zhang, E.S. Yamaguchi, M. Kasrai, G.M. Bancroft, X. Liu, M.E. Fleet, Tribofilms generated from ZDDP and DDP on steel surfaces: Part 2, chemistry, *Tribol. Lett.* 19 (2005) 221–229.
  - [151] Y. Shimizu, H.A. Spikes, The influence of aluminium–silicon alloy on ZDDP tribofilm formation on the counter-surface, *Tribol. Lett.* 65 (2017) 137.
  - [152] J. Jelita Rydel, K. Pagkalis, A. Kadiric, P.E.J. Rivera-Díaz-del-Castillo, The correlation between ZDDP tribofilm morphology and the microstructure of steel, *Tribol. Int.* 113 (2017) 13–25.
  - [153] L.J. Taylor, H.A. Spikes, Friction-Enhancing Properties of ZDDP Antiwear Additive: Part I—Friction and Morphology of ZDDP Reaction Films, *Tribol. Trans.*

- 46 (2003) 303–309.
- [154] A. Naveira-Suarez, A. Tomala, R. Pasaribu, R. Larsson, I.C. Gebeshuber, Evolution of ZDDP-derived reaction layer morphology with rubbing time, *Scanning*. 32 (2010) 294–303.
  - [155] A. Naveira Suarez, M. Grahm, R. Pasaribu, R. Larsson, The influence of base oil polarity on the tribological performance of zinc dialkyl dithiophosphate additives, *Tribol. Int.* 43 (2010) 2268–2278.
  - [156] O.L. Warren, J.F. Graham, P.R. Norton, J.E. Houston, T.A. Michalske, Nanomechanical properties of films derived from zinc dialkyldithiophosphate, *Tribol. Lett.* 4 (1998) 189–198.
  - [157] J.F. Graham, C. Mccague, P.R. Norton, Topography and nanomechanical properties of tribochemical films derived from zinc dialkyl and diaryl dithiophosphates, *Tribol. Lett.* 6 (1999) 149–157.
  - [158] M. Aktary, M.T. McDermott, G.A. McAlpine, Morphology and nanomechanical properties of ZDDP antiwear films as a function of tribological contact time, *Tribol. Lett.* 12 (2002) 155–162.
  - [159] J. Benedet, J.H. Green, G.D. Lamb, H.A. Spikes, Spurious mild wear measurement using white light interference microscopy in the presence of antiwear films, *Tribol. Trans.* 52 (2009) 841–846.
  - [160] S. Soltanahmadi, A. Morina, M.C.P. van Eijk, I. Nedelcu, A. Neville, Experimental observation of zinc dialkyl dithiophosphate (ZDDP)-induced iron sulphide formation, *Appl. Surf. Sci.* 414 (2017) 41–51.
  - [161] J. Dawczyk, E. Ware, M. Ardakani, J. Russo, H. Spikes, Use of FIB to Study ZDDP Tribofilms, *Tribol. Lett.* 66 (2018) 1–8.
  - [162] C.Minfray, J.M.Martin, C.Esnouf, T.L. Mogne, R.Kersting, B.Hagenhoff, A multi-technique approach of tribofilm characterisation, *Thin Solid Films*. 447 (2003) 272–277.
  - [163] P. Cann, A. Cameron, Studies of thick boundary lubrication - influence of zddp and oxidized hexadecane, *Tribol. Int.* 17 (1984) 205–208.
  - [164] P.K. and J.M.G. A. Tonck, J.M. Martin, Boundary lubrication with anti-wear additives: study of interface film formation by electrical contact resistance, *Tribol. Int.* 12 (1979) 209–213.
  - [165] H. Gao, J.S. McQueen, E.D. Black, A.K. Gangopadhyay, R.K. Jensen, Reduced phosphorus concentration effects on tribological performance of passenger car engine oils, *Tribol. Trans.* 47 (2004) 200–207.
  - [166] J.S. McQueen, H. Gao, E.D. Black, A.K. Gangopadhyay, R.K. Jensen, Friction and

- wear of tribofilms formed by zinc dialkyl dithiophosphate antiwear additive in low viscosity engine oils, *Tribol. Int.* 38 (2005) 289–297.
- [167] H. Fujita, H.A. Spikes, The formation of zinc dithiophosphate antiwear films, *Proc. Inst. Mech. Eng. Part J J. Eng. Tribol.* 218 (2004) 265–277.
  - [168] H. Fujita, H.A. Spikes, Study of zinc dialkyldithiophosphate antiwear film formation and removal processes, part II: Kinetic model, *Tribol. Trans.* 48 (2005) 567–575.
  - [169] H. Fujita, R.P. Glovnea, H.A. Spikes, Study of zinc dialkyldithiophosphate antiwear film formation and removal processes, part I: Experimental, *Tribol. Trans.* 48 (2005) 558–566.
  - [170] L. Taylor, A. Dratva, H.A. Spikes, Friction and wear behavior of zinc dialkyldithiophosphate additive, *Tribol. Trans.* 43 (2000) 469–479.
  - [171] J.U. Dawczyk, The Effect of Organic Friction Modifiers on ZDDP Tribofilm, PhD Thesis, Imp. Coll. London. (2018).
  - [172] G. Pereira, D. Munoz-Paniagua, A. Lachenwitzer, M. Kasrai, P.R. Norton, T.W. Capehart, T.A. Perry, Y.T. Cheng, A variable temperature mechanical analysis of ZDDP-derived antiwear films formed on 52100 steel, *Wear.* 262 (2007) 461–470.
  - [173] J. Ye, M. Kano, Y. Yasuda, Evaluation of local mechanical properties in depth in MoDTC/ZDDP and ZDDP tribochemical reacted films using nanoindentation, *Tribol. Lett.* 13 (2002) 41–47.
  - [174] S. Bec, A. Tonck, J.M. Georges, R.C. Coy, J.C. Bell, G.W. Roper, Relationship between mechanical properties and structures of zinc dithiophosphate anti-wear films, *Proc. R. Soc. A Math. Phys. Eng. Sci.* 455 (1999) 4181–4203.
  - [175] D. Shakhvorostov, K. Pöhlmann, M. Scherge, Structure and mechanical properties of tribologically induced nanolayers, *Wear.* 260 (2006) 433–437.
  - [176] L. Feng, R. Hao, S. Gaemers, C.P. Warrens, S.J. Dillon, Variation in zinc dialkyldithiophosphate yield strength measured by nanopillar compression, *Tribol. Int.* 123 (2018) 325–328.
  - [177] X. Liu, C.Y. Tang, R. Hao, K. Walsh, C. Zhou, S.J. Dillon, Local chemo-mechanical insights into the efficacy of ZDDP additives from in situ single asperity growth and mechanical testing, *Tribol. Int.* 112 (2017) 103–107.
  - [178] M. Kalin, E. Oblak, S. Akbari, Evolution of the nano-scale mechanical properties of tribofilms formed from low- and high-SAPS oils and ZDDP on DLC coatings and steel, *Tribol. Int.* 96 (2016) 43–56.
  - [179] J.M. Martin, Antiwear mechanisms of zinc dithiophosphate : a chemical hardness approach, *Tribol. Lett.* 6 (1999) 1–8.

- [180] M. Aktary, M.T. Mcdermott, J. Torkelson, Morphological evolution of films formed from thermooxidative decomposition of ZDDP, *Wear*. 247 (2001) 172–179.
- [181] J.J. Dickert, C.N. Rowe, Thermal decomposition of metal O, O-dialkyl phosphorodithioates, *J. Org. Chem.* 32 (1967) 647–653.
- [182] J.S. Ashford, L. Bretherick, P. Gould, The thermal decomposition of zinc di-(4-methylpentyl-2) dithiophosphate, *J. Appl. Chem.* 15 (1965) 170–178.
- [183] R.B. Jones, R.C. Coy, The chemistry of the thermal degradation of zinc dialkyldithiophosphate additives, *ASLE Trans.* 24 (1981) 91–97.
- [184] R.C. Coy, R.B. Jones, The thermal degradation and EP performance of zinc dialkyldithiophosphate additives in white oil, *ASLE Trans.* 24 (1981) 77–90.
- [185] P.A. Bennett, A surface effect associated with the use of oils containing zinc dialkyl dithiophosphate, *ASLE Trans.* 2 (1959) 78–90.
- [186] A.D. Brazier, J.S. Elliott, The thermal stability of zinc dithiophosphates, *J. Inst. Pet.* 53 (1967) 63–76.
- [187] F.G. Rounds, Some factors affecting the decomposition of three commercial zinc organodithiophosphates, *ASLE Trans.* 18 (1975) 79–89.
- [188] H. Spedding, R.C. Watkins, The antiwear mechanism of zddp's. Part I, *Tribol. Int.* 15 (1982) 9–12.
- [189] N. Soda, Y. Kimura, A. Tanaka, Wear of some fcc metals during unlubricated sliding Part I. Effects of load, velocity and atmospheric pressure on wear, *Wear*. 33 (1975) 1–16.
- [190] S. Al-Malaika, M. Coker, G. Scott, Mechanisms of antioxidant action: effect of processing on the transformation products of thiophosphoryl compounds in polyolefins, *Polym. Degrad. Stab.* 10 (1985) 173–183.
- [191] P.A. Willermet, L.R. Mahoney, C.M. Haas, The effects of antioxidant reactions on the wear behavior of a zinc dialkyldithiophosphate, *ASLE Trans.* 22 (1979) 301–306.
- [192] E.S. Yamaguchi, P.R. Ryason, Inelastic electron tunneling spectra of lubricant oil additives on native aluminum oxide surfaces, *Tribol. Trans.* 36 (1993) 367–374.
- [193] C.H. Bovington, B. Dacre, The adsorption and reaction of decomposition products of zinc di-isopropyldiophosphate on steel, *ASLE Trans.* 27 (1984) 252–258.
- [194] B. Dacre, C.H. Bovington, The adsorption and desorption of zinc di-isopropyldithiophosphate on steel, *ASLE Trans.* 25 (1982) 546–554.
- [195] A. V. Ivanov, O.N. Antzutkin, A.C. Larsson, M. Kritikos, W. Forsling, Polycrystalline and surface O,O'-dialkyldithiophosphate zinc(II) complexes: Preparation, <sup>31</sup>P CP/MAS NMR and single-crystal X-ray diffraction studies,

- Inorganica Chim. Acta. 315 (2001) 26–35.
- [196] B. Dacre, C.H. Bovington, The effect of metal composition on the adsorption of zinc di-isopropyldithiophosphate, ASLE Trans. 26 (1983) 333–343.
  - [197] Y. Shimizu, H.A. Spikes, The Influence of Slide–Roll Ratio on ZDDP Tribofilm Formation, Tribol. Lett. 64 (2016) 1–11.
  - [198] A. Kontou, M. Southby, N. Morgan, H.A. Spikes, Influence of Dispersant and ZDDP on Soot Wear, Tribol. Lett. 66 (2018) 1–15.
  - [199] V.H. Luther, D. Staeck, Investigation of the decomposition of dialkyldithiophosphates in mineral oil (in German), Erdol u Kohle-Erd.-Petr. (1969) 530–536.
  - [200] H. Teichmann, G. Hilgetag, Nucleophilic Reactivity of the Thiophosphoryl Group, Angew. Chemie Int. Ed. English. 6 (1967) 1013–1023.
  - [201] G. Hilgetag, H. Teichmann, The Alkylating Properties of Alkyl Thiophosphates, Angew. Chemie Int. Ed. English. 4 (1965) 914–922.
  - [202] Y.R. Li, G. Pereira, M. Kasrai, P.R. Norton, The effect of steel hardness on the performance of ZDDP antiwear films: A multi-technique approach, Tribol. Lett. 29 (2008) 201–211.
  - [203] J.S. Sheasby, T.A. Caughlin, W.A. Mackwood, The effect of steel hardness on the performance of antiwear additives, Wear. 201 (1996) 209–216.
  - [204] Y.C. Lin, H. So, Limitations on use of ZDDP as an antiwear additive in boundary lubrication, Tribol. Int. 37 (2004) 25–33.
  - [205] K.J. Kubiak, T.G. Mathia, M. Bigerelle, Influence of roughness on ZDDP tribofilm formation in boundary lubricated fretting, Tribol. - Mater. Surfaces Interfaces. 6 (2012) 182–188.
  - [206] H. Ji, M.A. Nicholls, P.R. Norton, M. Kasrai, T.W. Capehart, T.A. Perry, Y.T. Cheng, Zinc-dialkyl-dithiophosphate antiwear films: Dependence on contact pressure and sliding speed, Wear. 258 (2005) 789–799.
  - [207] V. Brizmer, C. Matta, I. Nedelcu, G.E. Morales-Espejel, The Influence of Tribolayer Formation on Tribological Performance of Rolling/Sliding Contacts, Tribol. Lett. 65 (2017) 1–18.
  - [208] K. Pagkalis, H. Spikes, J. Jelita-rydel, M. Ingram, A. Kadiric, The Influence of Steel Composition on the Formation and Effectiveness of Anti-wear Films in Tribological Contacts, Tribol. Lett. 69 (2021) 1–20.
  - [209] Z. Yin, M. Kasrai, M. Fuller, G.M. Bancroft, K. Fyfe, K.H. Tan, Application of soft X-ray absorption spectroscopy in chemical characterization of antiwear films generated by ZDDP Part I: the effects of physical parameters, Wear. 202 (1997)

172–191.

- [210] N.J. Mosey, M.H. Müser, T.K. Woo, Molecular mechanisms for the functionality of lubricant additives, *Science* (80-. ). 307 (2005) 1612–1615.
- [211] J.S. Tse, Y. Song, Z. Liu, Effects of temperature and pressure on ZDDP, *Tribol. Lett.* 28 (2007) 45–49.
- [212] K. Nakayama, Triboemission of charged particles and resistivity of solids, *Tribol. Lett.* 6 (1999) 37–40.
- [213] C.K. Kajdas, Importance of the triboemission process for tribochemical reaction, *Tribol. Int.* 38 (2005) 337–353.
- [214] C.G. Camara, J. V Escobar, J.R. Hird, S.J. Putterman, Correlation between nanosecond X-ray flashes and stick–slip friction in peeling tape, *Nature*. 455 (2008) 1089–1092.
- [215] D. Puhan, Triboemission-lubricant interactions, PhD Thesis, Imp. Coll. London. (2017).
- [216] N.N. Gosvami, J.A. Bares, F. Mangolini, A.R. Konicek, D.G. Yablon, R.W. Carpick, Mechanisms of antiwear tribofilm growth revealed in situ by single-asperity sliding contacts, *Science* (80-. ). 348 (2015) 102–106.
- [217] J. Zhang, H. Spikes, On the Mechanism of ZDDP Antiwear Film Formation, *Tribol. Lett.* 63 (2016) 1–15.
- [218] J. Zhang, J.P. Ewen, M. Ueda, J.S. Wong, H.A. Spikes, Mechanochemistry of Zinc Dialkyldithiophosphate on Steel Surfaces under Elastohydrodynamic Lubrication Conditions, *ACS Appl. Mater. Interfaces*. 12 (2020) 6662–6676.
- [219] T. Tsujimoto, A. Yaguchi, K. Yagishita, Operational performance of eco-friendly engine oils formulated with the sulfur-free additive ZP, *SAE Tech. Pap.* (2007) 596–602.
- [220] K. Hoshino, K. Yagishita, K. Tagawa, H. Spikes, Tribological properties of sulphur-free antiwear additives zinc dialkylphosphates (ZDPs), *SAE Trans.* 5 (2012) 504–510.
- [221] K. Hoshino, Film Forming and Friction Properties of Sulphur-Free Antiwear Additives Zinc Dialkylphosphates (ZDPs), PhD Thesis, Imp. Coll. London. (2011).
- [222] I. Hutchings, P. Shipway, *tribology: friction and wear of engineering materials*, Butterworth-Heinemann. (2017).
- [223] J.S. Sheasby, T.A. Caughlin, A.G. Blahey, K.F. Laycock, A reciprocating wear test for evaluating boundary lubrication, *Tribol. Int.* 23 (1990) 301–307.
- [224] M. Born, J.C. Hipeaux, P. Marchand, F. Pbtrole, The Relationship between Chemical Structure and Effectiveness of Some Metallic Dialkyl- and Diaryl-

- dithiophosphates in Different Lubricated Mechanisms, *Lubr. Sci.* 4–2 (1992) 93–116.
- [225] J. Fan, H. Spikes, New Test for Mild Lubricated Wear in Rolling- Sliding Contacts New Test for Mild Lubricated Wear in Rolling-Sliding Contacts, *Tribol. Trans.* 50 (2007) 145–153.
- [226] P. Parsaeian, M.C.P. Van Eijk, I. Nedelcu, A. Neville, A. Morina, Study of the interfacial mechanism of ZDDP tribofilm in humid environment and its effect on tribochemical wear; Part I: Experimental, *Tribol. Int.* 107 (2017) 135–143.
- [227] H. Cen, A. Morina, A. Neville, R. Pasaribu, I. Nedelcu, Effect of water on ZDDP anti-wear performance and related tribochemistry in lubricated steel/steel pure sliding contacts, *Tribol. Int.* 56 (2012) 47–57.
- [228] J.E. Booth, K.D. Nelson, T.J. Harvey, R.J.K. Wood, L. Wang, H.E.G. Powrie, J.G. Martinez, The feasibility of using electrostatic monitoring to identify diesel lubricant additives and soot contamination interactions by factorial analysis, *Tribol. Int.* 39 (2006) 1564–1575.
- [229] F.G. Rounds, Additive interactions and their effect on the performance of a zinc dialkyl dithiophosphate, *ASLE Trans.* 21 (1978) 91–101.
- [230] F. Rounds, Changes in Friction and Wear Performance Caused by Interactions Among Lubricant Additives, *Lubr. Sci.* 1 (1989) 333–363.
- [231] K. Fujita, Y. Esaki, M. Kawamura, The antiwear property of zinc dialkyldithiophosphates in used engine oils, *Wear.* 89 (1983) 323–331.
- [232] M. Masuko, T. Ohkido, A. Suzuki, T. Ueno, S. Okuda, T. Sagawa, Effect of ashless dispersant on deterioration of antiwear characteristics of zndtp due to decomposition during the oxidation inhibition process, *Tribol. Trans.* 50 (2007) 310–318.
- [233] Z. Zhang, E.S. Yamaguchi, M. Kasrai, G.M. Bancroft, Tribofilms generated from ZDDP and DDP on steel surfaces: Part 1, growth, wear and morphology, *Tribol. Lett.* 19 (2005) 211–220.
- [234] A.K. Landauer, W.C. Barnhill, J. Qu, Correlating mechanical properties and anti-wear performance of tribofilms formed by ionic liquids, ZDDP and their combinations, *Wear.* 354 (2016) 78–82.
- [235] G. Tripaldi, A. Vettor, H. Spikes, Friction behaviour of ZDDP films in the mixed, boundary/EHD regime, *SAE Trans.* (1996) 1819–1830.
- [236] J. Zhang, M. Ueda, S. Campen, H. Spikes, Boundary Friction of ZDDP Tribofilms, *Tribol. Lett.* 69 (2021) 1–17.
- [237] M. Muraki, H. Wada, Influence of the alkyl group of zinc dialkyldithiophosphate

- on the frictional characteristics of molybdenum dialkyldithiocarbamate under sliding conditions, *Tribol. Int.* 35 (2002) 857–863.
- [238] A. Morina, A. Neville, Understanding the composition and low friction tribofilm formation/removal in boundary lubrication, *Tribol. Int.* 40 (2007) 1696–1704.
- [239] A. Morina, A. Neville, M. Priest, J.H. Green, ZDDP and MoDTC interactions and their effect on tribological performance - Tribofilm characteristics and its evolution, *Tribol. Lett.* 24 (2006) 243–256.
- [240] M. Kasrai, J.N. Cutler, K. Gore, G. Canning, G.M. Bancroft, K.H. Tan, The chemistry of antiwear films generated by the combination of zddp and modtc examined by x-ray absorption spectroscopy, *Tribol. Trans.* 41 (1998) 69–77.
- [241] A. Morina, A. Neville, M. Priest, J.H. Green, ZDDP and MoDTC interactions in boundary lubrication—The effect of temperature and ZDDP/MoDTC ratio, *Tribol. Int.* 39 (2006) 1545–1557.
- [242] K. Topolovec Miklozic, H.A. Spikes, Application of atomic force microscopy to the study of lubricant additive films, *J. Tribol.* 127 (2005) 405–415.
- [243] D. Xu, C. Wang, C. Espejo, J. Wang, A. Neville, A. Morina, Understanding the Friction Reduction Mechanism Based on Molybdenum Disulfide Tribofilm Formation and Removal, *Langmuir*. 34 (2018) 13523–13533.
- [244] M.I. De Barros Bouchet, J.M. Martin, T. Le Mogne, P. Bilas, B. Vacher, Y. Yamada, Mechanisms of MoS<sub>2</sub> formation by MoDTC in presence of ZnDTP: effect of oxidative degradation, *Wear*. 258 (2005) 1643–1650.
- [245] Y. Sogawa, N. Yoshimura, H. Iwasaki, R&D on New Friction Modifier for Lubricant for Fuel economy improvement, Japan Pet. Energy Cent. Rep. E 1. 1 (2000) 1–14.
- [246] J.M. Martin, C. Grossiord, K. Varlot, B. Vacher, J. Igarashi, Synergistic effects in binary systems of lubricant additives: A chemical hardness approach, *Tribol. Lett.* 8 (2000) 193–201.
- [247] J. Graham, H. Spikes, R. Jensen, The friction reducing properties of molybdenum dialkyldithiocarbamate additives: part ii - durability of friction reducing capability, *Tribol. Trans.* 44 (2001) 637–647.
- [248] G.E. Morales-espejel, P. Rycerz, A. Kadiric, Prediction of micropitting damage in gear teeth contacts considering the concurrent effects of surface fatigue and mild wear, *Wear*. 398 (2018) 99–115.
- [249] E. Lainé, A. V. Olver, T.A. Beveridge, Effect of lubricants on micropitting and wear, *Tribol. Int.* 41 (2008) 1049–1055.
- [250] C. Benyajati, A. V. Olver, The effect of a ZnDTP anti-wear additive on micropitting



- resistance of carburised steel rollers, AGMA. (2004) 1–10.
- [251] C. Benyajati, A. V. Olver, C.J. Hamer, An experimental study of micropitting, using a new miniature test-rig, *Tribol. Ser.* 43 (2003) 601–610.
  - [252] E. Lainé, A. V. Olver, M.F. Lekstrom, B.A. Shollock, T.A. Beveridge, D.Y. Hua, The effect of a friction modifier additive on micropitting, *Tribol. Trans.* 52 (2009) 526–533.
  - [253] J. Huang, T. Shinohara, S. Tsujikawa, Effects of interfacial iron oxides on corrosion protection of carbon steel by TiO<sub>2</sub> coating under illumination, *Zairyo-to-Kankyo.* 46 (1997) 651–661.
  - [254] C.H. Hager, R.D. Evans, Friction and wear properties of black oxide surfaces in rolling/sliding contacts, *Wear.* 338–339 (2015) 221–231.
  - [255] A. Mihailidis, C. Salpistis, K. Panagiotidis, C. Sachanas, S. Gatsios, C. Hoffinger, V. Bakolas, Wear and smearing resistance of black iron mixed oxide coated steels, *Int. J. Surf. Sci. Eng.* 4 (2010) 337–359.
  - [256] M. Fowell, S. Ioannides, A. Kadiric, An Experimental Investigation into the Onset of Smearing Damage in Nonconformal Contacts with Application to Roller Bearings, *Tribol. Trans.* 57 (2014) 472–488.
  - [257] M.H. Evans, An updated review: white etching cracks (WECs) and axial cracks in wind turbine gearbox bearings, *Mater. Sci. Technol.* 32 (2016) 1133–1169.
  - [258] H.A. Al-Tameemi, H. Long, R.S. Dwyer-Joyce, Damage characterisation of white etching cracks in a black oxide coated wind turbine gearbox bearing, *Wear.* 432–433 (2019) 102923.
  - [259] R. Stadler, K., Han, B., Brizmer, V., and Pasaribu, Benefits of Using Black Oxidized Bearings in Wind Applications, *SKF Evol.* (2015).
  - [260] V. Brizmer, K. Stadler, M. van Drogen, B. Han, C. Matta, E. Piras, The Tribological Performance of Black Oxide Coating in Rolling/Sliding Contacts, *Tribol. Trans.* 60 (2017) 557–574.
  - [261] K. Ito, J.M. Martin, C. Minfray, K. Kato, Formation mechanism of a low friction ZDDP tribofilm on iron oxide, *Tribol. Trans.* 50 (2007) 211–216.
  - [262] G.M. Hamilton, L.E. Goodman, The stress field created by a circular sliding contact, *J. Appl. Mech. Trans. ASME.* 33 (1964) 371–376.
  - [263] A. Otsuka, H. Sugawara, M. Shomura, A test method for mode II fatigue crack growth relating to a model for rolling contact fatigue, *Fatigue Fract. Eng. Mater. Struct.* 19 (1996) 1265–1275.
  - [264] T.E. Tallian, Simplified contact fatigue life prediction model-part I: Review of published models, *J. Tribol.* 114 (1992) 207–213.

- [265] A. V. Olver, The mechanism of rolling contact fatigue: an update, *Proc. Inst. Mech. Eng. Part J J. Eng. Tribol.* 219 (2005) 313–330.
- [266] P. Rycerz, A. V. Olver, A. Kadiric, Propagation of surface initiated rolling contact fatigue cracks in bearing steel, *Int. J. Fatigue.* 97 (2017).
- [267] E. Ioannides, T.A. Harris, A new fatigue life model for rolling bearings, *J. Tribol.* 107 (1985) 367–377.
- [268] M. Kaneta, M. Suetsugu, Y. Murakami, Mechanism of surface crack growth in lubricated rolling/ sliding spherical contact, *J. Appl. Mech. Trans. ASME.* 53 (1986) 354–360.
- [269] A.F. Bower, The Influence of Crack Face Friction and Trapped Fluid on Surface Initiated Rolling Contact Fatigue Cracks, *J. Tribol.* 110 (1988) 704.
- [270] R. Balcombe, M.T. Fowell, A. V. Olver, S. Ioannides, D. Dini, A coupled approach for rolling contact fatigue cracks in the hydrodynamic lubrication regime: The importance of fluid/solid interactions, *Wear.* 271 (2011) 720–733.
- [271] P. Rycerz, A. Kadiric, The Influence of Slide–Roll Ratio on the Extent of Micropitting Damage in Rolling–Sliding Contacts Pertinent to Gear Applications, *Tribol. Lett.* 67 (2019) 63.
- [272] S. Soltanahmadi, A. Morina, M.C.P. Van Eijk, I. Nedelcu, A. Neville, Investigation of the effect of a diamine-based friction modifier on micropitting and the properties of tribofilms in rolling-sliding contacts, *J. Phys. D. Appl. Phys.* 49 (2016) 505302.
- [273] X. Li, B. Bhushan, A review of nanoindentation continuous stiffness measurement technique and its applications, *Mater. Charact.* 48 (2002) 11–36.
- [274] K.K. Kanazawa, J.G.G. II, The oscillation frequency of a quartz resonator in contact with liquid, *Anal. Chim. Acta.* 175 (1985) 99–105.
- [275] K.K. Kanazawa, J.G. Gordon, Frequency of a quartz microbalance in contact with liquid, *Anal. Chem.* 57 (1985) 1770–1771.
- [276] D. Berman, J. Krim, Impact of oxygen and argon plasma exposure on the roughness of gold film surfaces, *Thin Solid Films.* 520 (2012) 6201–6206.
- [277] M. Ueda, A. Kadiric, H.A. Spikes, On the Crystallinity and Durability of ZDDP Tribofilm, *Tribol. Lett.* 67 (2019) 1–13.
- [278] W. Willermet, P. A., Dailey, D. P., Carter Iii, R. O., Schmitz, P. J., & Zhu, W. Dailey, D. P., Carter Iii, R. O., Schmitz, P. J., & Zhu, Mechanism of formation of antiwear films from zinc dialkyldithiophosphates, *Tribol. Int.* 28 (1995) 177–187.
- [279] A. V Serguee, C. Song, R.Z. Valie, A.K. Mukherjee, Structure and properties of amorphous and nanocrystalline NiTi prepared by severe plastic deformation and annealing, *Mater. Sci. Eng. A.* 339 (2003) 159–165.

- [280] C. Fan, D. V. Louzguine, C. Li, and A. Inoue, Nanocrystalline composites with high strength obtained in Zr–Ti–Ni–Cu–Al bulk amorphous alloys, *Appl. Phys. Lett.* 75 (1999) 340.
- [281] S.J. Kalita, A. Bhardwaj, H.A. Bhatt, Nanocrystalline calcium phosphate ceramics in biomedical engineering, *Mater. Sci. Eng. C* 27 (2007) 441–449.
- [282] J.M. Martin, T. Onodera, M.I. De Barros Bouchet, N. Hatakeyama, A. Miyamoto, Anti-wear chemistry of ZDDP and calcium borate nano-additive. Coupling experiments, chemical hardness predictions, and MD calculations, *Tribol. Lett.* 50 (2013) 95–104.
- [283] M.A. Nicholls, T. Do, P.R. Norton, M. Kasrai, G.M. Bancroft, Review of the lubrication of metallic surfaces by zinc dialkyl-dithiophosphates, *Tribol. Int.* 38 (2005) 15–39.
- [284] A. Ghanbarzadeh, M. Wilson, A. Morina, D. Dowson, A. Neville, Development of a new mechano-chemical model in boundary lubrication, *Tribology Int.* 93 (2016) 573–582.
- [285] B. Vengudusamy, J.H. Green, G.D. Lamb, H.A. Spikes, Durability of ZDDP tribofilms formed in DLC/DLC contacts, *Tribol. Lett.* 51 (2013) 469–478.
- [286] M. Ueda, A. Kadiric, H. Spikes, Influence of Steel Surface Composition on ZDDP Tribofilm Growth Using Ion Implantation, *Tribol. Lett.* (2021) 1–14.
- [287] N.N. Gosvami, I. Lahouij, J. Ma, R.W. Carpick, Nanoscale in situ study of ZDDP tribofilm growth at aluminum-based interfaces using atomic force microscopy, *Tribol. Int.* 143 (2020) 106075.
- [288] K. Pagkalis, Influence of steel composition on the formation and effectiveness of lubricant boundary layers in tribological contacts, PhD Thesis, Imp. Coll. London. (2017).
- [289] M. Iwaki, Tribological Properties of Ion-implanted steels, *Mater. Sci. Eng.* 90 (1987) 263–271.
- [290] D.Q. Peng, X.D. Bai, X.W. Chen, Q.G. Zhou, X.Y. Liu, R.H. Yu, P.Y. Deng, Effect of Ni Ion Implantation on Corrosion Behavior of Zircaloy-4 in 0.5 M H<sub>2</sub>SO<sub>4</sub>, *J. Electrochem. Soc.* 151 (2004) B491.
- [291] F.A. Smidt, Recent advances in the application of ion implantation to corrosion and wear protection, *Nucl. Instruments Methods Phys. Res. Sect. B Beam Interact. with Mater. Atoms.* 10 (1985) 532–538.
- [292] N. Akbas, A. Oztarhan, O.R. Monteiro, I.G. Brown, Investigation on the tribology of Zr ion implanted tool steel, *Wear.* 252 (2002) 540–545.
- [293] M. Li, É.J. Knystautas, M. Krishnadev, Enhanced microhardness of four modern

- steels following nitrogen ion implantation, *Surf. Coatings Technol.* 138 (2001) 220–228.
- [294] D.H. Yang, Q.J. Xue, X.S. Zhang, H.Q. Wang, W.L. Lin, X.J. Ding, The influence of ion-implanted Mo on the tribological behavior of iron lubricated with oil containing antiwear additives, *Wear*. 173 (1994) 129–135.
- [295] D. Yang, J. Zhou, Q. Xue, Study of the tribochemical behavior of Al ion-implanted pure iron lubricated with ZDDP, *Surf. Coatings Technol.* 102 (1998) 223–232.
- [296] C.D. Warren, J.J. Wert., The influence of implanted transition metal ions on the adhesive wear of iron, *Wear*. 134 (1989) 149–164.
- [297] R. Saha, W.D. Nix, Effects of the substrate on the determination of thin film mechanical properties by nanoindentation, *Acta Mater.* 50 (2002) 23–38.
- [298] C. Notthoff, M. Winterer, A. Beckel, M. Geller, J. Heindl, Spatial high resolution energy dispersive X-ray spectroscopy on thin lamellas, *Ultramicroscopy*. 129 (2013) 30–35.
- [299] K.S. Kim, N. Winograd, X-ray photoelectron spectroscopic studies of nickel-oxygen surfaces using oxygen and argon ion-bombardment, *Surf. Sci.* 43 (1974) 625–643.
- [300] M.C. Biesinger, B.P. Payne, A.P. Grosvenor, L.W.M. Lau, A.R. Gerson, R.S.C. Smart, Resolving surface chemical states in XPS analysis of first row transition metals, oxides and hydroxides: Cr, Mn, Fe, Co and Ni, *Appl. Surf. Sci.* 257 (2011) 2717–2730.
- [301] A. Kocijan, I. Milošev, B. Pihlar, Cobalt-based alloys for orthopaedic applications studied by electrochemical and XPS analysis, *J. Mater. Sci. Mater. Med.* 15 (2004) 643–650.
- [302] J. Baltrusaitis, B. Mendoza-sanchez, V. Fernandez, R. Veenstra, N. Dukstiene, A. Roberts, N. Fairley, Applied Surface Science Generalized molybdenum oxide surface chemical state XPS determination via informed amorphous sample model, *Appl. Surf. Sci.* 326 (2015) 151–161.
- [303] J. Mendialdua, R. Casanova, Y. Barbaux, XPS studies of V<sub>2</sub>O<sub>5</sub>, V<sub>6</sub>O<sub>13</sub>, VO<sub>2</sub> and V<sub>2</sub>O<sub>3</sub>, *J. Electron Spectros. Relat. Phenomena*. 71 (1995) 249–261.
- [304] J.C. Phillips, Ionicity of the chemical bond in crystals, *Rev. Mod. Phys.* 42 (1970) 317.
- [305] F. Gao, J. He, E. Wu, S. Liu, D. Yu, D. Li, S. Zhang, Y. Tian, Hardness of Covalent Crystals, *Phys. Rev. Lett.* 91 (2003) 1–4.
- [306] M. Lenglet, Iono-covalent character of the metal-oxygen bonds in oxides: A comparison of experimental and theoretical data, *Act. Passiv. Electron.*

- Components. 27 (2004) 1–60.
- [307] W.G. Jones, M.I. Pope, The heats of adsorption of zinc di n-alkyl dithio phosphates onto pure iron, cast iron and ferric oxide surfaces, *Thermochim. Acta.* 130 (1988) 141–148.
  - [308] M. Ueda, A. Kadiric, H. Spikes, ZDDP Tribofilm Formation on Non-Ferrous Surfaces, *Tribol. Online.* 15 (2020) 318–331.
  - [309] Y. Tanita, T. Mine, K. Nakajima, Tribological reaction generated on ceramic - steel couples under boundary lubrication, *J. Tribol.* 112 (1990) 637–642.
  - [310] X. Zhao, J. Liu, B. Zhu, H. Miao, Z. Luo, Effects of antiwear additives on the friction and wear of Si<sub>3</sub>N<sub>4</sub>/steel sliding contacts, *Wear.* 201 (1996) 99–105.
  - [311] M. Burkinshaw, A. Neville, A. Morina, M. Sutton, ZDDP and its interactions with an organic antiwear additive on both aluminium-silicon and model silicon surfaces, *Tribol. Int.* 69 (2014) 102–109.
  - [312] F.X. Wang, Y.Q. Cheng, D.H. Guan, On the tribological behavior and surface analysis of a sliding PSZ ceramic-steel pair, *J. Tribol.* 117 (1995) 548–552.
  - [313] B. Vengudusamy, J.H. Green, G.D. Lamb, H.A. Spikes, Tribological properties of tribofilms formed from ZDDP in DLC/DLC and DLC/steel contacts, *Tribol. Int.* 44 (2011) 165–174.
  - [314] S. Equey, S. Roos, U. Mueller, R. Hauert, N.D. Spencer, R. Crockett, Tribofilm formation from ZnDTP on diamond-like carbon, *Wear.* 264 (2008) 316–321.
  - [315] B. Vengudusamy, J.H. Green, G.D. Lamb, H.A. Spikes, Influence of hydrogen and tungsten concentration on the tribological properties of DLC/DLC contacts with ZDDP, *Wear.* 298–299 (2013) 109–119.
  - [316] S. Equey, S. Roos, U. Mueller, R. Hauert, N.D. Spencer, R. Crockett, Reactions of zinc-free anti-wear additives in DLC/DLC and steel/steel contacts, *Tribol. Int.* 41 (2008) 1090–1096.
  - [317] H. Abdullah Tasdemir, T. Tokoroyama, H. Kousaka, N. Umehara, Y. Mabuchi, Influence of zinc dialkyldithiophosphate tribofilm formation on the tribological performance of self-mated diamond-like carbon contacts under boundary lubrication, *Thin Solid Films.* 562 (2014) 389–397.
  - [318] J.S. Sheasby, T.A. Caughlin, W.A. Mackwood, A comparison of the boundary lubrication of 52100 steel, zirconia and silicon nitride by S, P, S/P and zinc dialkyldithiophosphate additives, *Wear.* 196 (1996) 100–109.
  - [319] J.F. Archard, The temperature of rubbing surfaces, *Wear.* 2 (1959) 438–455.
  - [320] T. Reddyhoff, A. Schmidt, H. Spikes, Thermal Conductivity and Flash Temperature, *Tribol. Lett.* 67 (2019) 1–9.

- [321] A. Rossi, F.M. Piras, D. Kim, A.J. Gellman, N.D. Spencer, Surface reactivity of tributyl thiophosphate: Effects of temperature and mechanical stress, *Tribol. Lett.* 23 (2006) 197–208.
- [322] C. Rincón, G. Zambrano, A. Carvajal, P. Prieto, H. Galindo, E. Martínez, A. Lousa, J. Esteve, Tungsten carbide/diamond-like carbon multilayer coating on steel for tribological applications, *Surf. Coatings Technol.* 148 (2001) 277–283.
- [323] N.D.S. M. Eglin, A. Rossi, F.M. Piras, in *Surface Science Spectra*, Am. Chem. Soc. 8 (2002) 97.
- [324] M. Ueda, A. Kadiric, H. Spikes, Wear of hydrogenated DLC in MoDTC-containing oils, *Wear.* 474–475 (2021) 203869.
- [325] B. Vengudusamy, J.H. Green, G.D. Lamb, H.A. Spikes, Behaviour of MoDTC in DLC/DLC and DLC/steel contacts, *Tribol. Int.* 54 (2012) 68–76.
- [326] M. Masuko, T. Ono, S. Aoki, A. Suzuki, H. Ito, Tribology International Friction and wear characteristics of DLC coatings with different hydrogen content lubricated with several Mo-containing compounds and their related compounds, *Tribology Int.* 82 (2015) 350–357.
- [327] T. Shinyoshi, Y. Fuwa, Y. Ozaki, Wear Analysis of DLC Coating in Oil Containing Mo-DTC, *SAE Tech. Pap.* 2007-01-19 (2007) 956–960.
- [328] K. Ohara, K. Hanyuda, Y. Kawamura, K. Omura, I. Kameda, N. Umehara, H. Kousaka, Analysis of Wear Track on DLC Coatings after Sliding with MoDTC-Containing Lubricants, *Tribol. Online.* 12 (2017) 110–116.
- [329] Y. Yoshida, S. Kunitsugu, Friction wear characteristics of diamond-like carbon coatings in oils containing molybdenum dialkyldithiocarbamate additive, *Wear.* 414–415 (2018) 118–125.
- [330] K.A.M. Kassim, T. Tokoroyama, M. Murashima, N. Umehara, The wear classification of MoDTC-derived particles on silicon and hydrogenated diamond-like carbon at room temperature, *Tribol. Int.* 147 (2020) 106176.
- [331] C. Espejo, B. Thiébaud, F. Jarnias, C. Wang, A. Neville, A. Morina, MoDTC Tribochemistry in Steel/Steel and Steel/Diamond-Like-Carbon Systems Lubricated With Model Lubricants and Fully Formulated Engine Oils, *J. Tribol.* 141 (2018) 012301.
- [332] H. Okubo, S. Sasaki, D. Lancon, F. Jarnias, B. Thiébaud, Tribo-Raman-SLIM observation for diamond-like carbon lubricated with fully formulated oils with different wear levels at DLC/steel contacts, *Wear.* 454 (2020) 203326.
- [333] T. Kaneko, K. Yamamori, H. Suzuki, K. Onodera, S. Ogano, Friction Reduction Technology for Low Viscosity Engine Oil Compatible with LSPI Prevention

- Performance, SAE Tech. Pap. 1 (2016).
- [334] P. Erdemir, A., Bindal, C., Pagan, J. and Wilbur, Characterization of transfer layers on steel surfaces sliding against diamondlike carbon in dry nitrogen, *Surf. Coatings Technol.* 76 (1995) 559–563.
  - [335] F. Rabbani, Phenomenological evidence for the wear-induced graphitization model of amorphous hydrogenated carbon coatings, *Surf. Coatings Technol.* 184 (2004) 194–207.
  - [336] S. Kosarieh, A. Morina, E. Lainé, J. Flemming, A. Neville, Tribological performance and tribochemical processes in a DLC/steel system when lubricated in a fully formulated oil and base oil, *Surf. Coatings Technol.* 217 (2013) 1–12.
  - [337] A.J. Gant, M.G. Gee, L.P. Orkney, The wear and friction behaviour of engineering coatings in ambient air and dry nitrogen, *Wear.* 271 (2011) 2164–2175.
  - [338] Y. Niiyama, N. Shimizu, A. Kuwayama, H. Okada, T. Takeno, K. Kurihara, K. Adachi, Friction and Delamination Properties of Self-Mating Diamond-Like Carbon Coatings in Water, *Tribol. Lett.* 62 (2016) 1–7.
  - [339] T. Haque, A. Morina, A. Neville, Effect of friction modifiers and antiwear additives on the tribological performance of a hydrogenated DLC coating, *J. Tribol.* 132 (2010) 1–13.
  - [340] L. Cizaire, J.M. Martin, E. Gresser, N.T. Dinh, C. Heau, Tribochemistry of overbased calcium detergents studied by ToF-SIMS and other surface analyses, *Tribol. Lett.* 17 (2004) 715–721.
  - [341] A. Erdemir, G. Ramirez, O.L. Eryilmaz, B. Narayanan, Y. Liao, G. Kamath, S.K.R.S. Sankaranarayanan, Carbon-based tribofilms from lubricating oils, *Nature.* 536 (2016) 67–71.
  - [342] C. Grossiord, K. Varlot, J. Martin, T. Le Mogne, C. Esnouf, MoS<sub>2</sub> single sheet lubrication by molybdenum, *Tribol. Int.* 31 (1999) 737–743.
  - [343] M.I. De Barros'Bouchet, J.M. Martin, T. Le-Mogne, B. Vacher, Boundary lubrication mechanisms of carbon coatings by MoDTC and ZDDP additives, *Tribol. Int.* 38 (2005) 257–264.
  - [344] K. Arai, M. Yamada, S. Asano, S. Yoshizawa, H. Ohira, K. Hoshino, F. Ueda, K. Akiyama, Lubricant technology to enhance the durability of low friction performance of gasoline engine oils, SAE Tech. Pap. 104 (1995).
  - [345] M. Ueda, H. Spikes, A. Kadiric, In-situ observations of the effect of the ZDDP tribofilm growth on micropitting, *Tribol. Int.* 138 (2019) 342–352.
  - [346] A.V. Olver, *Wear of Hard Steel in Lubricated, Rolling Contact*, PhD Thesis, Imp. Coll. London. (1986).

- [347] F. Manieri, K. Stadler, G.E. Morales-Espejel, A. Kadiric, The origins of white etching cracks and their significance to rolling bearing failures, *Int. J. Fatigue*. 120 (2019) 107–133.
- [348] Y. Murakami, M. Kaneta, H. Yatsuzuka, Analysis of Surface Crack Propagation in Lubricated Rolling Contact, *ASLE Trans.* 28 (1985) 60–68.
- [349] T.H. Kim, A. V. Olver, Stress history in rolling-sliding contact of rough surfaces, *Tribol. Int.* 31 (1998) 727–736.
- [350] A. Kadiric, R.S. Sayles, X.B. Zhou, E. Ioannides, A Numerical Study of the Contact Mechanics and Sub-Surface Stress Effects Experienced Over a Range of Machined Surface Coatings in Rough Surface, *J. Trib.* 125 (2003) 720–730.
- [351] M. Ueda, H. Spikes, A. Kadiric, Influence of Black Oxide Coating on Micropitting and ZDDP Tribofilm Formation, *Tribol. Trans.* (2021) 1–21.
- [352] R. Glovnea, H. Fujita, H. Spikes, The behaviour of an anti-wear additive on different coatings in concentrated contacts, *Proc. Int. Conf. VAREHD 12 Suceava*. (2004).
- [353] Deutsches Institut für Normung E.V. (DIN), DIN 50938, Black Oxide Treatment of Ferrous Material; DIN 50938 Iron Oxide Coatings on Iron or Steel—Requirements and Test Methods, 2000.
- [354] R. Evans, C.H. Hager, Y.S. Kang, G. Doll, Comparison of black oxide and tungsten carbide–reinforced diamond-like carbon(wc/a-c:H) surface treatments for rolling element bearings, *Tribol. Trans.* 58 (2015) 444–453.
- [355] M.N. Webster, R.S. Sayles, A Numerical Model for the Elastic Frictionless Contact of Real Rough Surfaces, *J. Tribol.* 114 (1986) 334–340.
- [356] A. Kadiric, R.S. Sayles, E. Ioannides, Thermo-mechanical model for moving layered rough surface contacts, *J. Tribol.* 130 (2008).
- [357] M.H. Evans, White structure flaking (WSF) in wind turbine gearbox bearings: Effects of “butterflies” and white etching cracks (WECs), *Mater. Sci. Technol.* 28 (2012) 3–22.
- [358] J. Nyqvist, A. Kadiric, S. Ioannides, R. Sayles, Semi-analytical model for rough multilayered contacts, *Tribol. Int.* 87 (2015) 98–112.
- [359] E. V. Zaretsky, J. V. Poplawski, S.M. Peters, Comparison of life theories for rolling-element bearings, *Tribol. Trans.* 39 (1996) 237–248.
- [360] J. Guegan, A. Kadiric, H. Spikes, A Study of the Lubrication of EHL Point Contact in the Presence of Longitudinal Roughness, *Tribol. Lett.* 59 (2015) 1–18.
- [361] J. Guegan, A. Kadiric, A. Gabelli, H. Spikes, The Relationship Between Friction and Film Thickness in EHD Point Contacts in the Presence of Longitudinal



- Roughness, *Tribol. Lett.* 64 (2016) 1–15.
- [362] B. Mahmoudi, B. Tury, C.H. Hager, G.L. Doll, Effects of Black Oxide and a WC / a-C : H Coating on the Micropitting of SAE 52100 Bearing Steel, *Tribol. Lett.* 58 (2015) 20.
  - [363] M. Ueda, B. Wainwright, H. Spikes, A. Kadiric, The effect of friction on micropitting, *Wear*. 488–489 (2022) 204130.
  - [364] G.E. Morales-Espejel, V. Brizmer, Micropitting modelling in rolling–sliding contacts: Application to rolling bearings, *Tribol. Trans.* 54 (2011) 625–643.
  - [365] K.A. Matori, M.I. Sayyed, H.A.A. Sidek, M.H.M. Zaid, V.P. Singh, Comprehensive study on physical, elastic and shielding properties of lead zinc phosphate glasses, *J. Non. Cryst. Solids*. 457 (2017) 97–103.
  - [366] S.J. Cole, R.S. Sayles, A Numerical Model for the Contact of Layered Elastic Bodies With Real Rough Surfaces, *J. Tribol.* 114 (1992) 334–340.
  - [367] G.Z. Voyiadjis, R. Peters, Size effects in nanoindentation : an experimental, *Acta Mech.* 211 (2010) 131–153.
  - [368] W.D. Nix, H. Gao, Indentation size effects in crystalline materials: A law for strain gradient plasticity, *J. Mech. Phys. Solids*. 46 (1998) 411–425.
  - [369] Y. Enomoto, D. Tabor, The frictional anisotropy of diamond, *Proc. R. Soc. London. A. Math. Phys. Sci.* 373 (1981) 405–417.
  - [370] D.M. Bailey, R.S. Sayles, Effect of Roughness and Sliding Friction on Contact Stresses, *J. Tribol.* 113 (1991) 729–738.
  - [371] A.F. Bower, N.A. Fleck, Brittle fracture under a sliding line contact, *J. Mech. Phys. Solids*. 42 (1994) 1375–1396.
  - [372] A.P. Voskamp, Material response to rolling contact loading, *J. Tribol.* 107 (1984) 359–364.
  - [373] A. V. Olver, Micropitting and asperity deformation, *Dev. Numer. Exp. Methods Appl. to Tribol.* (1984) 319–323.
  - [374] T.E. Tallian, Y.P. Chiu, E. Van Amerongen, Prediction of traction and microgeometry effects on rolling contact fatigue life, *J. Tribol.* 100 (1978) 156–165.
  - [375] G.R. Miller, L.M. Keer, H.S. Cheng, The role of near-surface inclusions in the pitting of gears, *ASLE Trans.* 28 (1985) 111–116.
  - [376] I. Lee-Prudhoe, R.S. Sayles, A. Kadiric, Investigations into asperity persistence in heavily loaded contacts, *J. Tribol.* 121 (1999) 441–448.
  - [377] T.H.C. Childs, Persistence of Roughness Between Surfaces in Static Contact., *Proc R Soc London Ser A.* 353 (1977) 35–53.

- [378] K.L. Johnson, *Contact Mechanics*, 1987.
- [379] M. Kaneta, Y. Murakami, Effects of oil hydraulic pressure on surface crack growth in rolling/sliding contact, *Tribol. Int.* 20 (1987) 210–217.
- [380] A. V. Olver, L.K. Tiew, S. Medina, J.W. Choo, Direct observations of a micropit in an elastohydrodynamic contact, *Wear.* 256 (2004) 168–175.
- [381] W.J. Wang, R. Lewis, M.D. Evans, Q.Y. Liu, Influence of Different Application of Lubricants on Wear and Pre-existing Rolling Contact Fatigue Cracks of Rail Materials, *Tribol. Lett.* 65 (2017) 1–15.